



THE UNIVERSITY  
*of* ADELAIDE

**Development of New Generation**

**Chemoresistive VOC/Gas Sensors for Real-Field Applications**

By

**Kamrul Hassan**

Supervisors:

Professor Dusan Losic

Dr. Tran Thanh Tung

A thesis is submitted for the degree of

**Doctor of Philosophy**

In

School of Chemical Engineering and Advanced Materials

The University of Adelaide, Australia

November 2021

## Summary

Volatile organic compound (VOC) and gas sensors based on semiconducting metal oxides and metal oxide composites have paid much attention since 1960s due to their sensing capability. Compared to conventional methods (e.g., micro-extraction (SPME) and gas chromatography mass spectrometry (GC–MS)) for detecting VOCs and toxic gases, these fabricated devices are anticipated to play a vital role in personal healthcare, environmental protection, securities and industries. Consequently, in recent years, intensive research has been directed to advance their sensing deeds, predominantly to augment the sensitivity and limit of detection for such sensing devices. Besides, sensing technologies become the heart of the future intelligent system due to the prompt enhancement of the Internet of Things (IoT)-enabled real-field applications and associated automation. Sensor devices that can detect trace amounts of VOC/gas analytes presents the favourable ubiquitous nodes of these sensor platforms. For VOC/gas sensing application case selective, highly sensitive, and portable devices are required by employing the various gas sensing materials including metals, carbon nanotubes, conducting polymers, and two-dimensional (2D) materials for meeting the criteria of real-field application.

This thesis aims to develop chemoresistive sensors to address the challenges associated with current conventional sensors for VOC/gas detection by employing different fabrication methods. The specific objectives of this thesis are organized into seven chapters that will be presented in the form of a collection of the published papers which are the outcomes of the research. In addition, a literature review has been provided to establish the background of this research, which is also published in a review article. Overall, the main contributions of this thesis to the VOC/gas sensors field are designing and fabricating new sensing devices, and are summarized in following chapters:

- Chapter 3: Graphene inks for 3D extrusion micro printing of chemo-resistive sensing devices for VOCs detection (paper 1).
- Chapter 4: Fractal Design for Advancing the Performance of Chemoresistive Sensors (paper 2).
- Chapter 5: Extrusion printed CNT-graphene sensor array with embedded MXene/PEDOT: PSS heater for enhanced NO<sub>2</sub> sensing at low temperature (paper 3).
- Chapter 6: Fast response hydrogen gas sensor based on Pd/Cr nanogaps fabricated by a single-step bending deformation (paper 4).

## **Declaration**

I certify that this work contains no material which has been accepted for the award of any other degree or diploma in my name in any university or other tertiary institution and, to the best of my knowledge and belief, contains no material previously published or written by another person, except where due reference has been made in the text. In addition, I certify that no part of this work will, in the future, be used in a submission in my name for any other degree or diploma in any university or other tertiary institution without the prior approval of the University of Adelaide and where applicable, any partner institution responsible for the joint award of this degree.

The author acknowledges that copyright of published works contained within this thesis resides with the copyright holders of those works.

I give permission for the digital version of my thesis to be made available on the web, via the University's digital research repository, the Library Search and also through web search engines, unless permission has been granted by the University to restrict access for a period of time.

I acknowledge the support I have received for my research through the provision of an Australian Government Research Training Program Scholarship.

Kamrul Hassan

Date: November 10, 2021

## Acknowledgment

I would like to express my sincere appreciation to the following people and organizations, without whom this thesis would have not been possible.

- i. My principal supervisor **Professor Dusan Losic** for his valuable support, inspiration, and outstanding leadership throughout my Ph.D. journey. I have been so fortunate to be a member of a professional research group, where I have received significant support during stressful situations during my Ph.D. journey. His unwavering enthusiasm for discovering novel ideas always kept me constantly motivated for research. If it were not for him, I may not have discovered my desire for conducting research. It is difficult for me to express my sincere appreciation in few sentences to my supervisors.
- ii. My appreciation also extends to my co-supervisor **Dr. Tran Tung** for his highly precious advice, support, and assistance. His advice has been always so beneficial for me during my Ph.D. study.
- iii. I would like to convey my deepest appreciation to **Dr. Nathan Stanley, Le Yu, Dr. Pei Lay Yap, Dr. Hadi Rastin, Dr. Arash Mazinani, Dr. Julker Nine, Dr. Farzaneh Farivar, Mahnaz Dadkah Jazi, Dr. Grant Matthieson, and Dr. Jacqui McRae** for sharing their scientific insights and knowledge to help **for shaping** a better version of myself each day.
- iv. I also would like to thank the Adelaide microscopy, School of Chemical Engineering and Advanced Materials, and School of Petroleum Engineering for providing the support and facilities to proceed with this research.

Finally, I am indebted to my family and I would like to express my immense love and gratitude to my beloved father, mother, sister, and brothers for their never-ending support, inspiration, strength, and love. Especially, my lovely wife **Fatema-Tuz-Zohra Khanam** for his unconditional love, patience, and everlasting support to have brought me this far. Last but not least, I would like to dedicate my PhD to my lifeline, apple of my eye, my beloved son **Faizan Hassan**. Papa love you a lot **Faizan**,

**Kamrul Hassan**

## Publications

This Ph.D. thesis is submitted as a “thesis by publication” in accordance to the “Specifications for Thesis 2020” of The University of Adelaide. This thesis contains the following list of publications that resulted from my Ph.D candidature. The outcomes generated during my Ph.D candidature include 15 published journal papers (5 first-authored; 10 co-authored), 4 conference/workshop presentations and 2 awards.

### List of journal publications (first author):

1. **Hassan K**, Nine MJ, Tung TT, Stanley N, Yap PL, Rastin H, Yu L, Losic D, Functional inks and extrusion-based 3D printing of 2D materials: a review of current research and applications, **Nanoscale (IF. 7.79)**, 2021, 13, 5356-5368, [DOI: 10.1039/D0NR04933F](https://doi.org/10.1039/D0NR04933F)
2. **Hassan K**, Tung TT, Stanley N, Yap PL, Farivar F, Rastin H, Nine MJ, Losic D. Graphene ink for 3D extrusion micro printing of chemo-resistive sensing devices for volatile organic compound detection. **Nanoscale (IF. 7.79)**, 2021; 13, 5356-5368, [DOI: 10.1039/D1NR00150G](https://doi.org/10.1039/D1NR00150G)
3. **Hassan K**, Tung TT, Yap P.L, Rastin H, Stanley N, Nine MJ, Losic D, Fractal design for advancing performance of chemo-resistive sensors, **ACS Sensors (IF. 7.71)**, 2021, 6, 3685-3695, <https://doi.org/10.1021/acssensors.1c01449>
4. **Hassan K**, Tung TT, Yap PL, Nine MJ, Kim HC, Losic D. Extrusion printed CNT-graphene sensor array with embedded MXene/PEDOT:PSS heater for enhanced NO<sub>2</sub> sensing at low temperature. **Advanced Materials Interfaces (IF. 6.147)**, [DOI: 10.1002/admi.202101175](https://doi.org/10.1002/admi.202101175)
5. **Hassan K**, Tung TT, Yap PL, Nine MJ, Kim HC, Losic D. Fast response hydrogen gas sensor based on Pd/Cr nanogaps fabricated by a single-step bending deformation. **Analytica Chimica Acta (IF. 6.58)**, 1138 (2020), 49-58, [DOI: 10.1016/j.aca.2020.09.012](https://doi.org/10.1016/j.aca.2020.09.012)

### List of journal papers from collaboration (co-author):

1. Rastin H, Ramezanpour M, **Hassan K**, Mazinani A, Tung TT, Vreugde S, Losic D. 3D Bioprinting of a Cell-laden Antibacterial Polysaccharide Hydrogel

- Composite. **Carbohydrate Polymers** (IF. 9.38), 2021:117989, DOI: [10.1016/j.carbpol.2021.117989](https://doi.org/10.1016/j.carbpol.2021.117989)
2. Farivar F, Yap PL, **Hassan K**, Tung TT, Tran DNH, Pollard AJ, Losic D, Unlocking thermogravimetric analysis (TGA) in the fight against “Fake graphene” materials, **Carbon** (IF. 9.59), 179, 2021, 505-513. DOI: [10.1016/j.carbon.2021.04.064](https://doi.org/10.1016/j.carbon.2021.04.064)
  3. Rastin H, Mansouri N, Tran TT, **Hassan K**, Mazinani A, Ramezanzpour M, Yap P, Yu L, , Vreugde S, Losic D. Converging 2D Nanomaterials and 3D Bioprinting Technology: State-of-the-Art, Challenges and Potential Outlook in Biomedical Applications, **Advanced Healthcare Mater** (IF. 9.93), 2021, 2101439. DOI: [10.1002/adhm.202101439](https://doi.org/10.1002/adhm.202101439)
  4. Yap P. L., Md J. N., **Hassan K.**, Tung, T. T., Tran, D. N., & Losic, D. (2020). Graphene-based sorbents for multi-pollutants removal in water: A review of recent progress. **Advanced Functional Materials** (IF. 18.80), 2021, 31, 2007356. DOI: [10.1002/adfm.202007356](https://doi.org/10.1002/adfm.202007356)
  5. Rastin H, Zhang B, Mazinani A, **Hassan K**, Bi J, Tung TT, Losic D. 3D bioprinting of cell-laden electroconductive MXene nanocomposite bioinks. **Nanoscale** ((IF. 7.79), 2020;12(30):16069-16080. DOI: [10.1039/D0NR02581J](https://doi.org/10.1039/D0NR02581J)
  6. Rastin H, Zhang B, Bi J, **Hassan K**, Tung TT, Losic D. 3D printing of cell-laden electroconductive bioinks for tissue engineering applications. **Journal of Materials Chemistry B** (IF. 6.33), 2020;8(27):5862-5876. DOI: [10.1039/D0TB00627K](https://doi.org/10.1039/D0TB00627K)
  7. Yap P. L., Auyoong, Y. L., **Hassan K.**, Farivar, F., Tran, D. N. H., Ma, J., & Losic, D. Multithiol functionalized graphene bio-sponge via photoinitiated thiol-ene click chemistry for efficient heavy metal ions adsorption. **Chemical Engineering Journal** (IF. 13.27), 2020, 395, 124965. DOI: [10.1016/j.cej.2020.124965](https://doi.org/10.1016/j.cej.2020.124965)
  8. Yap P. L., **Hassan, K.**, Auyoong, Y. L., Mansouri, N., Farivar, F., Tran, D. N., & Losic, D. (2020). All-in-one bioinspired multifunctional graphene biopolymer foam for simultaneous removal of multiple water pollutants. **Advanced Materials Interfaces** (IF. 6.147), 2020, 2000664. DOI: [10.1002/admi.202000664](https://doi.org/10.1002/admi.202000664)
  9. Nine MJ, Hee AY, Tung TT, **Hassan K**, Losic D, Cross-overlapped flat-silver/hexagonal boron nitride for translucent heat-reflective coatings, **Applied Materials Today** (IF. 10.04), 20, 2020, 100764. DOI: [10.1016/j.apmt.2020.100764](https://doi.org/10.1016/j.apmt.2020.100764)

10. Tung TT, Tran MT, Feller J-F, Castro M, Ngo TV, **Hassan K**, Nine MJ, Losic D, Graphene and metal organic frameworks (MOFs) hybridization for tunable chemoresistive sensors for detection of volatile organic compounds (VOCs) biomarkers, **Carbon (IF. 9.59)**, 159, 2020, 333-344. [DOI: 10.1016/j.carbon.2019.12.010](https://doi.org/10.1016/j.carbon.2019.12.010)

### **List of conference/workshop presentations:**

1. **Hassan K**, Tung TT, Stanley N, Losic D., Extrusion micro-printing of conductive graphene composites for wearable electronics and sensing applications, ICONN, 2020. ([Oral presentation](#))
2. **Hassan K**, Tung TT, Stanley N, Losic D., A bio-inspired fractal designed high performance graphene ink based extrusion 3D printed breath sensor, Graphene and 2DM Industrial Forum, 2020. ([Oral presentation](#))
3. **Hassan K**, Tung TT, Stanley N, Losic D., Extrusion micro-printing of conductive graphene composites for wearable electronics and sensing applications, Graphene Hun Workshop, 2020. ([Poster presentation](#))
4. **Hassan K**, Tung TT, Losic D., Development of conductive graphene composites for extrusion-based 3D micro- printing and applied in sensing application. Adelaide-Chonqing Bilateral Research Webinar, 2020 ([Oral presentation](#))

### **List of awards:**

1. **Ph.D. Scholarship** – Research Training Program Scholarship (2018), Australia
2. **Top-up scholarship from ARC Graphene Research Hub**, Australia.

# Contents



<b>Summary</b> .....	<b>ii</b>
<b>Declaration</b> .....	<b>iii</b>
<b>Acknowledgment</b> .....	<b>iv</b>
<b>Publications</b> .....	<b>v</b>
<b>Chapter 1: Introduction and motivation</b> .....	<b>1</b>
1.1 Abstract.....	2
1.2 Research motivation.....	2
1.3 Research gaps.....	9
1.4 Research aims and questions.....	10
1.5 Hypothesis.....	11
1.6 Thesis outline .....	11
1.7 Format .....	14
1.8 References.....	14
<b>Chapter 2: Literature review</b> .....	<b>20</b>
<b>Chapter 3: Development of graphene ink for VOC detection</b> .....	<b>61</b>
<b>Chapter 4: Development of fractal designed VOC sensors</b> .....	<b>82</b>
<b>Chapter 5: Development of CNT-graphene sensor array for NO<sub>2</sub> sensing</b> .....	<b>103</b>
<b>Chapter 6: Development of Pd/Cr nanogap for H<sub>2</sub> sensing</b> .....	<b>127</b>
<b>Chapter 7: Conclusion and future directions</b> .....	<b>144</b>
7.1 Conclusion .....	145
7.2 Some challenges of performed PhD study .....	147
7.3 Recommendations for Future work.....	149



This page is left blank intentionally

# Chapter 1



## Introduction and motivation

---

**I**n this chapter, various types of designed sensor devices for detecting VOCs/gas are introduced. This chapter also highlights numerous sensing materials and device fabrication techniques that are prominent by addressing the challenges associated with conventional methods. Finally, this chapter discusses the motivation of this research, and current main research gaps, and subsequent research aims.

---

## 1.1 Abstract

The rapid advancement of the Internet of Things (IoT)-enabled applications and associated automation are progressively creating sensing technologies to be the heart of future intelligent systems. The prospective applications have wide-ranging implications, from chemical process control, industrial manufacturing, agriculture, environmental and nature conservation, to personal health monitoring, national defense and smart cities. Sensor devices that can detect trace amounts of volatile organic compounds/gas (VOC/gas) analytes present the most ubiquitous of these sensor networks. Specifically, the advent of nanostructured materials has considerably transformed this area. Selective, highly sensitive, and portable sensing devices are now imaginable because of the favorable transport characteristics, large surface to volume ratios, and tunable surface chemistry of the sensing materials. Most of the research in sensing field in past was mainly focused by developing the sensing materials to detect VOCs/gases with conventional sensor fabrication techniques using conventional materials such as metal oxides. In recent years advanced sensor fabrication methods based on printing and advanced manufacturing is under the spotlight by providing the enhanced sensor performance. The primary aim of this thesis is to present the development of new generation chemoresistive VOC/gas sensors by employing extrusion printing and new materials with advanced sensor architecture for real-field applications.

## 1.2 Research background and motivation

The emission of organic compounds such as alcohols, amides, carbonyls, alkenes, alkanes, aromatics, esters, and ethers result from our daily activities of cooking, driving a car, making a fire, painting the house, using pesticides, building materials or breathing. In general, organic compounds are released to the atmosphere because of the humans daily life activity [1]. From the beginning of industrial revolution, many industries for example petroleum industries have emitted anthropogenic contaminants including volatile organic compounds (VOCs) and toxic gases [2]. Petrochemical processes, petroleum refining waste water, water separation techniques, batch processes, natural gas processing, and paints are the common sources of emitting high levels of VOC's including vent gas. As a result, the resulting effect on the air purity due to the increased emission of VOC/gases is now considered as a vital concern.

In indoors, the density of VOCs are much higher compared to outdoors (> 10 times). Most importantly, more than 300 different types of VOCs may be detected in the air of homes, offices, commercial buildings, and schools at any given time [3]. Also, significant amounts of

VOCs are released into the air during the time of personal endeavour products uses. That is why, to evaluate the air quality of indoor atmosphere VOCs level is used as parameter [4].

Regarding the potential hazards of VOCs, several environmental safety agencies, such as the European Agency for Safety and Health at Work (EU-OSHA), National Institute of Occupational Safety (NIOSH), and Environmental Protection Agency (EPA), have established regulations on the uses of VOCs/gas for mankind within indoor and workplace atmosphere because of their unfavourable impacts on health [5].

In nature, some of the VOCs/gases have been acknowledged as highly toxic due to their long-term effects on human health as well as on the ecosystem. As a well-known example of carcinogenic substance, benzene has potential to damage humans both systematically (e.g., circulatory, nervous, reproductive, cardiovascular, immune, and respiratory systems) and specifically (e.g., kidneys, spleen, stomach, and the liver). Sick building syndrome (SBS), such as nausea, headaches, cough, eye irritation, etc are other examples of building occupants because of the odor, temperature, particulate matter and VOCs [6].

That is why, for the health monitoring and human well-being along with the control of atmospheric environment, there is a need for effective approaches to monitor VOCs/gases. For the precise quantification of VOCs, several highly sensitive analytical techniques including gas chromatography (GC) [7], spectrophotometry [8], and high performance liquid chromatography (HPLC) [9] have been used. However, despite their precision, these techniques usually have some drawbacks, such as lack of portability, great capital expense, low throughput, and high-power demand. Moreover, highly skilled operators along with the complex and time consuming pre-treatment steps are also required for these techniques. In addition, due to the involvements of on-site sampling of indoor air, the conventional procedure used for monitoring indoor VOCs is generally time-consuming. Clearly, real-time information cannot be accumulated from these procedures in the time frame of VOC/gas exposure. Therefore, small, inexpensive, and user-friendly gas sensing devices are much desired [10]. This is currently very demanding research field attracting many research groups working on development of small, inexpensive and fast VOCs/gas sensors for specific applications with high selectivity, sensitivity and stability [11]. Based on different sensing principles, e.g. gravimetric, electrochemical, optical, resistive, etc., a wide variety of VOCs/gas sensors and devices were demonstrated [5]. Different types of VOC/gas sensors with their features are presented in Figure.1 and Table 1.

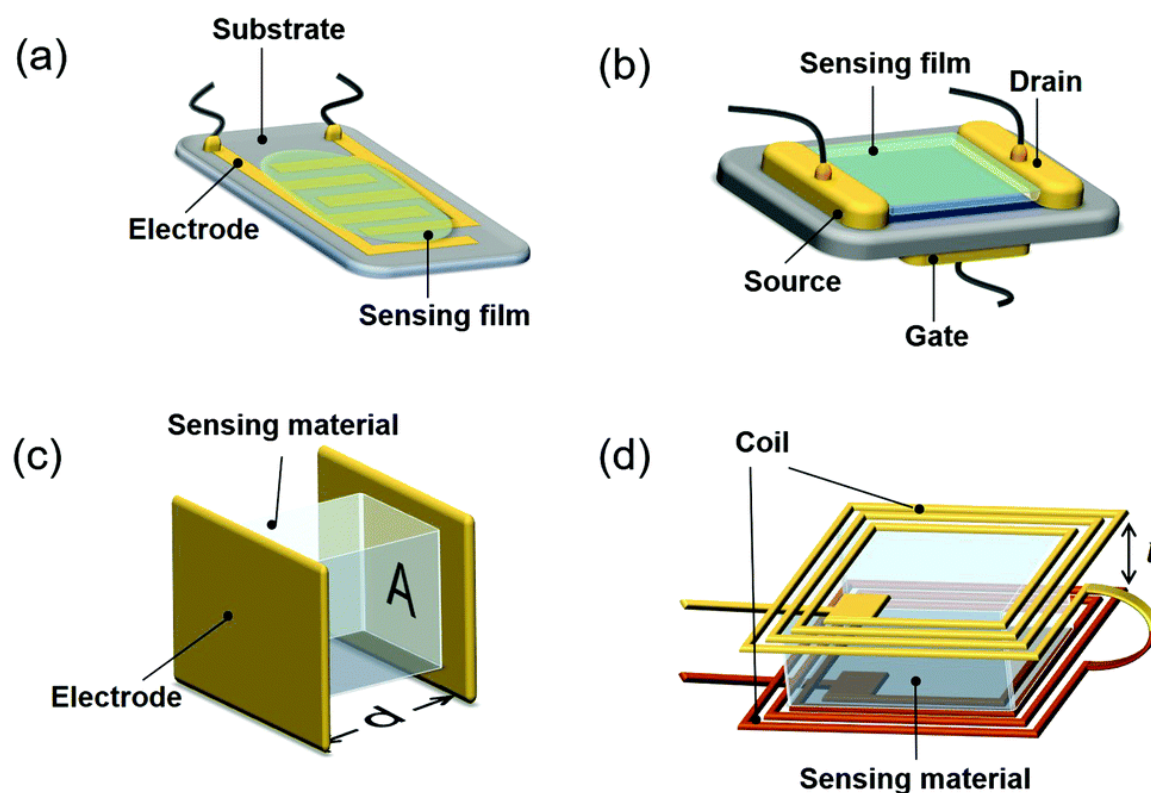


**Figure.1** Schematic illustration of (a) chemiresistive, (b) FET, (c) capacitive and (d) inductive gas sensors. [10] Copyright (2020) RSC

**Table 1:** Comparison table for different types of VOC sensors with their different parameters and working principal [12], [13]

Different types of sensors		Thermoconductive	Optical	Catalytic	Electrochemical	Resistive
Characterization parameters		Temperature Resistance Voltage	Transmission Reflectance Polarization Phase shift	Temperature Resistance	Potential current	Resistance
	Response time	Good	Good	Good	Poor	Excellent
	Sensitivity	Not good	Excellent	Good	Good	Excellent
	Stability	Good	Excellent	Good	Not good	Good
	Accuracy	Good	Excellent	Good	Good	Good

Parameters	Selectivity	Not good	Excellent	Not good	Good	poor
	Durability	Good	Excellent	Good	Poor	Good
	Portability	Good	Not good	Excellent	Poor	Excellent
	Cost	Cheap	Expensive	Cheap	Cheap	Cheap
	Maintenance	Good	Good	Excellent	Good	Excellent
	Safety	Good	Excellent	Risky	Excellent	Excellent
	Life time	Excellent	Good	Excellent	poor	Good

Until now, for a particular application, not a single sensor technology demonstrates optimal performance for multiple applications. Among all kinds of sensors, chemo-resistive type sensors based on polymers, graphene composites, carbon nanotubes, metal and metal oxide nanoparticles showed prominent performance for monitoring harmful VOCs. These types of sensors showed promising results because of their high sensitivity, ease of use, strong response, small dimensions, simple design, portability, rapid response time, on-line operation, compact size, low detection limits, and low power consumption [14], [15].

Lately, based on their enriched and improved lifetime, wearable sensors have attracted remarkable attentions [16]. Most importantly, these type of sensors can monitor the presence of VOCs produced or surrounding by human body in real time, which increases the demand in daily life applications. These characteristics are applicable in various applications such as energy harvesting [17], environment monitoring [18], point of care diagnostic, security and defence [19]. However, the development of wearable and wireless sensing devices is still at its beginning stages.

One of the important parameters to synthesize wearable sensors is miniaturizing the size of sensing material down to micro/nano scale. With the help of MEMS technology, the world smallest metal oxide VOC sensor was first introduced by the Figaro Engineering Inc. for the monitoring of indoor air quality. However, after packaging, dimensions of this sensors are increased in millimeter range which is likely to cause uneasiness when it is worn on skin. Moreover, with the miniature size of sensing elements, sensors are also required to stringent sensing atmosphere, such as customized gas chamber including gas delivering channels. Otherwise, the sensors goes to the saturated stage by interfacing with the atmosphere. That is why, it will be very difficult to miniaturize the gas sensing device by using this customized channels on rigid substrates, and as a result it is not possible to make this device comfortable for human being to be directly worn on skin.

In contrast, fabricating flexible sensors composed of sensing materials, flexible substrate, and electrodes may be a solution to offer wearable devices for mankind. Due to the movements of human body, all these types of sensors are mechanically deformable and durable. For this reason, sensor dimensions are not much concern regarding the issue of wearability. Until today, several types of flexible sensors were reported, where sensing materials are usually based on nano scale materials [20], [21], conductive polymers [22], and nanocomposites [23]. Moreover, most of these sensors are synthesized by low-cost and simple methods, such as dip coating [24], inkjet printing [25], and spin coating [26], [27], which is preferable for disposable consumer products used in rustic areas. Especially, for flexible sensors, response to strain issue should be solved for achieving the clear response to various gas analytes [28].

Last few decades, carbon nanotubes (CNT) have attracted more technological interest among the researchers because of their nanoscale size for nano-device fabrication, rapid response time, and high sensitivity [29]. That's why, for the development of next generation sensors, CNT is considered as a promising candidate. However, because of the toxicity properties of CNT it has some limitations to apply in direct contact with living organisms or food [30]. Lately, for the configuration of two-dimensional monolayer of  $sp^2$ -bonded carbon atoms, graphene illustrates outstanding optoelectronic properties, which exhibits potentiality of several applications including supercapacitors, transistors, transparent electrodes and sensors [31], [32]. Among several forms of graphene, chemically modified reduced graphene oxide (rGO) contains different oxygen functional groups, such as alcohols, carboxylic acids, and epoxides. Moreover, as a molecular sensors, rGO is considered to be a promising candidate because of its different range of surface sites and accessible surface area sensitive to adsorption/desorption of molecules. For this reason, for detecting several gas molecules including methanol, methyl acetate, acetone, toluene,  $NH_3$ , and  $NO_2$ , rGO-based sensors have been used [33], [34]. In addition, by using the hybridization techniques with metal nanoparticles (NP), response/recovery time and sensitivity of graphene to vapor can be enhanced. The hybridization of graphene with metal NP (i.e. Pt, Au, AgNP, and Pd) demonstrates the synergistic properties between them. However, this hybrid materials illustrates enhanced characteristics because of the synergistic effect, which is not presents on one individual material. However, most of these approaches, specifically related conduction polymers and carbon materials face different types of problems because of these single material related to sensors, such as low thermal stability, poor sensitivity, and/or selectivity at room temperature [35]. Figure.2 illustrates the evolution of sensing materials during the last five year for VOCs/gas sensor applications.

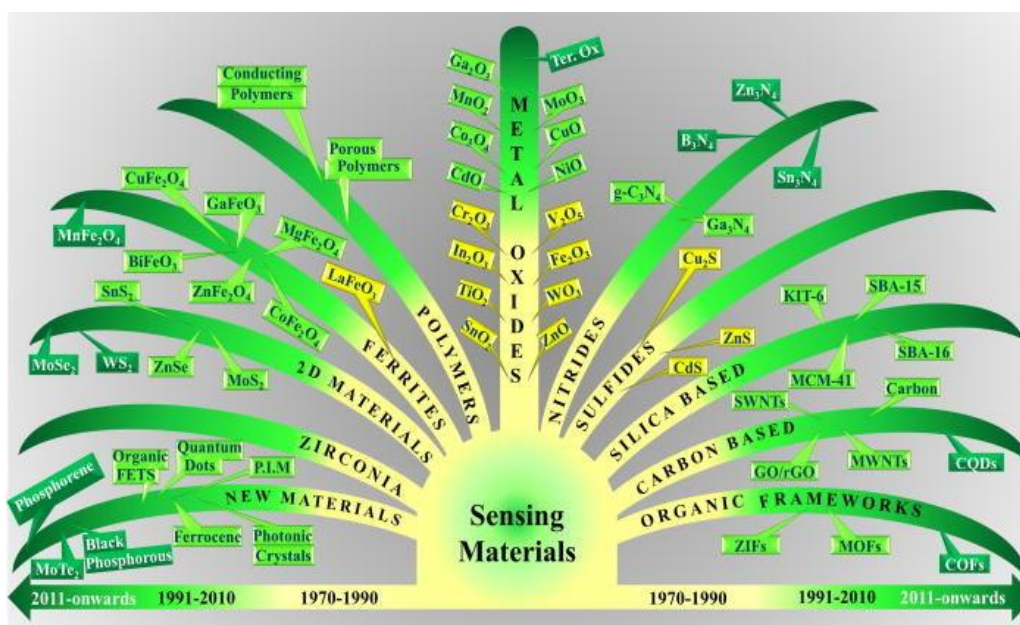


**Figure 2. A schematic of sensing materials evolution during the last five decades. [20] Copyright (2020) AIP**

Lately, combination of more than one material in nanoscale range with the intimate design shows promising results for developing VOC sensing device [36], [37]. This kind of material combination known as hybrid nanomaterials are considered to be the future generation of advance nanomaterials. Moreover, hybrid nanomaterials prepared by the different kind of materials such as graphene, conducting polymers, CNT, and metal nanoparticles for obtaining enhanced final properties. Based on the different applications and properties, these hybrid nanomaterials can be obtained through a wide range of distinct procedure such as electrospinning [38], self-assembly [39], and layer-by-layer (LbL) methods. Moreover, layered structure of opposite charged materials is selected in a substrate for LbL methods. For developing gas sensor, both of these methods are promising due to the high surface area/volume ratio of as-synthesized materials, which increases the absorption of gas molecules onto the sensing layer. Along with this, synergistic effects or intimate interface between the hybrid materials prepared by these methodologies improved the resultant properties of the sensing materials in terms of sensing. For an improved device design, the nature and ratio between the hybrid materials and also the synergistic interface are denoted as a key factor. Moreover, hybrid composites materials shows superior performance for designed the customized sensitive and selective sensors to meet the criteria of real-field sensors rather than individual's material.



Various types of VOC sensors based on hybrid materials have also been investigated by various researchers (table 2).

**Table 2:** State-of-the art for VOC/gas sensors based on hybrid materials

Journal and year	Sensing materials	Targeted VOCs	Response /recovery time	Detection range	Sensitivity	Limit of detection (LOD)	Operating temperature (°C)	Ref.
<b>Based on carbon materials</b>								
Adv. Sci (2017)	3D-GA	NO <sub>2</sub> NH <sub>3</sub>	11 sec	-	ppm	4.1 ppb	RT	[40]
Adv. Funct. Mater. (2016)	3D graphene (flower structure)	NO <sub>2</sub>	2 sec	-	ppm	100 ppb	-	[41]
Adv. Funct. Mater. (2016)	MoS <sub>2</sub> -GA	NO <sub>2</sub>	<1 min	-	50 ppb-3 ppm	50 ppb	RT	[42]
Sens. Actuators, B (2014)	3D graphene-ZnO composites	NO <sub>2</sub>	2 sec	-	10-200 ppm	30 ppm	-	[43]
Anal. Bioanal. Chem. (2014)	Ag-rGO	VOCs	10 sec/ 100 sec	-	1-200 ppm	1 ppm	-	[44]
Sens. Actuators, B (2016)	Pd/SnO <sub>2</sub> /rGO	NH <sub>3</sub>	7 min	5-150 ppm	0.995 ppm	-	RT	[45]
Sens. Actuators, B (2015)	PANI/MWCNTs	NH <sub>3</sub>	6 sec	2-10 ppm	0.955	-	RT	[46]
Sens. Actuators, B (2015)	Pd/SWCNTs	NH <sub>3</sub>	-	-	3.70	-	RT	[47]

J. Nanosci. Nanotechnol. (2015)	G/MoS <sub>2</sub>	MeOH	210 sec	10-50 ppm	-	-	RT	[48]
<b>Based on polymers</b>								
Sens. Actuators, B (2017)	PANI/GO/PANI/ZnO	NH <sub>3</sub>	30 sec	25-500 ppm	-	23 ppm	RT	[49]
Mod. Phys. Lett. B. (2017)	PANI-CdS	NO <sub>2</sub>	~ 14 sec	46 ppm	8.04	-	200	[50]
Sens. Actuators, B (2015)	PVDF-HFP/C65/CNT	Acetone	-	40-2000 ppm	-	-	22	[4]
<b>Based on metal oxides</b>								
Mater. Des. (2017)	SnO <sub>2</sub> /MWCNT	Acetone	2 sec	1-5 ppm	-	-	200-350	[51]
Sens. Actuators, B (2017)	Au/YSZ/Pt	Toluene	-	0.5-50 ppm	-	-	400-500	[52]
Sens. Actuators, B (2016)	YSZ/Pt	NH <sub>4</sub>	15 sec	1-100 ppm	0.99 ppm	-	550	[53]
Sens. Actuators, B (2016)	In <sub>2</sub> O <sub>3</sub> /Pt NPs	Acetone	-	0.01-1 ppm	< 10 ppb	-	100-250	[54]

### 1.3 Research gaps

In recent years we witnessed many studies on broad aspects of development of sensing materials and devices but only few studies on flexible VOCs and gas sensors sector that focuses on the hybrid materials and their synergetic effects for gas sensing. While researchers are more focused on development of sensing materials which are different in size and shape, and functionalised/modified materials for improving sensitivity and selectively. In particular, there is no specific research conducted on the engineering optimization for sensor fabrication with fundamental reasoning behind the sensing mechanism in hybrid materials. However, indeed, the sensor performance achieves based on three critical factors: sensing materials, sensor design and sensor fabrication technique. Most of the investigation was carried out mainly in metal

oxide, metal oxide composites and only carbon based materials. Numerous research has been conducted by using carbon materials, different metal oxides and their composites to fabricate solid state type VOCs/gas sensors. They designed this type of solid state resistive type sensors only for enhancing the sensing characteristics. These materials are normally deposited on commercialized interdigitate electrode (IDE) by simple coating or casting method. Therefore, designing of advanced sensor devices and new fabrication methods using new printing technologies are currently under considerable development and investigation.

#### 1.4 Research aims and questions

The primary aim of this thesis is to develop novel chemo-resistive sensors for VOC/gas detection applications using the advanced sensor fabrication techniques including 3D-extrusion printing method. This research generally attempts to design novel inks that can be printable along with the sensing capabilities. Sensor architecture for detecting VOC/gas molecules with enhanced performance is also consider over here. From the recognized knowledge gaps in the VOC/gas sensor field, the following research aims were developed:

- **Aim 1:** To design an advanced sensors by employing novel ink s with excellent 3D extrusion printability and stability for detection of trace amount VOCs.
- **Aim 2:** To explore the new design concept that is inspired by natural fractal structure for advancing the performance of chemoresistive sensors application.
- **Aim 3:** To design a hybrid materials ink by employing 1D and 2D materials for designing sensor arrays using 3D- extrusion printing method for detecting toxic gases (NO<sub>2</sub>) at moderate temperature.
- **Aim 4:** To design a fast response hydrogen sensors by employing nanogaps at room temperature.

This thesis attempts to address the following questions in separate chapters:

- **Question 1:** How to synthesize printable ink and how does advanced sensor architecture improve the VOCs sensor performance compare with conventional sensor design?
- **Question 2:** How does nature inspired fractal design affect the ultimate properties of the VOC sensors in terms of sensor characteristics?
- **Question 3:** How does hybrid ink enhance the NO<sub>2</sub> sensing properties with advance array design and embedded heating facilities?

➤ **Question 4:** How the single nanogaps can be produced by a single-step deformation techniques and how this nanogaps helps to improve the H<sub>2</sub> sensing performances?

### 1.5 Hypothesis

To address the above-mentioned aims and questions, the following hypothesis is made:

- 1) Graphene ink composed of ethyl-cellulose and eco-friendly Cyrene as a solvent allows the good printability of 3D-extrusion printing with enhanced VOC sensing characteristics.
- 2) Fractal designed sensors can enhance the VOC sensing characteristics due to the higher SA/V ratio.
- 3) Sensor array printed by 3D extrusion printer composed of hybrid 1D CNT and 2D graphene ink exhibits superior NO<sub>2</sub> sensing properties at moderate temperature. In addition, embedded MXene/PEDOT:PSS heater can resolve the problem of integration of heater with the sensor architecture.
- 4) Economical lithography-free fabrication method of single nanogap by bending deformation technique on Pd/Cr layer can exhibit enhanced hydrogen sensing characteristics at room temperature.

### 1.6 Thesis outline

This Ph.D. thesis is organized into seven chapters: introduction, literature review, four chapters adapted from the original research publications, and finally a chapter of conclusions and suggested future research works. A summary of each chapter is given below.

**Chapter 1: Introduction** introduces the problem of different types of toxic VOCs/gas, for humans and environment and the approach for detecting this VOCs/gas by employing various sensor devices. This chapter also highlights the promise of different sensing materials and device fabrication techniques by addressing the challenges associated with conventional methods. Finally, this chapter discusses the motivation of this research, and current main research gaps, and subsequent research aims.

**Chapter 2: Literature review** provides a comprehensive overview of the challenges associated with the design of advanced inks for extrusion-based 3D printing technology for real-field application. This chapter begins with the definition of ink and different modes of printing technology, followed by the main characteristics of extrusion printed inks. Next, application of this ink for different real-field applications has been presented. Next, the chapter

summarizes the strategies to overcome the challenges associated with sensor application by using this printable ink. Knowledge gaps are highlighted at the end of this chapter.

*The main contribution of this chapter is to provide a compressive literature review regarding the current printable ink for different applications and highlight the knowledge gap in this area.*

**Chapter 3: Development of a graphene ink for 3D extrusion micro printing of chemoresistive sensing devices for VOC detection.** This graphene ink took advantage of the printability of pristine graphene (pG) and the polymeric binder ethyl-cellulose (EC) with an eco-friendly solvent Cyrene. This chapter begins with the extensive characterization of graphene ink in terms of rheological properties, functionalization, thermo-gravimetric properties, mechanical behavior, and morphological features. Following this, the chapter provides a comprehensive analysis on printed pattern characterization of graphene ink in terms of printed device profile analysis, stability, and theoretical calculation. Finally, the 3D extrusion printed graphene ink based sensor device was evaluated to confirm the sensing capabilities of prepared graphene inks and their ability to be used for practical VOC sensor applications.

*The main contribution of this chapter is the sensing devices fabricated with this new graphene ink employing 3D-extrusion printer that display high-resolution patterning and improvement in the surface area/volume (SA/V) ratio compared to a conventional drop casting method. In addition, the extrusion printed sensors show enhanced sensing characteristics in terms of sensitivity and selectivity towards trace amount of VOC at room temperature (20 °C), which highlights that our method has highly promising potential in graphene printing technology for sensing applications*

**Chapter 4: Employing fractal design for advancing the performance of chemoresistive sensors.** This is the second results chapter of this thesis. In this chapter, a new bioinspired fractal approach to design chemoresistive sensors with fractal geometry is presented, which grasp the architecture of fern leaves represented by the geometric group of space-filling curves of fractal patterns. This chapter begins with the extensive characterization of printable ink in terms of rheological properties, functionalization, thermo-gravimetric properties, mechanical behavior, and morphological features. Following this, the chapter provides a comprehensive study on printed fractal pattern characterization in terms of printed device profile analysis, stability, and theoretical calculation. Finally, the fractal designed sensor

device was evaluated to confirm the new architecture compare with conventional sensor devise and also their ability to be used for practical VOC sensor applications.

*The main novelty and contribution of this chapter is to demonstrate new concept of nature inspired **fractal designed** sensors that is printed by an extrusion process on a flexible substrate (PET) using specially formulated graphene ink as a sensing material. This design provided significant enhancement of the active surface area to volume ratio and allowed high-resolution fractal patterning along with a reduced current transportation path. In addition, to demonstrate the advantages and influence of fractal geometry on sensor performance, here, three different kinds of sensors were fabricated based on different fractal geometrics (Sierpinski, Peano, and Hilbert), and the sensing performance was explored toward different VOC analytes (e.g., ethanol, methanol, and acetone). Finally, the practical application of this sensor was successfully demonstrated by monitoring food spoilage using a commercial box of strawberries as a model. Based on these presented results, this bio-fractal biomimetic VOC sensor is demonstrated for a prospective application in food monitoring.*

**Chapter 5: Development of an extrusion printed CNT-graphene sensor array with embedded MXene/PEDOT:PSS heater for enhanced NO<sub>2</sub> sensing at low temperature.** This is the third results chapter of this thesis. Herein, demonstration of a hybrid sensing material of one-dimensional CNTs and two-dimensional graphene and formulated a conductive ink is presented, which has been applied for fabricating an NO<sub>2</sub> gas sensor array within a compact design utilizing extrusion printing. In addition, to improve NO<sub>2</sub> sensing performance a reverse-side layer has been designed that functions as a Joule heater. Besides, challenges of integrating a heater on a flexible substrate for heating the sensor to optimal operating temperature has been overcome by controlling the loading of MXene and PEDOT:PSS.

*The main novelty and contribution of this chapter is the printed CNT-graphene-based sensor with embedded MXene/PEDOT:PSS heater, which was capable of detecting trace amount of NO<sub>2</sub> gas at moderate temperature. The sensor was able to distinguish between various gases/VOCs and target NO<sub>2</sub> gas based on their chemical affinities. In addition, the printed CNT-graphene sensor array also demonstrate a high-level of recoverability, promising stability, durability and reproducibility, which renders this sensor suitable candidate for practical applications.*

**Chapter 6: Development of a hydrogen gas sensor based on Pd/Cr nanogaps fabricated by a single-step bending deformation.** This is the fourth results chapter of this

thesis. Herein, fabrication and sensing performances of Pd/Cr nanogap hydrogen gas sensors is presented, where nanogap fabrication is performed by single step bending deformation process. Computational modelling for confirming the optimal deformation conditions and gap size is also presented. Finally, sensing performance of Pd/Cr nanogap based sensor has been evaluated to characterize the sensitivity and response time for hydrogen gases.

*The main novelty and contribution in this chapter is the unique design of Pd/Cr nanogap and the developed sensing device that meets major requirement of advanced H<sub>2</sub> gas sensor including room temperature operation, detection of trace amounts, good linearity, ultra-fast response recovery time and high selectivity. In addition, the presented economical lithography-free fabrication method has simple circuitry, low power consumption, recyclability, and favorable aging properties that promises great potential to be used for many practical applications of H<sub>2</sub> detection.*

**Chapter 7: Conclusion and Future directions.** This chapter provides the summary of this thesis by highlighting the main findings obtained from the results. Next, this chapter discusses the possible future directions for employing this work.

## 1.7 Format

The thesis entitled “Development of New Generation Chemoresistive VOC/Gas Sensors for Real-Field Applications” has been prepared as a portfolio of the publications based on the requirements of The University of Adelaide. The printed and online versions of this thesis are identical.

## 1.8 References

- [1] R. Koppmann, Volatile organic compounds in the atmosphere: Wiley Online Library; 2007.
- [2] H. Wang, L. Nie, J. Li, Y. Wang, G. Wang, J. Wang, et al., Characterization and assessment of volatile organic compounds (VOCs) emissions from typical industries, Chinese Science Bulletin, 58(2013) 724-30.
- [3] K.T. Valsaraj, E.M. Melvin, Elements of environmental engineering: thermodynamics and kinetics: CRC Press; 2009.
- [4] M. Leidinger, T. Sauerwald, T. Conrad, W. Reimringer, G. Ventura, A. Schütze, Selective detection of hazardous indoor VOCs using metal oxide gas sensors, Procedia Engineering, 87(2014) 1449-52.

- [5] P. Kumar, A. Deep, K.-H. Kim, R.J. Brown, Coordination polymers: Opportunities and challenges for monitoring volatile organic compounds, *Progress in Polymer Science*, 45(2015) 102-18.
- [6] K. Kawamura, M. Ishiyama, N. Nagatani, T. Hashiba, E. Tamiya, Development of a novel hand-held toluene gas sensor: Possible use in the prevention and control of sick building syndrome, *Measurement*, 39(2006) 490-6.
- [7] P. Vesely, L. Lusk, G. Basarova, J. Seabrooks, D. Ryder, Analysis of aldehydes in beer using solid-phase microextraction with on-fiber derivatization and gas chromatography/mass spectrometry, *Journal of agricultural and food chemistry*, 51(2003) 6941-4.
- [8] L.S. Teixeira, E.S. Leão, A.I.F. Dantas, H.L. Pinheiro, A.C. Costa, J.B. de Andrade, Determination of formaldehyde in Brazilian alcohol fuels by flow-injection solid phase spectrophotometry, *Talanta*, 64(2004) 711-5.
- [9] P.J. Sabourin, W.E. Bechtold, R.F. Henderson, A high pressure liquid chromatographic method for the separation and quantitation of water-soluble radiolabeled benzene metabolites, *Analytical biochemistry*, 170(1988) 316-27.
- [10] J. Dai, O. Ogebeide, N. Macadam, Q. Sun, W. Yu, Y. Li, B.-L. Su, T. Hasan, X. Huang, W. Huang, Printed Sensors, *Chem. Soc. Rev.*, 49 (2009), 1756.
- [11] V.K. Khanna, *Nanosensors: physical, chemical, and biological*: CRC Press; 2016.
- [12] X. Liu, S. Cheng, H. Liu, S. Hu, D. Zhang, H. Ning, A survey on gas sensing technology, *Sensors*, 12(2012) 9635-65.
- [13] T. Hübert, L. Boon-Brett, G. Black, U. Banach, Hydrogen sensors—a review, *Sensors and Actuators B: Chemical*, 157(2011) 329-52.
- [14] N. Yamazoe, K. Shimano, New perspectives of gas sensor technology, *Sensors and Actuators B: Chemical*, 138(2009) 100-7.
- [15] R. Jaaniso, O.K. Tan, *Semiconductor gas sensors*: Elsevier; 2013.
- [16] Y. Sun, J. Lopez, H.W. Lee, N. Liu, G. Zheng, C.L. Wu, et al., A Stretchable Graphitic Carbon/Si Anode Enabled by Conformal Coating of a Self-Healing Elastic Polymer, *Advanced Materials*, 28(2016) 2455-61.



- [17] F.R. Fan, W. Tang, Z.L. Wang, Flexible nanogenerators for energy harvesting and self-powered electronics, *Advanced Materials*, 28(2016) 4283-305.
- [18] Y.J. Yun, W.G. Hong, N.-J. Choi, B.H. Kim, Y. Jun, H.-K. Lee, Ultrasensitive and highly selective graphene-based single yarn for use in wearable gas sensor, *Scientific reports*, 5(2015) 10904.
- [19] K. Hsieh, A.S. Patterson, B.S. Ferguson, K.W. Plaxco, H.T. Soh, Rapid, Sensitive, and Quantitative Detection of Pathogenic DNA at the Point of Care through Microfluidic Electrochemical Quantitative Loop-Mediated Isothermal Amplification, *Angewandte Chemie*, 124(2012) 4980-4.
- [20] R. Malik, V.K. Tomer, Y.K. Mishra, L. Lin, Functional gas sensing nanomaterials: A panoramic view, *Appl. Phys. Rev.* 7(2020), 021301.
- [21] K. Parikh, K. Cattanach, R. Rao, D.-S. Suh, A. Wu, S.K. Manohar, Flexible vapour sensors using single walled carbon nanotubes, *Sensors and Actuators B: Chemical*, 113(2006) 55-63.
- [22] Y.S. Jung, W. Jung, H.L. Tuller, C. Ross, Nanowire conductive polymer gas sensor patterned using self-assembled block copolymer lithography, *Nano letters*, 8(2008) 3776-80.
- [23] K.J. Berean, J.Z. Ou, T. Daeneke, B.J. Carey, E.P. Nguyen, Y. Wang, et al., 2D MoS<sub>2</sub> PDMS nanocomposites for NO<sub>2</sub> separation, *Small*, 11(2015) 5035-40.
- [24] C. Piloto, F. Mirri, E.A. Bengio, M. Notarianni, B. Gupta, M. Shafiei, et al., Room temperature gas sensing properties of ultrathin carbon nanotube films by surfactant-free dip coating, *Sensors and Actuators B: Chemical*, 227(2016) 128-34.
- [25] K. Besar, S. Yang, X. Guo, W. Huang, A.M. Rule, P.N. Breyse, et al., Printable ammonia sensor based on organic field effect transistor, *Organic Electronics*, 15(2014) 3221-30.
- [26] H.Y. Jeong, D.-S. Lee, H.K. Choi, D.H. Lee, J.-E. Kim, J.Y. Lee, et al., Flexible room-temperature NO<sub>2</sub> gas sensors based on carbon nanotubes/reduced graphene hybrid films, *Applied physics letters*, 96(2010) 213105.
- [27] C. Wu, F. Li, W. Wu, W. Chen, T. Guo, Liquid-phase exfoliation of chemical vapor deposition-grown single layer graphene and its application in solution-processed

- transparent electrodes for flexible organic light-emitting devices, *Applied Physics Letters*, 105(2014) 243509.
- [28] S. Yao, Y. Zhu, Nanomaterial-enabled stretchable conductors: strategies, materials and devices, *Advanced materials*, 27(2015) 1480-511.
- [29] M. Castro, J. Lu, S. Bruzard, B. Kumar, J.-F. Feller, Carbon nanotubes/poly ( $\epsilon$ -caprolactone) composite vapour sensors, *Carbon*, 47(2009) 1930-42.
- [30] K. Donaldson, C.A. Poland, Nanotoxicology: new insights into nanotubes, *Nature Nanotechnology*, 4(2009) 708.
- [31] K.S. Novoselov, A.K. Geim, S. Morozov, D. Jiang, M. Katsnelson, I. Grigorieva, et al., Two-dimensional gas of massless Dirac fermions in graphene, *nature*, 438(2005) 197.
- [32] T.Y. Kim, H.W. Lee, M. Stoller, D.R. Dreyer, C.W. Bielawski, R.S. Ruoff, et al., High-performance supercapacitors based on poly (ionic liquid)-modified graphene electrodes, *ACS nano*, 5(2010) 436-42.
- [33] J.T. Robinson, F.K. Perkins, E.S. Snow, Z. Wei, P.E. Sheehan, Reduced graphene oxide molecular sensors, *Nano letters*, 8(2008) 3137-40.
- [34] T.T. Tung, M. Castro, T.Y. Kim, K.S. Suh, J.-F. Feller, Graphene quantum resistive sensing skin for the detection of alteration biomarkers, *Journal of Materials Chemistry*, 22(2012) 21754-66.
- [35] G. Korotcenkov, Metal oxides for solid-state gas sensors: What determines our choice?, *Materials Science and Engineering: B*, 139(2007) 1-23.
- [36] J. Zhang, X. Liu, G. Neri, N. Pinna, Nanostructured Materials for Room-Temperature Gas Sensors, *Advanced Materials*, 28(2016) 795-831.
- [37] N. Yamazoe, New approaches for improving semiconductor gas sensors, *Sensors and Actuators B: Chemical*, 5(1991) 7-19.
- [38] A.I. Uddin, D.-T. Phan, G.-S. Chung, Low temperature acetylene gas sensor based on Ag nanoparticles-loaded ZnO-reduced graphene oxide hybrid, *Sensors and Actuators B: Chemical*, 207(2015) 362-9.
- [39] V. Vaishnav, P. Patel, N. Patel, Indium Tin Oxide thin film gas sensors for detection of ethanol vapours, *Thin solid films*, 490(2005) 94-100.

- [40] J. Wu, K. Tao, Y. Guo, Z. Li, X. Wang, Z. Luo, et al., A 3D chemically modified graphene hydrogel for fast, highly sensitive, and selective gas sensor, *Advanced Science*, 4(2017) 1600319.
- [41] J. Wu, S. Feng, X. Wei, J. Shen, W. Lu, H. Shi, et al., Facile synthesis of 3D graphene flowers for ultrasensitive and highly reversible gas sensing, *Advanced Functional Materials*, 26(2016) 7462-9.
- [42] H. Long, A. Harley-Trochimczyk, T. Pham, Z. Tang, T. Shi, A. Zettl, et al., High surface area MoS<sub>2</sub>/graphene hybrid aerogel for ultrasensitive NO<sub>2</sub> detection, *Advanced Functional Materials*, 26(2016) 5158-65.
- [43] S. Liu, B. Yu, H. Zhang, T. Fei, T. Zhang, Enhancing NO<sub>2</sub> gas sensing performances at room temperature based on reduced graphene oxide-ZnO nanoparticles hybrids, *Sensors and Actuators B: Chemical*, 202(2014) 272-8.
- [44] T.T. Tung, M. Castro, T.Y. Kim, K.S. Suh, J.-F. Feller, High stability silver nanoparticles–graphene/poly (ionic liquid)-based chemoresistive sensors for volatile organic compounds' detection, *Analytical and bioanalytical chemistry*, 406(2014) 3995-4004.
- [45] K. Inyawilert, A. Wisitsora-At, A. Tuantranont, P. Singjai, S. Phanichphant, C. Liewhiran, Ultra-rapid VOCs sensors based on sparked-In<sub>2</sub>O<sub>3</sub> sensing films, *Sensors and actuators B: chemical*, 192(2014) 745-54.
- [46] S.F. Bamsaoud, S. Rane, R. Karekar, R. Aiyer, Nano particulate SnO<sub>2</sub> based resistive films as a hydrogen and acetone vapour sensor, *Sensors and Actuators B: Chemical*, 153(2011) 382-91.
- [47] Y.V. Kaneti, J. Moriceau, M. Liu, Y. Yuan, Q. Zakaria, X. Jiang, et al., Hydrothermal synthesis of ternary  $\alpha$ -Fe<sub>2</sub>O<sub>3</sub>–ZnO–Au nanocomposites with high gas-sensing performance, *Sensors and Actuators B: Chemical*, 209(2015) 889-97.
- [48] A. Vomiero, S. Bianchi, E. Comini, G. Faglia, M. Ferroni, N. Poli, et al., In<sub>2</sub>O<sub>3</sub> nanowires for gas sensors: morphology and sensing characterisation, *Thin Solid Films*, 515(2007) 8356-9.
- [49] L. Wang, Y. Kang, X. Liu, S. Zhang, W. Huang, S. Wang, ZnO nanorod gas sensor for ethanol detection, *Sensors and Actuators B: Chemical*, 162(2012) 237-43.

- 
- [50] J. Huang, Y. Dai, C. Gu, Y. Sun, J. Liu, Preparation of porous flower-like CuO/ZnO nanostructures and analysis of their gas-sensing property, *Journal of Alloys and Compounds*, 575(2013) 115-22.
- [51] K. Huang, L. Kong, F. Yuan, C. Xie, In situ diffuse reflectance infrared Fourier transform spectroscopy study of formaldehyde adsorption and reactions on nano  $\gamma$ -Fe<sub>2</sub>O<sub>3</sub> films, *Applied Surface Science*, 270(2013) 405-10.
- [52] V.N. Singh, B.R. Mehta, R.K. Joshi, F.E. Kruis, S.M. Shivaprasad, Enhanced gas sensing properties of In<sub>2</sub>O<sub>3</sub>: Ag composite nanoparticle layers; electronic interaction, size and surface induced effects, *Sensors and Actuators B: Chemical*, 125(2007) 482-8.
- [53] T. Chen, Q. Liu, Z. Zhou, Y. Wang, The fabrication and gas-sensing characteristics of the formaldehyde gas sensors with high sensitivity, *Sensors and Actuators B: Chemical*, 131(2008) 301-5.
- [54] A. Mirzaei, K. Janghorban, B. Hashemi, G. Neri, Metal-core@ metal oxide-shell nanomaterials for gas-sensing applications: a review, *Journal of Nanoparticle Research*, 17(2015) 371.

## Chapter 2

# Literature review

---

**A**fter introducing the significance of VOC/gas sensor technology in the previous chapter, an overview of the challenges associated with the design and fabrication procedure of sensor devices by employing 3D-extrusion printing method is discussed in the second chapter. First, the terminology of ink and different mode of printing method is provided, followed by an introduction of 2D materials as the dominant sensing materials in the formulation of printable inks. Next, the key characteristics of printable ink for 3D-extrusion printing are discussed in detail. As the main focus of this chapter, the application of this printable inks, especially in VOC/gas sensing applications were discussed through the definition of device fabrication and characterizations window. Next, the current gaps in the design of an ideal ink working as a selective sensing materials are recognized that are considered as the aims of this thesis.

The outcome of this chapter is a published as review paper in “Nanoscales” journal as follows:

“**Hassan K**, Nine MJ, Tung TT, Stanley N, Yap P, Rastin H, Yu L, Losic D, Functional inks and extrusion-based 3D printing of 2D materials: a review of current research and applications, **Nanoscales**, 2021, **13**, 5356-5368”.

## Statement of Authorship

Title of Paper	Functional inks and extrusion-based 3D printing of 2D materials: a review of current research and applications
Publication Status	<input checked="" type="checkbox"/> Published <input type="checkbox"/> Accepted for Publication <input type="checkbox"/> Submitted for Publication <input type="checkbox"/> Unpublished and Unsubmitted work written in manuscript style
Publication Details	Hassan K, Nine MJ, Tung TT, Stanley N, Yap PL, Rastin H, Yu L, Losic D, Functional inks and extrusion-based 3D printing of 2D materials: a review of current research and applications, Nanoscales, 2021, 13, 5356-5368

### Principal Author

Name of Principal Author (Candidate)	Kamrul Hassan
Contribution to the Paper	Prepared, edited and revised the review manuscript.
Overall percentage (%)	85%
Certification:	This paper reports on original research I conducted during the period of my Higher Degree by Research candidature and is not subject to any obligations or contractual agreements with a third party that would constrain its inclusion in this thesis. I am the primary author of this paper.
Signature	Date 19/10/2021

### Co-Author Contributions

By signing the Statement of Authorship, each author certifies that:

- i. the candidate's stated contribution to the publication is accurate (as detailed above);
- ii. permission is granted for the candidate to include the publication in the thesis; and
- iii. the sum of all co-author contributions is equal to 100% less the candidate's stated contribution.

Name of Co-Author	Md Julker Nine
Contribution to the Paper	Edited and revised the manuscript.
Signature	Date 01-11-2021

Name of Co-Author	Tran Thanh Tung
Contribution to the Paper	Co-supervised and revised the manuscript.
Signature	Date 26/10/2021

Please cut and paste additional co-author panels here as required.

# Statement of Authorship

Title of Paper	Functional inks and extrusion-based 3D printing of 2D materials: a review of current research and applications
Publication Status	<input checked="" type="checkbox"/> Published <input type="checkbox"/> Accepted for Publication <input type="checkbox"/> Submitted for Publication <input type="checkbox"/> Unpublished and Unsubmitted work written in manuscript style
Publication Details	Hassan K., Nine MJ, Tung TT, Stanley N, Yap PL, Rastin H, Yu L, Losic D, Functional inks and extrusion-based 3D printing of 2D materials: a review of current research and applications, Nanoscales, 2021, 13, 5356-5368

## Principal Author

Name of Principal Author (Candidate)	Kamrul Hassan
Contribution to the Paper	Prepared, edited and revised the review manuscript.
Overall percentage (%)	85%
Certification:	This paper reports on original research I conducted during the period of my Higher Degree by Research candidature and is not subject to any obligations or contractual agreements with a third party that would constrain its inclusion in this thesis. I am the primary author of this paper.
Signature	_____ Date 19/10/2021

## Co-Author Contributions

By signing the Statement of Authorship, each author certifies that:

- i. the candidate's stated contribution to the publication is accurate (as detailed above);
- ii. permission is granted for the candidate to include the publication in the thesis; and
- iii. the sum of all co-author contributions is equal to 100% less the candidate's stated contribution.

Name of Co-Author	Nathan Stanley
Contribution to the Paper	Edited and revised the manuscript.
Signature	_____ Date 28.10.2021

Name of Co-Author	Pei Lay Yap
Contribution to the Paper	Edited and revised the manuscript.
Signature	_____ Date 26/10/21

Please cut and paste additional co-author panels here as required.

# Statement of Authorship

Title of Paper	Functional inks and extrusion-based 3D printing of 2D materials: a review of current research and applications
Publication Status	<input checked="" type="checkbox"/> Published <input type="checkbox"/> Accepted for Publication <input type="checkbox"/> Submitted for Publication <input type="checkbox"/> Unpublished and Unsubmitted work written in manuscript style
Publication Details	Hassan K., Nire MJ, Tung TT, Stanley N, Yap PL, Rastin H, Yu L, Losic D, Functional inks and extrusion-based 3D printing of 2D materials: a review of current research and applications, Nanoscales, 2021, 13, 5358-5368

## Principal Author

Name of Principal Author (Candidate)	Kamrul Hassan
Contribution to the Paper	Prepared, edited and revised the review manuscript.
Overall percentage (%)	85%
Certification:	This paper reports on original research I conducted during the period of my Higher Degree by Research candidature and is not subject to any obligations or contractual agreements with a third party that would constrain its inclusion in this thesis. I am the primary author of this paper.
Signature	<div style="border-bottom: 1px solid black; width: 100%;"></div>
Date	19/10/2021

## Co-Author Contributions

By signing the Statement of Authorship, each author certifies that:

- i. the candidate's stated contribution to the publication is accurate (as detailed above);
- ii. permission is granted for the candidate to include the publication in the thesis; and
- iii. the sum of all co-author contributions is equal to 100% less the candidate's stated contribution.

Name of Co-Author	Hadi Rastin
Contribution to the Paper	Edited and revised the manuscript.
Signature	<div style="border-bottom: 1px solid black; width: 100%;"></div>
Date	29.10.2021

Name of Co-Author	Le Yu
Contribution to the Paper	Edited and revised the manuscript.
Signature	<div style="border-bottom: 1px solid black; width: 100%;"></div>
Date	26/10/2021

Please cut and paste additional co-author panels here as required.



# Statement of Authorship

Title of Paper	Functional inks and extrusion-based 3D printing of 2D materials: a review of current research and applications
Publication Status	<input checked="" type="checkbox"/> Published <input type="checkbox"/> Accepted for Publication <input type="checkbox"/> Submitted for Publication <input type="checkbox"/> Unpublished and Unsubmitted work written in manuscript style
Publication Details	Hassan K., Nine MJ, Tung TT, Stanley N, Yap PL, Rastin H, Yu L, Losic D, Functional inks and extrusion-based 3D printing of 2D materials: a review of current research and applications, Nanoscales, 2021, 13, 5356-5368

## Principal Author

Name of Principal Author (Candidate)	Kamrul Hassan
Contribution to the Paper	Prepared, edited and revised the review manuscript.
Overall percentage (%)	85%
Certification:	This paper reports on original research I conducted during the period of my Higher Degree by Research candidature and is not subject to any obligations or contractual agreements with a third party that would constrain its inclusion in this thesis. I am the primary author of this paper.
Signature	Date 19/10/2021

## Co-Author Contributions

By signing the Statement of Authorship, each author certifies that:

- i. the candidate's stated contribution to the publication is accurate (as detailed above);
- ii. permission is granted for the candidate to include the publication in the thesis; and
- iii. the sum of all co-author contributions is equal to 100% less the candidate's stated contribution.

Name of Co-Author	Dusan Losic
Contribution to the Paper	Supervised the development of work, edited, revised the manuscript and acted as the corresponding author.
Signature	Date 26 Oct 2021

Name of Co-Author	
Contribution to the Paper	
Signature	Date

Please cut and paste additional co-author panels here as required.

Cite this: *Nanoscale*, 2020, 12, 19007

## Functional inks and extrusion-based 3D printing of 2D materials: a review of current research and applications

Kamrul Hassan,<sup>a,b</sup> Md Julker Nine,<sup>a,b</sup> Tran Thanh Tung,<sup>a,b</sup> Nathan Stanley,<sup>a,b</sup> Pei Lay Yap,<sup>a,b</sup> Hadi Rastin,<sup>a,b</sup> Le Yu<sup>a,b</sup> and Dusan Losic<sup>a,b\*</sup>

Graphene and related 2D materials offer an ideal platform for next generation disruptive technologies and in particular the potential to produce printed electronic devices with low cost and high throughput. Interest in the use of 2D materials to create functional inks has exponentially increased in recent years with the development of new ink formulations linked with effective printing techniques, including screen, gravure, inkjet and extrusion-based printing towards low-cost device manufacturing. Exfoliated, solution-processed 2D materials formulated into inks permits additive patterning onto both rigid and conformable substrates for printed device design with high-speed, large-scale and cost-effective manufacturing. Each printing technique has some sort of clear advantages over others that requires characteristic ink formulations according to their individual operational principles. Among them, the extrusion-based 3D printing technique has attracted heightened interest due to its ability to create three-dimensional (3D) architectures with increased surface area facilitating the design of a new generation of 3D devices suitable for a wide variety of applications. There still remain several challenges in the development of 2D material ink technologies for extrusion printing which must be resolved prior to their translation into large-scale device production. This comprehensive review presents the current progress on ink formulations with 2D materials and their broad practical applications for printed energy storage devices and sensors. Finally, an outline of the challenges and outlook for extrusion-based 3D printing inks and their place in the future printed devices ecosystem is presented.

Received 1st July 2020,  
Accepted 4th September 2020  
DOI: 10.1039/d0nr04933f  
[rsc.li/nanoscale](http://rsc.li/nanoscale)

### 1. Introduction

Graphene and related two-dimensional (2D) materials hold great promise for developing the technologies of tomorrow.<sup>1,2</sup> Beyond single-layer graphene, a broad range of 2D materials including transition metal dichalcogenides (TMDs), hexagonal boron nitride (hBN), black phosphorus (BP), MXenes, and non-layered materials [e.g. MnO<sub>2</sub>, Co(OH)<sub>2</sub>, and Ni(OH)<sub>2</sub>] have been discovered and explored over the last 15 years.<sup>3,4</sup> By employing low-cost and scalable exfoliation techniques such as mechanical exfoliation,<sup>5,6</sup> chemical exfoliation,<sup>7,8</sup> electrochemical exfoliation,<sup>9,10</sup> and thermal exfoliation,<sup>11,12</sup> it is possible to produce 2D materials in large quantities from their inexpensive layered bulk precursors. Based on the specific application, the exfoliated 2D materials may be sorted in order of

thickness and size to formulate uniform dispersions.<sup>13</sup> Most of these 2D materials have good solution processability and can be further modified to fine-tune the electrical and other characteristics which make them attractive candidates for formulation of functional printable inks, as the key element required for conventional and new printing technologies as well as low-cost and high-volume manufacturing.<sup>14</sup>

Among many applications of 2D materials, printable electronics and wearable devices fabricated by printing techniques are of considerable interest and emerging as one of the most rapidly developing research topics in recent years.<sup>15,16</sup> From an economic landscape point of view, it is projected that by 2021 an attractive market of USD 124 billion will be available to the printing industry.<sup>17</sup> Such a notable economic significance has encouraged the development of diverse printing methods undergoing continuous advancement, including screen printing,<sup>18</sup> spray coating,<sup>19</sup> inkjet printing,<sup>20</sup> and extrusion-based 3D printing.<sup>21</sup> These types of printing technologies are broadly used to apply additive patterning of ink materials onto rigid, conformable and flexible surfaces. The techniques enabling traditional low-cost, high-speed, and large-scale manufacture

<sup>a</sup>School of Chemical Engineering and Advanced Materials, The University of Adelaide, Adelaide, SA 5005, Australia. E-mail: [dusan.losic@adelaide.edu.au](mailto:dusan.losic@adelaide.edu.au), [kamrul.hassan@adelaide.edu.au](mailto:kamrul.hassan@adelaide.edu.au)

<sup>b</sup>ARC Research Hub for Graphene Enabled Industry Transformation, The University of Adelaide, Adelaide, SA 5005, Australia

of everyday documents, newspapers, packaging materials, and magazines are evolving to accommodate device manufacturing by adapting inks with 2D materials.

The emergence of solution-processed 2D materials has heightened interest in their value-added application for device development using printing technologies, offering the promise of economically viable, scalable manufacturing for future industries.<sup>2</sup> However, the execution of the developed printing methods is highly dependent on the functional ink formulation, which must be matched to known printing methods and equipment. The development of inks has a long history that can be traced back to as early as the 3<sup>rd</sup> century in China and related to the production of paper and calligraphy.<sup>22</sup> Yet even today, the formulation of inks with the required rheological characteristics while being compatible with various substrate materials is still challenging.

Graphene-based conductive inks for direct inkjet printing of flexible conductive patterns for application in electric circuits was first reported in 2011 by L. Huang *et al.*<sup>23</sup> Further application of printed 2D material was reported in 2012, where field-effect transistors (FETs) were fabricated *via* inkjet printing of exfoliated graphene prepared by a solution processing approach.<sup>24</sup> This area of research has since experienced a rapid improvement in ink formulation methodology along with device fabrication. In conjunction with graphene, several other 2D materials have been considered as key active additives.<sup>25–27</sup> Although the first-generation inks using exfoliated 2D materials were not optimised for the appropriate printing methods, different 2D material ink formulations with functionalization are now starting to emerge. The viability and

scope of aqueous dispersions, organic solvents, and solvent mixtures for functional ink formulation has now been well demonstrated.<sup>28,29</sup> For formulating conventional inks, polymers and surfactants were introduced as additives and binders.<sup>27,30</sup> The adaptation and adjustment of ink formulations has permitted the fluidic characteristics, drying dynamics and interaction with different substrates of the inks to be optimised not only for inkjet printing but also for extrusion-based 3D printing, screen, gravure and flexographic printing.<sup>31–34</sup> As a result, apart from electronics, a range of printable 2D material applications such as conductive inks, optoelectronics (*e.g.* photodetectors), photonics (*e.g.* non-linear optical devices), batteries, super-capacitors and sensors have been revealed.<sup>25–27,30–35</sup>

To date, simple printing methods along with the convenience of machines at affordable prices make the extrusion-based 3D-printing method the most common among all 3D-printing technologies. Extrusion-based 3D-printing techniques generally consist of the deposition of the functional material which is liquefied prior to dispensing *via* a nozzle head. The usual 3D printing technology utilizing this method is known as fused deposition modelling (FDM) which produces 3D architectures composed of thermoplastic materials, first developed by Scott Crump in 1989.<sup>36</sup> In this method, before the extrusion process begins *via* dispenser nozzle, thermoplastic materials are heated to a semi-molten state immediately before deposition onto the substrate in a layer-by-layer manner. Once the semi-molten materials are deposited on the substrates, the solidification properties of this material produce a uniform solid layer which stacks on top of the pre-



(From left to right) Hadi Rastin, Le Yu, Md Julker Nine, Dusan Losic, Pei Lay Yap, Nathan Stanley, Kamrul Hassan, Tran Thanh Tung

*The Losic Group, led by Prof. Dusan Losic, is based at the School of Chemical Engineering and Advanced Materials, University of Adelaide. The Losic Group research interests focus on graphene and other advanced materials and include fundamental and applied aspects across disciplines of nanotechnology, chemistry, materials science, engineering, medicine and agriculture. The group is part of ARC Research Hub for Graphene Enabled Industry Transformation. (From left) Hadi Rastin is a third year PhD*

*student in the group and is working on development of bio-inks for soft tissue engineering and biomedical application. Le Yu is a third year PhD student in the group and is working on development of radiation shielding composites using graphene and other 2D materials. Md Julker Nine is a postdoctoral researcher in the group, working on synthesis and application of multifunctional inks and paints and coatings based on graphene and 2D materials for broad applications. Dusan Losic is a professor at the School of Chemical Engineering and Advanced Materials, the University of Adelaide, and leader of Nano research group with 20 researchers. Also, he is The Director of ARC Graphene Research HUB and ARC Future Fellow. Pei Lay Yap is a third year PhD student in the group, working on the development of graphene 3D composites for environmental and water remediation. Nathan Stanley is now a postdoctoral researcher in the group, working on innovative potential of materials for the creation of biosensors to transform medical diagnosis and nanocomposites to realize the technologies of tomorrow. Kamrul Hassan is a third year PhD student in the group and is working on engineering nanomaterials for printed electronics, sensing and energy. Tran Thanh Tung is a Research Fellow in the group, working on carbon nanomaterials, conducting polymers and nanocomposites for sensors and electronic applications.*

vious layer based on the sliced model design. Creation of multi-material architectures can be accomplished by using several nozzles with different materials. Using a related principle, direct ink writing (DIW) methods permit the controlled deposition of various materials providing that they are in the form of an ink, which is in a viscous liquid state and able to maintain shape after deposition before drying. This direct ink writing 3D-printing technology is highly adaptable since a vast array of diverse materials can be deposited, ranging from ceramics, plastics, food to living cells as well as functional 2D materials.<sup>37,38</sup>

Since 2012, we have witnessed tremendous advancements in functional ink formulations and their printing applications using 2D materials with progress being presented in several reviews.<sup>2,39,40</sup> However, there remains a gap in comprehensive reviews, recent development and guidance on how graphic ink formulations, and extrusion-based 3D printing technologies can be aligned for formulating functional inks along with printing of 2D materials. In particular, a complete summary on the latest advancements in extrusion-based 3D printable applications of 2D materials, and specifically the economic and research scenarios for use of functional 2D materials inks is lacking. Having this in mind, the aim of this review paper is to provide readers with a comprehensive overview of recent progress in this field. The review is composed in the following sections starting with a brief preface to introduce key 2D materials and recent advances in their exfoliation methods and processing strategies. In the following section, physical characteristics, general composition, and processing principles of inks, and the demonstrated functional ink formulations of 2D materials for extrusion-based 3D printing processes are presented. The fourth section covers the working principles of several printing methods; and finally, the fifth section covers the most recent progress in applications of extrusion-based 3D printed functional 2D materials from published literature and industry practices. The concluding section summarizes our observations on the recent trends, technology convergence, economic landscape and potential impact of functional 2D

material inks and extrusion-based 3D printing technology and their future trends.

## 2. 2D Materials for Inks

### 2.1. Printable 2D materials: properties for inks and other applications

Among many 2D layered materials known, graphene, transition metal carbides and/or carbonitrides (MXene), transition metal dichalcogenides (TMD, e.g. MoS<sub>2</sub>), hexagonal boron nitrides (hBN) and black phosphorus (BP), in particular have shown great potential for use in printed flexible electronics and devices due to their atomic thickness, mechanical flexibility, their own unique properties along with their integrated properties. A graphical representation of the 2D structures of these materials and corresponding energy band diagrams are presented in Fig. 1.

The key properties of these selected 2D materials are highlighted below:

Graphene, commonly referred to as a single layer of graphite and consisting of an atomically thin layer of hexagonally arranged carbon atoms, is the most studied representative of the 2D material family. Graphene possesses many remarkable properties such as outstanding electrical conductivity, good optical transparency (97%), mechanical strength (~1 TPa and 1 GPa) and flexibility, high thermal conductivity (5000 Wm<sup>-1</sup> K<sup>-1</sup>), inherently high mobility charge carriers (200 000 cm<sup>2</sup> V<sup>-1</sup> s<sup>-1</sup>) with a carrier density of 10<sup>12</sup> cm<sup>-2</sup> and a large surface area (theoretical value, 2630 m<sup>2</sup> g<sup>-1</sup>).<sup>41–46</sup> Other distinctive properties of graphene include gas impermeability, chemical resistance (acid/base/salt), antibacterial potential, thermal stability and eco-friendliness.<sup>47,48</sup> The prevailing method for scalable production of graphene-based materials requires direct de-lamination from a graphite precursor. Another common method is oxidative intercalation and exfoliation of graphite into single or few layer graphene oxides (GO), followed by partial restoration of electrical/thermal conductivity and struc-

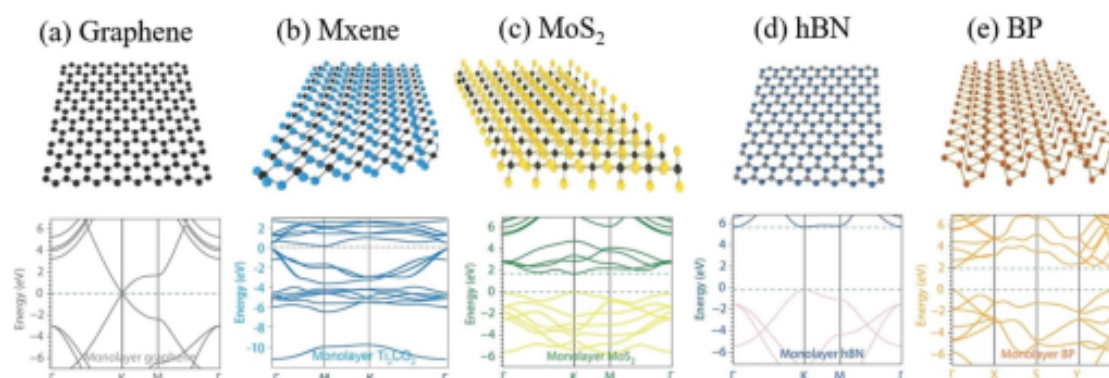


Fig. 1 Atomic structure of representative 2D materials and their band structure of (a) graphene, (b) MXene, (c) MoS<sub>2</sub>, (d) hBN and (e) BP, respectively. Reproduced with permission from ref. 40 Copyright [2019] Wiley-VCH.

tural integrity *via* chemical or thermal reduction processes.<sup>49</sup> The chemically derived graphene sheets, known as reduced graphene oxide (rGO) contain functional groups and defects, restricting their application in applied physics and electronics. However, the material may be efficiently deposited on substrates *via* the functional groups through covalent bonding or interfacial adhesion and is easy to handle as water-based dispersions, in contrast to exfoliated graphene.<sup>50,51</sup>

MXene is a single layer of transition metal carbides, carbonitrides and nitrides with a general formula of  $M_{n+1}X_n$ , where M is a transition metal (Ti, Cr, Mo, Sc, Zr, V, Nb, etc.), and X represents carbon and/or nitrogen. The name 'MXene' was given to describe both its single layer structure similar to graphene and the precursor MAX phase. MXenes are exfoliated from MAX phase by wet-etching in hydrofluoric acid (HF) or by an *in situ* HF etchant which adds surface-terminated functional groups such as -O, -OH and -F.<sup>52</sup> MXene possesses a hydrophilic surface and high metallic conductivities ( $\sim 6000\text{--}8000\text{ S cm}^{-1}$ ), allowing application across fields such as energy storage, transparent electrodes, EMI shielding, sensors and transistors. The major challenge hindering the application of MXene is poor ambient stability due to oxidation in the presence of either water or oxygen.<sup>53</sup>

Molybdenum disulfide ( $\text{MoS}_2$ ), is an inorganic compound that exists in nature in the mineral molybdenite, has a hexagonal layered structure similar to graphene, displays both semi-conducting and metallic behaviour, and excellent dry lubrication properties.<sup>54</sup> The layer-dependent bandgap of  $\text{MoS}_2$  makes it attractive for application in electronics, optoelectronics and photonics. The band-gap value of this material is higher than the band-gap of graphene, which enables a higher ON-OFF ratio ( $>10^6$ ) making it effective for fabrication of switching devices.<sup>55</sup>

Black phosphorus, a relatively rare allotrope of phosphorus, has recently emerged as a useful 2D material for photonics and optoelectronic applications due to its direct band-gap semiconductor properties. The 2D black phosphorus exhibits a distinctive wrinkled structure with the high hole mobility up to  $1000\text{ cm}^2\text{ V}^{-1}\text{ s}^{-1}$ , excellent mechanical properties, tunable band structures as well as anisotropic thermal, electrical and optical properties.<sup>56</sup> This material is promising for application in electronics and optoelectronics in the near infrared region.<sup>57</sup> However, the wrinkled layered structure and poor environmental stability and degradation *via* oxidation, limits application to some extent.

Hexagonal boron nitride (hBN) belongs to a hexagonal system, sometimes referred to as 'white graphene', is an isomorph of graphene with a very similar layered structure. The hBN is a lattice consisting of alternately arranged BN atoms in a 2D plane, which are bonded *via*  $sp^2$  orbitals to form strong  $\sigma$  bonds in a honeycomb structure.<sup>58</sup> It has unique characteristics, specifically exotic opto-electrical properties, resistance to chemical oxidation, mechanical robustness, thermal stability, and chemical inertness.<sup>59</sup> Thus, hBN has attracted researchers to use this material in the application of field effect transistors (FETs), tunnelling devices, deep UV emitters/

detectors, photoelectric devices, and as a nanofiller, especially in the water industry as a replacement for both classical bulk and nano-adsorbents.

In order to exploit the characteristics of 2D materials for printing technology, stable ink formulations along with compatible printing properties are required.<sup>22</sup> The formulation of 2D printing inks has adopted a three-component strategy analogous to conventional graphic inks, comprising 2D materials, solvents and additives which allows the inks to behave similarly to graphical printing inks. In this context, the 2D materials play the role of conductive fillers (*e.g.* graphene, MXene and BP) for synthesizing functional printable inks with enhanced electrical conductivity, mechanical reinforcement, tunable band structures and thermal conductivity (hBN and BP). Solvents that make up the body of the inks can be water or organic compounds such as ethanol, toluene, DMF, NMP or terpineol. Additives, such as binders, dispersants and surfactants are used to enhance and tune the ink rheological properties. However, the additives are usually insulators which reduce conductivity, thus their content needs to be optimized. Some 2D materials (*e.g.* graphene oxide, MXene, TMDs and BP) can be used to formulate inks using solvents and co-solvents without any binders (binder-free inks). These electrically conductive 2D inks are far cheaper than inks containing precious metal nanoparticles (*e.g.* Ag, Au, Pt) and unlike those containing copper, nickel and aluminium nanoparticles, 2D material inks are not prone to oxidation. 2D materials are opening new windows of opportunity for manufacturing the advanced electronics and devices of the future, replacing traditional semiconductor technologies.

The processing of 2D materials inks generally follows a three-step scheme, including selection of an optimal 2D material concentration, dispersion of the materials by mechanical action and dilution or let down with ink varnishes. Developed inks would form a diverse source of 2D crystals in which their characteristics would be advantageous in a broad range of applications including optoelectronics, sensors, catalysts and energy storage.<sup>60</sup> As an example, graphene has been used to fabricate the world's fastest photodetector.<sup>24</sup> Graphene based field-effect transistors (GFETs) have also presented brilliant prospects for sensing applications because of their single gas molecule sensitivity along with higher selectivity. For the application of optoelectronics, among all the semiconductor materials, the absorption cross-sections of 2D TMDs are among the highest reported of any material. In addition, these 2D TMDs are an attractive candidate for photovoltaic acceptors in heterojunction solar cells because of their atomically thin layered structure and superior self-passivated optical absorption capability.<sup>61</sup> The large defect sites and various morphologies of these materials allow them to fulfil dual roles as absorbers and catalysts for photoelectrochemical and photocatalytic reactions.<sup>62</sup> Moreover, the direct band gaps in the visible part of the electromagnetic spectrum grant them unprecedented performance improvements in optoelectronic devices such as photovoltaics.<sup>63</sup> Importantly, compared with bulk material, and composites, TMDs 2D materials such as gra-

Table 1 Key characteristics, properties and application of 2D materials<sup>58,75</sup>

2D materials	Definition	Properties	Applications
Graphene derivatives (pG, GO, rGO)	Covalently-bonded hexagonal lattice of carbon atoms	Semimetal (bandgap: Zero) for pristine graphene, semiconductor for GO (bandgap: ~2.2 eV) and RGO (bandgap ~1.00 to 1.69 eV); high electron mobility and electrical conductivity, excellent thermal stability and mechanical properties	Transistors and optoelectronics, flexible circuits, active sensing layers, electromagnetic adsorption, film electrodes, environmental remediation and mechanical reinforcements
MXenes (e.g. $M_nX_m$ )	A 'clay-like' 2D material composed of early transition metals (such as titanium) and carbon atoms	Semimetal or semiconductor (bandgap: 0–1.86 eV), high electrical conductivity, electronic, optical, plasmonic and thermoelectric properties, having surface terminations allowed them to be easily dispersed in aqueous suspensions and inks (without binders)	Transistors, gas and bio sensors, flexible circuits, active sensing layers, EMI shielding, electrodes energy storage, reinforcement for composites, water purification, lubrication, photo and electro-catalysis
TMD ( $MX_2$ ), e.g.: $MoS_2$ , $WS_2$ , $MoSe_2$ .	Two atoms thick, consisting of the metal layer sandwiched between two chalcogenide layers, various morphologies with exposed edges that include triangular, hexagonal or star-shaped clusters and nanoribbons.	Semiconducting characteristics (bandgap: 1–2.5 eV), remarkable optical and electronic properties, photoelectrochemical, thermoelectric and lubrication properties	Active sensing layer, nonlinear photonic devices, visible to near-infrared photodetectors, field effect transistor, thermoelectric, electrochemical, photocatalytic
BP	A layered, stable allotrope of elemental phosphorus, its monolayer structure is not planar, but buckled	Semiconductor (bandgap: 0.3–2 eV), featuring highly anisotropic properties, bandgap semiconductor with a puckered honeycomb structure, extremely high carrier mobility	Field effect transistors, sensors, nonlinear photonic devices, visible to near-infrared photodetectors
hBN	An isomorph of graphene, where has boron and nitrogen atoms instead of carbon	wide-bandgap insulator (~6 eV), thermal stability, Hyperbolic properties, photonics functionalities	Gate dielectric layer in field effect transistors, sensor material, protective cover in devices, <sup>76</sup> deep UV emitters and detectors. <sup>58,75</sup>

phene show enhanced Seebeck coefficients because of higher thermoelectric power factor properties.<sup>64</sup> Key characteristics of 2D materials along with their properties and potential applications are summarised in Table 1.

## 2.2. Methods, medium and surfactants for top-down exfoliation of 2D materials

The quality of ink formulation of 2D materials is highly dependent on the exfoliation methods and medium. Numerous top-down synthesis approaches for 2D materials were established within the last decade which show excellent scalability, and facile processing pathways for obtaining single and few layer 2D materials with desired properties. Many of these synthesis processes were already collated, reviewed and discussed by experts in detail which cover mechanical exfoliation,<sup>6</sup> electrochemical exfoliation,<sup>65</sup> and related methods principally based on liquid-phase exfoliation and ion-intercalation.<sup>66,67</sup> The exfoliation of 2D materials (graphene, MXene, TMD, BP, hBN) from their bulk are significantly influenced by the exfoliation approach, the medium of exfoliation and the surfactants used during the process. Therefore, this section outlines the fundamental mechanisms of widely used synthesis routes, and the influence of different groups of media, and effect of interacting surfactants, to achieve a high-yield synthesis of 2D materials.

**2.2.1. Methods of exfoliation of 2D materials.** Most of the top-down routes for exfoliation of 2D materials can be classified into four categories: (a) mechanical, (b) chemical, (c)

electrochemical and (d) thermal exfoliation, as well as their combinations.

**2.2.1.1. Mechanical exfoliations.** Mechanical exfoliation is based on the mechanical influence in exfoliation *via* fragmentation of the bulk layered materials by means of shear and frictional force, compressive and tensile force, and multidirectional vibration.<sup>68,69</sup> These forces can be introduced by different processing methods such as ball-milling,<sup>70</sup> three-roll-milling,<sup>71</sup> vortex chamber,<sup>3</sup> sonication,<sup>72</sup> and other relevant rotating mechanical-mixture,<sup>73</sup> as shown in Fig. 2.

Sonication (Fig. 2a) causes generation and distribution of cavitation-induced microbubbles through the liquid medium during the exfoliation process. Due to pressure differences, the collapse of these bubbles generates micro-jets and shock waves, causing compression stresses on the particles and tensile stresses in the opposite direction to the compression which drives mechanical exfoliation and fragmentation of the bulk layered materials.<sup>6,74</sup>

Ball-milling,<sup>70</sup> and three-roll-milling,<sup>71</sup> primarily creates shear stress and collision impact (*e.g.* compression) leading to exfoliation and fragmentation of the bulk particles. The shear force cleaves layered bulk into 2D sheets from the outer surface while the compression forces act laterally, often breaking the particles into smaller fragments (Fig. 2b). The production yield of mono- and few-layer material *via* milling depends on the rotation speed, duration and exfoliation medium.<sup>6</sup>

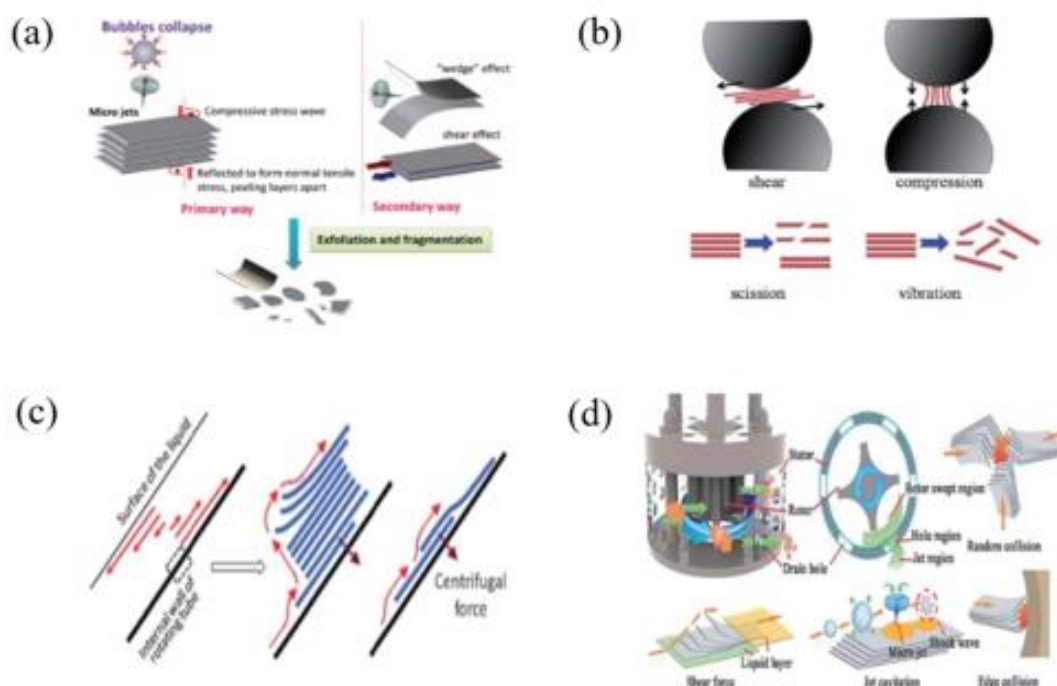


Fig. 2 Mechanical exfoliation. (a) Schematic representation of the mechanism for exfoliation via sonication. Reproduced with permission from ref. 6 Copyright (2015) Royal Society of Chemistry. (b) Mechanism of mechanical exfoliation via ball milling. Reproduced with permission from ref. 70 Copyright (2012) Royal Society of Chemistry. (c) Pressure driven shear force for exfoliation of 2D materials. Reproduced with permission from ref. 5 Copyright (2012) Royal Society of Chemistry. (d) Schematic of a high shear generator to exfoliate 2D materials. Reproduced with permission from ref. 73 Copyright (2014) Royal Society of Chemistry.

The effects of fluid-dynamics were harnessed to produce multiple mechanical forces for exfoliation, by designing special mechanical devices such as a flow channel with high-pressure/velocity gradient,<sup>77</sup> and vortex chamber,<sup>5</sup> as shown in Fig. 2c. The inherent cavitation in low pressure zones and the collapse of cavitation micro bubbles can generate shockwaves which impact on layered materials with the velocity gradient-induced viscous shear stress. Furthermore, the flow channel-induced collisions and turbulence-induced Reynolds shear stress can generate lateral forces capable of cleaving bulk layered materials. A high-shear generator is another device that consists of a specially designed rotor blade possessing a rotor swept-region, a hole-region and a jet-region (Fig. 2d).<sup>78</sup> The system combines the mechanisms observed in sonication and ball-milling such as shear, micro jet cavitation and collision towards a high yield synthesis of 2D materials.<sup>73</sup>

These aforementioned mechanical methods were applied to exfoliate most of the known 2D materials such as graphene, hBN,<sup>5</sup> TMD (e.g. MoS<sub>2</sub>, WS<sub>2</sub>, MoSe<sub>2</sub>),<sup>66</sup> phosphorene,<sup>79</sup> and antimonene.<sup>80</sup>

**2.2.1.2. Chemical exfoliation.** Chemical exfoliation of layered bulk materials was predominantly driven by chemical oxidation,<sup>81–83</sup> chemical etching,<sup>84</sup> and ion-intercalation.<sup>85</sup> These oxidation approaches involved strong oxidising agents (e.g. KMnO<sub>4</sub>, K<sub>2</sub>FeO<sub>4</sub>) in an acidic medium (e.g. H<sub>2</sub>SO<sub>4</sub>, HNO<sub>3</sub>) to break the van der Waals (vdW) forces between layers (e.g.

graphite, hBN) as presented in Fig. 3a,<sup>7</sup> while acid etching with hydrofluoric acid (HF) or hydrochloric acid (HCl) was performed to remove the targeted metallic layer in the layered bulk of ternary carbide and nitride M<sub>n+1</sub>AX<sub>n</sub> phase.<sup>86,87</sup>

Although Brodie revealed acid oxidation of graphite in 1859 using NaNO<sub>3</sub> and H<sub>2</sub>SO<sub>4</sub>,<sup>88</sup> most current chemical exfoliation of graphite *via* oxidation is based on Hummers' method reported in 1958 for graphite oxidation.<sup>89</sup> The method uses KMnO<sub>4</sub> and NaNO<sub>3</sub> in concentrated H<sub>2</sub>SO<sub>4</sub> for chemical treatment which was modified and improved by substituting NaNO<sub>3</sub> and optimizing the composition for efficient and high-yield production of oxidised graphene.<sup>7,90</sup> However, the chemical oxidation leads to rigorous disruption of the lattice structure of 2D materials by the introduction of oxygen-containing functional groups on basal plane and edges of the layers, creating a material which exhibits low electrical and thermal conductivity. To address this problem, different oxidising agents (e.g. peroxyacetic acid) with H<sub>2</sub>SO<sub>4</sub> were introduced as an alternative to exfoliate graphite into few-layer graphene in a single step at room temperature.<sup>91</sup> In this process, the exfoliated graphene derivative contains less oxygen (1.2%) and structural defects than previously reported chemical exfoliation methods hence exhibits superior electrical and thermal conductivity.

Etching is a chemical process to subtract or remove materials which was applied to the exfoliation of 2D materials,

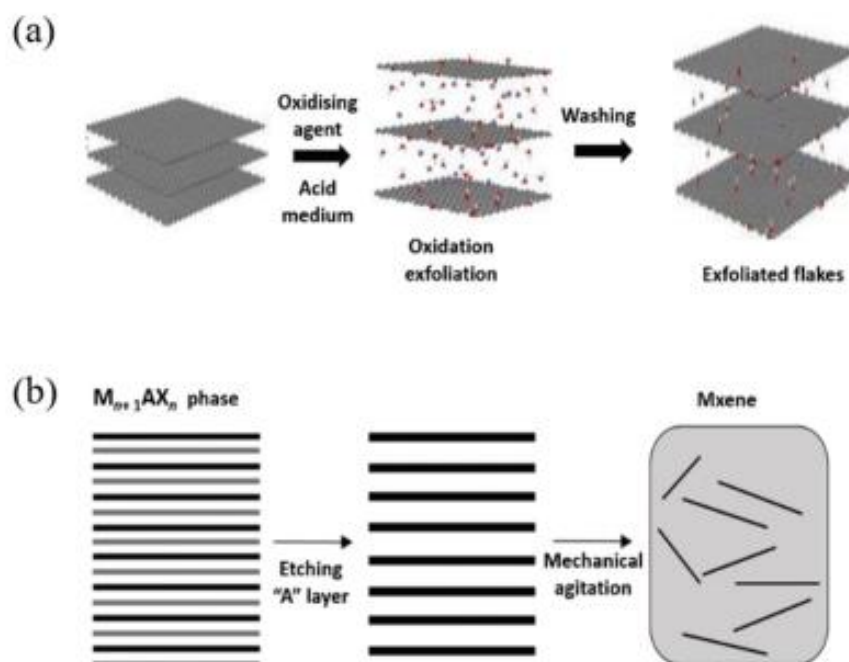


Fig. 3 Chemical exfoliation process via (a) oxidation exfoliation of 2D materials using oxidising agent and acid. Reproduced with permission from ref. 7 and 91 Copyright (2019) Elsevier. (b) Chemical etching of MAX phase to produce MXene. Reproduced with permission from ref. 94 Copyright (2019) Springer Nature.

particularly for the synthesis of MXene from its carbide  $M_{n+1}AX_n$ -phase as shown in Fig. 3b.<sup>92</sup> The process starts with an HF-treatments of the MAX-phase (e.g.  $Ti_3AlC_3$ ) where Al atoms are replaced by OH after reaction with HF followed by the breaking of hydrogen bonds and separation of nanosheets by mechanical forces (e.g. sonication).<sup>86,92</sup>

**2.2.1.3. Electrochemical exfoliation.** The electrochemical process is an extension of chemical exfoliation wherein the chemical reaction takes place by the application of an electrical current in liquid-phase. This process has been widely explored for synthesis of graphene and other 2D materials (e.g. hBN, TMD, MXene, phosphorene).<sup>9,65,93</sup> Basically, the cell consists of two electrodes, an electrolyte and external power-supply wherein both anodic and cathodic approaches can be applied for the exfoliation of 2D materials as shown in Fig. 4a. The working electrode is made of the target materials for exfoliation which might be in the form of foil, plate, rod and placed as either anode or cathode corresponding to the selected type of intercalants (e.g. anionic or cationic intercalants).<sup>95</sup> In the case of graphite, anodic intercalation results in oxidised graphene while non-oxidized exfoliated graphene were synthesized in the cathodic regime. The limitation of the electrochemical route is the need to provide an unbroken voltage bias which does not occur in ideal case. Few-layered 2D materials, even multilayered chunks are produced as the ionic intercalation and exfoliation will occur simultaneously at all edges of the working electrode in contact with the electrolyte.<sup>96</sup>

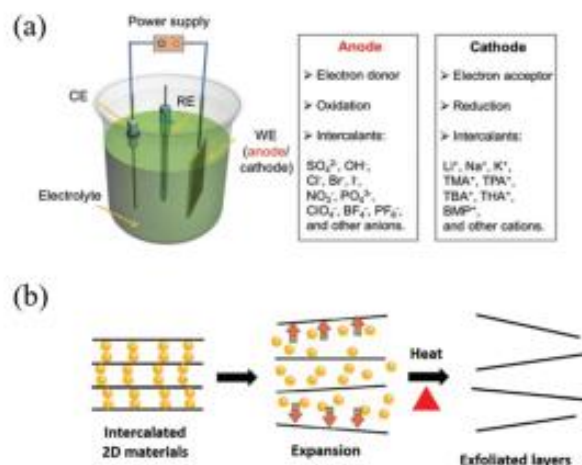


Fig. 4 Electrochemical exfoliation. (a) A typical configuration of electrochemical cell and the representative reactions at the anode and cathode, respectively. Reproduced with permission from ref. 9 Copyright (2019) Wiley-VCH. (b) High-temperature exfoliation under an atmospheric pressure. Reprinted with permission from ref. 97 Copyright (2009) American Chemical Society.

**2.2.1.4. Thermal exfoliation.** Thermal exfoliation of layered materials requires heating to trigger thermally active intercalating compounds between layers causing internal pressure that results in the exfoliation of layers. The rise in internal pressure enhances spacing distance between layers by releasing interca-



lant dependent gaseous species (e.g. H<sub>2</sub>O-vapor, CO<sub>2</sub>, SO<sub>2</sub> etc.) hence, overcoming interlayer vdW attraction of graphite and boron nitride-like materials.<sup>98,99</sup> The heating source can be a furnace, oven or microwave/infrared radiation.<sup>100,101</sup>

The heating can be slow or rapid depending on the heating process adopted based on intercalating compounds employed. Slow heating to high temperature can oxidise materials in an air atmosphere allowing oxygen atoms (O<sub>2</sub>) to enter between layers. In the case of boron nitride, heating at 1000 °C in air allows diffusion of O<sub>2</sub> between layers which leads to the formation of exfoliated hydroxylated boron nitride.<sup>98</sup> Self-curling assisted layer by layer exfoliation of BN can also be achieved by heat-induced intercalation of molten hydroxides which initiates self-exfoliation of BN.<sup>102</sup> However, intercalation using oxidising agents in acidic media is very common and has been primarily investigated for the intercalation of graphite and TMDs (e.g. MoS<sub>2</sub>, WS<sub>2</sub>) to obtain their derivatives (Fig. 4b).<sup>85,103</sup> To increase the exfoliation yield using a similar process, the heating can be performed in vacuum or ambient conditions.<sup>97,104</sup> Rapid heating using microwaves has become a widely used route which can generate up to 93% yield of exfoliated material with a high selectivity (95%) towards 'single-layer' graphene in ionic liquid.<sup>105,106</sup>

**2.2.2. Medium for liquid exfoliation process.** Prior to the exfoliation by any of these methods, understanding the interaction between solvents and bulk-flakes is important to assist in choosing the right solvent for high yielding exfoliation of 2D materials. In practice, an ideal solvent for liquid phase exfoliation must be able to vigorously exfoliate the material at the highest concentration and have ability to increase the metastable lifetime of the suspension by reducing interparticle attraction.<sup>66,107</sup> To achieve this objective, researchers initially considered Hildebrand ( $\delta$ ) solubility parameter (non-polar),<sup>12</sup> and Hansen solubility parameters (HSP) (dispersive forces, dipolar forces and hydrogen bond),<sup>108</sup> however neither models were found suitable for determining optimum solvent for carbon nanomaterials.<sup>109</sup> Liquid phase exfoliation of 2D materials involves different groups of media, (a) non-ionic media by matching the surface energy of materials,<sup>66</sup> (b) ionic exfoliation media based on the size of ions and their efficient intercalating ability through layers materials,<sup>67</sup> (c) combination of ionic and non-ionic media to change the interfacial interaction,<sup>110</sup> and (d) diffusion of supercritical fluids and decompression.<sup>111</sup> In this section, we will discuss how a group media in a cohort functions in exfoliation of layered materials.

**2.2.2.1. Non-ionic liquids.** Non-ionic liquids do not dissociate into ions, hence showing negligible or no electrical conductivity. However, these liquids may be polar or non-polar and many polar non-ionic liquids may be able to form hydrogen bonds (protic) and some cannot (aprotic) which affects their surface tension. The strong intermolecular forces between the solvent molecules decreases wettability and dispersion ability, which results in poor yields of 2D materials during exfoliation.<sup>66</sup> Fig. 5a displays the wettability of a series of solvents on the solid surfaces of layered materials (e.g. BN, graphite, MoS<sub>2</sub>, WS<sub>2</sub>). A new library of 40 solvents and their

different mixtures was built by Shen *et al.*<sup>66</sup> to match surface tension components between solvents and 2D materials to achieve better exfoliation and solubility. With the assistance of a mechanical exfoliation device (e.g. sonicator, high-shear mixer), it becomes straightforward to obtain highly efficient exfoliation of 2D materials as shown in Fig. 5b and c. A list of non-ionic liquids used to exfoliate 2D materials is presented in Table 2.

**2.2.2.2. Ionic liquid/molten salt medium.** Ionic liquids (ILs) or molten salts (*i.e.* Polyatomic organic or inorganic ions) were explored to a great extent for exfoliation of layered materials due to their ability to penetrate through the interlayer space of layered materials.<sup>67</sup> The presence of ILs makes it easier to obtain high yield exfoliation by simple mechanical agitation by means of sonication or stirring as shown in Fig. 5d(i).<sup>112</sup> The intercalation of the small ionic species (cations, e.g. Li<sup>+</sup>, Na<sup>+</sup> and K<sup>+</sup>, and anions, e.g. Cl<sup>-</sup>, Br<sup>-</sup>, I<sup>-</sup>, OH<sup>-</sup>, SO<sub>4</sub><sup>2-</sup>) enlarges the interlayer gap of layered materials resulting in reduction of the energy required to break the vdW forces during exfoliation. The efficient ion intercalation and exfoliation can be performed by mechanical, chemical, and electrochemical approaches which were discussed above in the section: methods of exfoliation. In the presence of ILs, ion exchange is also a common phenomenon occurring in some group of layered materials (e.g. layered double hydroxides, clays, and some metal oxides) which contain ions between the layers. In liquid medium, the ion can be exchanged to balance the charge on the layers which results in exfoliation by mild agitation as shown in Fig. 5d(ii).<sup>112,113</sup> A list of frequently used ILs for exfoliation of layered materials is shown in Table 2.

**2.2.2.3. Super-critical fluids.** Supercritical fluids (SCFs) do not possess distinct liquid and gas phases above their critical temperature and pressure as shown in Fig. 5e.<sup>114</sup> At this phase, the substances behave like both gas and liquid phase with almost zero surface energy, high diffusion coefficients, excellent wetting of surfaces that enables them to effuse through solids like a gas, and dissolve materials like a liquid.<sup>115</sup> The density, viscosity, and dielectric constants are temperature and pressure dependent, hence diffusivity and wettability can be easily altered. These features make SCFs useful for exfoliating layered materials by allowing them to diffuse through the layers, resulting in the increase in interlayer gap by weakening interlayer vdW forces (Fig. 5f). Recently many solvents at their supercritical state (enlisted in Table 1) were used for efficient exfoliation of 2D materials.<sup>111</sup> The spontaneous depressurization of gaseous SCFs make them highly suitable for synthesizing 2D materials with minimal solvent residuals while the liquid state SCFs requires slight change in critical parameters to enhance their exfoliation ability.

**2.2.2.4. Mixed solvents strategy.** The above discussed three different type of exfoliation medium can be mixed with each other to improve solubility parameters which enables a second degree yield of exfoliation with enhanced stabilization.<sup>110</sup> The mixture of polar/polar, non-polar/polar solvents, or combining them with Ionic liquids (ILs) as well as SCFs with other co-solvents (e.g. pyrene and pyrene-derivatives),<sup>116</sup> becomes a

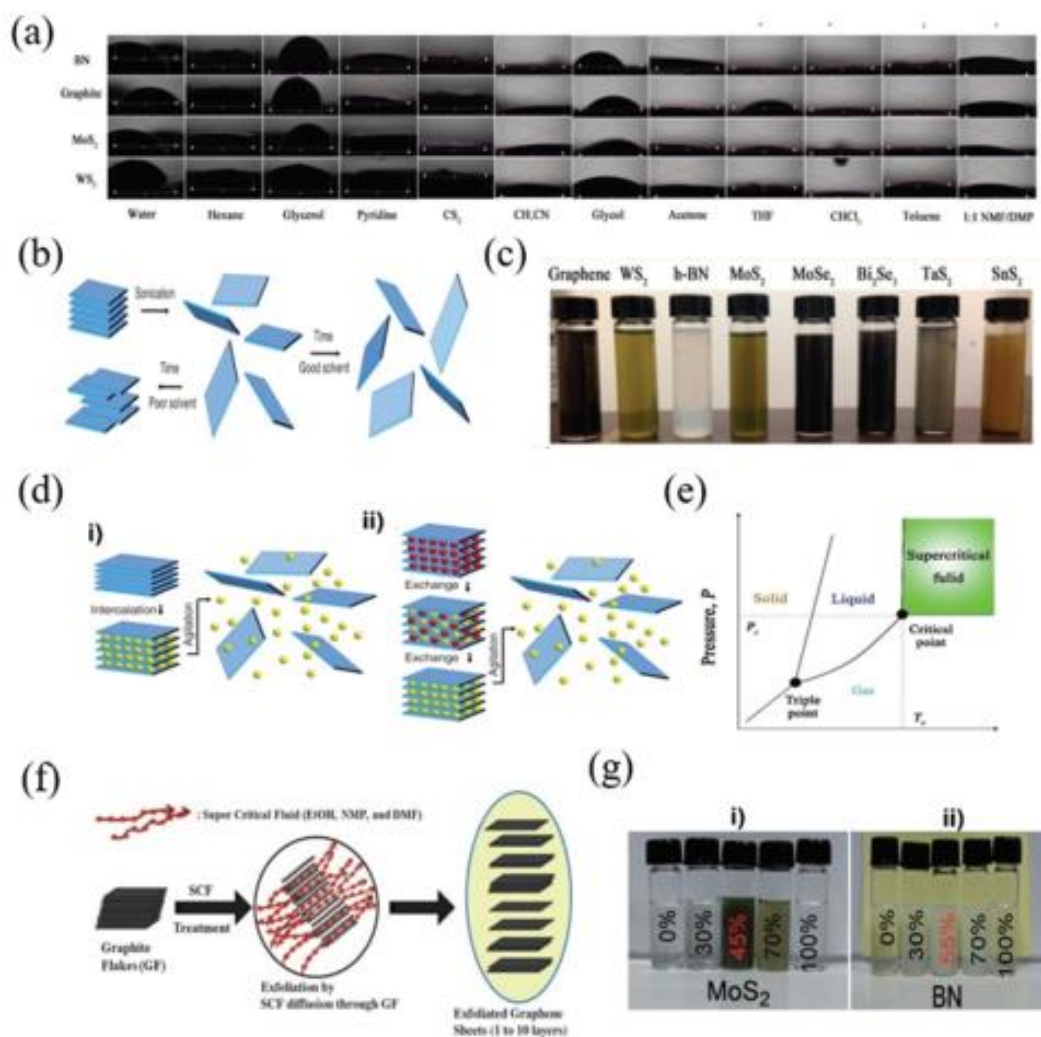


Fig. 5 (a) Typical contact angle images of hBN, graphite and  $\text{MoS}_2$ ,  $\text{WS}_2$  with 12 different solvents. Reproduced with permission from ref. 66 Copyright (2015) American Chemical Society. (b) The layered crystal is sonicated in a solvent, resulting in exfoliation and nanosheet formation. Reprinted with permission from ref. 112 Copyright (2013) The American Association for the Advancement of Science. (c) The stable suspension of different layered materials in solvent of the matched surface tension fluids. Reprinted with permission from ref. 66 Copyright (2009) American Chemical Society. (d) (i) Ion intercalation, and (ii) ion exchange procedure during exfoliation. Reproduced with permission from ref. 112 Copyright (2013) The American Association for the Advancement of Science. (e) Schematic illustrations of a pressure–temperature phase diagram. Reproduced with permission from ref. 111 and 114 Copyright (2004) American Chemical Society. (f) Example of the SCFs induced exfoliation of bulk layered materials (e.g. graphite). Reproduced with permission from ref. 130 Copyright (2019) Wiley-VCH. (g) Photographs of (i)  $\text{MoS}_2$ , and (ii) BN dispersions in various ethanol/water mixtures, which have been stored under ambient conditions for a week. Reproduced with permission from ref. 110 Copyright (2011) Wiley-VCH.

common strategy to obtain an enhanced outcome in exfoliation and stabilization of suspension.<sup>117</sup> Fig. 5g presents exfoliation of  $\text{MoS}_2$  and BN in different ethanol/water mixture wherein 45% ethanol in water results in high concentration of exfoliation and stable dispersion which is 55% for BN.<sup>110</sup> The high solubility composition of solvents can be explained by HSP to evaluate the compatibility between solvents and solutes for high quality dispersion. The alteration in HSP distance can be achieved by mixing two or three solvent in different ratios.

The smaller the HSP distance, the higher the solubility of solvents.

### 2.3. Designing functional 2D material inks

Conventional printing technologies, such as screen printing, gravure printing and flexographic printing are based on different operating principles that require the properties of the inks (e.g. viscosity, surface tension, solvent system, binder,

Table 2 Frequently used exfoliation media for 2D materials

Non-ionic liquids	Ionic liquids	Supercritical (Sc) fluids	Mixed fluids
Graphite – Water, <sup>118</sup> acetonitrile, <sup>119</sup> ethylene glycol, <sup>120</sup> <i>N,N</i> -dimethyl formamide (DMF), <sup>121</sup> <i>N</i> -Methyl-2-pyrrolidone (NMP), <sup>122</sup> Glycerol, <i>N,N</i> -dimethyl Acetamide (DMA)	Graphite – [C4mim][Ti <sub>2</sub> N], <sup>123</sup> ([EMim]Cl), <sup>124</sup> [TRPIL], <sup>125</sup>	Graphite – Sc-CO <sub>2</sub> , <sup>126,127</sup> Sc-NH <sub>3</sub> , <sup>128</sup> Sc-Acetonitrile, <sup>129</sup> Sc-NMP/Sc-EtOH/Sc-DM, <sup>130</sup> Sc-H <sub>2</sub> O, <sup>131</sup>	Graphite – Isopropanol/water, <sup>132</sup> ethanol/water, <sup>133,134</sup> water/acetone, <sup>135</sup> water/ammonia solution, <sup>136</sup>
TMDs (MX <sub>2</sub> ) – MoS <sub>2</sub> -Methyl-2-pyrrolidone (NMP), <sup>137</sup> Cyclohexylpyrrolidone, <sup>138</sup>	TMDs (MX <sub>2</sub> ) – MoS <sub>2</sub> -[TRPIL], <sup>125</sup>	TMDs (MX <sub>2</sub> ) – Sc-DMF (MoS <sub>2</sub> ) <sup>139,140</sup> ; (MoS <sub>2</sub> , MoSe <sub>2</sub> ) <sup>141</sup> Sc-CO <sub>2</sub> , <sup>142</sup> (MoS <sub>2</sub> ) <sup>142,143</sup> (WS <sub>2</sub> ) <sup>144</sup>	TMDs (MX <sub>2</sub> ) – ethanol/water, <sup>140</sup>
Hexagonal boron nitride (hBN) – Isopropyl alcohol (IPA), <sup>145</sup> <i>N,N</i> -dimethylformamide (DMF), <sup>146</sup> Dimethyl sulfoxide (DMSO), <sup>147</sup> and <i>N</i> -methylpyrrolidone (NMP), <sup>148</sup>	Hexagonal boron nitride (hBN) – Molten hydroxide (NaOH/KOH (molar ratio = 51.5/48.5)), <sup>102</sup> [Emim][Ti <sub>2</sub> N], [Hmim][Ti <sub>2</sub> N], [bpy][Ti <sub>2</sub> N], [Bmim][TfO], [Emim][BF <sub>4</sub> ], [Bmim][BF <sub>4</sub> ], [Bmim][PF <sub>6</sub> ], [Hmim][PF <sub>6</sub> ], <sup>149</sup> [TRPIL], <sup>125</sup>	Hexagonal boron nitride (hBN) – Sc-Isopropanol/H <sub>2</sub> O (hBN) <sup>150</sup> , Sc-EtOH (V <sub>2</sub> O <sub>5</sub> powder) <sup>151</sup>	Hexagonal boron nitride (hBN) – ethanol/water, <sup>110</sup> ammonia water/isopropyl alcohol (IPA), <sup>152</sup> <i>tert</i> -butanol/water. <sup>153</sup>
Black phosphorus (BP)-Iso-propyl alcohol (IPA), <sup>154</sup> acetone, <sup>155</sup> acetonitrile, <sup>156</sup> ethanol, <sup>157</sup> tetrahydrofuran (THF), <i>N,N</i> -dimethylformamide (DMF), <sup>158</sup> Dimethyl sulfoxide (DMSO), <sup>159</sup> <i>N</i> -methyl-2-pyrrolidone (NMP), <sup>79</sup> <i>N</i> -cyclohexyl-2-pyrrolidone, <sup>160</sup>	Black phosphorus (BP)-[HOEMIM][TfO], <sup>161</sup> [Emim][Ti <sub>2</sub> N] and [Bmim][Ti <sub>2</sub> N] <sup>162</sup>	Black phosphorus (BP)-Sc-CO <sub>2</sub> <sup>163</sup>	Black phosphorus (BP)-NMP/NaOH solution, <sup>164</sup> Triton X-100/DI water. <sup>165</sup>
Mxene – *MAX phase (Exfoliation media used after dissolving the A layer from MAX phase by etching), DMSO, <sup>166</sup> Tetraalkylammonium salts, <sup>92,167</sup> Tetrabutylammonium hydroxide (TBAOH) <sup>92</sup> , Choline hydroxide, <sup>168</sup> <i>n</i> -butylamine, <sup>168</sup> Aryl diazonium salt in water, <sup>169</sup> Lithium fluoride (LiF) sodium fluoride (NaF), <sup>170</sup> Hydrochloric acid (HCl). <sup>170</sup>			

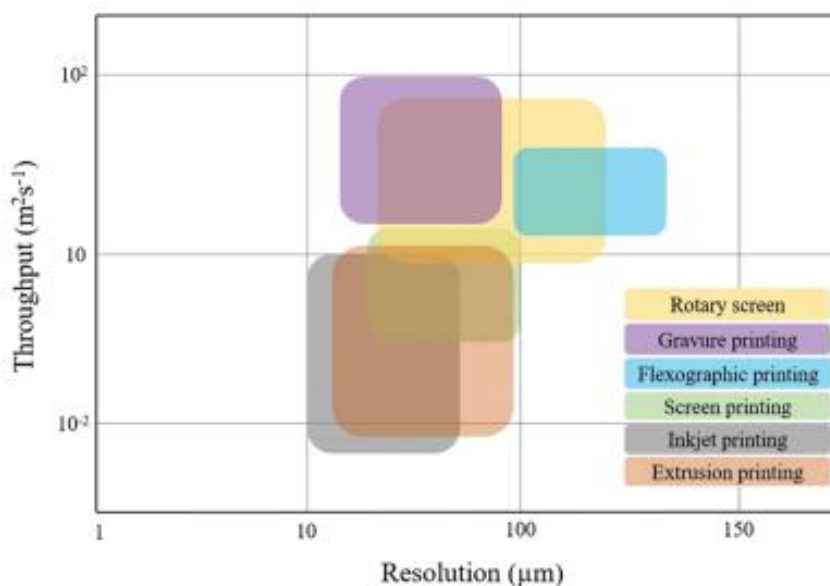


Fig. 6 Comparison graph of conventional printing technologies in terms of print throughput and best achievable resolutions. Reproduced with permission from ref. 2 Copyright (2018) Royal Society of Chemistry.

nanomaterial loading) to be tailored accordingly. Likewise, the printing resolution and production speed differs according to technique. The various techniques are compared visually in Fig. 6. Consequently, selection of suitable printing methods mostly depends on the target printed feature size but is also affected by the printed substrates.<sup>171</sup> Therefore, it is essential

to select a particular printing method and ink which are carefully matched to the target application. In this section, we discuss the fundamental principles of functional 2D material inks formulation, providing a context for printable 2D material application with a particular focus on extrusion-based 3D printing.

**2.3.1. Basic principles of ink systems.** Direct to substrate, mask-less, stencil-free additive electronics printing represents an increasingly valuable tool in the fabrication of electronic circuits and sensing devices. Digital extrusion printing of 2D materials is a largely untapped technique for high precision patterning towards the electronic sensing devices of the future. This section outlines the state of the art regarding 2D material inks, comparing the required characteristics for differing printing methods, highlighting the particular strengths and limitations of each and finally how extrusion printing fits into the future printed electronics ecosystem.

**2.3.1.1. Ink composition.** The inks are traditionally composed of pigments dispersed in a fluid vehicle consisting of a polymeric binder dissolved in one or more solvents, collectively referred to as a varnish. Many conventional inks include other additives to improve printing adhesion and drying, maintain pigment dispersion and prevent growth of microbes. When formulating functional inks based on 2D materials, however, the use of additives is largely avoided to maximize the electrical, thermal, dielectric and semi-conductive functionality of the printed ink. Ideally, the 2D material dispersion, equivalent to the traditional pigment, will be uniformly dispersed within the varnish and remain dispersed on storage without settling or re-agglomeration (Fig. 7). The main relevant difference between printing techniques is the maximum loading of 2D material which may be achieved. High resolution printing techniques such as inkjet require very low viscosity and surface tension which necessitates a high solvent loading and low 2D material loading. Each print pass deposits a layer of ink less than 1  $\mu\text{m}$  thick, which in turn only comprises a small amount of active material. This requires many print passes which creates a bottleneck to obtaining sufficient active material patterned on the substrate surface. By contrast, high viscosity, high loading inks such as those used for screen and extrusion printing can achieve suitable functionality by patterning of a thick layer of active material in the micron range in a single pass. Though the resolution of this type of printing is lower than inkjet, it is much more suitable for printed devices where a thicker layer with more functional 2D material may be deposited on the substrate much faster. Extrusion printing technology can easily accommodate the

same ink formulations as screen printing, while allowing digital patterning without the need for a stencil or mask. This section includes key highlights on the composition and formulation of printable inks with 2D functional materials.

#### 2.3.1.1.1 Ink composition for 2D functional material

The active component of the ink is the functional material, in this case a selected 2D material (e.g. graphene, MXene, black phosphorous, molybdenum disulfide, hexagonal boron nitride). Due to the differing properties of each 2D material, the required formulations vary, but each requires a uniform dispersion of the material throughout the solvent or vehicle to facilitate printing. Important aspects of recent 2D ink formulation are outlined in Table 3, with particular attention to binders, solvents, drying/annealing temperature and tested substrates. Each aspect of ink formulation is covered in more detail thereafter.

#### 2.3.1.1.2 Binders and additives

The ink binder is vital for acquiring the final rheological properties matched with the printing technique and for ensuring substrate adhesion. There are many binders reported including ethyl cellulose (EC),<sup>176,178,183</sup> polycarbonate,<sup>189</sup> polyaniline (PANI),<sup>190</sup> polyvinylpyrrolidone-polyvinylacetate copolymer (PVP-PVAc),<sup>191</sup> cellulose acetyl butyrate (CAB),<sup>173</sup> polyvinylpyrrolidone (PVP),<sup>192,193</sup> nitrocellulose,<sup>177</sup> polydimethylsiloxane (PDMS),<sup>194</sup> polystyrene sulfonate (PSS)<sup>195</sup> and carboxymethylcellulose (CMC).<sup>179,196</sup> However, the choice of binder should be linked with the desired solvent system, printing technique and substrate to maximize the print quality. The choice of binder may also be influenced by the final application of the printed device as some binder materials may be incompatible or unstable when in contact with water, acids, bases or organic solvents. While binders are essential for most practical ink applications, excessive binder loading adversely affects the functional properties of the ink such as electrical and thermal conductivity and dielectric constant, thus the binder loading must be optimised.

The fate of the binder after ink drying has been studied by Loh *et al.* where SEM imaging revealed the presence of clumps of ethyl cellulose binder scattered over the surface of the dried graphene ink after a single extrusion-printed layer (Fig. 8).<sup>178</sup> Further investigation showed that by increasing the number of printed layers that the clumps of EC become draped with graphene sheets after five printed layers, so increasing the conductivity of the final structures and minimizing binder interference.

Some inks require additives such as dispersants, surfactants, humectants, adhesion modifiers or rheology modifiers to meet printing specifications. One common dispersant is 1-pyrenesulfonic acid sodium salt first reported by Yang and his colleagues in 2013.<sup>197</sup> This dispersant interacts with the 2D material by  $\pi$ - $\pi$  stacking and the large, polar sulfonate group prevents re-agglomeration of the particles. This has the added effect of improving dispersion in polar solvents including water. Occasionally surfactants such as the anionic sodium dodecyl sulfate (SDS) or non-ionic Triton X-100 are employed which play a similar role to pyrene sulfonic acid, but with less

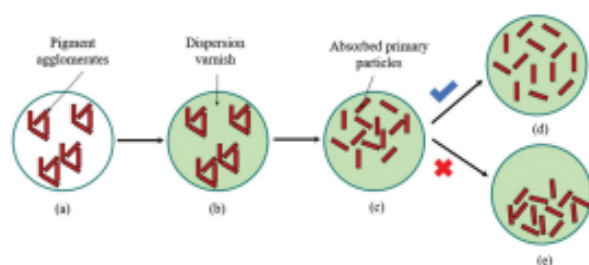


**Fig. 7** Visual concept for ideal versus non-ideal 2D material ink formulation. The dispersion mechanism, (a) pigment agglomeration, (b) agglomerates are wetted from outside, (c) pigment wetting, (d) homogeneous dispersion of primary particles, and (e) unsuccessful dispersion.

Table 3 Comparison of 2D material Ink formulations and processing

2D material	Type	Binder	Solvent(s)	Drying/ annealing	Substrate	Printing method
Graphene	Conductive	Na-1-PSA	Water	40 °C	Paper (PEL P60)	Inkjet <sup>172</sup>
		EC	Cyclohexanone, terpineol	250 °C	Polyimide	Inkjet <sup>20</sup>
		EC	terpineol	375 °C	Glass, polyimide, SiO <sub>2</sub> /Si	Inkjet <sup>173</sup>
	Biosensor	EC	Terpineol	300 °C	Polyimide	Screen <sup>174</sup>
		CAB	Dihydrolevoglucosenone (Cyrene)	100 °C	Paper	Screen <sup>175</sup>
		EC	Ethanol, terpineol	250 °C	Polyimide	Aerosol Jet <sup>176</sup>
		NC	Dibutyl phthalate, ethyl lactate (1 : 9 v/v)	350 °C	Polyimide	Aerosol Jet <sup>177</sup>
		Gas sensor	EC	Terpineol	415 °C	Glass, SiO <sub>2</sub> /Si
	CMC		Water, octanol (2% v/v)	25 °C, 350 °C	Monolith	DIW <sup>179</sup>
	MXenes (M <sub>2</sub> C <sub>x</sub> T <sub>2</sub> )	Conductive	None	Water	60 °C	Paper
Electro-optical		None	IPA	50 °C	PET, glass, SiO <sub>2</sub> /Si	Inkjet <sup>181</sup>
Black phosphorus (BP)	Semi-conductive	None	NMP, IPA, <i>n</i> -BuOH	60 °C	PET, glass, SiO <sub>2</sub> /Si	Inkjet <sup>182</sup>
		EC	DMF, terpineol	450 °C	SiO <sub>2</sub> /Si	Inkjet <sup>183</sup>
		None	NMP	60 °C	PET, Teslin	Inkjet <sup>184</sup>
		None	DMF	—	SiO <sub>2</sub> /Si	Spray (Laser Patterning) <sup>185</sup>
Molybdenum disulfide (MoS <sub>2</sub> )	Semi-conductive	—	(-)-Ethyl <i>l</i> -lactate, butyl lactate, ethylene di(acetate), dimethyl succinate	60 °C	SPE	Screen <sup>186</sup>
		HPMC	Water, propylene glycol (5.7% v/v)	80 °C	Polyimide	Aerosol Jet <sup>187</sup>
		Na-1-PSA	Water	25–150 °C	SiO <sub>2</sub> /Si	Inkjet <sup>188</sup>
Hexagonal boron nitride (h-BN)	Semi-conductive	Polycarbonate	DMF, chloroform	25–150 °C	BoPET	Screen <sup>189</sup>
	Dielectric		Ethanol, water		SiO <sub>2</sub> /Si	Inkjet <sup>188</sup>
Tungsten disulfide (WS <sub>2</sub> )	Electro-optical					Inkjet <sup>188</sup>

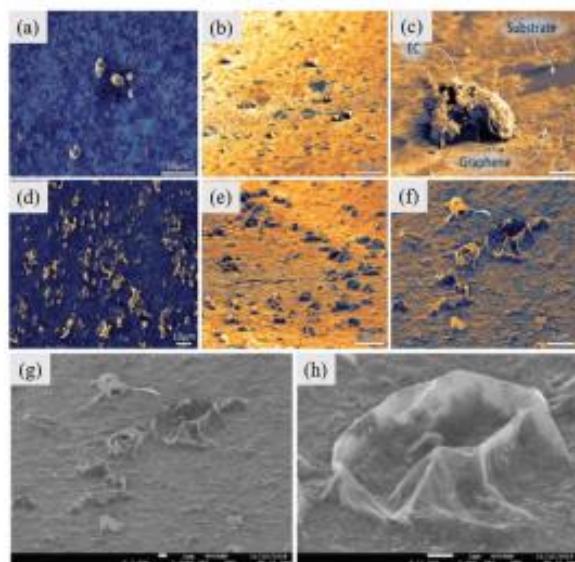


Fig. 8 SEM images of (a–f) extrusion-printed graphene gas sensing element showing ethyl-cellulose (EC) clumps after 1 print layer and (g and h) graphene sheets covering the EC after five print layers. Reprinted with permission from ref. 178 Copyright (2019) American Chemical Society.

specificity. Surfactants can improve the ability of the ink to wet the substrate surface by decreasing the ink surface tension.

For extrusion printing, generally no dispersant is required due to the high loading of 2D material in the varnish. The formulation of 2D material inks for extrusion printing may incorporate common binders suitable for formulation of screen print inks such as ethyl cellulose, cellulose acetate butyrate (CAB), PDMS or even no added binder as in the case of a water-based MXene ink.

#### 2.3.1.1.3 Solvents

The ideal solvent for printable inks is water because it is abundant, inexpensive, non-flammable and non-toxic. The use of water as a solvent for inks development is hampered by the viscosity, polarity and surface tension demands of both the printing technique and the 2D materials to be dispersed. Several solvents often used for exfoliation and formulation of inkjet inks, such as DMF and NMP have recently raised awareness of their toxicity.<sup>198</sup> As such, future exfoliation methods and ink formulations should avoid using these solvents. One excellent replacement has recently been identified, a newly developed bio-solvent, dihydrolevoglucosenone, marketed as Cyrene. This new solvent has closely matched solubility properties with DMF and NMP and has shown excellent performance for exfoliation and dispersion of graphene.<sup>199</sup> Alternatively, an industrially established, non-toxic solvent

## Nanoscale

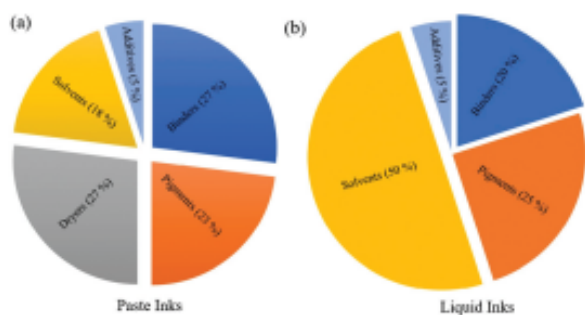


Fig. 9 Percentage composition of (a) paste inks compared with (b) liquid inks.

such as dimethylsulfoxide (DMSO) may be employed. Inks can be divided into two types based largely on the solvent content. Paste inks such as those required for screen and extrusion printing typically have a low solvent content, for example 18% v/v, whereas liquid inks required for inkjet or aerosol jet printing may have a solvent content in excess of 50% v/v (Fig. 9). For liquid inks, the choice of solvent becomes much more important to achieve the desired rheology, adhesion and resolution of the printed structures.

Table 4 highlights the critical specifications for many commonly used solvents typically used for formulation of all ink types. For liquid inks, a blend of solvents is often employed consisting of at least one higher boiling solvent and one lower boiling solvent to meet the requirements for droplet formation in inkjet printing, to avoid the coffee ring effect and facilitate uniform patterning and drying. Other relevant solvents specifications such as cost, toxicity and flammability should also be investigated before making a selection for ink formulation. Due to the high 2D material loading in extrusion printing inks, a solvent blend with a relatively high boiling point is

Table 4 Key properties of commonly used solvents for ink formulation<sup>200</sup>

Solvent	Viscosity (mPa s)	Surface tension (mN m <sup>-1</sup> )	Boiling point (°C)	Polarity (log P) <sup>a</sup>
Acetone	0.31	23.0	56	-0.16
Cyclohexanone	2.02	34.4	156	0.81
Cyrene	10.5	33.6	227	-1.52
n-limonene	0.92	28.5	176	4.23
DMP	0.79	34.4	153	-0.83
DMSO	2.00	43.5	189	-1.35
Ethanol	1.07	22.0	78	-0.18
Ethyl acetate	0.46	23.2	77	0.71
Ethylene glycol	16.1	48.4	197	-1.30
Isopropanol	2.04	23.3	83	0.16
NMP	1.67	44.6	202	-0.38
p-Cymene	0.75	28.1	177	4.10
Terpineol	6.92	31.9	219	3.28
Toluene	0.53	28.5	111	2.68
Water	0.89	72.7	100	-1.40

<sup>a</sup> Higher logP indicates greater hydrophobicity.

usually selected to avoid the ink drying in the dispenser during storage or clogging the nozzle during printing.

**2.3.1.2. Ink viscosity.** The accurate composition of the ink components defines the physical characteristics of the inks. Parameters such as density, viscosity, drying rate and surface tension can affect the printing process, however for any particular printing method, the ink viscosity is a key parameter. As an example, viscous inks exhibiting thixotropic fluid behaviour are required for screen printing, while in contrast low viscosity fluids are required for inkjet printing. Table 5 summarizes the ink compositions along with their static viscosities for usual print technologies relevant to 2D materials.

From the literature it is evident that the viscosity property of the ink is a rheological representation of a fluid with respect to the shear stress, the shear rate and the shear time.<sup>206–208</sup> Fig. 10a displays the common rheological behaviours of fluids, where each fluid has been categorised as either Newtonian fluids or non-Newtonian fluids. A Newtonian fluid is an ideal fluid with a linear shear stress/shear rate relationship and a constant viscosity. In practise very few fluids exhibit this type of behaviour. On the other hand, a pseudoplastic fluid presents decreased shear stress under increased shear rate along with drop in viscosity. This type of fluid requires less force to maintain flow at higher shear rates. For this reason, pseudoplastic characteristics are significant for formulating functional ink, as the ink pigments are more readily dispersed under stress. Each printing technique has slightly different demands in terms of ink viscosity. For example, screen printing requires the highest viscosity ink ranging from around 1000 up to 10 000 Pa s. This requirement

Table 5 Typical compositions and viscosity properties of inks for general printing technologies<sup>2,201–205</sup>

	Wet Ink composition (wt%)				Viscosity (mPa s)
	Binder	Additive	Solvent	Pigment	
Inkjet printing	5–20	1–5	65–95	5–10	4–30
Screen printing	45–65	1–5	20–30	12–20	1k–10k
Gravure printing	20–35	1–2	60–65	12–17	100–1k
Flexo printing	40–45	1–5	25–45	12–17	1k–2k
Extrusion printing	40–60	1–5	25–35	10–15	1k–10k

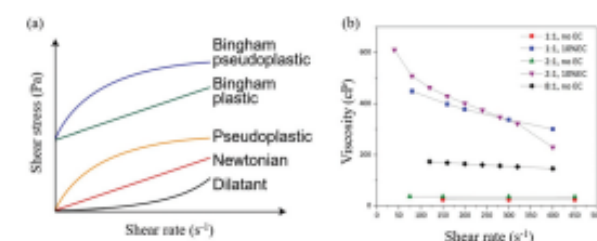


Fig. 10 (a) Schematic showing shear stress of different fluids with respect to shear rate.<sup>2</sup> (b) Effect on viscosity versus shear of a graphene/terpineol DIW ink system with and without addition of ethyl cellulose (EC) binder. Reprinted with permission from ref. 178 Copyright (2019) American Chemical Society.

## Review

is similar to that for extrudable ink applied to direct ink writing (DIW). In order to obtain an ink within the range suitable for screen or DIW printing, polymeric binders are usually required. When formulating a graphene DIW ink, Loh and co-workers clearly showed the requirement for an ethyl cellulose binder, without which the required viscosity range could not be achieved (Fig. 10b).<sup>178</sup>

**2.3.1.3. Ink processing.** In the literature, the formulation of inks usually begins with liquid exfoliation of the 2D material, sometimes with the desired binder or dispersion agent already discussed in section 2.1 and 2.2, however this has been shown to be an extremely inefficient process. For example, one study revealed the yield of dry ink material to be around 0.1 mg mL<sup>-1</sup> using a 100-fold excess of ethyl cellulose binder.<sup>30</sup> While the exfoliation solution may be reused multiple times, it requires the process to be repeated many times to collect sufficient material even for small scale ink development. Liquid exfoliation is carried out by either ultra-sonication or high shear mixing processes and is responsible not only for exfoliation of the 2D material, but also for dispersion of the nanosheets within the polymeric binder. If the formulated ink requires further blending to ensure a homogeneous mixture, this is often carried out by simple bath sonication in the case of low viscosity inks or by ball milling or three roll milling as in the case of highly viscous screen print inks. Low viscosity inkjet or aerosol jet inks are usually filtered at 0.3, 0.45 or 3 μm to remove larger particles due to the nozzle size constraints. Extrusion printing ink may be formulated by a solvent exchange process where the 2D material is dispersed with binder in a lower boiling, less viscous solvent before being exchanged for a higher boiling, more viscous solvent by removal of the first solvent under rotary vacuum evaporation. Alternatively, the 2D material may be directly blended into the varnish, consisting of binder and solvent system by three roll milling.

**2.3.1.4. Ink spreading and drying.** To obtain high fidelity printed patterns, the ink should exhibit minimal spread after application to the substrate. The ink must adhere to the substrate after drying with controllable shrinkage characteristics. Ideally, the ink will be cured or annealed at relatively low temperature to ensure the highest range of compatible substrates. Where the ink has a high solvent loading, particularly with inkjet printing, but also with flexographic and gravure printing, the surface energy of the substrate should be matched to the surface tension of the solvent system.

The relationship between the surface wetting of a substrate by a given fluid ink can be understood through Young's eqn (1), given  $\gamma_{s/v}$ ,  $\gamma_{s/l}$  and  $\gamma_{l/v}$  representing the interfacial tensions between the substrate surface (s), the fluid ink (l) and the vapour above the ink ( $\gamma$ ).<sup>209</sup> The key to determining good substrate wetting is the factor  $\theta$ , representing the contact angle of the fluid on the substrate in degrees.

$$\gamma_{s/v} = \gamma_{s/l} + \gamma_{l/v} \cos \theta \quad (1)$$

Fig. 11 illustrates the measurement of solvent droplet contact angles on a substrate showing the appearance of poor



Fig. 11 Left to right diagram showing a range of contact angles for inks on poorly wetted substrates to fully wetted substrates (ink spreading).

wetting of the substrate by the solvent where  $\theta > 90^\circ$ , good wetting of the substrate where  $\theta < 90^\circ$  and finally solvent spreading where  $\theta = 90^\circ$  that fully wets the substrate.

Particularly for liquid inks, to achieve the required viscosity, surface tension and drying parameters, several solvents are often blended to formulate the final ink. Due to the high solvent content of liquid inks such as those used for inkjet printing, the coffee ring effect often prevents high resolution patterning. The coffee ring effect is caused by flow of dispersed particles towards the outer rim of printed droplets as the solvent evaporates from the droplet edges, causing particle concentration at the edges and uneven printing. A phenomenon known as Marangoni flow can help to attenuate this effect if the correct blend of solvents is chosen.<sup>210</sup> These effects are illustrated in Fig. 12. In formulating versatile inks, many commercially relevant target substrates should be considered including paper, polyethylene terephthalate (PET), polyimide, silicon, epoxy (FR2/4), glass, ceramic and polystyrene and the surface energy properties taken into account.

All inks require a post-printing step to dry or anneal the printed features. This step is vital to ensure sufficient adhesion to the substrate and to maximize possible electrical conductivity. Many reported 2D material inks have been shown to require a high temperature post-printing treatment (e.g.

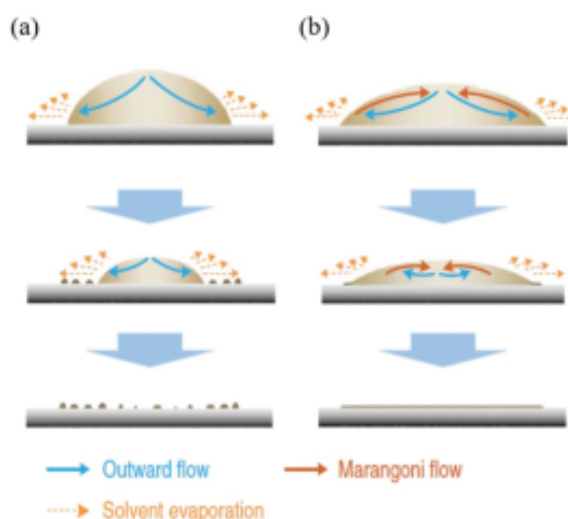


Fig. 12 (a) Illustration of coffee ring effect and (b) elimination of the effect due to Marangoni flow inside printed droplets. Reproduced with permission from ref. 182 Copyright (2017) Springer Nature.

## Nanoscale

250–450 °C) in order to gain the highest functionality.<sup>30,173,176–178,183,211</sup> This is most likely due to the selection of binder, often ethyl-cellulose in the case of graphene, which requires temperatures of at least 200 °C to initiate binder decomposition.<sup>30,178</sup> Numerous literature examples also employ photonic annealing, a technique adopted from metal nanoparticle ink curing methodology where short, very high energy pulses of light cause molecular heating within the ink material and subsequent decomposition of the polymeric binder.<sup>212</sup> Due to the fact that only the ink absorbs energy, photonic annealing widens to range of substrate compatibility to include PET and paper which are not suitable for high temperature annealing.<sup>213,214</sup> The inks formulated for extrusion printing have a high viscosity and show thixotropic behaviour which means that after leaving the printing nozzle, the ink will have minimal flow over the surface of the substrate. This effect is beneficial to improve the *x-y* printing resolution; however, it results in a relatively thick layer of deposited ink compared to inkjet printing. The layer thickness of extrusion printed 2D material may in the range of 5–20 microns which lends itself very well to applications in sensing and energy storage where a high area to volume ratio of the printed structures is desirable. Due to the high loading of active material in extrusion ink, the printed structures are usually dried at ambient or mild temperatures (e.g. 50–80 °C) sometimes under vacuum to ensure all residual solvent is removed. The decomposition of polymeric binder is usually not required due to a low binder to 2D material ratio. Where the extrusion printed ink is printed in multiple layers along the *z*-axis, the resulting 3D structures may be freeze-dried to obtain aerogel or sponge-like porous structures.<sup>215</sup> These structures are also ideal as printed battery electrodes, gas sensors or as bio-compatible scaffolds for tissue engineering.<sup>216</sup> This further highlights the versatility of extrusion printing.

### 3. Printing techniques

Printing technologies can be classified into two distinct schemes: conventional methods and digital printing.<sup>217</sup> In this study, screen printing and gravure printing are described as conventional mass printing schemes whereas inkjet and extrusion printing are described as digital printing schemes. Besides these printing methods, other printing methods do exist, although in this study we consider the latent printing

approach, which permits scaling-up for wide production at an industrially attainable scale. Moreover, the resolution of printed structures reasonably achievable with various printing techniques outlined herein as summarized in Table 6, along with the throughput (speed), setup cost, required viscosity range, acceptable particle size and overall 2D material loading. In the following section, key performances of these methods are summarised.

#### 3.1. Extrusion-based 3D printing

Extrusion-based 3D printing, relative to other printing processes, provides greater flexibility in the variation of ink materials as well as the large range of printed structures with featured sizes from micro to macro-scale.<sup>227</sup> This process can also fabricate robust 3D structures by printing and embedding materials into substrates, which benefits from wide adoption, easy operation, and precise printing of complex-geometry, with multiple solidification methods, which is not possible by other printing methods.<sup>228</sup>

In the last decade, the extrusion 3D printing has improved from single component or material printing to complex multi-component printing, facilitated by the use of customized combinations, open source software and printers.<sup>229</sup> The fundamentals of extrusion 3D printing are summarised in the following steps.

Firstly, this process utilizes a screw device or pneumatic actuator to feed the material using a cartridge and then transferred into a needle or nozzle for deposition, which is commonly used for compatibility with a large range of materials.<sup>229</sup> The material deposition in the *x*, *y* and *z* axes is monitored by an actuator which regulates the nozzle position in 3D space, enabling the printing of complex geometries where each layer is built on the top of the previous layer.<sup>230</sup>

Secondly, a user needs to employ 3D geometry design software *via* CAD to set up a model for the extrusion 3D printing system, where specific parameters can be defined to interpolate the surface properties or inner geometry.<sup>231</sup> For the purpose of construction of perfusion process, fluid dynamics simulations can be used to model a fluid flow through exchange and diffusion in and out of the fabricated object.<sup>232</sup>

The final step is to fabricate an extruded 3D construct and generate the pattern for the printer. To complete this process, the slicing program will take overall produced geometry *via*

Table 6 Summary of printing techniques comparing resolution, speed and cost<sup>212,218–226</sup>

Printing technique	Resolution (μm)	Speed	Setup cost	Ink viscosity (mPa s)	Particle size	2D material loading <sup>a</sup> (wt%)
Extrusion	50–200	++	S	5–500 000	+++	12–40
Screen	30–100	+++	S	1000–10 000	+++	12–20
Inkjet	20–100	+	SS	4–30	+	2–10
Aerosol Jet	20–200	++	SSS	1–500	++	5–12
Flexographic	30–100	++++	SSSS	1000–2000	+++	12–17
Rotogravure	25–100	+++	SSSS	100–1000	+++	12–17

<sup>a</sup> Wet ink.



CAD software to slice them into layers, creating a tool path for material deposition.<sup>233</sup> During the slicing process, the set-up spacing between layers is very critical to make sure there is enough contact between layers to prevent delamination.<sup>234</sup> However, the *z* height can change between layers from 75–100% of the strand diameter. According to the mechanical properties of the materials being deposited, strand-to-strand spacing can be altered to prevent layer sagging, especially for unsupported regions, and these can be modified by changing strand diameter *via* (1) extrusion rate, (2) needle diameter, (3) printed head speed, extrude material viscosity and (5) nozzle temperature.<sup>229</sup> Therefore, it is important to control these parameters to ensure high printing fidelity and maintain structural integrity.

Regarding the materials used for extrusion printing, a range of different approaches exist, from solid filament melting to ink-droplet deposition onto the substrate. Direct-ink-writing (DIW) and fused-deposition-modelling (FDM) are the two best known methods for the production of intricate structures using a range of various base materials, and a scheme indicates the processing set-up of FDM 3D printing in Fig. 13a.<sup>235</sup> Fig. 13(b and c) depicts two typical cellular printing structures produced by FDM, where the successful FDM needs a supporting substrate deposited by a secondary nozzle.<sup>236</sup> This approach can be applied to produce fully or partially solid structures with the size of a few hundred micrometres.<sup>237</sup>

As previously mentioned, another technique analogous to FDM is DIW, in which a viscoelastic ink can be extruded from a nozzle and then deposited onto a printing-bed surface by an external force including screws and mechanical piston.<sup>238</sup> The printing bed and ink can be cooled or heated to a designated temperature using a cooling and heating system, it is also possible to employ ambient conditions.<sup>241</sup> Fig. 13d illustrates the 3D printing procedure, which is applied to fabricate metamaterials with different porosities, ranging from a porous structure to a solid beam. Similar to FDM processing, a variety of particles, such as ceramic particles, may be infused with the ink for the purpose of production of a various range of material structures.<sup>242</sup> However, the fabricated structures normally present a soft texture, due to the use of a viscoelastic ink for printing.<sup>235</sup> Post-processing approaches (curing and sintering) are needed in order to fabricate rigid pattern and enhance the structural integrity.<sup>242</sup>

In summary, we can say that DIW extrusion-based 3D printing is capable of bridging the gap between 2D printing and 3D printing, allowing a layer of ink with greater thickness than that achievable with inkjet printing, but with a single print pass allowing a higher resolution compared to extrusion-based 3D printing due to layer boundary effects.<sup>225</sup> For example, Ho *et al.* have clearly shown the utility of this technique for constructing layered zinc micro-batteries back in 2010.<sup>243</sup> More recently, researchers at West Virginia University employed a custom built extrusion ink printing system to precisely pattern 1.7 × 8.0 mm lines of graphene/ethyl cellulose ink onto diced silicon wafer for the creation of an active gas sensor.<sup>178</sup>

Photographs of the computer-controlled *x*–*y*–*z* positioning and extrusion setup are displayed in Fig. 13g.

Capitalizing on the high conductivity of MXene 2D material, Zhang *et al.* succeeding in formulating a binder-free aqueous ink with sufficient viscosity to be used directly for extrusion printing. Taking advantage of the solvent wicking properties of a porous paper substrate, multiple layers of MXene ink could be built up to pattern electrodes with suitable conductivity for building printed microsupercapacitors.<sup>180</sup> Fig. 14 illustrates the formulated ink viscosity and printed structures, resistance decrease with successive printed layers and SEM imaging of the printed MXene material.

### 3.2. 3D printing

3D printing aims to automatically fabricate complex-shaped 3D parts from digital (CAD) data without using any tooling.<sup>244</sup> This is an additive manufacturing process, where materials can be deposited onto each other in layers to produce a 3D object.<sup>245</sup> Ink for 3D printing consists of polymers in the form of solid, liquid or powder, which is different with previous 2D printing methods.<sup>246</sup> This automated fabrication has some advantages, such as computer-aided design, quick design editing of the CAD model and precise dimensioning, compared to other manual or moulding processes.<sup>247</sup> Current and evolving 3D printing methods have some procedural features: the surface of the CAD model needs to be first created, and then the model is converted into layers with predetermined thickness by using slicing software for each 3D printing machine. These layered cross-sections can define the shape of the printed part and the collected information about each sliced section can be transmitted to the 3D printing device layer by layer.<sup>248</sup> The basic 3D printing process can be summarised as the following five steps: (1) creation of a designed CAD model, (2) conversion of the CAD model to an STL file, (3) slicing the STL file to several 2D layered cross-sections, (4) 3D printing the prototypes, and (5) post processing.<sup>249</sup>

### 3.3. Screen printing

The principle of screen printing or serigraphy is a stencil-based process where ink is transferred to the substrates by a stencil screen made of a fine and porous mesh of fabric, silk, metal threads or synthetic fibres.<sup>250</sup> The porous mesh is tightly stretched over a wood or metal frame, wherein the pores are blocked in the non-imaging areas using a photo-polymerised resin, while the remaining pores in the imaging areas are kept open to let ink flow through.<sup>251</sup> Fig. 15a demonstrates a schematic illustration of a flatbed screen printing process. During the printing, the ink is firstly flooded over the screen, and a squeegee is used to draw across it, forcing the ink through the open pores using shear force. At the same time, the substrate is held in place to make contact with the screen for receiving the ink. Moreover, high efficiency cylinder presses are possible to employ for roll-to-roll (R2R) with higher speed sheet-fed operation shown in Fig. 15b. Screen printing has been applied to directly print 2D materials on substrates, such as paper, plastic and glass (Fig. 15c).<sup>247</sup>

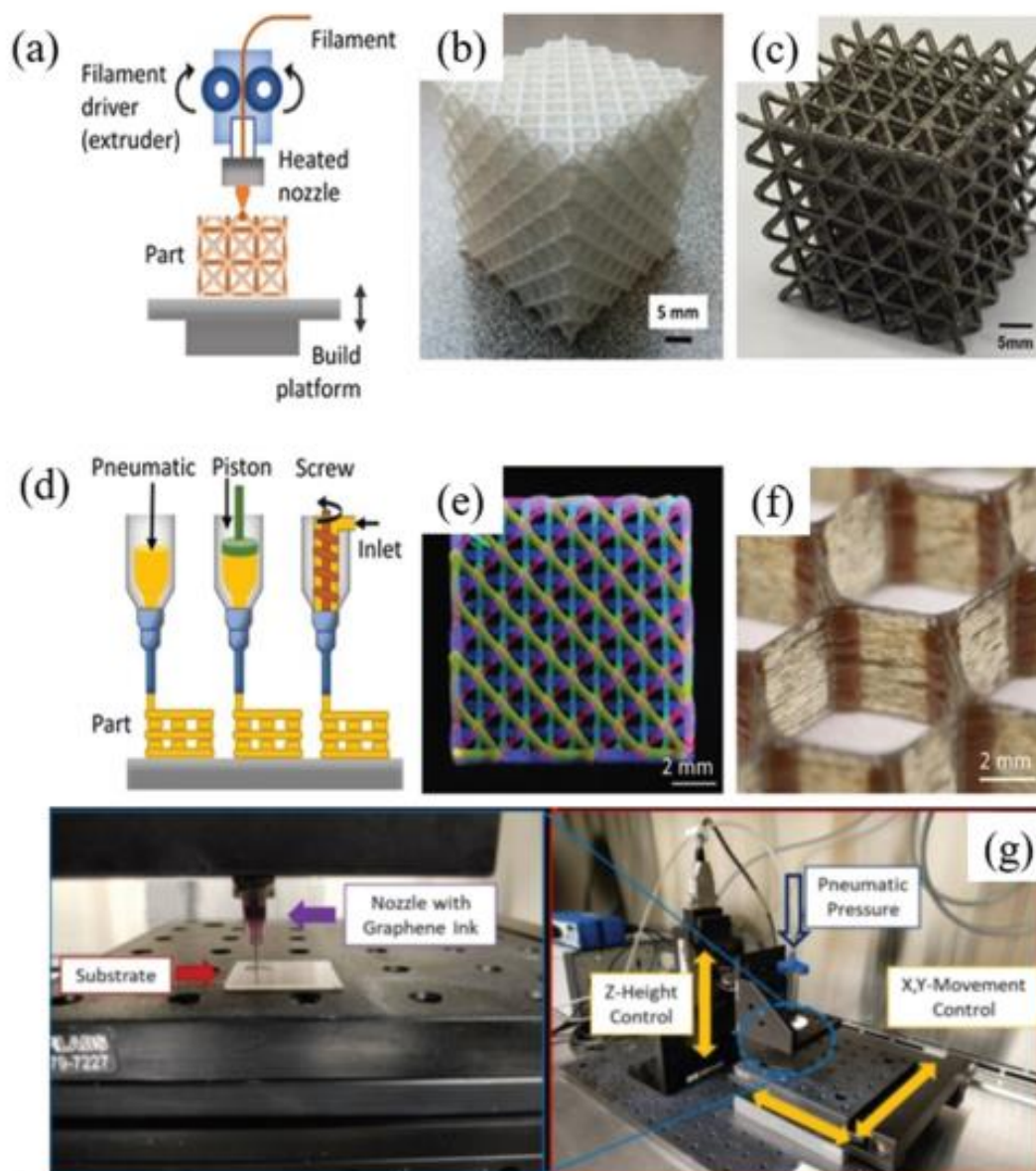


Fig. 13 Extrusion-based 3D printing methods. (a) Schematic illustration of the basic working principle and setup for Fused Deposition Modelling (FDM). Reproduced with permission from ref. 237 Copyright (2017) Elsevier. (b) A polymer octet-truss lattice fabricated by FDM. Reproduced with permission from ref. 237 Copyright (2017) Elsevier. (c) A composite lattice with polymer core and Ni outer shell synthesized through FDM and electroless plating. Reproduced with permission from ref. 239 Copyright (2018) Elsevier. (d) Schematic of the working principle behind Direct Ink Writing (DIW) using viscoelastic inks. Reproduced with permission from ref. 240 Copyright (2019) Wiley-VCH. (e) 3D micro lattice fabricated by multi-material DIW. Reproduced with permission from ref. 240 Copyright (2019) Wiley-VCH. (f) Balsa wood-inspired fibre-filled epoxy honeycomb composite printed using DIW. Reproduced with permission from ref. 240 Copyright (2019) Wiley-VCH. (g) Custom-built extrusion printing system for Direct Ink Writing of graphene. Reprinted with permission from ref. 178 Copyright (2019) American Chemical Society.

### 3.4. Gravure printing

Gravure printing technology is commonly applied to printing for packaging onto substrates such as foils, plastics and boxes and is a direct process where the ink is carried from the ink trough to the substrate using a gravure cylinder.<sup>247</sup> This print-

ing process relies on the viscosity of ink in the range of 100–1000 mPa s, and is particularly suitable for high-speed and low-cost fabrication of 2D printed applications due to high throughput.<sup>244</sup> Fig. 16a illustrates how the designed pattern is directly engraved into a metal cylinder, where the cells are filled with ink as the cylinder passes through the ink

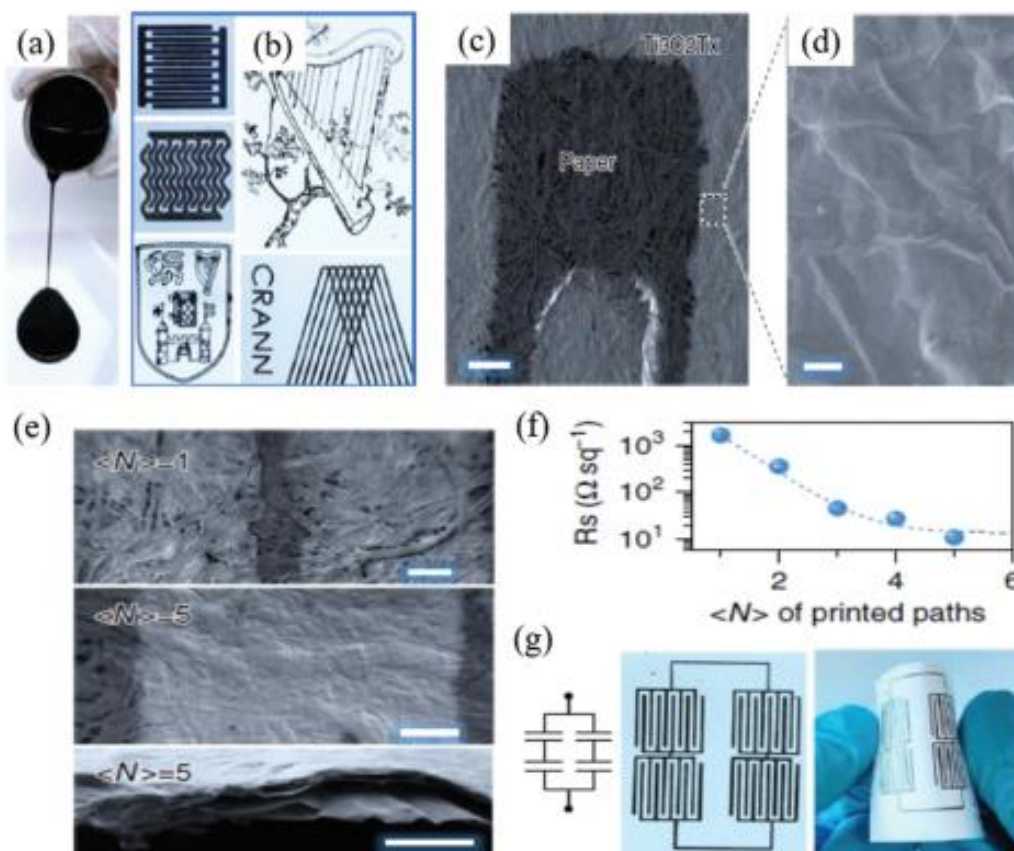


Fig. 14 (a and b) Extrusion-printed water-based MXene ink used to create micro-supercapacitor electrodes on paper; (c and d) SEM images of printed ink; (e) SEM images of ink layering and ink cross-section; (f) decrease in resistance with number of path layers printed; (g) combined series and parallel design and final printed electrodes on flexible paper. Reproduced with permission from ref. 180 Copyright (2019) Springer Nature.

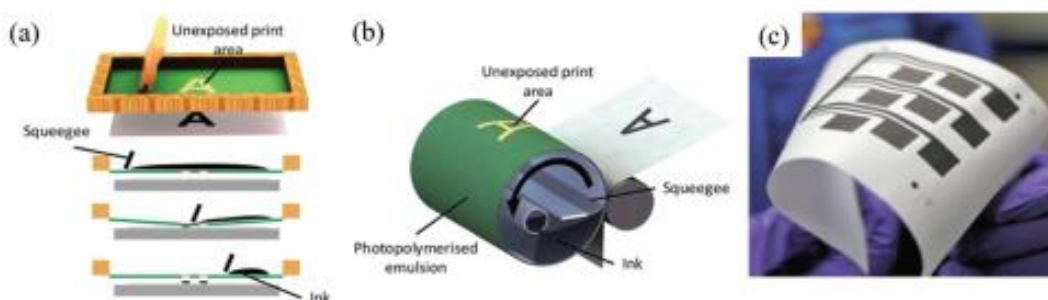


Fig. 15 Schematic of (a) flatbed and (b) rotary screen printer. (c) Screen-printed conductive graphene ink on paper when bent. Reproduced with permission from ref. 2 Copyright (2018) Royal Society of Chemistry.

trough. The ink is delivered by passing the substrate between an impression roller and a gravure cylinder.<sup>252</sup> In an ideal gravure printing process, the cells are filled with the ink during inking phase and become empty when the roller contacts the substrate.<sup>244</sup> This process depends on three distinct forces: (1) cohesive force ( $F_c$ ), (2) adhesive force on the cell

surface ( $F_{IC}$ ), and (3) adhesive force on the substrate ( $F_{IS}$ ). An ink transfer is in ideal condition when  $F_{IS} > F_{IC}$ .

### 3.5. Inkjet printing

Inkjet printing is a digital process where printing is achieved in a non-contact manner whereby ink droplets are propelled

## Nanoscale

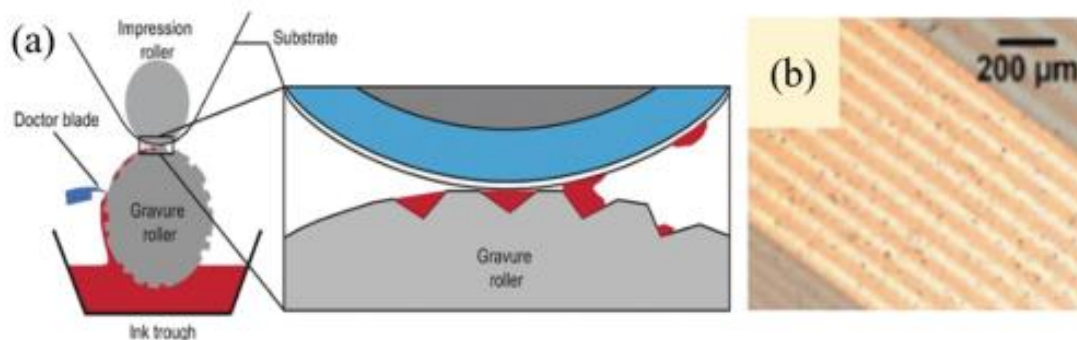


Fig. 16 (a) 2D schematic of gravure printing. Inset shows the magnified schematic of ink transfer from gravure roller to substrate. (b) Optical microscopy images of printed graphene lines using cell sizes of  $15\ \mu\text{m}$  (lines printed without the specified cell size are shaded grey). Reproduced with permission from ref. 2 Copyright (2018) Royal Society of Chemistry.

and deposited in fast succession onto the substrates to produce pre-designed images.<sup>253</sup> Inkjet is a digital method due to the fact that deposition of ink droplets and printing patterns are both monitored electronically.<sup>254</sup> Rapid and flexible fabrication is feasible, especially at the prototyping stage, as 2D materials are introduced to inkjet printing.<sup>255</sup> There are two major droplet jetting mechanisms: one is continuous inkjet (CIJ), and the other is drop-on-demand inkjet (DOD). CIJ is a technique where a stream of ink droplets is constantly produced and jetted out of an ink reservoir.<sup>247</sup> Fig. 17a indicates that ink droplets firstly pass through an electrostatic field are either charged or not charged by electrodes, these charged droplets are deflected onto a substrate, while the uncharged droplets are gathered by the ink catcher.<sup>256</sup> Fig. 17(b and c) shows that the ink droplets are produced *via* either a piezoelectric or a thermal process. In the DOD process, stabilized jetting of single droplets is an important requirement under electrical impulses without any satellite droplets occurring.<sup>257</sup> The behaviours of droplet jetting are mainly determined by the properties of the ink fluids, and characterized by a dimensional inverse Ohnesorge (Oh) number,  $Z$ . Importantly, the value of  $Z$  should be in the range of 1–14 for producing stable ink jetting.

### 3.6. Other printing techniques

**3.6.1 Flexographic printing.** The principle of flexographic printing is a relief process with a positive impression patterned on the outside of the printing cylinder as opposed to a

flat plate used for screen printing or an embossed cylinder used for gravure printing.<sup>258</sup> To print an image, the flexible relief printing plates are assembled and registered on a plate cylinder. Ink is firstly applied to the surface of the printing plates *via* an anilox roller, which is rolled through the ink trough to fill the cells with ink. Excessive ink will be removed by a doctor blade, keeping an even metering of the ink on the surface of the anilox roller, and then ink is transferred to a plate cylinder with the relief printing plate (Fig. 18).<sup>244</sup>

**3.6.2 Aerosol jet printing.** There is a growing body of published research related to application of aerosol jet printing to 2D materials. A schematic of the aerosol jetting process is depicted in Fig. 19. An inert carrier gas flowing through the nanoparticle ink creates an aerosol consisting of tiny ink droplets. The reservoir of ink may also be simultaneously ultrasonicated to maintain uniform particle dispersion. Gas pressure carries the aerosol to the printhead where an inert sheath gas focuses the stream of droplets through a narrow bore nozzle. The gas flow coupled with rapid solvent evaporation creates a very thin stream of particles which is patterned onto the substrate by a digitally-controlled precision gantry.<sup>219</sup>

The aerosol jet technique allows a wide range of fluid viscosities while providing access to high resolution patterning, including on three-dimensional substrates. Drawbacks include the high equipment cost and the requirement for a fixed substrate making this a low-throughput technique, currently. Various diameter nozzles may be used depending on the

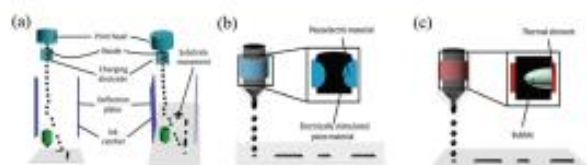


Fig. 17 (a) Continuous inkjet (CIJ), (b) drop-on-demand inkjet (DOD), and (c) DOD printer with thermal head. Reproduced with permission from ref. 2 Copyright (2018) Royal Society of Chemistry.

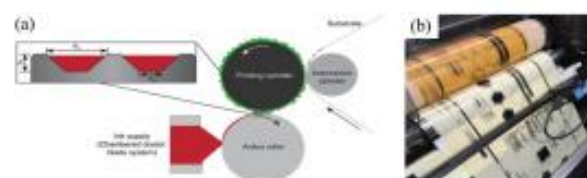


Fig. 18 (a) Schematic illustration of a flexographic printing system and (b) flexographic press during operation. Reproduced with permission from ref. 2 Copyright (2018) Royal Society of Chemistry.

## Review

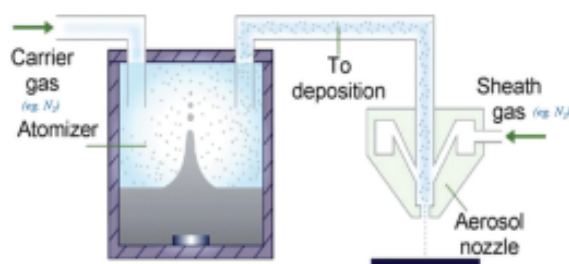


Fig. 19 Schematic of aerosol jet printing system. Reproduced with permission from ref. 225 Copyright (2008) Elsevier.

resolution required, however, the requirement for particles with lateral dimension in the nanometre range may limit the resolution achievable with some 2D materials.<sup>226</sup>

## 4. Extrusion printed 2D materials and their applications

Extrusion-based 3D printing of functional 2D material inks with suitable characteristics have been applied for many applications such as printed batteries, energy storage devices, sensors, electronics, optoelectronics and photonics. We note that many of the extrusion-based 3D printing applications based on functional 2D material inks not included in this section can potentially stand to benefit from functional 2D material ink formulations with the advancement of scalable extrusion-based 3D printed devices. Current progress on extrusion 3D printing for device fabrication for these applications is summarized in the following sections.

### 4.1. Extrusion-printed batteries

In energy storage, batteries, notably lithium-ion batteries, play a significant role due to their high power and capacity, which are generally used in stationary grids, electric vehicles, and portable electronics, for storing renewable energy.<sup>261,262</sup> Batteries are basically made of separators, electrodes and an electrolyte, with a metal or plastic casing. Generally, active materials, polymer binders and conductive additives are used to fabricate anode and cathode of an electrode. These materials are usually slurry-casted onto metal-foil current collectors for producing planar electrodes. Extrusion-printed electrodes can be obtained from printable inks. By modifying the viscosity and composition of the inks, and the parameters of printing such as pressure and speed; the dimension, shape, and thickness of an electrode can be controlled utilizing extrusion-printing. 3D electrodes have several advantages over 2D planar electrodes for example low tortuosity, high areal-loading density, and short ion diffusion distance.<sup>263–267</sup> Additionally, fluidic and combustible electrolytes are generally used in conventional batteries which may cause safety and capacity decay problems because of probable leakage and the evaporation of liquid electrolyte<sup>259</sup>. These issues can be opti-

mized by the extrusion-printed electrolyte because of its safer operation, enhanced electrochemical properties, and structural stability. With the advancement of extrusion-printing technology, several 3D printed batteries and electrodes have been widely developed and studied. In this section, the current advances of extrusion-printing in battery applications are reviewed.<sup>259,268–270</sup>

In 2013, Lewis *et al.* first worked on 3D-printed batteries using an extrusion-type 3D printer.<sup>268</sup> They fabricated interdigitated electrodes (IDEs) for Li-ion micro-battery architectures based on a layer by layer direct printing of anode and cathode on the top surface of a current collector. However, the current collector was made of gold and patterned on a substrate before initializing printing. After electrode printing, in a sealed case, 3D-IDEs and electrodes were placed by maintaining a small gap which was finally filled with liquid electrolytes. It is worthy to say that for extrusion printing technology, electrode ink with high electrical conductivity is an important parameter to improve the electrochemical properties of a battery. Reduced graphene oxide (rGO) has been proposed as a potential material to improve the electrical conductivity of extrusion printed electrodes for superior battery performance. Recently, Hu *et al.* reported graphene oxide (GO)-based inks for Li-ion battery electrode which employed by extrusion-printing technique.<sup>259</sup> In this study, aqueous graphene oxide-based inks were composed of electrode active materials as well as concentrated graphene oxide sheets. In this GO-based solution for ink formulation, water is used as a non-toxic, non-flammable solvent enabling low-cost manufacturing, simple processing and rapid drying. On the other hand, GO is used for this ink formulation because of its high surface area which helps to load electrode materials onto the surface of the flakes. Through extrusion-3D printing technology, GO flakes tend to coordinate along the extrusion direction owing to shear stress employed by the extruding nozzle providing an unbroken electron pathway. Besides, these GO flakes can also offer a wide space to accommodate the electrolyte within the extruded porous structure. As displayed in Fig. 20a, 3D-printed full cell has been constructed using IDEs where the cathode and anode were fabricated by LFP/GO ink and LTO/GO ink. Inset of Fig. 20a illustrates the large porous fragment structure of GO sheets. In this design, first,  $\text{Al}_2\text{O}_3$  nanoparticles (NPs) and poly(vinylidene fluoride) cohexafluoropropylene (PVDF-co-HFP) were soaked in a liquid electrolyte to fabricate solid-state electrolyte followed by printing a within the channel between two IDEs both creating a gel-polymer electrolyte as well as an insulated separator.<sup>259</sup>

To achieve high quality extrusion-printing of graphene oxide (GO)-based electrode inks, appropriate rheological properties are necessary. Fig. 22b illustrates the comparison between the apparent viscosity as a function of shear rate for pure GO, GO/LFP, and GO/LTO inks. From the figure, it can be observed that all synthesized materials (GO, GO/LFP, and GO/LTO) exhibited analogous viscosity curves, which suggests that the behaviour of the composite inks was dominated by the graphene oxide even though a large number of active nano-

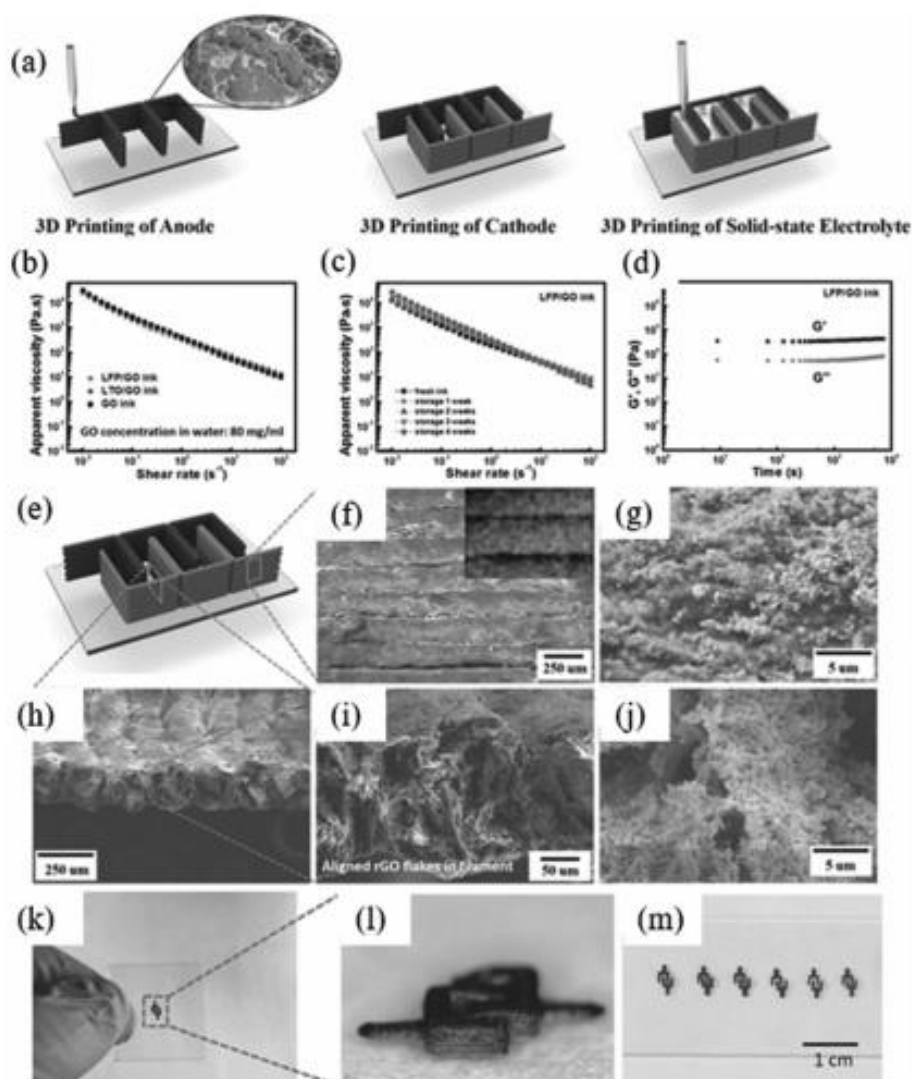


Fig. 20 (a) Schematic illustrations of extrusion-based 3D-printed interdigitated batteries. (Inset of Fig. 20a illustrates the large porous fragment structure of the extruded 3D printed gel-polymer composite containing GO sheets.) (b) Apparent viscosity vs. shear rate analysis for pure GO, GO/LFP, and GO/LTO inks, respectively. (c) Analogy of apparent viscosity for GO/LFP ink all-along four-week storage. (d) Storage- and loss-modulus aging characteristics as a function of time for GO/LFP. (e–j) Morphological characterizations of the annealed rGO/LFP electrodes. (k–l) Optical images of a miniaturized extrusion-based 3D printed electrodes. (m) Optical image of extrusion-based 3D printed electrodes array. Reproduced with permission from ref. 259 Copyright (2016) Wiley-VCH.

particles were added. Non-Newtonian inks can ensure printability due to shear-thinning characteristics along with a large apparent viscosity. These as-synthesized inks also exhibited retained their apparent viscosities over four weeks of storage time which confirmed the stable viscosity of GO-based ink for an prolonged storage period (Fig. 20c). To analyze the stability of the storage modulus ( $G'$ ) and loss modulus ( $G''$ ), the structural requirements under applied shear were also determined by using an oscillatory time sweep with a shear of 6 Pa at a frequency of 1 Hz for 3 hours which confirms the relative independence of the moduli over time (Fig. 20d).<sup>259</sup> Moreover, the

solidification process of the electrodes was performed by a freeze-drying and annealing process after completing printing. Post-print thermal reduction of graphene oxide was carried out to ensure sufficient electrical conductivity. After performing the annealing process, the rGO/LFP and rGO/LTO electrodes exhibited electrical conductivities of  $31.6$  and  $6.1 \text{ S cm}^{-1}$ , respectively. Fig. 20e–j shows the morphologies of the annealed rGO-based interdigitated electrodes, which were constructed of stacked filaments. In addition, GO sheets were coated with the electrode active materials. The inner part of the circular printed filament showed a porous structure which

## Review

was aligned with the rGO sheets. Fig. 20k and l, represents a pair of multilayer miniaturized IDEs (3 mm × 2 mm) prepared from printed graphene oxide-based electrode inks. By following this design, an array of IDEs was printed out on a flexible substrate to fulfil the battery current and voltage requirements (Fig. 20m). This array may be used as an energy storage unit to incorporate with other portable electronics for simplifying a printable electronics arrangement.<sup>259</sup>

#### 4.2. Extrusion-printed in-plane electrochemical capacitors

Compared to solid-state capacitors, electrochemical capacitors show higher cycling stability and high-power density<sup>272–274</sup>. Right now, in-plane electrochemical capacitors are attracting special attention due to their capability for complementing/replacing batteries as well as electrolytic capacitors.<sup>275–277</sup> As a result, extrusion-based 3D printing approaches enable convenient and programmable patterning of micro-electrodes on arbitrary substrates over conventional micro-fabrication techniques<sup>260</sup>. Unlike batteries, this type of in-plane two electrode system in an electrochemical capacitor may comprise similar or differing materials providing symmetrical and asymmetrical electrochemical capacitors, respectively.<sup>278,279</sup> Sun *et al.* reported this kind of symmetrical in-plane micro-supercapacitors printed by extrusion-based 3D printing, with graphene oriented interdigitated micro-electrodes.<sup>260</sup> They managed to build a 3D micro-extrusion system for printing the GO viscous ink (20 mg mL<sup>-1</sup>). As depicted in Fig. 21a, the interdigitated extrusion-printed GO ink micro-electrodes were patterned on the substrate for fabrication of symmetrical micro-supercapacitors. Fig. 21b, illustrates the thickness vs. printed layers curve for this micro-electrode which is linearly proportional. Moreover, from the electrochemical test results, it is evident that the usual electrical double-layer electrochemical behaviours and areal capacitance were dependent on the thickness of the electrode layers. With a four-layer printed device the capacitance value reached 19.8 mF cm<sup>-2</sup>. Remarkably, the reduced extrusion-printed GO films on a polyethylene terephthalate (PET) substrate demonstrated not only an outstanding flexibility through good mechanical robustness but also showed steady electrochemical behaviour as well (Fig. 21c and d). Jiang *et al.* developed a functional putty-like graphene oxide (GO) material which was employed for direct extrusion-based 3D printing of anticipated architectures along with tailor-patterned structures.<sup>280</sup> These tailored IDEs integrated into planar supercapacitors demonstrated an areal capacitance of 41.6 mF cm<sup>-2</sup> with a current density of 8.4 mA cm<sup>-2</sup>. However, due to the high-power density properties, these type of in-plane electrochemical capacitors may be used as a vital element in the field of electrochemical energy storage devices (EESDs), which are preferable for high power-consumption micro-sized devices. Though, the specific confined energy delivery hinders their practical applications. Thus, it is anticipated that researchers will focus more on improving the energy densities for this type of micro-capacitor without sacrificing their power densities.

#### 4.3. Extrusion-printed free-standing supercapacitors

Additive manufacturing (AM) mechanization arrives as an example for manufacturing scalable electrochemical energy storage devices, where free-standing 3D structures are generally required but are difficult to attain by conventional techniques. The integration of these technologies and advanced material compositions are of increasing interest because integration augments the accessible surface area along with the transportation of ions within the electrodes, at the same time reducing device volume. Yang *et al.* introduced an organic ink formulation with the maximum loading of MXene material (2D Ti<sub>3</sub>C<sub>2</sub>T<sub>x</sub>) based on ideal viscoelastic characteristic for developing different structures. They developed several sizes and shapes of freestanding extrusion-based 3D printed architectures with high specific surface area (Fig. 22(a–d)). Other studies reported that compared with conventional colloidal techniques, wet-processed materials (large-aspect-ratio and high surface charge) such as MXene, clay, and graphene oxide (GO) are more efficient for tuning the rheological characteristics.<sup>282–284</sup> In particular, the positive edges<sup>285</sup> and highly negatively charged surfaces of bi-dimensional MXenes provide favourable electrostatic characteristics along with the ability to intercalate water which is similar behaviour to some clays.<sup>170</sup> Yang *et al.* reported extrusion-based 3D printable ink which is composed of few-layer thick MXene flakes (large lateral size) in a water medium.

In addition, without using any sacrificial additives they successfully tuned the rheological characteristics of the ink.<sup>287–290</sup> They synthesized Ti<sub>3</sub>C<sub>2</sub>T<sub>x</sub> flakes with a thickness of 1–3 nm and ~8 μm lateral size (length/thickness ≈4000) to satisfy the suitability of 2D structured MXenes for extrusion-based 3D printing (Fig. 22(e–g)). Following this, the material was applied as a current collector and electrode material which they used to directly print interdigitated symmetric micro-supercapacitors (MSCs) along with a solid electrolyte using Ti<sub>3</sub>C<sub>2</sub>T<sub>x</sub> which removes the requirement for noble metals<sup>291</sup> as a current collector in extrusion-based 3D printed architectures.<sup>285,289,292</sup> Fig. 22h depicts the gravimetric capacitance (242 F g<sup>-1</sup>), areal capacitance (2.1 F cm<sup>-2</sup>) for the fabricated electrodes with 8.5 mg cm<sup>-2</sup> loading of active material at 0.2 A g<sup>-1</sup>. These devices also demonstrated high power with large energy densities and capacitance retention of more than 90% after 10 000 cycles. Compared with graphene or carbon nanotube (CNT) hybrids, these extrusion-based 3D-printed Ti<sub>3</sub>C<sub>2</sub>T<sub>x</sub> micro-supercapacitors showed enhanced energy density along with power density.<sup>293</sup> Not only that, it showed similar characteristics compared with Ruthenium(IV) oxide (RuO<sub>2</sub>)/Ti<sub>3</sub>C<sub>2</sub>T<sub>x</sub> hybrid material-based capacitor<sup>294</sup> (Fig. 22j). It is worth noting that the energy density of these MSCs is limited to some degree by the very narrow voltage window. Accordingly, to overcome this limitation, the use of an organic electrolyte or ionic liquid as well as designing asymmetric supercapacitors with different materials (*e.g.* graphene) will be further developed as impressive strategies to boost the energy density.

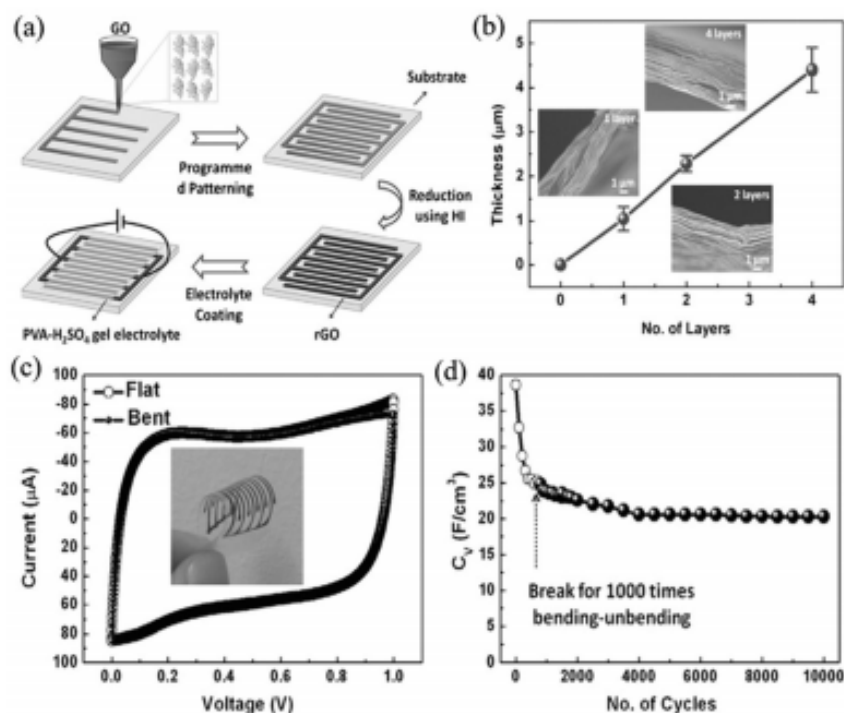


Fig. 21 (a) Schematic illustrations of the device fabrication techniques. (b) The thickness of laminated reduced graphene oxide (rGO) film with deviations of layers ( $n = 4$  samples). (c) cyclic-voltammety of the printed MSC with different bending states. (d) Cycling stability of the as-fabricated MSC. Reproduced with permission from ref. 260 Copyright (2015) Elsevier.

#### 4.4. Extrusion-printed sensing devices

2D nanomaterials have been enormously favoured in sensing applications due to their high aspect ratio, abundance of functional groups on their surface and high sensitivity<sup>295–297</sup>. Additive manufacturing technology offers feasible approaches for transmitting the exceptional intrinsic qualities of 2D nanomaterials into 3D macroscopic architectures to fabricate different kinds of sensors for temperature, chemicals, gases and vapours, and strain sensors. In this segment, the current advances of extrusion-printing in sensing applications are reviewed.<sup>298,299</sup>

**4.4.1. Temperature sensors.** Wearable temperature sensors are of great interest in the medical field that enable better personal health monitoring regardless of movement or device flexing.<sup>281</sup> The ideal temperature sensors should possess high sensitivity, quick response to temperature alteration, and stability in physiological conditions. The exploitation of 2D nanomaterials in temperature sensing applications has been widely investigated. For example, Wang *et al.* developed a printable ink composed of a graphene nanoplatelet and PDMS composite in which PDMS functions as a stretchable matrix with high printability while graphene provides the temperature sensitivity. Fig. 23a presents the fabrication method of graphene/PDMS temperature sensors *via* direct ink writing. The ink was patterning into three different structures including grid, triangular, and hexagonal designs and compared with solid com-

posite in terms of temperature sensitivity (Fig. 23b). It was found that the electrical resistance of the device followed a linear pattern over the temperature ramp for both printed and solid composites, showing high temperature sensitivity of 0.008 °C (Fig. 23c). In addition, the temperature sensitivity of solid composite decreased upon application of external strain or bending, while the sensitivity of the printed grid structure remained almost stable (Fig. 23d and e).

**4.4.2. Chemical sensors.** Kim *et al.*<sup>286</sup> reported the fabrication of freestanding reduced graphene oxide nanowires without supporting material *via* meniscus-guided growth in which a meniscus of GO ink formed once the micropipette was placed close to the surface. Pulling the micropipette resulted in the stretching of the meniscus and evaporation of water from GO colloidal solution (Fig. 24a). The GO wire radius could be tuned by adjusting the pulling rate of the micropipette (Fig. 24a). The GO wires were converted into rGO by thermal or chemical treatment. Different structures were constructed using rGO wires, showing the ability of rGO wires formation at any direction and site (Fig. 24b). The as-prepared rGO nanowires can serve as 3D transducers in gas sensing applications in which the electrical conductivity of rGO depends on the CO<sub>2</sub> concentration. Since the electrical conductivity of rGO depends on the positive charge carriers and CO<sub>2</sub> is electron donor, the electron transfer from CO<sub>2</sub> to rGO decreases the hole numbers and electrical conductivity (Fig. 24c).



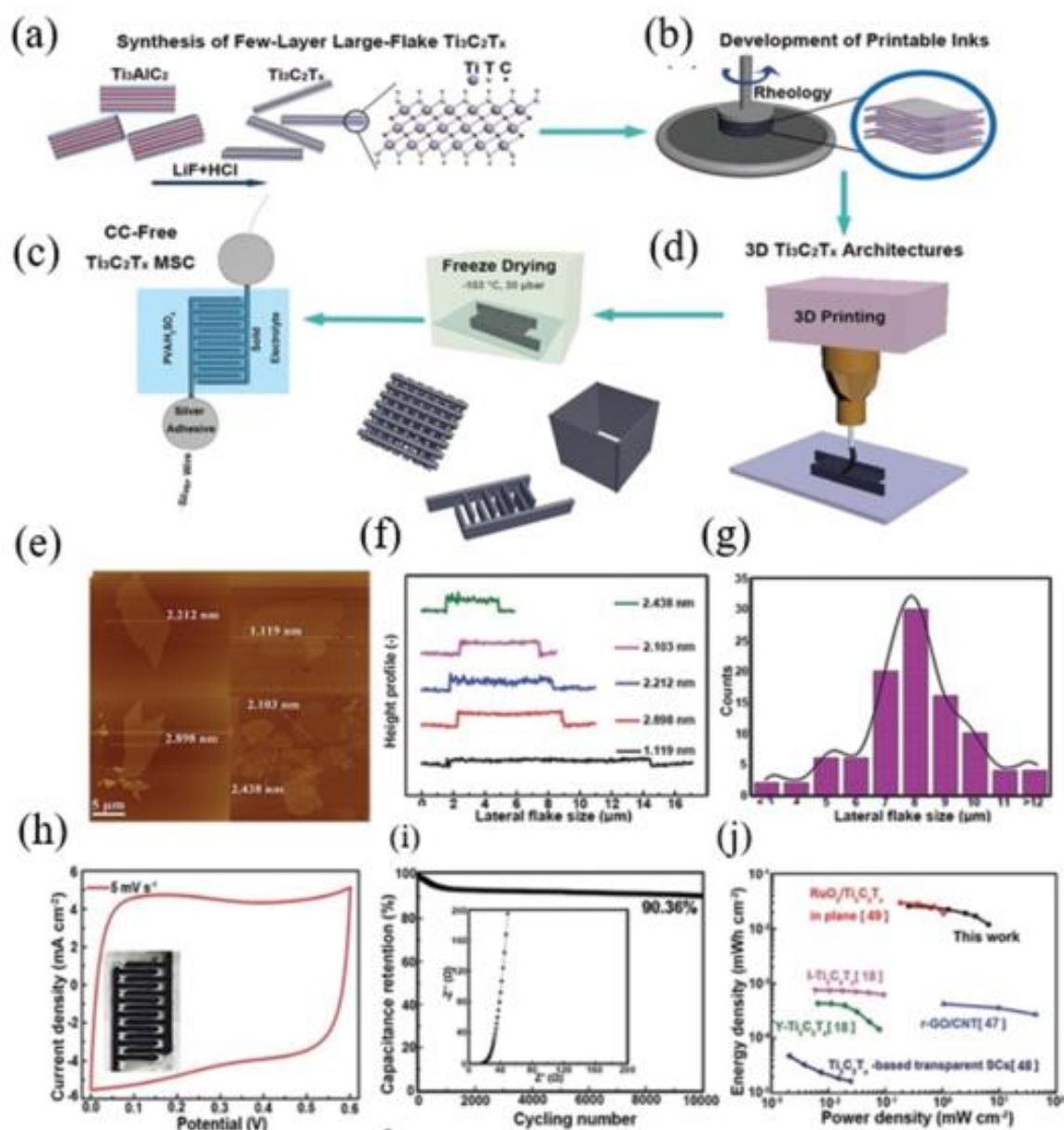


Fig. 22 Schematic illustrations of the developing strategy for extrusion-based 3D printing of freestanding MXene structures and micro super-capacitor (MSC) demonstration. (a) Synthesis process of 2D  $\text{Ti}_3\text{C}_2\text{Tx}$ , (b) Advancement of  $\text{Ti}_3\text{C}_2\text{Tx}$  inks at neutral pH and study of their compatibility for extrusion-based 3D printing via specific rheological property, (c) 3D printing of as-synthesized inks with compatible viscoelastic properties to produce different 3D architecture. The following freeze-drying procedure allows fabrication of freestanding 3D designs that maintain their dimensions and shape. (d) Probing the compatibility of the printable inks to develop high-performance symmetrical current-collector-free (CC-Free)  $\text{Ti}_3\text{C}_2\text{Tx}$  solid-state MSCs. (e–g) Atomic force microscopy (AFM) of dimensional analysis for  $\text{Ti}_3\text{C}_2\text{Tx}$  flakes, (h) cyclic voltammetry (CV) at  $5 \text{ mV s}^{-1}$  showing the ideal capacitive behaviour. The MSC MXene interdigitated electrode configuration is shown in the inset (5 mm smallest lateral size) (i) Cycling stability test showing over 90% capacitance retention after 10 000 cycles at  $1 \text{ A g}^{-1}$ , and (j) Ragone plots of the 3D-printed  $\text{Ti}_3\text{C}_2\text{Tx}$  super-capacitors together with other reported values for comparison. Reproduced with permission from ref. 271 Copyright (2019) Wiley-VCH.

4.4.3. **Strain sensors.** Flexible wearable strain sensors have drawn significant attention due to their broad application. An *et al.*<sup>300</sup> fabricated a stretchable, wearable sensor with graphene aerogel that showed high conductivity and sensitivity to

deformation. Fig. 25a outlines the fabrication process of the graphene aerogel sensors in which GO solution with different concentrations was prepared and printed by extrusion printing. Next, the printed GO structures were freeze dried, chemi-

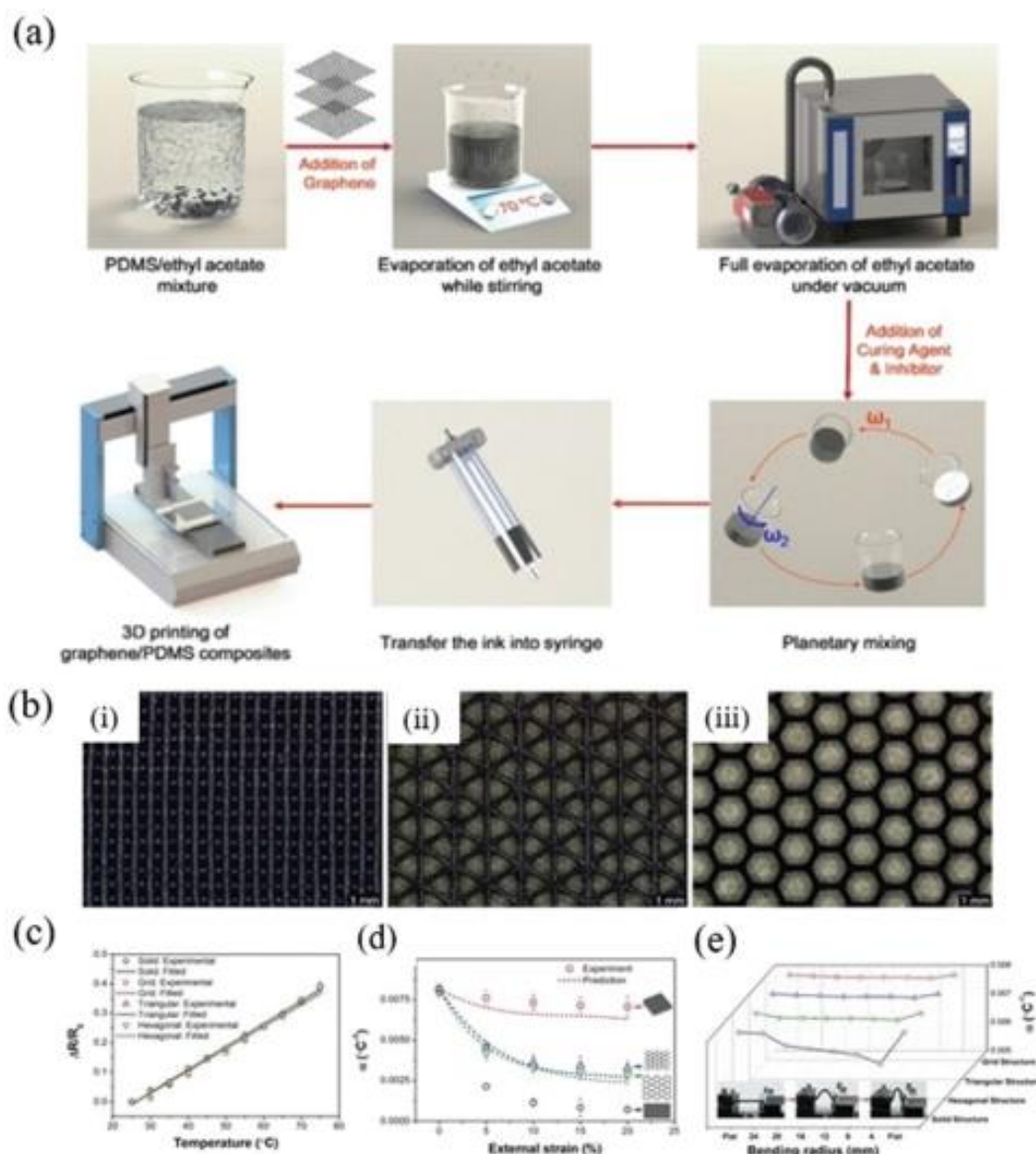


Fig. 23 (a) Schematic illustration of the fabrication process of the graphene/PDMS composite, (b) different patterns including grid, triangular, and hexagonal designs printed by the ink, (c) change in the electrical resistance of printed patterns and solid composite over temperature ramp, (c and d) temperature sensitivity of printed and solid composite under application of external strain and bending. Reprinted with permission from ref. 281 Copyright (2018) American Chemical Society.

cally reduced and sandwiched between PDMS layers. The microstructure of graphene aerogel can be tuned by adjusting the initial concentration of GO (Fig. 25b). After attachment of five devices to a glove, the printed graphene aerogel can monitor complicated hand gestures. Deconvolution of the combined changes in electrical resistance of the aerogel devices was demonstrated by principal component analysis (Fig. 25c).

In another study, fumed silica was combined with GO solution to improve the shear thinning and yield stress behaviour

of the ink which was reflected in better printability of the GO solution (Fig. 26a).<sup>38</sup> Fumed silica is a viscosity enhancing nanofiller that can be removed from the structure by etching with hydrofluoric acid solution. The ink was printed to produce macroscopic 3D architectures within an organic liquid bath (isooctane) which prevented evaporation of the water solution during printing and gelation. Supercritical CO<sub>2</sub> was used to dry the printed GO ink followed by reduction at high temperature and etching of the fumed silica with hydrofluoric acid solution. The electrical resistance of the printed

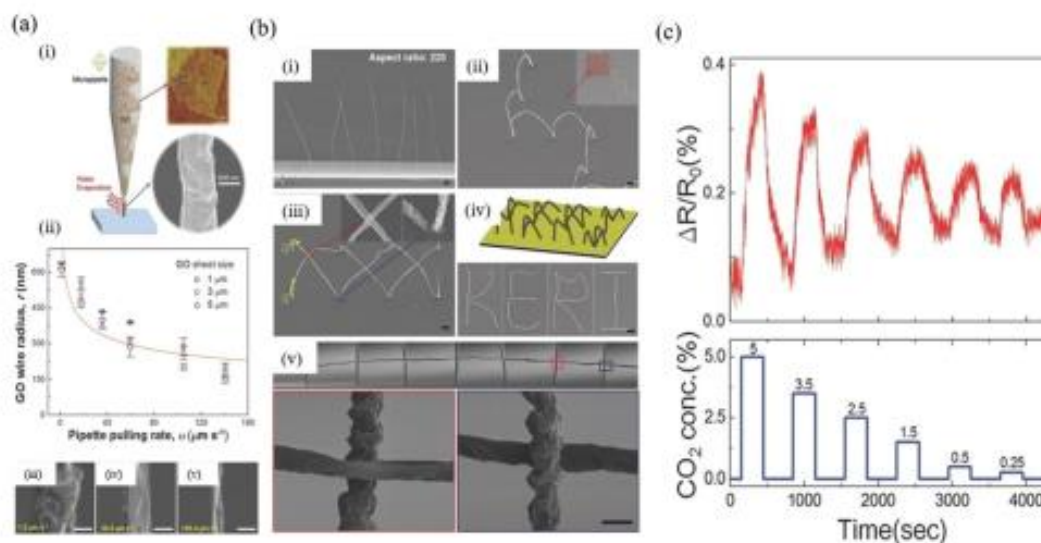


Fig. 24 (a) Schematic illustration of rGO wires formation via meniscus-guided growth and the dependence of wire radius to the pipette pulling rate, (b) fabrication of different 3D structures by rGO wires, (c) change in the electrical resistance of printed rGO wires once exposed to different concentration of  $\text{CO}_2$ . Reproduced with permission from ref. 286 Copyright (2015) Wiley-VCH.

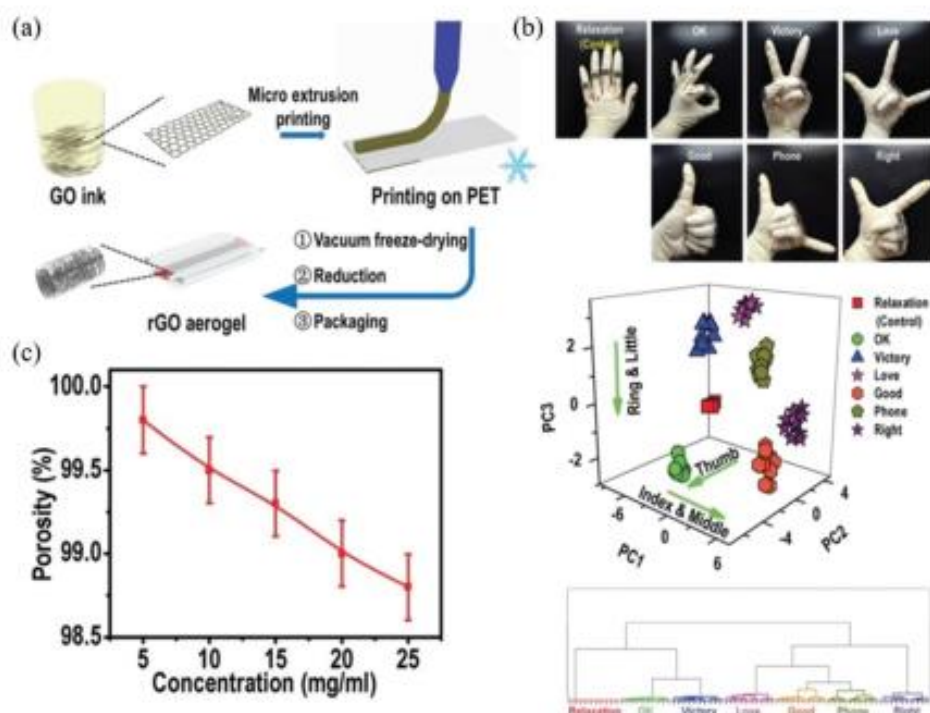


Fig. 25 (a) Schematic representation of the rGO aerogel formation, (b) tuning the porosity of printed aerogel by adjusting the GO concentrations, (c) placing the printed aerogel to the joints and analysis of the measured electrical conductivity over seven different gestures by employing principal component analysis (PCA), and hierarchical cluster analysis (HCA) statistical operations. Reproduced with permission from ref. 300 Copyright (2016) Royal Society of Chemistry.

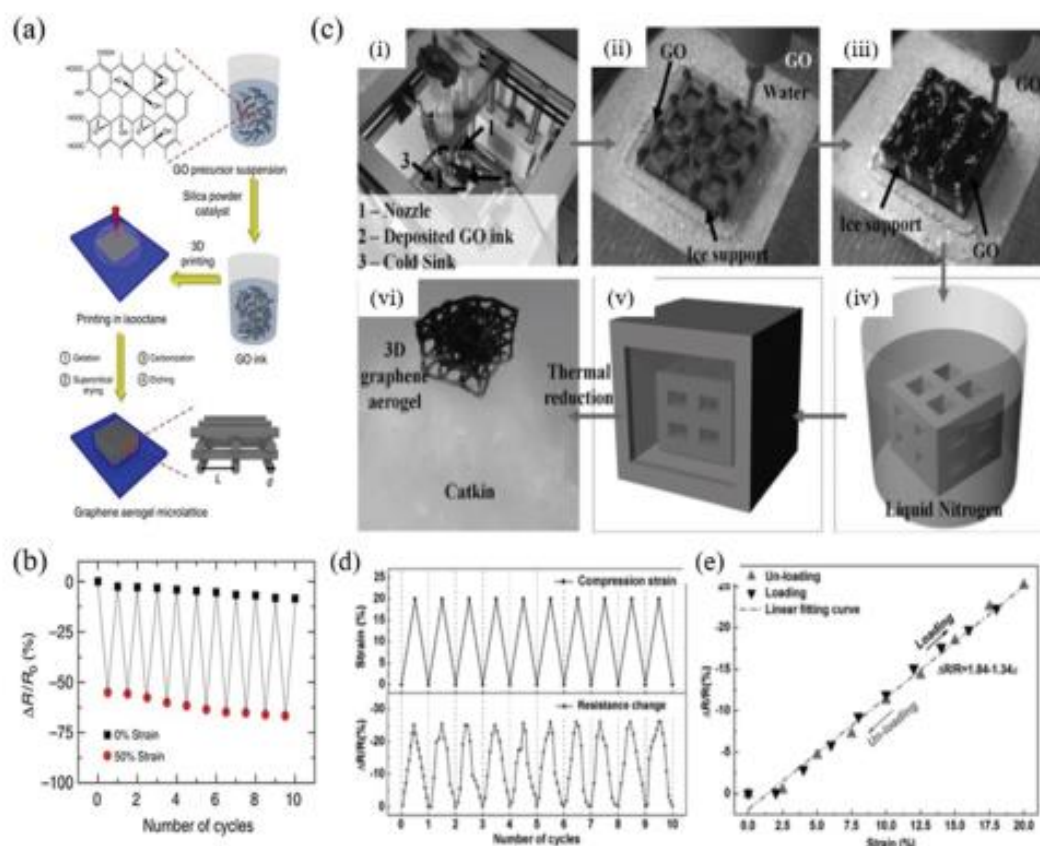


Fig. 26 (a) Schematic representation of the graphene/fumed silica ink, reproduced with permission from ref. 38 Copyright (2016) Springer Nature. (b) Change in the electrical resistance during application of multiple strains, (c) printing of GO ink with low concentration on cold bath for solidification of printed layers, (d) electrical sensitivity of the printed graphene aerogel over compression, (e) hysteresis of electrical resistance over loading and unloading strains. Reproduced with permission from ref. 301 Copyright (2016) Wiley-VCH.

3D rGO aerogel upon application of strain over multiple cycles, showed a high sensitivity of printed aerogel to deformation (Fig. 26b). Elsewhere, GO solutions with low concentration were printed in a cold bath ( $-25\text{ }^{\circ}\text{C}$ ) to immediately solidify the printed layers (Fig. 26c).<sup>301</sup> Afterwards, the printed structures were freeze-dried and reduced at high temperature to achieve 3D rGO aerogels. The electrical resistance of the 3D printed aerogel showed a high sensitivity to compression strain over multiple cycles (Fig. 26d). In addition, the electrical resistance of the printed rGO aerogel demonstrated high recoverability over loading and unloading strains (Fig. 26e).

It is clear that extrusion-based 3D printed flexible electronic devices play a significant role in changing the approach of human interaction with electrical devices as well as improving the outlook of human life by enhancing electronic devices with particular customization. However, the complete application of extrusion-based 3D printing technology is yet to be realized with further research and development required to match the capabilities of 2D extrusion inks with suitable 3D printing technologies. We conclude that novel flexible func-

tional 2D conductive material design and fabrication are suitable for several extrusion-based 3D printing technologies which can promote the rapid improvement of extrusion-based 3D printed flexible devices in several fields including biomedical, opto-electronics and soft-robotics.

## 5. Conclusions and perspectives

### 5.1. Conclusions

As a growing technology, printed portable electronics are achieving an ever-increasing consideration by society, not only in the arena of research but also in industry. The application of printable 2D material inks for fabricating portable electronics, including batteries, super-capacitors, sensors, opto-electronics, has enormous potential for rapid manufacturing and large-scale production. These multipurpose printable platforms will grant an abundance of opportunities for the fabrication of next-generation smart devices. Moreover, additive manufacturing, usually known as extrusion-based 3D printing, has

## Review

become more widespread due to the introduction of inexpensive and straightforward printing machines. This extrusion-based 3D-printing technology is increasingly being adopted by many entities worldwide, including research laboratories, industry, and research institutions. Not only that, it has even reached to individuals for personal use. With the help of this printing method, people will soon be able to design and fabricate wide-ranging devices with exciting capabilities in the comfort of their own home.

In this review, we have summarized the current progress development and advancements of functional 2D material inks and several printing techniques with a highlight on extrusion-based 3D printing with their real-world applications. Since the first demonstration of graphene-based printed electronics, this printing arena has experienced four considerable advances: first, the functional material demand has expanded from graphene alone to a broader choice of available 2D materials. Second, 2D material inks have progressed from simple solution-processed dispersions toward formulated functional inks adapted for meeting the specific criteria for several print processes. Third, the available printing methods have expanded from inkjet printing techniques to a wider printing stage including screen-printing, flexographic printing, gravure printing, as well as extrusion-based 3D printing that offers quicker production rates along with complex device architectures. Fourth, the examined applications for extrusion-based 3D printing have expanded to numerous major technological areas, including opto-electronics, energy storage devices (battery & super-capacitors), sensors and photonics. Taken together these represent significant developments for the scope of functional 2D material inks, and associated extrusion-based 3D printing, as a promising podium for the future generation of disruptive technologies.

Despite these developments, there are numerous prospects for improving the quality and performance of the fabricated device applications discussed above. There is considerable need to scale-up extrusion-based 3D printing technology from laboratory scale to device manufacturing scale preparing for real applications. With this scenario in mind, noteworthy improvement steps were taken to develop the ideal ink for particular applications through the underlying materials processing and ink formulations. Although remarkable advancement has been observed in the previous decade, still there is opportunity to study 2D material processing to develop the exfoliation productivity, to increase the manufacturing yield and decrease the manufacturing cost, and to better sort the exfoliated flakes. Certainly, it is significant to achieve a high manufacturing yield of mono-layers as well as mono-dispersed 2D material flakes with precisely controlled flake size and thickness. On this basis, optimising the process of functional ink formulations for achieving ideal fluidic properties, ink-substrate interactions, drying dynamics along with fundamental studies into additive, solvent and binder compatibility are of demanding concern. As for the formulation of functional printable inks, there is still a gap between active materials and printable inks.

## 5.2. Future research directions

To date, several 2D materials have been used to commercially formulate functional inks for existing printing methods. However, it is difficult to recommend a common formulation process for 2D-materials-based printable inks that can satisfy various requirements (e.g. rheology, thermal, and electrical stability) of a particular printing method. This complexity of functional ink formulation stems from various factors. From a materials viewpoint, the intrinsic dispersibility of 2D materials is influenced by material species, functional groups, size distribution, and surface charge which make the formulation process different for every single material. For example, the surface negative charge and hydrophilicity of MXene flakes permits the facile synthesis of additive free along with concentrated aqueous MXenes dispersions. By contrast, realizing additive free inks with graphene flakes without functionalization is exceptionally difficult. On the other hand, every printing method has its specific rheological requirements for functional inks, such as viscosity, volatility, wettability and viscoelasticity. That is why a multipurpose functional ink formulation process is thus considered impossible. Still, we can put efforts to realize these parameters and put forward some guidelines for tailoring them. To establish the required rheological characteristics, developed inks typically contain more or less additives requiring a post-treatment step for their removal.

The proposed post-treatments procedure such as annealing at elevated temperatures is incompatible with most flexible substrates, which hinders their flexible electronics applications. Lastly, a few matters of current methods are remaining to be solved such as scalability of present printing methods from lab-scale to industry-scale for extended production along with printing resolution of various miniaturized devices. In spite of continuing progress, development of advanced printing methods that can acquire high resolution and promising scalability for 2D material inks is of tremendous interest for fabricating printable electronics.

Nowadays, there are various types of 3D printing technologies available in the market. More importantly, different materials can be used in these technologies for continuing the fabrication process which have already benefited many fields of application such as medicine, mechanical, electrical, and material engineering, chemistry, the arts and design, and core sciences of physics by rapid prototyping using extrusion-based 3D-printing. Electrochemistry will surely benefit from the development of such novel devices *via* rapid prototyping with enhanced performance and at reduced cost. Because of the simplicity of testing new ideas and prototypes fabrication, a new era in sensing, energy-storage, and energy-related applications, as well as electrochemistry-assisted syntheses are now being progressively studied *via* extrusion-based 3D printing.

In the longer term, this amalgam of technologies, and materials functionality will lead to the production of flexible, high-level integrated and miniaturised functional 2D material-based printable electronics, sensing and interactive devices.

## Nanoscale

This will need accurately controlled, additive patterning of multiple 2D materials and other functional materials over large areas and for thousands of devices with tight manufacturing tolerance, and could potentially lead to the improvement of all printed, complex device structures for novel applications in light detection and imaging, energy storage, interactive touch surfaces, wearable sensors, RFID tags and even artificial skins. It is thus concluded that there are still enormous opportunities in 2D materials-based functional inks formulation for extrusion-based 3D printing methods and more efforts are required to achieve their real-world applications.

## Abbreviations

BMP	1-Butyl-1-methyl-pyrrolidinium	HF	Hydrofluoric acid
[HOEMIM][TfO]	1-Hydroxyethyl-3-methylimidazolium trifluoromethanesulfonate	HSP	Hansen solubility parameters
[Emim][Tf2N]	1-Ethyl-3-methylimidazolium bis(trifluoromethylsulfonyl)imide	HCA	Hierarchical cluster analysis
[Bmim][Tf2N]	1-Butyl-3-methylimidazolium bis(trifluoromethylsulfonyl)imide	HCl	Hydrochloric acid
[Emim][BF4]	1-Ethyl-3-methylimidazolium tetrafluoroborate	HPMC	Hydroxypropylmethyl cellulose
[Bmim][BF4]	1-Butyl-3-methylimidazolium tetrafluoroborate	ILs	Ionic liquids
[C4mim][Tf2N]	1-Butyl-3-methylimidazolium bis(trifluoromethylsulfonyl)imide	IPA	Isopropanol
AM	Additive manufacturing	IDEs	Interdigitated electrodes
AFM	Atomic force microscopy	LiF	Lithium fluoride
BP	Black phosphorus	LTO	Lithium-titanate
Co(OH) <sub>2</sub>	Cobalt(II) hydroxide	LPE	Liquid phase exfoliation
CE	Counter electrode	LFP	Lithium iron phosphate
CO	Carbon dioxide	MnO <sub>2</sub>	Manganese dioxide
CAB	Cellulose acetate butyrate	MoS <sub>2</sub>	Molybdenum disulfide
CMC	Carboxymethylcellulose	MoSe <sub>2</sub>	Molybdenum diselenide
CAD	Computer-aided design	MSC	Micro-supercapacitors
CIJ	Continuous inkjet	Ni(OH) <sub>2</sub>	Nickel(II) hydroxide
CNT	Carbon nanotube	NMP	N-Methyl-2-pyrrolidone
CC-Free	Current-collector-free	HNO <sub>3</sub>	Nitric acid
CV	Cyclic voltammetry	NC	Nitrocellulose
CE	Counter electrode	NMP	N-Methylpyrrolidinone
DIW	Direct ink writing	1-Butanol	<i>n</i> -BuOH –
DMF	Dimethylformamide	Pt	Platinum
DMSO	Dimethylsulfoxide	PG	Pristine graphene
DOD	Drop-on-demand inkjet	KMnO <sub>2</sub>	Potassium; oxido(oxo)manganese
EMI	Electromagnetic	K <sub>2</sub> FeO <sub>4</sub>	Potassium ferrate
[EMIm]Cl	Ethyl-3-methylimidazolium chloride-aluminum chloride	PANI	Polyaniline
EC	Ethyl cellulose	PVP-PVAc	Polyvinylpyrrolidone-polyvinylacetate copolymer
EESDs	Electrochemical energy storage devices	PVP	Polyvinylpyrrolidinone
FETs	Field-effect transistors	PDMS	Polydimethylsiloxane
FDM	Fused deposition modelling	PSS	Polystyrene sulfonate
FDM	Fused-deposition-modelling	PET	Polyethylene terephthalate
Au	Gold	PVDF-co-HFP	Poly(vinylidene fluoride) cohexafluoropropylene
hBN	Hexagonal boron nitride	PCA	Principal component analysis
		RE	Reference electrode
		Ag	Silver
		SiO <sub>2</sub>	Silicon dioxide
		H <sub>2</sub> SO <sub>4</sub>	Sulfuric acid
		NaNO <sub>3</sub>	Sodium nitrate
		NaF	Sodium fluoride
		SO <sub>2</sub>	Sulfur dioxide
		SCFs	Supercritical fluids
		Na-1-PSA	Sodium 1-pyrenesulfonate
		SPE	Screen-printed electrodes
		SDS	Sodium dodecyl sulfate
		TMDs	Transition metal dichalcogenides
		WS <sub>2</sub>	Tungsten disulfide
		TMA	Tetra-methyl-ammonium
		TPA	Tetra-propyl-ammonium
		TBA	Tetra- <i>n</i> -butylammonium
		THA	Tetra- <i>n</i> -heptylammonium
		□	Thermoresponsive polyionic liquid
		vdW	van der Waals
		WE	Working electrode

## Conflicts of interest

There are no conflicts to declare.

## Acknowledgements

The authors acknowledge financial support from the Australian Research Council (ARC, IH150100003).

## References

- 1 A. C. Ferrari, F. Bonaccorso, V. Fal'Ko, K. S. Novoselov, S. Roche, P. Boggild, S. Borini, F. H. Koppens, V. Palermo and N. Pugno, *Nanoscale*, 2015, 7, 4598–4810.
- 2 G. Hu, J. Kang, L. W. Ng, X. Zhu, R. C. Howe, C. G. Jones, M. C. Hersam and T. Hasan, *Chem. Soc. Rev.*, 2018, 47, 3265–3300.
- 3 K. S. Novoselov, A. K. Geim, S. V. Morozov, D. Jiang, Y. Zhang, S. V. Dubonos, I. V. Grigorieva and A. A. Firsov, *science*, 2004, 306, 666–669.
- 4 S. Z. Butler, S. M. Hollen, L. Cao, Y. Cui, J. A. Gupta, H. R. Gutierrez, T. F. Heinz, S. S. Hong, J. Huang, A. F. Ismach Ruoff, S. Salahuddin, J. Shan, L. Shi, M. G. Spencer, M. Ter renes, W. Windl and J. E. Goldberger, Progress, challenges, and opportunities in two-dimensional materials beyond graphene, *ACS Nano*, 2013, 7, 2898–2926.
- 5 X. Chen, J. F. Dobson and C. L. Raston, *Chem. Commun.*, 2012, 48, 3703–3705.
- 6 M. Yi and Z. Shen, *J. Mater. Chem. A*, 2015, 3, 11700–11715.
- 7 D. C. Marcano, D. V. Kosynkin, J. M. Berlin, A. Sinitskii, Z. Sun, A. Slesarev, L. B. Alemany, W. Lu and J. M. Tour, *ACS Nano*, 2010, 4, 4806–4814.
- 8 T. Habib, X. Zhao, S. A. Shah, Y. Chen, W. Sun, H. An, J. L. Lutkenhaus, M. Radovic and M. J. Green, *npj 2D Mater. Appl.*, 2019, 3, 1–6.
- 9 S. Yang, P. Zhang, A. S. Nia and X. Feng, *Adv. Mater.*, 2020, 32, 1907857.
- 10 C. Low, F. Walsh, M. Chakrabarti, M. Hashim and M. Hussain, *Carbon*, 2013, 54, 1–21.
- 11 M. Matsumoto, Y. Saito, C. Park, T. Fukushima and T. Aida, *Nat. Chem.*, 2015, 7, 730.
- 12 Y. Hernandez, M. Lotya, D. Rickard, S. D. Bergin and J. N. Coleman, *Langmuir*, 2010, 26, 3208–3213.
- 13 J. Kang, V. K. Sangwan, J. D. Wood and M. C. Hersam, *Acc. Chem. Res.*, 2017, 50, 943–951.
- 14 F. Bonaccorso, A. Bartolotta, J. N. Coleman and C. Backes, *Adv. Mater.*, 2016, 28, 6136–6166.
- 15 A. Kamysny and S. Magdassi, *Chem. Soc. Rev.*, 2019, 48, 1712–1740.
- 16 W. Wu, *Nanoscale*, 2017, 9, 7342–7372.
- 17 Technavio, *Ind. Biotechnol.*, 2016, 12, 216–218.
- 18 S. Khan, L. Lorenzelli and R. S. Dahiya, *IEEE Sens. J.*, 2014, 15, 3164–3185.
- 19 A. Moridi, S. M. Hassani-Gangaraj, M. Guagliano and M. Dao, *Surf. Eng.*, 2014, 30, 369–395.
- 20 G. Cummins and M. P. Desmulliez, *Circuit World*, 2012, 38(4), 193–213.
- 21 X. Tian, J. Jin, S. Yuan, C. K. Chua, S. B. Tor and K. Zhou, *Adv. Energy Mater.*, 2017, 7, 1700127.
- 22 L. Ng, G. Hu, R. Howe, X. Zhu, Z. Yang, C. G. Jones and T. Hasan, *Printing of Graphene and Related 2D Materials*, Springer, 2018.
- 23 L. Huang, Y. Huang, J. Liang, X. Wan and Y. Chen, *Nano Res.*, 2011, 4, 675–684.
- 24 F. Torrisi, T. Hasan, W. Wu, Z. Sun, A. Lombardo, T. S. Kulmala, G.-W. Hsieh, S. Jung, F. Bonaccorso and P. J. Paul, *ACS Nano*, 2012, 6, 2992–3006.
- 25 D. J. Finn, M. Lotya, G. Cunningham, R. J. Smith, D. McCloskey, J. F. Donegan and J. N. Coleman, *J. Mater. Chem. C*, 2014, 2, 925–932.
- 26 A. G. Kelly, T. Hallam, C. Backes, A. Harvey, A. S. Esmaily, I. Godwin, J. Coelho, V. Nicolosi, J. Lauth and A. Kulkarni, *Science*, 2017, 356, 69–73.
- 27 D. McManus, S. Vranic, F. Withers, V. Sanchez-Romaguera, M. Macucci, H. Yang, R. Sorrentino, K. Parvez, S.-K. Son and G. Iannaccone, *Nat. Nanotechnol.*, 2017, 12, 343.
- 28 G. Hu, T. Albrow-Owen, X. Jin, A. Ali, Y. Hu, R. C. Howe, K. Shehzad, Z. Yang, X. Zhu and R. I. Woodward, *Nat. Commun.*, 2017, 8, 1–10.
- 29 V. Bianchi, T. Carey, L. Viti, L. Li, E. H. Linfield, A. G. Davies, A. Tredicucci, D. Yoon, P. G. Karagiannidis and L. Lombardi, *Nat. Commun.*, 2017, 8, 1–9.
- 30 E. B. Secor, P. L. Prabhurashi, K. Puntambekar, M. L. Geier and M. C. Hersam, *J. Phys. Chem. Lett.*, 2013, 4, 1347–1351.
- 31 Y. Xu, M. G. Schwab, A. J. Strudwick, I. Hennig, X. Feng, Z. Wu and K. Müllen, *Adv. Energy Mater.*, 2013, 3, 1035–1040.
- 32 P. G. Karagiannidis, S. A. Hodge, L. Lombardi, F. Tomarchio, N. Decorde, S. Milana, I. Goykhman, Y. Su, S. V. Mesite and D. N. Johnstone, *ACS Nano*, 2017, 11, 2742–2755.
- 33 J. Baker, D. Deganello, D. Gethin and T. Watson, *Mater. Res. Innovations*, 2014, 18, 86–90.
- 34 E. B. Secor, S. Lim, H. Zhang, C. D. Frisbie, L. F. Francis and M. C. Hersam, *Adv. Mater.*, 2014, 26, 4533–4538.
- 35 T. Carey, S. Cacovich, G. Divitini, J. Ren, A. Mansouri, J. M. Kim, C. Wang, C. Ducati, R. Sordan and F. Torrisi, *Nat. Commun.*, 2017, 8, 1–11.
- 36 S. Crump, *Apparatus and Method for Creating Three-Dimensional Objects Patent US*, 1992, p. 5121329.
- 37 U. G. Wegst, H. Bai, E. Saiz, A. P. Tomsia and R. O. Ritchie, *Nat. Mater.*, 2015, 14, 23–36.
- 38 C. Zhu, T. Y.-J. Han, E. B. Duoss, A. M. Golobic, J. D. Kuntz, C. M. Spadaccini and M. A. Worsley, *Nat. Commun.*, 2015, 6, 1–8.

- 39 T. S. Tran, N. K. Dutta and N. R. Choudhury, *Adv. Colloid Interface Sci.*, 2018, **261**, 41–61.
- 40 L. Wang, S. Chen, T. Shu and X. Hu, *ChemSusChem*, 2019, **13**, 1330–1353.
- 41 S. Park and R. S. Ruoff, *Nat. Nanotechnol.*, 2009, **4**, 217.
- 42 Y. Hernandez, V. Nicolosi, M. Lotya, F. M. Blighe, Z. Sun, S. De, I. McGovern, B. Holland, M. Byrne and Y. K. Gun'ko, *Nat. Nanotechnol.*, 2008, **3**, 563.
- 43 M. Naguib, O. Mashtalir, J. Carle, V. Presser, J. Lu, L. Hultman, Y. Gogotsi and M. W. Barsoum, *ACS Nano*, 2012, **6**, 1322–1331.
- 44 C. Lee, X. Wei, J. W. Kysar and J. Hone, *Science*, 2008, **321**, 385–388.
- 45 A. A. Balandin, S. Ghosh, W. Bao, I. Calizo, D. Teweldebrhan, F. Miao and C. N. Lau, *Nano Lett.*, 2008, **8**, 902–907.
- 46 K. I. Bolotin, K. Sikes, Z. Jiang, M. Klima, G. Fudenberg, J. Hone, P. Kim and H. Stormer, *Solid State Commun.*, 2008, **146**, 351–355.
- 47 M. J. Nine, M. A. Cole, D. N. H. Tran and D. Losic, *J. Mater. Chem. A*, 2015, **3**, 12580–12602.
- 48 K. S. Novoselov, V. Fal, L. Colombo, P. Gellert, M. Schwab and K. Kim, *Nature*, 2012, **490**, 192–200.
- 49 A. Ciesielski and P. Samori, *Chem. Soc. Rev.*, 2014, **43**, 381–398.
- 50 T. T. Tung, M. J. Nine, M. Krebsz, T. Pasinszki, C. J. Coghlan, D. N. Tran and D. Losic, *Adv. Funct. Mater.*, 2017, **27**, 1702891.
- 51 T. T. Tung, M. T. Tran, J.-F. Feller, M. Castro, T. Van Ngo, K. Hassan, M. J. Nine and D. Losic, *Carbon*, 2020, **159**, 333–344.
- 52 M. Alhabeb, K. Maleski, B. Anasori, P. Lelyukh, L. Clark, S. Sin and Y. Gogotsi, *Chem. Mater.*, 2017, **29**, 7633–7644.
- 53 X. Xiao, H. Wang, P. Urbankowski and Y. Gogotsi, *Chem. Soc. Rev.*, 2018, **47**, 8744–8765.
- 54 M. Chhowalla, H. S. Shin, G. Eda, L.-J. Li, K. P. Loh and H. Zhang, *Nat. Chem.*, 2013, **5**, 263.
- 55 X. Tong, E. Ashalley, F. Lin, H. Li and Z. M. Wang, *Nano-Micro Lett.*, 2015, **7**, 203–218.
- 56 P. Chen, N. Li, X. Chen, W.-J. Ong and X. Zhao, *2D Mater.*, 2017, **5**, 014002.
- 57 F. Xia, H. Wang, J. C. Hwang, A. C. Neto and L. Yang, *Nat. Rev. Phys.*, 2019, **1**, 306–317.
- 58 W. Auwärter, *Surf. Sci. Rep.*, 2019, **74**, 1–95.
- 59 K. Zhang, Y. Feng, F. Wang, Z. Yang and J. Wang, *J. Mater. Chem. C*, 2017, **5**, 11992–12022.
- 60 J. N. Coleman, M. Lotya, A. O'Neill, S. D. Bergin, P. J. King, U. Khan, K. Young, A. Gaucher, S. De and R. J. Smith, *Science*, 2011, **331**, 568–571.
- 61 D. Jariwala, S. L. Howell, K.-S. Chen, J. Kang, V. K. Sangwan, S. A. Filippone, R. Turrissi, T. J. Marks, L. J. Lauhon and M. C. Hersam, *Nano Lett.*, 2016, **16**, 497–503.
- 62 X. Zong, H. Yan, G. Wu, G. Ma, F. Wen, L. Wang and C. Li, *J. Am. Chem. Soc.*, 2008, **130**, 7176–7177.
- 63 J. Wong, D. Jariwala, G. Tagliabue, K. Tat, A. R. Davoyan, M. C. Sherrott and H. A. Atwater, *ACS Nano*, 2017, **11**, 7230–7240.
- 64 T. Wang, C. Liu, F. Jiang, Z. Xu, X. Wang, X. Li, C. Li, J. Xu and X. Yang, *Phys. Chem. Chem. Phys.*, 2017, **19**, 17560–17567.
- 65 Y. Yang, H. Hou, G. Zou, W. Shi, H. Shuai, J. Li and X. Ji, *Nanoscale*, 2019, **11**, 16–33.
- 66 J. Shen, Y. He, J. Wu, C. Gao, K. Keyshar, X. Zhang, Y. Yang, M. Ye, R. Vajtai, J. Lou and P. M. Ajayan, *Nano Lett.*, 2015, **15**, 5449–5454.
- 67 S. Ravula, S. N. Baker, G. Kamath and G. A. Baker, *Nanoscale*, 2015, **7**, 4338–4353.
- 68 Z. Lin, P. S. Karthik, M. Hada, T. Nishikawa and Y. Hayashi, *Nanomaterials*, 2017, **7**, 125.
- 69 C. Zhang, J. Tan, Y. Pan, X. Cai, X. Zou, H.-M. Cheng and B. Liu, *Natl. Sci. Rev.*, 2019, **7**, 324–332.
- 70 Y. Yao, Z. Lin, Z. Li, X. Song, K.-S. Moon and C.-P. Wong, *J. Mater. Chem.*, 2012, **22**, 13494–13499.
- 71 J. Chen, M. Duan and G. Chen, *J. Mater. Chem.*, 2012, **22**, 19625–19628.
- 72 T. T. Tung, J. Yoo, F. K. Alotaibi, M. J. Nine, R. Karunakaran, M. Krebsz, G. T. Nguyen, D. N. H. Tran, J.-F. Feller and D. Losic, *ACS Appl. Mater. Interfaces*, 2016, **8**, 16521–16532.
- 73 L. Liu, Z. Shen, M. Yi, X. Zhang and S. Ma, *RSC Adv.*, 2014, **4**, 36464–36470.
- 74 M. V. Bracamonte, G. I. Lacconi, S. E. Urreta and L. E. F. Foa Torres, *J. Phys. Chem. C*, 2014, **118**, 15455–15459.
- 75 J. D. Caldwell, I. Aharonovich, G. Cassabois, J. H. Edgar, B. Gil and D. Basov, *Nat. Rev. Mater.*, 2019, **4**, 552–567.
- 76 M. J. Nine, A. C. Hee, T. T. Tung, K. Hassan and D. Losic, *Appl. Mater. Today*, 2020, **20**, 100764.
- 77 M. Yi, Z. Shen and J. Zhu, *Chin. Sci. Bull.*, 2014, **59**, 1794–1799.
- 78 A. T. Utomo, M. Baker and A. W. Pacey, *Chem. Eng. Res. Des.*, 2008, **86**, 1397–1409.
- 79 M. Batmunkh, A. Shrestha, M. Bat-Erdene, M. J. Nine, C. J. Shearer, C. T. Gibson, A. D. Slattery, S. A. Tawfik, M. J. Ford, S. Dai, S. Qiao and J. G. Shapter, *Angew. Chem., Int. Ed.*, 2018, **57**, 2644–2647.
- 80 M. Bat-Erdene, G. Xu, M. Batmunkh, A. S. R. Bati, J. J. White, M. J. Nine, D. Losic, Y. Chen, Y. Wang, T. Ma and J. G. Shapter, *J. Mater. Chem. A*, 2020, **8**, 4735–4739.
- 81 G. Shao, Y. Lu, F. Wu, C. Yang, F. Zeng and Q. Wu, *J. Mater. Sci.*, 2012, **47**, 4400–4409.
- 82 S. Stankovich, D. A. Dikin, G. H. Dommett, K. M. Kohlhaas, E. J. Zimney, E. A. Stach, R. D. Piner, S. T. Nguyen and R. S. Ruoff, *Nature*, 2006, **442**, 282–286.
- 83 S. Stankovich, D. A. Dikin, R. D. Piner, K. A. Kohlhaas, A. Kleinhammes, Y. Jia, Y. Wu, S. T. Nguyen and R. S. Ruoff, *Carbon*, 2007, **45**, 1558–1565.
- 84 A. Feng, Y. Yu, Y. Wang, F. Jiang, Y. Yu, L. Mi and L. Song, *Mater. Des.*, 2017, **114**, 161–166.



- 85 H. S. S. Ramakrishna Matte, A. Gomathi, A. K. Manna, D. J. Late, R. Datta, S. K. Pati and C. N. R. Rao, *Angew. Chem., Int. Ed.*, 2010, **49**, 4059–4062.
- 86 W. Sun, S. A. Shah, Y. Chen, Z. Tan, H. Gao, T. Habib, M. Radovic and M. J. Green, *J. Mater. Chem. A*, 2017, **5**, 21663–21668.
- 87 Y. Gogotsi and B. Anasori, *ACS Nano*, 2019, **13**, 8491–8494.
- 88 B. C. Brodie, *Philos. Trans. R. Soc. London*, 1859, **149**, 249–259.
- 89 W. S. Hummers and R. E. Offeman, *J. Am. Chem. Soc.*, 1958, **80**, 1339–1339.
- 90 H. Yu, B. Zhang, C. Bulin, R. Li and R. Xing, *Sci. Rep.*, 2016, **6**, 36143.
- 91 M. Liu, X. Zhang, W. Wu, T. Liu, Y. Liu, B. Guo and R. Zhang, *Chem. Eng. J.*, 2019, **355**, 181–185.
- 92 M. Naguib, M. Kurtoglu, V. Presser, J. Lu, J. Niu, M. Heon, L. Hultman, Y. Gogotsi and M. W. Barsoum, *Adv. Mater.*, 2011, **23**, 4248–4253.
- 93 A. M. Abdelkader, A. J. Cooper, R. A. W. Dryfe and I. A. Kinloch, *Nanoscale*, 2015, **7**, 6944–6956.
- 94 T. Habib, X. Zhao, S. A. Shah, Y. Chen, W. Sun, H. An, J. L. Lutkenhaus, M. Radovic and M. J. Green, *npj 2D Mater. Appl.*, 2019, **3**, 8.
- 95 C. T. J. Low, F. C. Walsh, M. H. Chakrabarti, M. A. Hashim and M. A. Hussain, *Carbon*, 2013, **54**, 1–21.
- 96 Y. L. Zhong, Z. Tian, G. P. Simon and D. Li, *Mater. Today*, 2015, **18**, 73–78.
- 97 W. Lv, D.-M. Tang, Y.-B. He, C.-H. You, Z.-Q. Shi, X.-C. Chen, C.-M. Chen, P.-X. Hou, C. Liu and Q.-H. Yang, *ACS Nano*, 2009, **3**, 3730–3736.
- 98 Z. Cui, A. J. Oyer, A. J. Glover, H. C. Schniepp and D. H. Adamson, *Small*, 2014, **10**, 2352–2355.
- 99 C. Zhang, W. Lv, X. Xie, D. Tang, C. Liu and Q.-H. Yang, *Carbon*, 2013, **62**, 11–24.
- 100 M. J. McAllister, J.-L. Li, D. H. Adamson, H. C. Schniepp, A. A. Abdala, J. Liu, M. Herrera-Alonso, D. L. Milius, R. Car and R. K. Prud'homme, *Chem. Mater.*, 2007, **19**, 4396–4404.
- 101 Y. Zhu, S. Murali, M. D. Stoller, K. Ganesh, W. Cai, P. J. Ferreira, A. Pirkle, R. M. Wallace, K. A. Cychoz and M. Thommes, *Science*, 2011, **332**, 1537–1541.
- 102 X. Li, X. Hao, M. Zhao, Y. Wu, J. Yang, Y. Tian and G. Qian, *Adv. Mater.*, 2013, **25**, 2200–2204.
- 103 M. J. McAllister, J.-L. Li, D. H. Adamson, H. C. Schniepp, A. A. Abdala, J. Liu, M. Herrera-Alonso, D. L. Milius, R. Car, R. K. Prud'homme and I. A. Aksay, *Chem. Mater.*, 2007, **19**, 4396–4404.
- 104 Y. Zhu, S. Murali, M. D. Stoller, A. Velamakanni, R. D. Piner and R. S. Ruoff, *Carbon*, 2010, **48**, 2118–2122.
- 105 M. Matsumoto, Y. Saito, C. Park, T. Fukushima and T. Aida, *Nat. Chem.*, 2015, **7**, 730–736.
- 106 A. V. Talyzin, T. Szabó, I. Dékány, F. Langenhorst, P. S. Sokolov and V. L. Solozhenko, *J. Phys. Chem. C*, 2009, **113**, 11279–11284.
- 107 P. L. Cullen, K. M. Cox, M. K. Bin Subhan, L. Picco, O. D. Payton, D. J. Buckley, T. S. Miller, S. A. Hodge, N. T. Skipper, V. Tileli and C. A. Howard, *Nat. Chem.*, 2017, **9**, 244–249.
- 108 C. M. Hansen, *Hansen solubility parameters: a user's handbook*, CRC press, 2007.
- 109 S. D. Bergin, Z. Sun, D. Rickard, P. V. Streich, J. P. Hamilton and J. N. Coleman, *ACS Nano*, 2009, **3**, 2340–2350.
- 110 K.-G. Zhou, N.-N. Mao, H.-X. Wang, Y. Peng and H.-L. Zhang, *Angew. Chem., Int. Ed.*, 2011, **50**, 10839–10842.
- 111 Z. Sun, Q. Fan, M. Zhang, S. Liu, H. Tao and J. Texter, *Adv. Sci.*, 2019, **6**, 1901084.
- 112 V. Nicolosi, M. Chhowalla, M. G. Kanatzidis, M. S. Strano and J. N. Coleman, *Science*, 2013, **340**, 1226419.
- 113 Y. Jung, Y. Zhou and J. J. Cha, *Inorg. Chem. Front.*, 2016, **3**, 452–463.
- 114 P. S. Shah, T. Hanrath, K. P. Johnston and B. A. Korgel, *J. Phys. Chem. B*, 2004, **108**, 9574–9587.
- 115 O. Kajimoto, *Chem. Rev.*, 1999, **99**, 355–390.
- 116 J.-H. Jang, D. Rangappa, Y.-U. Kwon and I. Honma, *J. Mater. Chem.*, 2011, **21**, 3462–3466.
- 117 U. Halim, C. R. Zheng, Y. Chen, Z. Lin, S. Jiang, R. Cheng, Y. Huang and X. Duan, *Nat. Commun.*, 2013, **4**, 2213.
- 118 J.-H. Ding, H.-R. Zhao and H.-B. Yu, *Sci. Rep.*, 2018, **8**, 5567.
- 119 M. H. Chakrabarti, N. S. A. Manan, N. P. Brandon, R. C. Maher, F. S. Mjalli, I. M. AlNashef, S. A. Hajimolana, M. A. Hashim, M. A. Hussain and D. Nir, *Chem. Eng. J.*, 2015, **274**, 213–223.
- 120 A. Amiri, M. Shanbedi, G. Ahmadi, H. Eshghi, S. N. Kazi, B. T. Chew, M. Savari and M. N. M. Zubir, *Sci. Rep.*, 2016, **6**, 32686.
- 121 G. P. Keeley, A. O'Neill, N. McEvoy, N. Peltekis, J. N. Coleman and G. S. Duesberg, *J. Mater. Chem.*, 2010, **20**, 7864–7869.
- 122 J. N. Coleman, *Adv. Funct. Mater.*, 2009, **19**, 3680–3695.
- 123 X. Wang, P. F. Fulvio, G. A. Baker, G. M. Veith, R. R. Unocic, S. M. Mahurin, M. Chi and S. Dai, *Chem. Commun.*, 2010, **46**, 4487–4489.
- 124 H. Lei, J. Tu, Z. Yu and S. Jiao, *ACS Appl. Mater. Interfaces*, 2017, **9**, 36702–36707.
- 125 X. Wang and P. Wu, *ACS Appl. Mater. Interfaces*, 2018, **10**, 2504–2514.
- 126 Y. Gao, W. Shi, W. Wang, Y. Wang, Y. Zhao, Z. Lei and R. Miao, *Ind. Eng. Chem. Res.*, 2014, **53**, 2839–2845.
- 127 W. Wang, Y. Wang, Y. Gao and Y. Zhao, *J. Supercrit. Fluids*, 2014, **85**, 95–101.
- 128 S. P. Sasikala, K. Huang, B. Giroire, P. Prabhakaran, L. Henry, A. Penicaud, P. Poulin and C. Aymonier, *ACS Appl. Mater. Interfaces*, 2016, **8**, 30964–30971.
- 129 W. Qian, X. Cui, R. Hao, Y. Hou and Z. Zhang, *ACS Appl. Mater. Interfaces*, 2011, **3**, 2259–2264.
- 130 D. Rangappa, K. Sone, M. Wang, U. K. Gautam, D. Golberg, H. Itoh, M. Ichihara and I. Honma, *Chem. – Eur. J.*, 2010, **16**, 6488–6494.

- 131 S. Suresh Balaji, M. Karnan and M. Sathish, *Int. J. Hydrogen Energy*, 2018, **43**, 4044–4057.
- 132 J. Zhang, L. Xu, B. Zhou, Y. Zhu and X. Jiang, *J. Colloid Interface Sci.*, 2018, **513**, 279–286.
- 133 W.-W. Liu, B.-Y. Xia, X.-X. Wang and J.-N. Wang, *Front. Mater. Sci.*, 2012, **6**, 176–182.
- 134 J. S. Y. Chia, M. T. T. Tan, P. S. Khiew, J. K. Chin, H. Lee, D. C. S. Bien and C. W. Siong, *Chem. Eng. J.*, 2014, **249**, 270–278.
- 135 M. Yi, Z. Shen, X. Zhang and S. Ma, *J. Phys. D: Appl. Phys.*, 2012, **46**, 025301.
- 136 H. Ma, Z. Shen, M. Yi, S. Ben, S. Liang, L. Liu, Y. Zhang, X. Zhang and S. Ma, *J. Colloid Interface Sci.*, 2017, **503**, 68–75.
- 137 A. Jawaid, D. Nepal, K. Park, M. Jespersen, A. Qualley, P. Mirau, L. F. Drummy and R. A. Vaia, *Chem. Mater.*, 2016, **28**, 337–348.
- 138 G. Cunningham, M. Lotya, C. S. Cucinotta, S. Sanvito, S. D. Bergin, R. Menzel, M. S. P. Shaffer and J. N. Coleman, *ACS Nano*, 2012, **6**, 3468–3480.
- 139 P. Thangasamy and M. Sathish, *J. Mater. Chem. C*, 2016, **4**, 1165–1169.
- 140 V. Gunasekaran, M. K. Devaraju, S. Yuvaraj, V. J. Y. Surya, V. Singh, K. Karthikeyan and S. J. Kim, *Mater. Sci. Semicond. Process.*, 2017, **66**, 81–86.
- 141 Q. D. Truong, M. Kempaiah Devaraju, Y. Nakayasu, N. Tamura, Y. Sasaki, T. Tomai and I. Honma, *ACS Omega*, 2017, **2**, 2360–2367.
- 142 Y. Qi, Q. Xu, Y. Wang, B. Yan, Y. Ren and Z. Chen, *ACS Nano*, 2016, **10**, 2903–2909.
- 143 Y. Qi, N. Wang, Q. Xu, H. Li, P. Zhou, X. Lu and G. Zhao, *Chem. Commun.*, 2015, **51**, 6726–6729.
- 144 P. Zhou, Q. Xu, H. Li, Y. Wang, B. Yan, Y. Zhou, J. Chen, J. Zhang and K. Wang, *Angew. Chem., Int. Ed.*, 2015, **54**, 15226–15230.
- 145 J. Shang, F. Xue, C. Fan and E. Ding, *Mater. Lett.*, 2016, **181**, 144–147.
- 146 C. Zhi, Y. Bando, C. Tang, H. Kuwahara and D. Golberg, *Adv. Mater.*, 2009, **21**, 2889–2893.
- 147 T. K. Mukhopadhyay and A. Datta, *J. Phys. Chem. C*, 2017, **121**, 811–822.
- 148 X. Chen, R. A. Boulos, J. F. Dobson and C. L. Raston, *Nanoscale*, 2013, **5**, 498–502.
- 149 T. Morishita, H. Okamoto, Y. Katagiri, M. Matsushita and K. Fukumori, *Chem. Commun.*, 2015, **51**, 12068–12071.
- 150 P. Thangasamy and M. Sathish, *CrystEngComm*, 2015, **17**, 5895–5899.
- 151 Q. An, Q. Wei, L. Mai, J. Fei, X. Xu, Y. Zhao, M. Yan, P. Zhang and S. Huang, *Phys. Chem. Chem. Phys.*, 2013, **15**, 16828–16833.
- 152 L. Cao, S. Emami and K. Lafdi, *Mater. Express*, 2014, **4**, 165–171.
- 153 K. L. Marsh, M. Souliman and R. B. Kaner, *Chem. Commun.*, 2015, **51**, 187–190.
- 154 S. Lin, Y. Li, W. Lu, Y. S. Chui, L. Rogée, Q. Bao and S. P. Lau, *2D Mater.*, 2017, **4**, 025001.
- 155 A. E. Del Rio Castillo, V. Pellegrini, H. Sun, J. Buha, D. A. Dinh, E. Lago, A. Ansaldo, A. Capasso, L. Manna and F. Bonaccorso, *Chem. Mater.*, 2018, **30**, 506–516.
- 156 Z. Yan, X. He, L. She, J. Sun, R. Jiang, H. Xu, F. Shi, Z. Lei and Z.-H. Liu, *J. Materiomics*, 2018, **4**, 129–134.
- 157 H. Mu, S. Lin, Z. Wang, S. Xiao, P. Li, Y. Chen, H. Zhang, H. Bao, S. P. Lau, C. Pan, D. Fan and Q. Bao, *Adv. Opt. Mater.*, 2015, **3**, 1447–1453.
- 158 A. Ambrosi, Z. Sofer and M. Pumera, *Angew. Chem., Int. Ed.*, 2017, **56**, 10443–10445.
- 159 V. Sresht, A. A. H. Pádua and D. Blankschtein, *ACS Nano*, 2015, **9**, 8255–8268.
- 160 D. Hanlon, C. Backes, E. Doherty, C. S. Cucinotta, N. C. Berner, C. Boland, K. Lee, A. Harvey, P. Lynch, Z. Gholamvand, S. Zhang, K. Wang, G. Moynihan, A. Pokle, Q. M. Ramasse, N. McEvoy, W. J. Blau, J. Wang, G. Abellan, F. Hauke, A. Hirsch, S. Sanvito, D. D. O'Regan, G. S. Duesberg, V. Nicolosi and J. N. Coleman, *Nat. Commun.*, 2015, **6**, 8563.
- 161 W. Zhao, Z. Xue, J. Wang, J. Jiang, X. Zhao and T. Mu, *ACS Appl. Mater. Interfaces*, 2015, **7**, 27608–27612.
- 162 M. Lee, A. K. Roy, S. Jo, Y. Choi, A. Chae, B. Kim, S. Y. Park and I. In, *Nanotechnology*, 2017, **28**, 125603.
- 163 S. Yan, B. Wang, Z. Wang, D. Hu, X. Xu, J. Wang and Y. Shi, *Biosens. Bioelectron.*, 2016, **80**, 34–38.
- 164 Z. Guo, H. Zhang, S. Lu, Z. Wang, S. Tang, J. Shao, Z. Sun, H. Xie, H. Wang, X.-F. Yu and P. K. Chu, *Adv. Funct. Mater.*, 2015, **25**, 6996–7002.
- 165 V. Kumar, J. R. Brent, M. Shorie, H. Kaur, G. Chadha, A. G. Thomas, E. A. Lewis, A. P. Rooney, L. Nguyen, X. L. Zhong, M. G. Burke, S. J. Haigh, A. Walton, P. D. McNaughton, A. A. Tedstone, N. Savjani, C. A. Murny, P. O'Brien, A. K. Ganguli, D. J. Lewis and P. Sabherwal, *ACS Appl. Mater. Interfaces*, 2016, **8**, 22860–22868.
- 166 Q. Tang, Z. Zhou and P. Shen, *J. Am. Chem. Soc.*, 2012, **134**, 16909–16916.
- 167 X. Yu, X. Cai, H. Cui, S.-W. Lee, X.-F. Yu and B. Liu, *Nanoscale*, 2017, **9**, 17859–17864.
- 168 M. Naguib, R. R. Unocic, B. L. Armstrong and J. Nanda, *Dalton Trans.*, 2015, **44**, 9353–9358.
- 169 H. Wang, J. Zhang, Y. Wu, H. Huang, G. Li, X. Zhang and Z. Wang, *Appl. Surf. Sci.*, 2016, **384**, 287–293.
- 170 M. Ghidui, M. R. Lukatskaya, M.-Q. Zhao, Y. Gogotsi and M. W. Barsoum, *Nature*, 2014, **516**, 78–81.
- 171 K. Suganuma, *Introduction to printed electronics*, Springer Science & Business Media, 2014.
- 172 K. Parvez, R. Worsley, A. Alieva, A. Felten and C. Casiraghi, *Carbon*, 2019, **149**, 213–221.
- 173 J. Li, F. Ye, S. Vaziri, M. Muhammed, M. C. Lemme and M. Östling, *Adv. Mater.*, 2013, **25**, 3985–3992.
- 174 W. J. Hyun, E. B. Secor, M. C. Hersam, C. D. Frisbie and L. F. Francis, *Adv. Mater.*, 2015, **27**, 109–115.
- 175 K. Pan, Y. Fan, T. Leng, J. Li, Z. Xin, J. Zhang, L. Hao, J. Gallop, K. S. Novoselov and Z. Hu, *Nat. Commun.*, 2018, **9**, 5197.
- 176 E. Jabari and E. Toyserkani, *Mater. Lett.*, 2016, **174**, 40–43.

- 177 K. Parate, S. V. Rangnekar, D. Jing, D. L. Mendivelso-Perez, S. Ding, E. B. Secor, E. A. Smith, J. M. Hostetter, M. C. Hersam and J. C. Claussen, *ACS Appl. Mater. Interfaces*, 2020, **12**, 8592–8603.
- 178 H. A. Loh, A. R. Graves, C. D. Stinespring and K. A. Sierros, *ACS Appl. Nano Mater.*, 2019, **2**, 4104–4112.
- 179 H. Ding, S. Barg and B. Derby, *Nanoscale*, 2020, **12**, 11440–11447.
- 180 C. Zhang, L. McKeon, M. P. Kremer, S.-H. Park, O. Ronan, A. Seral-Ascaso, S. Barwich, C. Ó. Coileáin, N. McEvoy, H. C. Nerl, B. Anasori, J. N. Coleman, Y. Gogotsi and V. Nicolosi, *Nat. Commun.*, 2019, **10**, 1795.
- 181 X. Jiang, W. Li, T. Hai, R. Yue, Z. Chen, C. Lao, Y. Ge, G. Xie, Q. Wen and H. Zhang, *npj 2D Mater. Appl.*, 2019, **3**, 34.
- 182 G. Hu, T. Albrow-Owen, X. Jin, A. Ali, Y. Hu, R. C. T. Howe, K. Shehzad, Z. Yang, X. Zhu, R. I. Woodward, T.-C. Wu, H. Jussila, J.-B. Wu, P. Peng, P.-H. Tan, Z. Sun, E. J. R. Kelleher, M. Zhang, Y. Xu and T. Hasan, *Nat. Commun.*, 2017, **8**, 278.
- 183 J. Li, M. M. Naiini, S. Vaziri, M. C. Lemme and M. Östling, *Adv. Funct. Mater.*, 2014, **24**, 6524–6531.
- 184 D. J. Finn, M. Lotya, G. Cunningham, R. J. Smith, D. McCloskey, J. F. Donegan and J. N. Coleman, *J. Mater. Chem. C*, 2014, **2**, 925–932.
- 185 L. Cao, S. Yang, W. Gao, Z. Liu, Y. Gong, L. Ma, G. Shi, S. Lei, Y. Zhang, S. Zhang, R. Vajtai and P. M. Ajayan, *Small*, 2013, **9**, 2905–2910.
- 186 S. J. Rowley-Neale, G. C. Smith and C. E. Banks, *ACS Appl. Mater. Interfaces*, 2017, **9**, 22539–22548.
- 187 S. Lu, J. A. Cardenas, R. Worsley, N. X. Williams, J. B. Andrews, C. Casiraghi and A. D. Franklin, *ACS Nano*, 2019, **13**, 11263–11272.
- 188 F. Withers, H. Yang, L. Britnell, A. P. Rooney, E. Lewis, A. Felten, C. R. Woods, V. Sanchez Romaguera, T. Georgiou, A. Eckmann, Y. J. Kim, S. G. Yeates, S. J. Haigh, A. K. Geim, K. S. Novoselov and C. Casiraghi, *Nano Lett.*, 2014, **14**, 3987–3992.
- 189 A. M. Joseph, B. Nagendra, E. Bhoje Gowd and K. P. Surendran, *ACS Omega*, 2016, **1**, 1220–1228.
- 190 Y. Xu, I. Hennig, D. Freyberg, A. James Strudwick, M. Georg Schwab, T. Weitz and K. Chih-Pei Cha, *J. Power Sources*, 2014, **248**, 483–488.
- 191 K. Arapov, E. Rubingh, R. Abbel, J. Laven, G. de With and H. Friedrich, *Adv. Funct. Mater.*, 2016, **26**, 586–593.
- 192 T. Juntunen, H. Jussila, M. Ruoho, S. Liu, G. Hu, T. Albrow-Owen, L. W. T. Ng, R. C. T. Howe, T. Hasan, Z. Sun and I. Tittonen, *Adv. Funct. Mater.*, 2018, **28**, 1800480.
- 193 S. Santra, G. Hu, R. C. T. Howe, A. De Luca, S. Z. Ali, F. Udrea, J. W. Gardner, S. K. Ray, P. K. Guha and T. Hasan, *Sci. Rep.*, 2015, **5**, 17374.
- 194 Z. Wang, Q. Zhang, Y. Yue, J. Xu, W. Xu, X. Sun, Y. Chen, J. Jiang and Y. Liu, *Nanotechnology*, 2019, **30**, 345501.
- 195 S. Stankovich, R. D. Piner, X. Chen, N. Wu, S. T. Nguyen and R. S. Ruoff, *J. Mater. Chem.*, 2006, **16**, 155–158.
- 196 D. Sinar and G. K. Knopf, *Nanomaterials*, 2018, **8**, 123.
- 197 H. Yang, Y. Hernandez, A. Schlierf, A. Felten, A. Eckmann, S. Johal, P. Louette, J. J. Pireaux, X. Feng, K. Mullen, V. Palermo and C. Casiraghi, *Carbon*, 2013, **53**, 357–365.
- 198 L. Bergkamp and N. Herbatschek, *Review of European, Comparative & International Environmental Law*, 2014, vol. 23, pp. 221–245.
- 199 H. J. Salavagione, J. Sherwood, M. De Bruyn, V. L. Budarin, G. J. Ellis, J. H. Clark and P. S. Shuttleworth, *Green Chem.*, 2017, **19**, 2550–2560.
- 200 D. Enterprises, Viscosity, Surface Tension, Specific Density and Molecular Weight of Selected Liquids, [https://www.accudynetest.com/visc\\_table.html?rd=self&](https://www.accudynetest.com/visc_table.html?rd=self&), Accessed 5 May, 2020.
- 201 R. H. Leach, R. J. Pierce, E. P. Hickman, M. J. Mackenzie and H. G. Smith, *The Printing Ink Manual*, 1993, DOI: 10.1007/978-1-4020-6187-5.
- 202 E. W. Flick, *Printing ink and overprint varnish formulations*, William Andrew, 1999.
- 203 A. A. Tracton, *Coatings technology handbook*, CRC press, 2005.
- 204 T. Smith, *Pigm. Resin Technol.*, 1986, **15**(3), 11–12.
- 205 H. Kipphan, *Handbook of print media: technologies and production methods*, Springer Science & Business Media, 2001.
- 206 G. Pangalos, J. Dealy and M. Lyne, *J. Rheol.*, 1985, **29**, 471–491.
- 207 D. Doraiswamy, *Rheol. Bull.*, 2002, **71**, 1–9.
- 208 H. A. Barnes, J. F. Hutton and K. Walters, *An introduction to rheology*, Elsevier, 1989.
- 209 R. J. Good, *J. Am. Chem. Soc.*, 1952, **74**, 5041–5042.
- 210 H. Hu and R. G. Larson, *J. Phys. Chem. B*, 2006, **110**, 7090–7094.
- 211 J. Baker, D. Deganello, D. T. Gethin and T. M. Watson, *Mater. Res. Innovations*, 2014, **18**, 86–90.
- 212 K. Arapov, G. Bex, R. Hendriks, E. Rubingh, R. Abbel, G. de With and H. Friedrich, *Adv. Eng. Mater.*, 2016, **18**, 1234–1239.
- 213 E. B. Secor, B. Y. Ahn, T. Z. Gao, J. A. Lewis and M. C. Hersam, *Adv. Mater.*, 2015, **27**, 6683–6688.
- 214 E. B. Secor, T. Z. Gao, M. H. Dos Santos, S. G. Wallace, K. W. Putz and M. C. Hersam, *ACS Appl. Mater. Interfaces*, 2017, **9**, 29418–29423.
- 215 H. Rastin, B. Zhang, A. Mazinani, K. Hassan, J. Bi, T. T. Tung and D. Losic, *Nanoscale*, 2020, **12**, 16069–16080.
- 216 H. Rastin, B. Zhang, J. Bi, K. Hassan, T. T. Tung and D. Losic, *J. Mater. Chem. B*, 2020, **8**, 5862–5876.
- 217 Y. Aleeva and B. Pignataro, *J. Mater. Chem. C*, 2014, **2**, 6436–6453.
- 218 F. C. Krebs, *Sol. Energy Mater. Sol. Cells*, 2009, **93**, 394–412.
- 219 L. J. Deiner and T. L. Reitz, *Adv. Eng. Mater.*, 2017, **19**, 1600878.
- 220 T. Smith, *Pigm. Resin Technol.*, 1986, **15**, 11–12.
- 221 H. A. D. Nguyen, C. Lee, K. Shin and D. Lee, *IEEE Trans. Compon., Packag., Manuf. Technol.*, 2015, **5**, 1516–1524.

- 222 M. Lahti, S. Leppävuori and V. Lantto, *Appl. Surf. Sci.*, 1999, **142**, 367–370.
- 223 H. Lievens, *Surf. Coat. Technol.*, 1995, **76–77**, 744–753.
- 224 F. Bonaccorso, A. Lombardo, T. Hasan, Z. Sun, L. Colombo and A. C. Ferrari, *Mater. Today*, 2012, **15**, 564–589.
- 225 K. K. B. Hon, L. Li and I. M. Hutchings, *CIRP Ann.*, 2008, **57**, 601–620.
- 226 E. B. Secor, *Flexible Printed Electron.*, 2018, **3**, 035002.
- 227 P. Calvert, T. L. Lin and H. Martin, *High Perform. Polym.*, 2016, **9**, 449–456.
- 228 C. A. Mire, A. Agrawal, G. G. Wallace, P. Calvert and M. In Het Panhuis, *J. Mater. Chem.*, 2011, **21**, 2671–2678.
- 229 J. K. Placone and A. J. Engler, *Adv. Healthcare Mater.*, 2018, **7**, e1701161.
- 230 H. Yoo and C. Kim, *Colloids Surf., A*, 2015, **468**, 234–245.
- 231 J. Boetker, J. J. Water, J. Aho, L. Arnfast, A. Bohr and J. Rantanen, *Eur. J. Pharm. Sci.*, 2016, **90**, 47–52.
- 232 Q. Gu, E. Tomaskovic-Crook, R. Lozano, Y. Chen, R. M. Kapsa, Q. Zhou, G. G. Wallace and J. M. Crook, *Adv. Healthcare Mater.*, 2016, **5**, 1429–1438.
- 233 J. S. Miller, K. R. Stevens, M. T. Yang, B. M. Baker, D. H. Nguyen, D. M. Cohen, E. Toro, A. A. Chen, P. A. Galie, X. Yu, R. Chaturvedi, S. N. Bhatia and C. S. Chen, *Nat. Mater.*, 2012, **11**, 768–774.
- 234 D. B. Kolesky, R. L. Truby, A. S. Gladman, T. A. Busbee, K. A. Homan and J. A. Lewis, *Adv. Mater.*, 2014, **26**, 3124–3130.
- 235 J. U. Surjadi, L. Gao, H. Du, X. Li, X. Xiong, N. X. Fang and Y. Lu, *Adv. Eng. Mater.*, 2019, **21**, 1800864.
- 236 J. Xue, L. Gao, X. Hu, K. Cao, W. Zhou, W. Wang and Y. Lu, *Nano-Micro Lett.*, 2019, **11**(46), 1–13.
- 237 M. Kaur, T. G. Yun, S. M. Han, E. L. Thomas and W. S. Kim, *Mater. Des.*, 2017, **134**, 272–280.
- 238 J. A. Lewis, *Adv. Funct. Mater.*, 2006, **16**, 2193–2204.
- 239 J. Song, L. Gao, K. Cao, H. Zhang, S. Xu, C. Jiang, J. U. Surjadi, Y. Xu and Y. Lu, *Compos. Struct.*, 2018, **203**, 750–763.
- 240 J. U. Surjadi, L. Gao, H. Du, X. Li, X. Xiong, N. X. Fang and Y. Lu, *Adv. Eng. Mater.*, 2019, **21**, 1800864.
- 241 Z. Tan, C. Parisi, L. Di Silvio, D. Dini and A. E. Forte, *Sci. Rep.*, 2017, **7**, 16293.
- 242 R. L. Truby and J. A. Lewis, *Nature*, 2016, **540**, 371–378.
- 243 C. C. Ho, J. W. Evans and P. K. Wright, *J. Micromech. Microeng.*, 2010, **20**, 104009.
- 244 G. Hu, J. Kang, L. W. T. Ng, X. Zhu, R. C. T. Howe, C. G. Jones, M. C. Hersam and T. Hasan, *Chem. Soc. Rev.*, 2018, **47**, 3265–3300.
- 245 C. Schubert, M. C. van Langeveld and L. A. Donoso, *Br. J. Ophthalmol.*, 2014, **98**, 159–161.
- 246 R. Noorani, *3D Printing : Technology, Applications, and Selection*, CRC Press LLC, 1st edn, 2017.
- 247 L. W. T. Ng, G. Hu, R. C. T. Howe, X. Zhu, Z. Yang, C. G. Jones and T. Hasan, in *Printing of Graphene and Related 2D Materials: Technology, Formulation and Applications*, Springer International Publishing, Cham, 2019, pp. 103–134, DOI: 10.1007/978-3-319-91572-2\_4.
- 248 D. Zhang, B. Chi, B. Li, Z. Gao, Y. Du, J. Guo and J. Wei, *Synth. Met.*, 2016, **217**, 79–86.
- 249 K. Fu, Y. Wang, C. Yan, Y. Yao, Y. Chen, J. Dai, S. Lacey, Y. Wang, J. Wan, T. Li, Z. Wang, Y. Xu and L. Hu, *Adv. Mater.*, 2016, **28**, 2587–2594.
- 250 R. J. Pierce, E. P. Hickman, M. J. Mackenzie and H. G. Smith, *The Printing Ink Design*, Springer Netherlands, 5th edn, 2008.
- 251 S. P. Sreenilayam, I. U. Ahad, V. Nicolosi, V. Acinas Garzon and D. Brabazon, *Mater. Today*, 2020, **32**, 147–177.
- 252 H. A. D. Nguyen, K. Shin and C. Lee, *Int. J. Precis. Eng. Manuf.*, 2015, **16**, 517–523.
- 253 M. Singh, H. M. Haverinen, P. Dhagat and G. Jabbour, *Adv. Mater.*, 2010, **22**, 673–685.
- 254 G. Hu, T. Albrow-Owen, X. Jin, A. Ali, Y. Hu, R. C. T. Howe, K. Shehzad, Z. Yang, X. Zhu, R. I. Woodward, T. C. Wu, H. Jussila, J. B. Wu, P. Peng, P. H. Tan, Z. Sun, E. J. R. Kelleher, M. Zhang, Y. Xu and T. Hasan, *Nat. Commun.*, 2017, **8**, 278.
- 255 A. Dani, *Compos. Sci. Technol.*, 1996, **56**, 911–920.
- 256 I. M. Hutchings and G. D. Martin, *Inkjet Technology for Digital Fabrication*, Wiley & Hoboken, 2012.
- 257 D. Jang, D. Kim and J. Moon, *Langmuir*, 2009, **25**, 2629–2635.
- 258 B. Kang, W. H. Lee and K. Cho, *ACS Appl. Mater. Interfaces*, 2013, **5**, 2302–2315.
- 259 K. Fu, Y. Wang, C. Yan, Y. Yao, Y. Chen, J. Dai, S. Lacey, Y. Wang, J. Wan, T. Li, Z. Wang, Y. Xu and L. Hu, *Adv. Mater.*, 2016, **28**, 2587–2594.
- 260 G. Sun, J. An, C. K. Chua, H. Pang, J. Zhang and P. Chen, *Electrochem. Commun.*, 2015, **51**, 33–36.
- 261 B. Scrosati and J. Garche, *J. Power Sources*, 2010, **195**, 2419–2430.
- 262 M. Armand and J.-M. Tarascon, *Nature*, 2008, **451**, 652–657.
- 263 H. Zhang, X. Yu and P. V. Braun, *Nat. Nanotechnol.*, 2011, **6**, 277–281.
- 264 J. Liu, N. Li, M. D. Goodman, H. G. Zhang, E. S. Epstein, B. Huang, Z. Pan, J. Kim, J. H. Choi and X. Huang, *ACS Nano*, 2015, **9**, 1985–1994.
- 265 J. H. Pikul, H. G. Zhang, J. Cho, P. V. Braun and W. P. King, *Nat. Commun.*, 2013, **4**, 1–5.
- 266 J. Liu, H. G. Zhang, J. Wang, J. Cho, J. H. Pikul, E. S. Epstein, X. Huang, J. Liu, W. P. King and P. V. Braun, *Adv. Mater.*, 2014, **26**, 7096–7101.
- 267 J. Liu, X. Chen, J. Kim, Q. Zheng, H. Ning, P. Sun, X. Huang, J. Liu, J. Niu and P. V. Braun, *Nano Lett.*, 2016, **16**, 4501–4507.
- 268 K. Sun, T. S. Wei, B. Y. Ahn, J. Y. Seo, S. J. Dillon and J. A. Lewis, *Adv. Mater.*, 2013, **25**, 4539–4543.
- 269 J. Hu, Y. Jiang, S. Cui, Y. Duan, T. Liu, H. Guo, L. Lin, Y. Lin, J. Zheng and K. Amine, *Adv. Energy Mater.*, 2016, **6**, 1600856.

- 270 C. C. Ho, K. Murata, D. A. Steingart, J. W. Evans and P. K. Wright, *J. Micromech. Microeng.*, 2009, **19**, 094013.
- 271 W. Yang, J. Yang, J. J. Byun, F. P. Moissinac, J. Xu, S. J. Haigh, M. Domingos, M. A. Bissett, R. A. Dryfe and S. Barg, *Adv. Mater.*, 2019, **31**, 1902725.
- 272 G. Xiong, C. Meng, R. G. Reifengerger, P. P. Irazoqui and T. S. Fisher, *Energy Technol.*, 2014, **2**, 897–905.
- 273 D. P. Dubal, O. Ayyad, V. Ruiz and P. Gomez-Romero, *Chem. Soc. Rev.*, 2015, **44**, 1777–1790.
- 274 T. Tooming, T. Thomberg, H. Kurig, A. Jänes and E. Lust, *J. Power Sources*, 2015, **280**, 667–677.
- 275 J. Maeng, Y.-J. Kim, C. Meng and P. P. Irazoqui, *ACS Appl. Mater. Interfaces*, 2016, **8**, 13458–13465.
- 276 W. Si, C. Yan, Y. Chen, S. Oswald, L. Han and O. G. Schmidt, *Energy Environ. Sci.*, 2013, **6**, 3218–3223.
- 277 X. Dong, Z. Guo, Y. Song, M. Hou, J. Wang, Y. Wang and Y. Xia, *Adv. Funct. Mater.*, 2014, **24**, 3405–3412.
- 278 V. Ganesh, S. Pitchumani and V. Lakshminarayanan, *J. Power Sources*, 2006, **158**, 1523–1532.
- 279 J. Zhang, J. Jiang, H. Li and X. Zhao, *Energy Environ. Sci.*, 2011, **4**, 4009–4015.
- 280 Y. Jiang, H. Shao, C. Li, T. Xu, Y. Zhao, G. Shi, L. Jiang and L. Qu, *Adv. Mater.*, 2016, **28**, 10287–10292.
- 281 Z. Wang, W. Gao, Q. Zhang, K. Zheng, J. Xu, W. Xu, E. Shang, J. Jiang, J. Zhang and Y. Liu, *ACS Appl. Mater. Interfaces*, 2018, **11**, 1344–1352.
- 282 B. Akuzum, K. Maleski, B. Anasori, P. Lelyukh, N. J. Alvarez, E. C. Kumbur and Y. Gogotsi, *ACS Nano*, 2018, **12**, 2685–2694.
- 283 M. J. Solomon, A. S. Almusallam, K. F. Seefeldt, A. Somwangthanoj and P. Varadan, *Macromolecules*, 2001, **34**, 1864–1872.
- 284 S. Naficy, R. Jalili, S. H. Aboutalebi, R. A. Gorkin III, K. Konstantinov, P. C. Innis, G. M. Spinks, P. Poulin and G. G. Wallace, *Mater. Horiz.*, 2014, **1**, 326–331.
- 285 V. Natu, M. Sokol, L. Verger and M. W. Barsoum, *J. Phys. Chem. C*, 2018, **122**, 27745–27753.
- 286 J. H. Kim, W. S. Chang, D. Kim, J. R. Yang, J. T. Han, G.-W. Lee, J. T. Kim and S. K. Seol, *Adv. Mater.*, 2015, **27**, 157–161.
- 287 E. García-Tuñón, S. Barg, J. Franco, R. Bell, S. Eslava, E. D'Elia, R. C. Maher, F. Guitian and E. Saiz, *Adv. Mater.*, 2015, **27**, 1688–1693.
- 288 V. G. Rocha, E. Garcia-Tunon, C. Botas, F. Markoulidis, E. Feilden, E. D'Elia, N. Ni, M. Shaffer and E. Saiz, *ACS Appl. Mater. Interfaces*, 2017, **9**, 37136–37145.
- 289 B. G. Compton and J. A. Lewis, *Adv. Mater.*, 2014, **26**, 5930–5935.
- 290 W. Wu, A. DeConinck and J. A. Lewis, *Adv. Mater.*, 2011, **23**, H177–H177.
- 291 Y.-Y. Peng, B. Akuzum, N. Kurra, M.-Q. Zhao, M. Alhabeab, B. Anasori, E. C. Kumbur, H. N. Alshareef, M.-D. Ger and Y. Gogotsi, *Energy Environ. Sci.*, 2016, **9**, 2847–2854.
- 292 T. S. Wei, B. Y. Ahn, J. Grotto and J. A. Lewis, *Adv. Mater.*, 2018, **30**, 1703027.
- 293 M. Beidaghi and C. Wang, *Adv. Funct. Mater.*, 2012, **22**, 4500–4500.
- 294 Q. Jiang, N. Kurra, M. Alhabeab, Y. Gogotsi and H. N. Alshareef, *Adv. Energy Mater.*, 2018, **8**, 1703043.
- 295 X. Li, T. Yang, Y. Yang, J. Zhu, L. Li, F. E. Alam, X. Li, K. Wang, H. Cheng and C. T. Lin, *Adv. Funct. Mater.*, 2016, **26**, 1322–1329.
- 296 Y. Cai, J. Shen, G. Ge, Y. Zhang, W. Jin, W. Huang, J. Shao, J. Yang and X. Dong, *ACS Nano*, 2018, **12**, 56–62.
- 297 A. N. Abbas, B. Liu, L. Chen, Y. Ma, S. Cong, N. Aroonyadet, M. Köpf, T. Nilges and C. Zhou, *ACS Nano*, 2015, **9**, 5618–5624.
- 298 H. Ota, S. Emaminejad, Y. Gao, A. Zhao, E. Wu, S. Challa, K. Chen, H. M. Fahad, A. K. Jha and D. Kiriya, *Adv. Mater. Technol.*, 2016, **1**, 1600013.
- 299 H. W. Choi, T. Zhou, M. Singh and G. E. Jabbour, *Nanoscale*, 2015, **7**, 3338–3355.
- 300 B. An, Y. Ma, W. Li, M. Su, F. Li and Y. Song, *Chem. Commun.*, 2016, **52**, 10948–10951.
- 301 Q. Zhang, F. Zhang, S. P. Medarametla, H. Li, C. Zhou and D. Lin, *Small*, 2016, **12**, 1702–1708.

# Chapter 3

## Development of graphene ink for VOC detection

In this chapter, graphene-based ink have been utilized in 3D extrusion-printing for fabricating chemo-resistive sensors to detect VOC biomarkers such as acetone, ethanol and methanol. Herein, the sensor is printed in continuous mode consisting of multiple lines overlaid onto printed silver connections. To evaluate the sensing performance of the extrusion printed sensors, a comparative study with the sensors fabricated by a conventional drop casting method is performed. The results obtained demonstrate the extrusion-printing method as a promising fabrication technique for low-cost and scalable sensor production, and have significant advantages with printed electrode structures having a higher SA/V aspect ratio, sensitivity and selectivity compared with those from the conventional method.

This chapter has been published as research paper in “Nanoscales” journal as follows:

“**Hassan K**, Tung TT, Stanley N, Yap PL, Farivar F, Rastin H, Nine MJ, Losic D. Graphene ink for 3D extrusion micro printing of chemo-resistive sensing devices for volatile organic compound detection. *Nanoscale*. 2021; **13**, 5356-5368.”

## Statement of Authorship

Title of Paper	Graphene ink for 3D extrusion micro printing of chemo-resistive sensing devices for volatile organic compound detection.
Publication Status	<input checked="" type="checkbox"/> Published <input type="checkbox"/> Accepted for Publication <input type="checkbox"/> Submitted for Publication <input type="checkbox"/> Unpublished and Unsubmitted work written in manuscript style
Publication Details	Hassan K, Tung TT, Stanley N, Yap PL, Farivar F, Rastin H, Nire MJ, Losic D. Graphene ink for 3D extrusion micro printing of chemo-resistive sensing devices for volatile organic compound detection. <i>Nanoscale</i> . 2021; 13, 5356-5368.

### Principal Author

Name of Principal Author (Candidate)	Kamrul Hassan
Contribution to the Paper	Prepared and characterized on all the samples, interpreted data as well as wrote the manuscripts.
Overall percentage (%)	85%
Certification:	This paper reports on original research I conducted during the period of my Higher Degree by Research candidature and is not subject to any obligations or contractual agreements with a third party that would constrain its inclusion in this thesis. I am the primary author of this paper.
Signature	<div style="border-bottom: 1px solid black; width: 100%;"></div>
Date	19/10/2021

### Co-Author Contributions

By signing the Statement of Authorship, each author certifies that:

- i. the candidate's stated contribution to the publication is accurate (as detailed above);
- ii. permission is granted for the candidate to include the publication in the thesis; and
- iii. the sum of all co-author contributions is equal to 100% less the candidate's stated contribution.

Name of Co-Author	Tran Thanh Tung
Contribution to the Paper	Co-supervised and revised the manuscript.
Signature	<div style="border-bottom: 1px solid black; width: 100%;"></div>
Date	20/10/2021

Name of Co-Author	Nathan Stanley
Contribution to the Paper	Edited and revised the manuscript.
Signature	<div style="border-bottom: 1px solid black; width: 100%;"></div>
Date	28.10.2021

Please cut and paste additional co-author panels here as required.

## Statement of Authorship

Title of Paper	Graphene ink for 3D extrusion micro printing of chemo-resistive sensing devices for volatile organic compound detection.
Publication Status	<input checked="" type="checkbox"/> Published <input type="checkbox"/> Accepted for Publication <input type="checkbox"/> Submitted for Publication <input type="checkbox"/> Unpublished and Unsubmitted work written in manuscript style
Publication Details	Hassan K, Tung TT, Stanley N, Yap PL, Farivar F, Rastin H, Nine MJ, Losic D. Graphene ink for 3D extrusion micro printing of chemo-resistive sensing devices for volatile organic compound detection. <i>Nanoscale</i> . 2021; 13, 5356-5368.

### Principal Author

Name of Principal Author (Candidate)	Kamrul Hassan		
Contribution to the Paper	Prepared and characterized on all the samples, interpreted data as well as wrote the manuscripts.		
Overall percentage (%)	85%		
Certification:	This paper reports on original research I conducted during the period of my Higher Degree by Research candidature and is not subject to any obligations or contractual agreements with a third party that would constrain its inclusion in this thesis. I am the primary author of this paper.		
Signature		Date	19/10/2021

### Co-Author Contributions

By signing the Statement of Authorship, each author certifies that:

- i. the candidate's stated contribution to the publication is accurate (as detailed above);
- ii. permission is granted for the candidate to include the publication in the thesis; and
- iii. the sum of all co-author contributions is equal to 100% less the candidate's stated contribution.

Name of Co-Author	Pei Lay Yap		
Contribution to the Paper	Edited and revised the manuscript.		
Signature		Date	26/10/21

Name of Co-Author	Farzaneh Farivar		
Contribution to the Paper	Edited and revised the manuscript.		
Signature		Date	

Please cut and paste additional co-author panels here as required.



## Statement of Authorship

Title of Paper	Graphene ink for 3D extrusion micro printing of chemo-resistive sensing devices for volatile organic compound detection.
Publication Status	<input checked="" type="checkbox"/> Published <input type="checkbox"/> Accepted for Publication <input type="checkbox"/> Submitted for Publication <input type="checkbox"/> Unpublished and Unsubmitted work written in manuscript style
Publication Details	Hassan K, Tung TT, Stanley N, Yap PL, Farivar F, Rastin H, Nine MJ, Losic D. Graphene ink for 3D extrusion micro printing of chemo-resistive sensing devices for volatile organic compound detection. <i>Nanoscale</i> . 2021; 13, 5356-5368.

### Principal Author

Name of Principal Author (Candidate)	Kamrul Hassan		
Contribution to the Paper	Prepared and characterized on all the samples, interpreted data as well as wrote the manuscripts.		
Overall percentage (%)	85%		
Certification:	This paper reports on original research I conducted during the period of my Higher Degree by Research candidature and is not subject to any obligations or contractual agreements with a third party that would constrain its inclusion in this thesis. I am the primary author of this paper.		
Signature		Date	19/10/2021

### Co-Author Contributions

By signing the Statement of Authorship, each author certifies that:

- i. the candidate's stated contribution to the publication is accurate (as detailed above);
- ii. permission is granted for the candidate to include the publication in the thesis; and
- iii. the sum of all co-author contributions is equal to 100% less the candidate's stated contribution.

Name of Co-Author	Hadli Rastin		
Contribution to the Paper	Edited and revised the manuscript.		
Signature		Date	29.10.2021

Name of Co-Author	Md Julker Nine		
Contribution to the Paper	Edited and revised the manuscript.		
Signature		Date	01-11-2021

Please cut and paste additional co-author panels here as required.

## Statement of Authorship

Title of Paper	Graphene ink for 3D extrusion micro printing of chemo-resistive sensing devices for volatile organic compound detection.		
Publication Status	<input checked="" type="checkbox"/> Published	<input type="checkbox"/> Accepted for Publication	
	<input type="checkbox"/> Submitted for Publication	<input type="checkbox"/> Unpublished and Unsubmitted work written in manuscript style	
Publication Details	Hassan K, Tung TT, Stanley N, Yap PL, Farivar F, Rastin H, Nime MJ, Losic D. Graphene ink for 3D extrusion micro printing of chemo-resistive sensing devices for volatile organic compound detection. <i>Nanoscale</i> . 2021; 13, 5358-5368.		

### Principal Author

Name of Principal Author (Candidate)	Kamrul Hassan		
Contribution to the Paper	Prepared and characterized on all the samples, interpreted data as well as wrote the manuscripts.		
Overall percentage (%)	85%		
Certification:	This paper reports on original research I conducted during the period of my Higher Degree by Research candidature and is not subject to any obligations or contractual agreements with a third party that would constrain its inclusion in this thesis. I am the primary author of this paper.		
Signature		Date	19/10/2021

### Co-Author Contributions

By signing the Statement of Authorship, each author certifies that:

- i. the candidate's stated contribution to the publication is accurate (as detailed above);
- ii. permission is granted for the candidate to include the publication in the thesis; and
- iii. the sum of all co-author contributions is equal to 100% less the candidate's stated contribution.

Name of Co-Author	Dusan Losic		
Contribution to the Paper	Supervised the development of work, edited, revised the manuscript and acted as the corresponding author.		
Signature		Date	26 Oct 2021

Name of Co-Author			
Contribution to the Paper			
Signature		Date	

Please cut and paste additional co-author panels here as required.

Cite this: *Nanoscale*, 2021, 13, 5356

## Graphene ink for 3D extrusion micro printing of chemo-resistive sensing devices for volatile organic compound detection†

Kamrul Hassan,<sup>a,b</sup> Tran Thanh Tung,<sup>a,b</sup> Nathan Stanley,<sup>a,b</sup> Pei Lay Yap,<sup>a,b</sup> Farzaneh Farivar,<sup>a,b</sup> Hadi Rastin,<sup>a,b</sup> Md Julker Nine<sup>a,b</sup> and Dusan Losic<sup>a,b</sup>

Printed electronic sensors offer a breakthrough in the availability of low-cost sensor devices for improving the quality of human life. Conductive ink is the core of printing technology and also one of the fastest growing sector among all ink industries. Among many developed conductive inks, graphene-based inks are especially recognized as very promising for future fabrication of devices due to their low cost, unique properties, and compatibility with various platforms such as plastics, textiles, and paper. The development of graphene ink formulations for achieving high conductivity and high resolution printing is highly realized in 2D inkjet printing. Unfortunately, the ongoing development of graphene inks is possibly hampered by the non-uniform particle size and structures (e.g., different shapes and number of layers), which adversely affect printing resolution, conductivity, adhesion, and structural integrity. This study presents an environmentally sustainable route to produce graphene inks specifically designed for 3D extrusion-printing. The application of the prepared ink is demonstrated by mask-free automatic patterning of sensing devices for the detection of volatile organic compounds (VOCs). The sensing devices fabricated with this new ink display high-resolution patterning (average height/thickness of ~12 μm) and a 10-fold improvement in the surface area/volume (SA/V) ratio compared to a conventional drop casting method. The extrusion printed sensors show enhanced sensing characteristics in terms of sensitivity and selectivity towards trace amount of VOC (e.g. 5 ppm ethanol) at room temperature (20 °C), which highlights that our method has highly promising potential in graphene printing technology for sensing applications.

Received 10th January 2021,  
Accepted 6th February 2021

DOI: 10.1039/d1nr00150g

rsc.li/nanoscale

### 1. Introduction

Printed electronics is introduced as an attractive alternative to conventional semiconductor technologies by enabling the fabrication of low-cost, large-area, flexible devices<sup>1</sup> for application in health diagnostics,<sup>2</sup> energy storage,<sup>3</sup> electronic displays,<sup>4</sup> and medical, environmental and food control sensors.<sup>5</sup> Printing techniques such as inkjet, screen, gravure and flexographic printing have been successfully used to deliver additive patterning of ink materials onto rigid, flexible and conformable surfaces enabling large-scale, high-speed and low-cost scalable production.<sup>6,7</sup> These technologies are associated with liquid-phase conductive inks having markedly different

physical properties including the concentration of fillers and additives, viscosity and surface tension. Many conductive fillers have been used including carbon nanotubes, carbon nanodots, graphene, metals, metal oxides and conductive polymers.<sup>6,7</sup> Among them, metal based inks particularly silver and copper are widely used for flexible electronics due to their high conductivity, reliability and their previous conversant use in solid state electronics. However, these metals have some disadvantages such as high cost and oxidation problems,<sup>8</sup> which can reduce their conductivity over time and the performance of sensing devices, especially their lifetime. Graphene has become a prime candidate for printed flexible electronics and a competitive alternative to metal-based inks due to its excellent mechanical, thermal, and electrical properties with an exceptional carrier mobility of up to  $2 \times 10^5 \text{ cm}^2 \text{ V}^{-1} \text{ cm}^{-2}$ .<sup>9–11</sup> There is good precedent for the development of graphene-based ink formulations with previous studies comparing different types of graphene materials, solvents, binders and dispersants to achieve optimised viscosity and rheological parameters required for different printing techniques.<sup>6,7</sup> These

<sup>a</sup>School of Chemical Engineering and Advanced Materials, The University of Adelaide, Adelaide, SA 5005, Australia. E-mail: dusan.losic@adelaide.edu.au

<sup>b</sup>ARC Research Hub for Graphene Enabled Industry Transformation, The University of Adelaide, Adelaide, SA 5005, Australia

† Electronic supplementary information (ESI) available. See DOI: 10.1039/d1nr00150g

studies have shown that it is critical to use highly conductive single to few-layer graphene sheets with large surface area and low defects for high performance graphene inks, where its production on an industrial scale still remains a challenge. Conventional methods such as the oxidation–reduction process (reduced graphene oxide, RGO) or electrochemical and mechanical exfoliation (referred to as pristine graphene) offer advantages such as inexpensive raw graphite materials, scalability, low cost and compatibility with ink formulations produced using most printing techniques. Indeed, graphene inks with different formulations and properties have been reported to produce patterned structures with different resolution and complexity using inkjet printing,<sup>12</sup> screen and gravure printing,<sup>13</sup> spraying,<sup>14,15</sup> and flexographic techniques. These inks have been applied for successful fabrication of many devices including organic thin-film transistor electrodes,<sup>16</sup> chemical, volatile organic compound (VOC), and temperature sensors,<sup>17</sup> radio frequency identification (RFID) devices,<sup>18</sup> super capacitors,<sup>19</sup> and solar cells.<sup>20</sup> Although great progress has been made, the design of graphene inks is yet to be accomplished to meet the printing and device performance requirements for many applications.

The chemical vapour sensor sector is a fast growing market (growth rate *ca.* 8% p.a) which is expected to exceed USD 40.8 billion globally by 2024.<sup>21</sup> The integration of chemical sensors with wearable electronics will be a major driving force for this market growth, linked with medical, safety, security, and environmental demands from a broad range of sectors such as health monitoring, industrial, environmental and defence sectors.<sup>22,23</sup> The development of user-friendly, lightweight, low cost sensors with high sensitivity, selectivity and small dimensional features is a crying need nowadays for real world applications. Until now, a growing market share for these advanced sensors utilizing advanced nanoscale materials based on conductive polymers,<sup>24,25</sup> nanoscale metal/metal oxides,<sup>26,27</sup> and nanocomposites<sup>9,28</sup> has been reported. Besides, fabrication processes of these sensors are developed by applying simple and low-cost techniques, such as dip-coating<sup>10</sup> and spin-coating,<sup>11,29</sup> which are especially suitable for low-cost commercial products, unfortunately, with a limitation of uncontrolled fabrication processes. Recently, fabrication of electrodes and chemo-resistive sensing elements for VOC detection using graphene inks and inkjet printing has been the most widely used method because it is a low-cost, moderately simple, non-contact and high throughput method that is able to provide high resolution and complex 2D printed structures on various substrates. Nevertheless, the major disadvantage of inkjet printing for fabrication of chemo-resistive sensors is the low surface area to volume ratio of printed electrodes. Low surface area of printed electrodes limits the sensitivity performances along with the sensor recovery time. Previous studies have shown that the performance of chemo-resistive sensors is improved by a high surface area/volume (SA/V) aspect ratio, and the use of printing methods that could meet this requirement is advantageous. Among the available manufacturing techniques, the 3D extrusion-printing-based technique com-

monly used for fabrication of 3D structures is a promising approach that could satisfy these requirements.<sup>30</sup> The main advantages of this technology include digital and additive patterning, reduction in material waste, and compatibility with a variety of substrates with different degrees of mechanical flexibility and form factor. This method has been successfully used for fabrication of transistors,<sup>31</sup> solar cells,<sup>32</sup> and light-emitting diodes using graphene inks with different additives. The main challenge for using extrusion-printing is to design high viscosity graphene inks which require the addition of binders that can significantly reduce the electrical conductivity of printed devices. Moreover, many of the graphene inks reported in the literature for this purpose use toxic or flammable organic solvents such as *N*-methyl-2-pyrrolidone (NMP) and dimethylformamide (DMF) which are unsuitable for sustainable industrial-scale production.

The aim of this work is to demonstrate the application of 3D extrusion-printing technology for the fabrication of chemo-resistive patterned electrodes with a higher SA/V aspect ratio for enhanced VOC detection, in which a specially formulated graphene ink is used. To address the drawbacks of the previously reported formulations of high-viscosity graphene inks based on polymer binders and toxic solvents, herein, we report the use of a low cost, environmentally friendly, sustainable, and highly conductive graphene ink formulation that is optimised for extrusion printing. The concept is illustrated in Fig. 1. First, we have developed a graphene ink formulation that can be printed under ambient conditions *via* extrusion from a computer-controlled mechanically or pneumatically driven standard syringe. It is worth noting that the graphene conductive ink associated with a room-temperature extrusion 3D printing process is distinct from the widely used fused deposition 3D printing approaches, which utilize thermoplastic filaments extruded at elevated temperatures. To adapt printing requirements, our graphene ink consisting of few-layer graphene is formulated using a cellulose-derived binder dihydrolevoglucosenone (Cyrene) solvent, which in addition to being non-toxic is environmentally-friendly and sustainable. This ink also provides high graphene loading, high conductivity and controllable viscosity which are important parameters for 3D printing performance and large scale production.<sup>33</sup> Herein, we demonstrate the utility of graphene-based ink in 3D extrusion-printing of chemo-resistive electrodes for VOC detection of biomarkers such as acetone, ethanol and methanol. The sensor is printed in continuous mode consisting of multiple lines with an average layer thickness of 12  $\mu\text{m}$  overlaid onto printed silver connections. To evaluate the sensing performance of the extrusion printed sensors, a comparative study with the sensors fabricated by a conventional drop casting method was performed. The results obtained demonstrate the extrusion-printing method as a promising fabrication technique for low-cost and scalable sensor production, and have significant advantages with printed electrode structures having a higher SA/V aspect ratio, sensitivity and selectivity compared with those from the conventional method.

Paper

View Article Online

Nanoscale

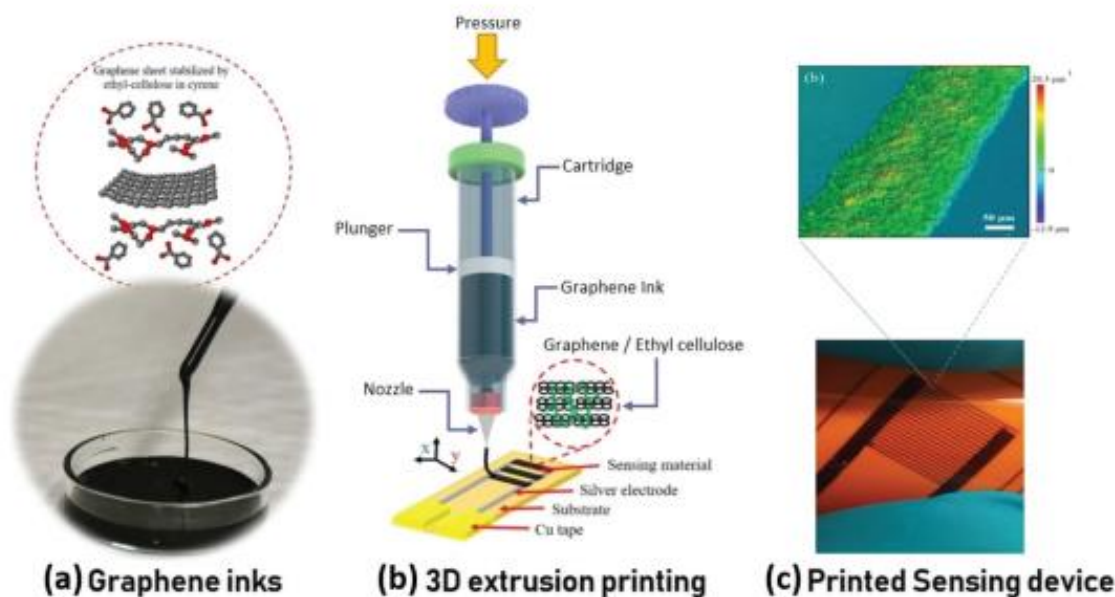


Fig. 1 Overview of graphene ink development, 3D extrusion printing process and example of an extrusion printed chemo-resistive VOC sensing device.

## 2. Experimental section

### 2.1. Graphene dispersion and processing

Pristine graphene (pG) (500 mg) with a particle size of  $\sim 5 \mu\text{m}$  was provided by First Graphene Ltd (Australia) and it was dispersed in a solution of 4% w/v ethyl cellulose (EC) (Aldrich, viscosity 10 cP) in toluene/ethanol 80 : 20 (500 mL), in a stainless steel beaker. The dispersion was mixed using a high shear mixer system (Silverson L5M) for 60 min at 10 000 rpm with cooling in an ice water bath. The dispersion was then subjected to ultrasonication using a probe sonication system (Fisher Scientific Sonic Dismembrator Model 500, 13 mm Branson tip) for 60 minutes at 80 W with cooling in the ice water bath. An aqueous solution of NaCl ( $0.08 \text{ g mL}^{-1}$ , Sigma-Aldrich, >99.5%) was added to this dispersion in a 1 : 2 volume ratio. The resulting mixture was separated by centrifugation at 4200 rpm over 30 minutes, after which the supernatant was discarded. To remove the residual salt, the resulting pG/EC solid was washed thoroughly with deionized water. The isolated pG/EC product was dried using a vacuum oven for 18 h, yielding 300 mg of fine black powder.

### 2.2. Ink preparation and characterization

To prepare the ink for extrusion printing, the pG/EC powder was dispersed in an 85 : 15 isopropanol/cyrene mixture at a concentration of 0.9 wt% by bath sonication. Solvent exchange was accomplished by removal of isopropanol by rotary evaporation under vacuum. When no further isopropanol was condensing, the remaining pG/EC/Cyrene dispersion was collected.

An illustration of the polymer-stabilized graphene in Cyrene is shown in Fig. 1(a and b). Compared with the original isopropanol dispersion, pG/EC in the final Cyrene dispersion was concentrated by about 50 times. This ink can be directly applied for extrusion printing as depicted in Fig. 1(c). The shear viscosity of the ink was measured using a Physica MCR 300 rheometer equipped with a 50 mm cone and plate geometry at shear rates of  $1\text{--}1000 \text{ s}^{-1}$ . The temperature was controlled with a Peltier plate for viscosity measurement. The rheological properties of samples were measured in oscillation mode by measuring  $G'$  and  $G''$  over time. In this way, low (1%) and high (50%) strain were applied repetitively to the samples and the response of the samples to the applied strain was traced over four cycles.

### 2.3. Extrusion printing patterning and sensor fabrication

Sensing devices were produced by direct extrusion printing of ink materials onto a Kapton film ( $125 \mu\text{m}$  thickness) as illustrated in Fig. 2(d). Thin couple lines of Ag ( $300 \mu\text{m}$ ) were printed on the flexible Kapton film using an extrusion printer to connect to the positive and negative electrodes. The as-prepared ink was then printed following the planar design on the pre-patterned silver using the extrusion printer (V-One, Voltera Inc.) with a 3-axis motion control system and a positioning resolution of  $1 \mu\text{m}$ . A dispensing tip ( $225 \mu\text{m}$  inner nozzle diameter) was used to print the inks. The tip moving speed was set at  $400 \text{ mm min}^{-1}$  and the tip-to-substrate distance was varied from 50 to  $100 \mu\text{m}$ . After printing, the printed electrodes were dried in an oven at  $70 \text{ }^\circ\text{C}$  for 1 h (in air) to remove all solvents. In order to create an electrical connector, two copper

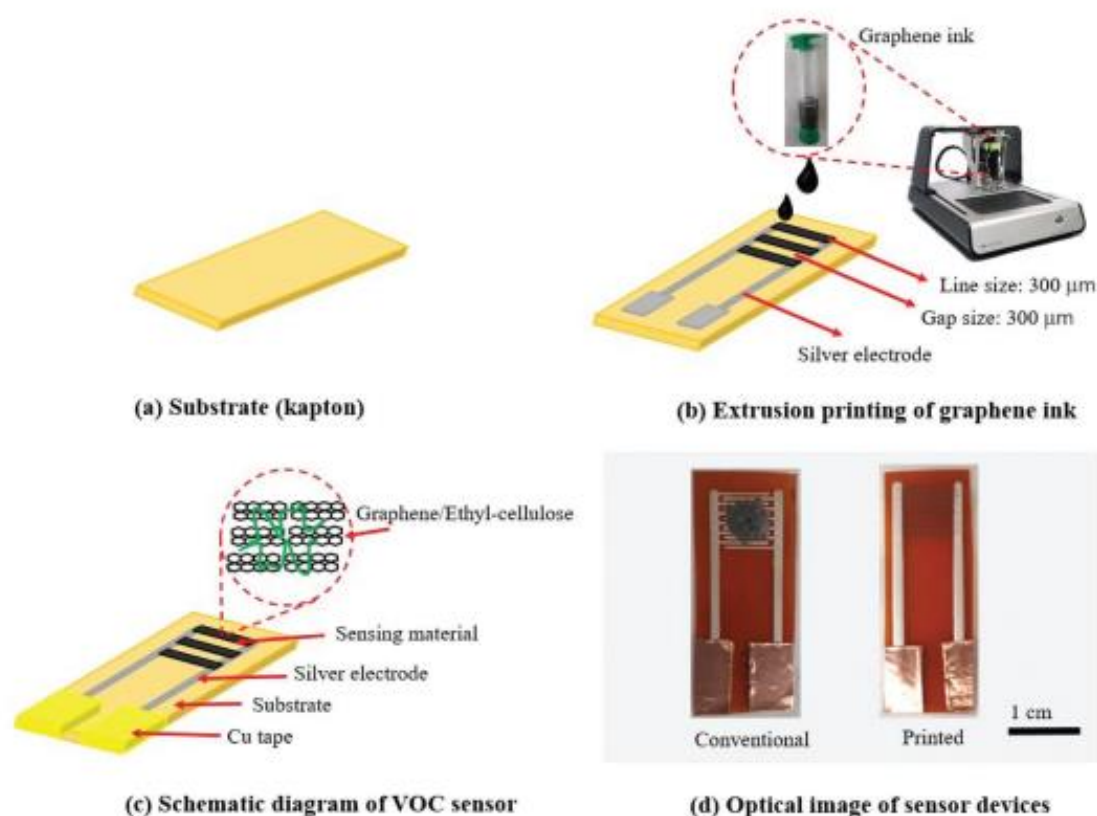


Fig. 2 Schematic diagram of the fabrication process of 3D extrusion micro printing of chemo-resistive sensors for VOC detection using graphene inks.

contact pads were connected with the silver electrodes to prevent the silver contact pads from being scratched by electric wire clamps and to provide electrical connection to the electrochemical workstation for testing. A conventional sensor was also prepared almost in the same way except that instead of printing, the same amount of graphene composite was drop-casted on the electrodes. A schematic diagram of the fabrication process of 3D extrusion printed graphene ink-based VOC sensor is shown in Fig. 2.

#### 2.4. Characterization of VOC sensors

The VOC sensing characteristics of pG/EC were investigated by recording the chemo-electrical response upon exposure to compressed air and VOC vapour produced through a bubbler, in which the concentration was controlled by varying the compressed air flow rate ( $200 \text{ mL min}^{-1}$  to  $4 \text{ mL min}^{-1}$ ) through 100% liquid VOCs at room temperature ( $20 \text{ }^\circ\text{C}$ ). Sensors were tested in a sealed vacuum chamber under ambient conditions with a set of VOCs including methanol, ethanol, and acetone, which are normally present in the environment and human breath.<sup>24</sup> The relative differential resistance response ( $A_R$ ) of the sensing device was recorded with an electrochemical work-

station (CH Instruments) using a computer. The sensor response is defined by the following equation:

$$A_R = (R - R_0)/R_0 \quad (1)$$

where  $R_0$  and  $R$  are the electrical resistance of the sensor in air and in tested VOC vapour.

#### 2.5. Characterization of materials

A scanning electron microscope (SEM-FEI QUANTA 450, Japan) operated at a voltage of 20 kV was used to analyze the morphological properties of pure pristine graphene and composites, which were coated with platinum by sputtering (3 nm). Transmission electron microscopy (TEM) was performed using a TECNAI 20 microscope operated at 120 kV. Raman spectra were obtained using a Horiba XploRA Raman microscope equipped with a 532 nm laser. The peak intensity ratios indicate the average and standard deviation of five different spectra collected at different points. The vibrational stretching modes of different molecular bonds in the pure and as-synthesized samples were studied by Fourier transform infrared spectroscopy (FTIR) (Nicolet 6700 Thermo Fisher, USA). The powder XRD patterns were recorded by X-ray diffraction (XRD)

(Rigaku Miniflex 600, Japan). The printed pattern thickness on extrusion-printed Kapton films was measured using a Dektak 150 Stylus Surface Profiler. The surface resistance was obtained using a CMT series JANDEL four-point probe at room temperature in which a current of 10  $\mu\text{A}$  was applied. Sessile drop water contact angle (WCA) measurement was performed using an Attension Theta optical tensiometer (KSV instruments, Finland). Thermal gravimetric analysis (TGA) was carried out using a TGA/DSC-2 Star system (Mettler Toledo) with a heating rate of 10  $^{\circ}\text{C min}^{-1}$  in air. The shear viscosity of the inks was measured with an Anton Paar Physica MCR 302 rheometer equipped with a 50 mm, 1 $^{\circ}$  cone and plate geometry at shear rates of 1–1000  $\text{s}^{-1}$ . A Peltier plate was used to control the temperature.

### 3. Results and discussion

#### 3.1. Characterization of formulated graphene inks and their ingredients

The morphological features of pG, pG/EC dried powder, and cyrene based graphene ink were investigated by using a combination of TEM and SEM (Fig. 3). The typical morphology of bare pG is shown in the representative SEM and TEM images (Fig. 3(a and b)). These images confirm the high degree of

exfoliation as most graphene sheets contain several layers. The extent of sheet formation can be observed along with the tendency of sheets to fold into overlapped regions. In addition, the lateral size of all the graphene platelets was in the range of 5 micrometers without the presence of small fragments. The SEM and TEM images of the pG/EC composite are presented in Fig. 3(c and d). As a consequence of the use of the polymeric binder (EC), the graphene flakes formed a condensed structure (elliptical spot) in the pG/EC composite (Fig. 3(d)). Fig. 3(a) illustrates that bare pG is curly and has poor adhesion between the flakes because of inert surface chemistry and random stacking with each other. As a result, gaps (viewed as dark holes) appear in between the sheets and they cause poor contact or break the electrical pathways that hinder electron flow resulting in a relatively large sheet resistance. Hence, the polymeric binder (EC) in between the graphene sheets plays an effective role in lowering the sheet resistance by enhancing connectivity and filling the gaps (Fig. 3(c)). As evidenced in Fig. 3(e), the surface of the graphene sheets is no longer coarse because of EC and Cyrene encapsulated graphene sheets. In addition, the graphene flakes allow them to be well distributed and in good contact, which causes a reduction in the sheet resistance. The XRD patterns were used to characterize the crystallinity of the as synthesized graphene inks (Fig. 3(f)). The observed characteristic peaks of graphene at the  $2\theta$  values around 26.49 $^{\circ}$ , 31.82 $^{\circ}$ , 45.54 $^{\circ}$ , 54.68 $^{\circ}$ , 75.44 $^{\circ}$ , and 62.85 $^{\circ}$  can be indexed. The intensity of the peak at 26.49 $^{\circ}$  is significantly higher than those of any other peaks. In addition, diffraction peaks observed at the  $2\theta$  values of 20.77 $^{\circ}$  corresponded to the structure of EC.

Fourier transform infrared spectroscopy (FTIR) and Raman spectroscopy were used to investigate the associated functional groups in the graphene structure and their EC composite inks (pG/EC). Fig. 4(a) shows the FTIR spectra of pG, EC and their composite (pG/EC) before and after annealing at 250  $^{\circ}\text{C}$ . EC is a polymer which has a large number of hydroxyl ( $-\text{OH}$ ) groups, which showed a broad  $-\text{OH}$  absorption peak located at 1053  $\text{cm}^{-1}$  (black line). However, no peaks associated with  $-\text{OH}$  ( $\sim 1340 \text{ cm}^{-1}$ ) and  $-\text{COOH}$  ( $\sim 1710\text{--}1720 \text{ cm}^{-1}$ ) groups were detected (green line) for pG, which provides evidence that the graphene is pristine in nature.<sup>35</sup> The intensity of the characteristic peak of  $-\text{OH}$  at 1053  $\text{cm}^{-1}$  for EC was reduced in the pG/EC composite before annealing. More importantly, after annealing the intensity of this peak significantly decreased and the peaks ( $\sim 2028\text{--}2159 \text{ cm}^{-1}$ ) associated with graphene appeared, which provides evidence that after annealing the polymeric binder has partially decomposed. The Raman spectra of pG and the pG/EC composite are shown in Fig. 4(b). In the figure, it was observed that the breathing mode or the  $E_{2g}$  vibration mode of  $\text{sp}^2$  carbon atoms appeared as the D-band (1355  $\text{cm}^{-1}$ ), G-band (1583  $\text{cm}^{-1}$ ), and relatively wide 2D-band at 2697  $\text{cm}^{-1}$ . This was happened because of double resonance transitions resulting from two phonons with opposite momenta for the graphene material, which are present for both bare pG and composite material.<sup>36</sup> Fig. 4(c) and (d)

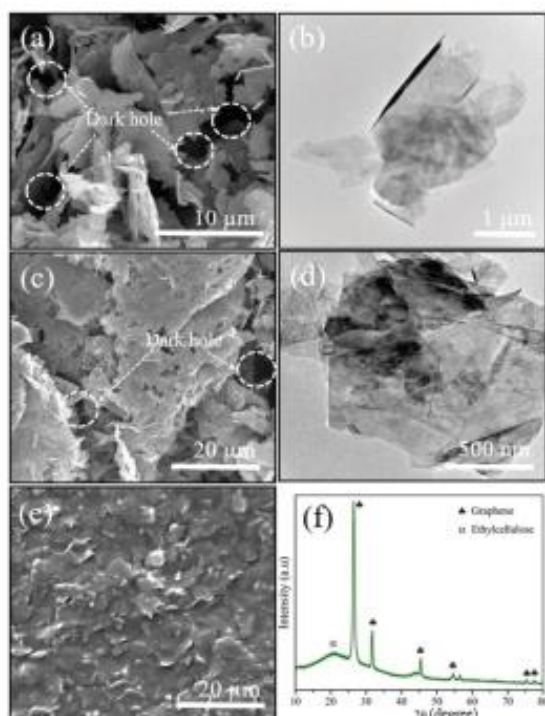


Fig. 3 FESEM and TEM micrographs of (a and b) pristine graphene (pG), (c and d) pristine graphene/ethyl-cellulose (pG/EC) powder, and (e) cyrene based graphene ink. (f) XRD spectrum of the pG/EC composite.

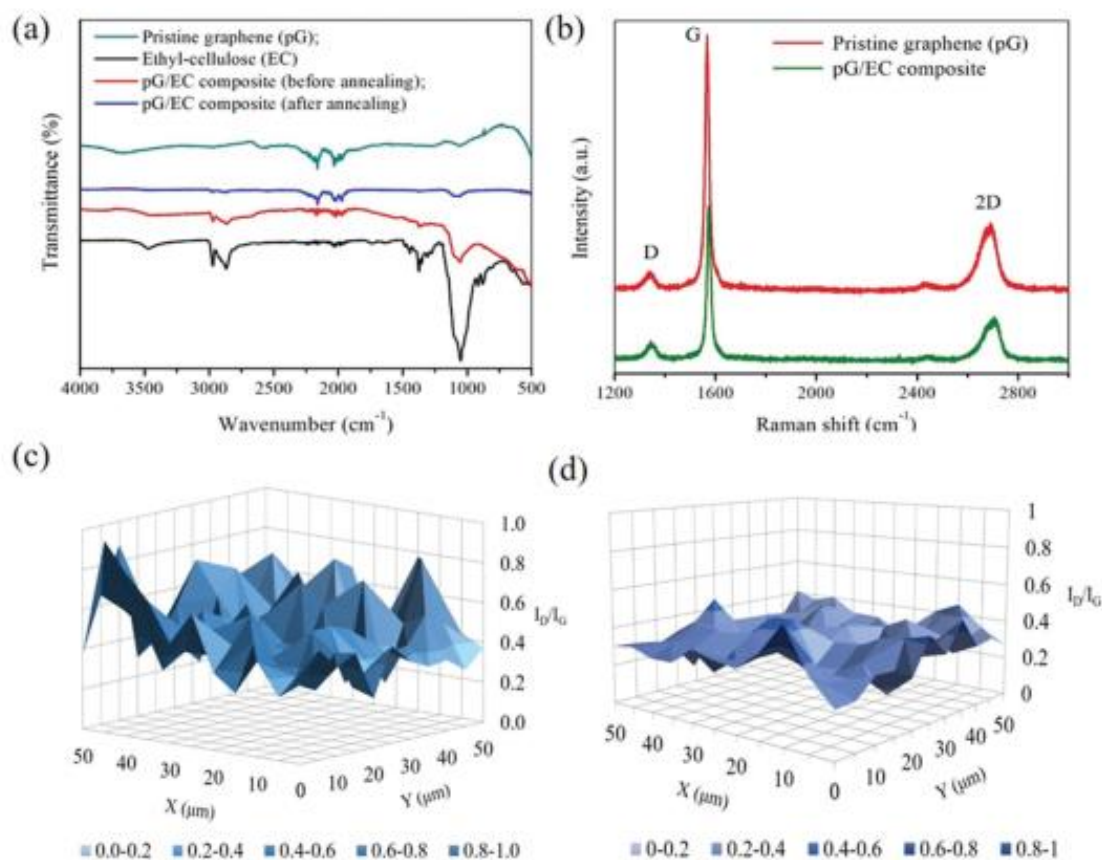


Fig. 4 Quality of the extrusion printed graphene ink. (a) FTIR characterization of pristine graphene (pG), ethyl-cellulose (EC), and the pG/EC composite with and without annealing. (b) Raman spectra of pG and the pG/EC composite. Raman 3D mapping with the calculated  $I_D/I_G$  ratio for (c) pG and (d) the pG/EC composite.

show the 3D Raman mapping with the ratio of  $I_D/I_G$  for pG and the pG/EC composite, respectively. From the results it was observed that the  $I_D/I_G$  ratio for the pG/EC composite (0.8) was not much higher than that for pG (0.5). A low  $I_D/I_G$  ratio indicates a low level of defects on graphene flakes, which is significant for electron flow. Moreover, the Raman analysis suggests no structural changes in the graphene flakes within the graphene ink composite.

The success of 3D extrusion printing is strongly influenced by various physical properties of the ink, such as viscosity and surface tension. Typical formulations of high viscosity inks reported in the literature are based on polymer binders and additives which negatively influence the electrical conductivity of the formulated inks. To address this problem, we used Cyrene as solvent for dispersion of graphene at high concentration that stabilizes pG within the EC polymer composite without additional binders.<sup>33</sup>

The viscosity of the synthesized ink was measured at room temperature, as shown in Fig. 5(a). The viscous ink with a high loading of graphene exhibits a viscosity of 50–60 Pa s,

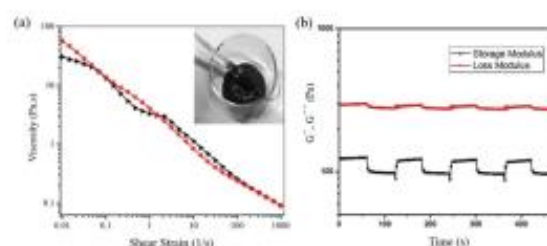


Fig. 5 Rheological properties of graphene inks. (a) Viscosity as a function of shear rate (inset shows the optical images of viscous graphene inks) and (b) storage and loss modulus as a function of time at room temperature relevant for extrusion printing.

which is within the suitable range (10–100 Pa s) for extrusion printing. As can be seen from Fig. 5(b), the storage modulus ( $G'$ ) is lower than the loss modulus ( $G''$ ), showing the fluid state of the sample at both low and high strain. When strain is applied to the graphene ink,  $G'$  and  $G''$  values rapidly



decrease and return to their initial values after removing the load. This behaviour is indicative of the recoverability of the graphene ink which demonstrates important thixotropic behaviour of printable inks. In addition, the key printing parameters, including the speed and pressure of extrusion *via* printer nozzle and the speed of printing, were optimized in terms of ink rheological properties to print various patterns.

Fig. 6(a-c) shows that the extrusion printing of graphene ink lines on Kapton yielded a line width of  $\sim 188.6 \mu\text{m}$ . The successful ink formulation is evidenced by the uniform dome-shaped cross-sectional profile across the lines with an average thickness of  $\sim 12 \mu\text{m}$ . Unlike dilute inks applied for inkjet printing, the extrusion printing technique avoids the

undesirable coffee ring effect on printed lines. In addition, this advantageous cross-sectional profile was maintained for all of the printing lines on the fabricated devices, as shown in Fig. 6(c). This domed morphology of the printed features is attributed to solvent evaporation during drying, which causes the inward Marangoni flow established by the surface tension gradient.<sup>37</sup> Moreover, the coffee ring effect is suppressed through the printing passes due to the Marangoni flow.<sup>38,39</sup> This flow homogenizes the droplet composition, resulting in a uniform morphology of the printed features. In addition, the  $\text{sp}^2$  bonding and small lateral size of the graphene sheets minimize folding or buckling of the printed flakes, which promotes low surface roughness and well-defined flake to flake contacts.

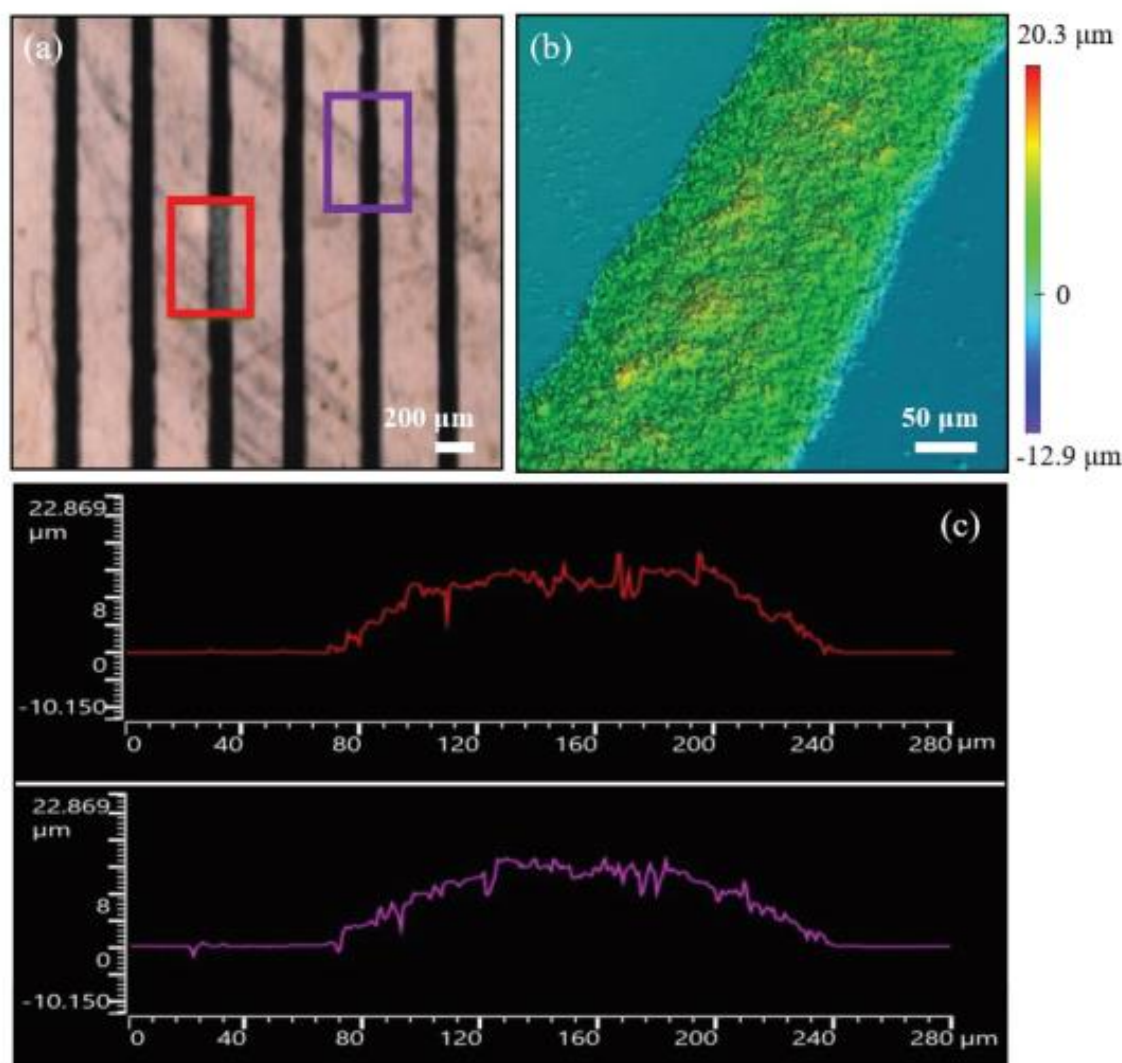


Fig. 6 Results of 3D profile measurements of printed inks using a 3D optical profilometer. (a) 2D image of printed patterns on Kapton, (b) 3D profile map of the representative printed line and (c) averaged cross-sectional profiles of printed lines for the selected region.

To obtain highly electrically conductive features in the pG/EC ink, thermal annealing is necessary. In the graphene ink, graphene sheets are encapsulated with EC as a polymeric binder after solvent evaporation. To study the electrical characteristics of these ink materials, films were blade-coated onto glass slides and annealed in air with systematic variation of the annealing time and temperature. Fig. 7(a) illustrates that films annealed at 250 °C for 30 min showed high electrical conductivity compared with other annealing temperatures, possibly due to decomposition of the polymeric binder. Moreover, resistivity of the prepared films increased due to the oxidized graphene material and oxidative burn EC at 400 °C. In addition, at 250 °C, annealing for just 20 min was optimal to acquire low resistivity (Fig. 7(b)). In addition, shortly after printing the printed lines had good wettability on the substrate surface and showed small water contact angles (Fig. S1(a)†). Due to this wetting characteristic, the freshly printed ink can pin the contact line and suppress the coffee ring effect. After annealing at 250 °C the solvent evaporated, the polymer binder began to decompose and as a result the contact angle increased (Fig. S1(b)†) with high interfacial free energy, which

increased the adhesion of the annealed ink. In order to determine the surface energy, the following equations by Owens and Wendt<sup>38</sup> and Wu<sup>39</sup> were used:

$$\gamma_{sl} = \gamma_{sv} + \gamma_{lv} - 2 \left( \sqrt{\gamma_{sv}^D \gamma_{lv}^D} + \sqrt{\gamma_{sv}^P \gamma_{lv}^P} \right) \quad (2)$$

$$\gamma_{sl} = \gamma_{sv} + \gamma_{lv} - 4 \left( \frac{\gamma_{lv}^D \times \gamma_{sv}^D}{\gamma_{lv}^D + \gamma_{sv}^D} + \frac{\gamma_{lv}^P \times \gamma_{sv}^P}{\gamma_{lv}^P + \gamma_{sv}^P} \right) \quad (3)$$

where  $\gamma_{lv}^D$ ,  $\gamma_{sv}^D$  and  $\gamma_{lv}^P$ ,  $\gamma_{sv}^P$  are the dispersive and polar components of liquid–vapour ( $\gamma_{lv}$ ) energy and solid–vapour ( $\gamma_{sv}$ ) energy, respectively.

The surface energies were calculated using the above equations for all samples following a similar fashion. The maximum contact angle of the annealed samples represents the minimum surface energy. Moreover, it has been reported in the literature that the surface roughness is directly proportional to the contact angle and thereby inversely proportional to the surface energy.<sup>40</sup> The contact angle and surface energy of each sample calculated using the above equations are listed in Table S1.† For this study, an annealing

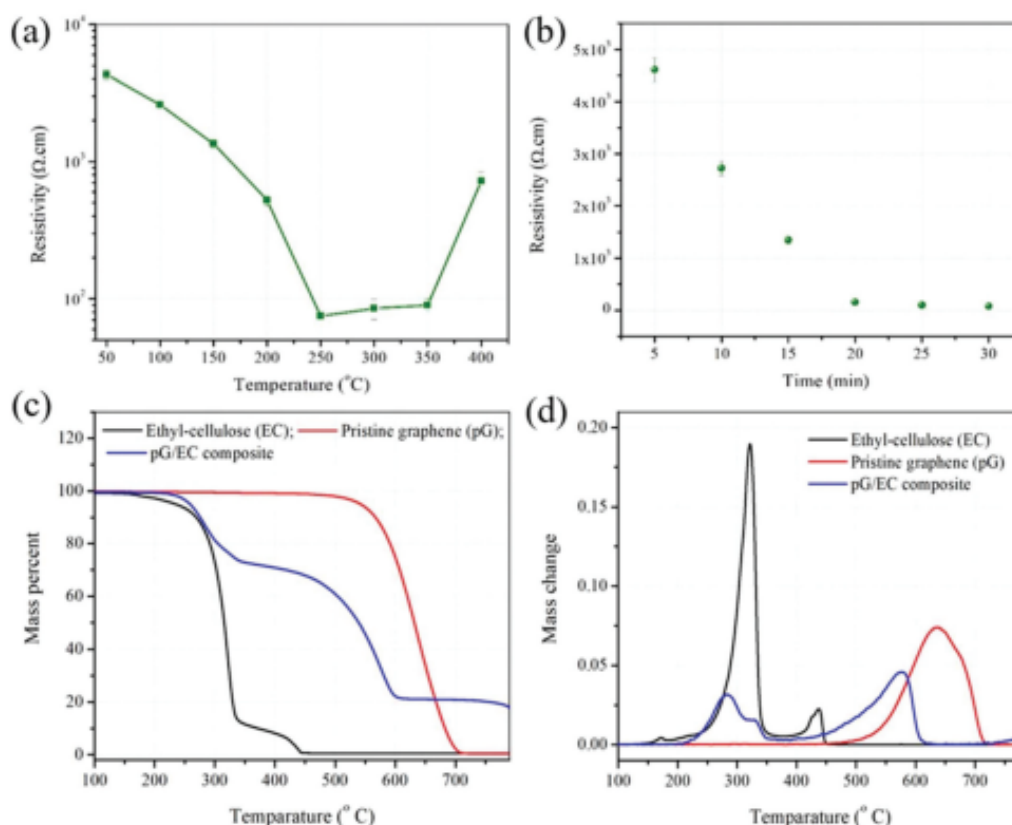


Fig. 7 Electrical characterization of graphene ink, (a) resistivity vs. annealing temperature of blade-coated films for a fixed annealing time of 30 min and (b) resistivity vs. annealing time of the prepared films at a fixed annealing temperature of 250 °C. Thermal gravimetric analysis (TGA) of pure EC, pG, and the PG/EC composite, showing (c) mass as a function of temperature and (d) the differential mass loss.

## Paper

View Article Online

Nanoscale

temperature of 250 °C and a time of 30 min were identified as optimum for printing and sensing applications.

Thermal gravimetric analysis (TGA) of pure EC indicates that decomposition initiates at 200 °C and no residue remains above 400 °C (Fig. 7(c)). By comparison, pG fully decomposes above 700 °C (in an air environment). Meanwhile, EC decomposition occurs in two stages for the pG/EC composite. At low temperature (below 250 °C), EC starts charring while volatilization and removal of the EC residues occurs above 400 °C (Fig. 7(d)). The decomposition threshold for EC shifts to higher temperatures in the pG/EC composite due to the presence of the graphene sheets. This observation coupled with the high electrical conductivity observed after annealing at temperatures of 250–350 °C suggests that the initial decomposition of EC improves graphene sheet to sheet contact and so enables efficient charge transport through the graphene network. It has been shown that thermal decomposition of cellulose derivatives can result in the formation of aromatic species which form  $\pi$ - $\pi$  stacking between the residues and the graphene sheets. This phenomenon happened in a graphene composite with comparatively efficient charge transport characteristics.<sup>41,42</sup> In addition, annealing above 350 °C causes higher resistivity because of the decomposition of residual EC in the pG/EC composite and the breakdown of the graphene charge transport network.

### 3.2. Characterization of 3D extrusion printed VOC sensors

Fig. 8(a) and (b) show the real-time response of the graphene sensors fabricated by two different methods (drop cast and printed method) when exposed to ethanol, methanol and acetone vapour at room temperature. The relative resistance of both sensors was found to increase upon exposure to these analytes and returned to the baseline upon exposure to synthetic air. From Fig. 8, it can be observed that the sensor response for the fully printed device is higher than that for the drop cast sensor for all analytes. The performance of the printed sensors was enhanced due to the patterned structure compared to sensors prepared by conventional methods in the literature. The mechanism is mainly based on the surface area to volume ratio enhancement of the effective sensing materials. To calculate the ratio of the active surface area to volume (SA : V) of two different sensors, the thickness ( $T$ ) and width ( $d$ ) of the sensing materials were obtained from the optical profilometer measurement. The effective active area of sensing materials for the conventional sensor was calculated using the below equation:

$$\text{Active area}_{\text{eff}} (A_{\text{conventional}}) = N \times \pi r^2 \quad (4)$$

where  $N$  is the number of circles and  $r$  is the radius of the circles.

The active area of the printed sensing material was calculated using the below equation:

$$\text{Active area}_{\text{eff}} (A_{\text{printed}}) = N \times (L \times d) \quad (5)$$

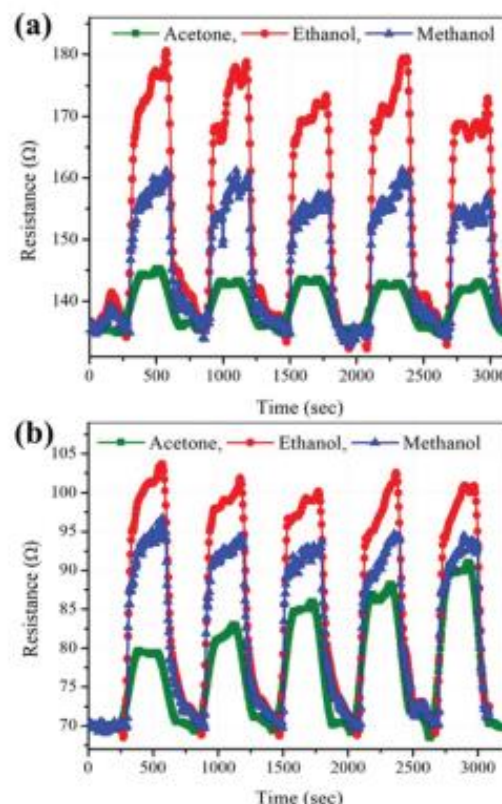


Fig. 8 Comparative sensing response of sensors fabricated by the (a) conventional method and (b) printed method towards different 100 ppm VOCs at room temperature (20 °C).

where  $N$  is the number of printed lines, and  $L$  is the length and  $d$  is the width of one printed line.

Based on this calculation the effective volume of the sensing materials can be further calculated by taking into account the average thickness:

$$\text{Active volume}_{\text{eff}} = \text{Active area}_{\text{eff}} \times T_{\text{avg}} \quad (6)$$

The ratio of the surface area to volume is calculated as follows:

$$\text{SA} : \text{V} = \text{Active area}_{\text{eff}} / \text{Active volume}_{\text{eff}} \quad (7)$$

The results showed a 10-fold increase of SA : V for the printed sensors compared to the conventional sensor. The higher SA : V ratio results in a much higher relative exposure and pressure of the analytes on the active surface of the printed sensor which increases the sensing efficiency. The detailed calculation results for SA : V for both sensors are provided in Table S2.† Moreover, because of the diverse adsorption capabilities of the sensors to analytes with various polarities, the fabricated sensors have superior sensitivity to more polar (ethanol and methanol) versus less polar (acetone) analytes (shown in Fig. 9(a-c)). This can be better understood

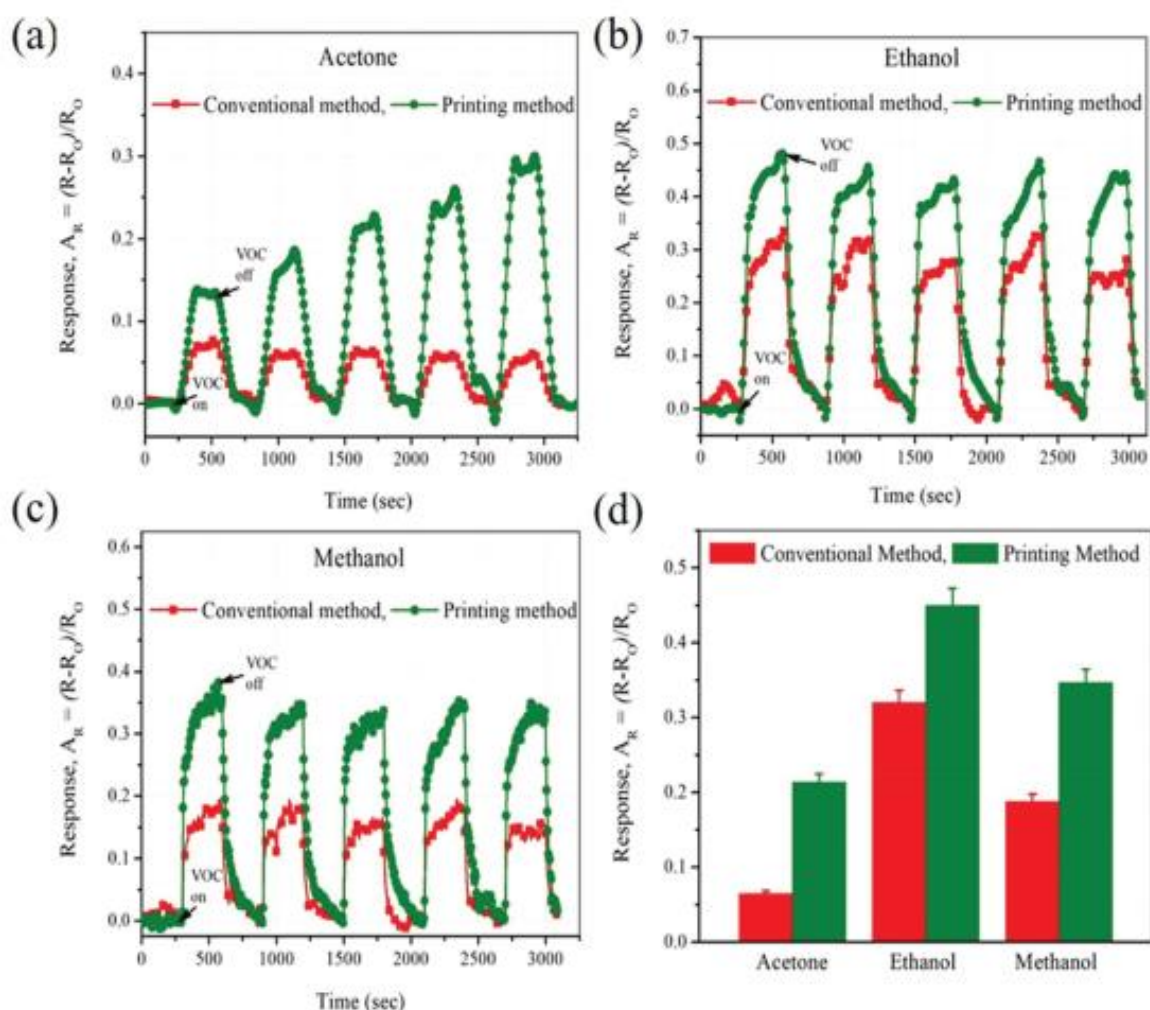


Fig. 9 Response of fabricated sensors towards different 100 ppm VOC analytes at room temperature (20 °C) such as (a) acetone, (b) ethanol, and (c) methanol. (d) A comparative transient response of fabricated sensors to 100 ppm VOC analytes at room temperature (20 °C).

by considering the polar defect sites on the pG and EC which can interact more efficiently with highly polar analytes than with less polar analytes.<sup>35,43–45</sup> In addition, based on the sensing mechanism, upon adsorption of a chemical vapour analyte, the sensor volume expands, which thus increases the average distance between the neighbouring graphene sheets, which leads to an increase of the carrier tunnelling barrier and thus the resistance of the sensing device is increased.<sup>46,47</sup> Consequently, the sensor adsorbs more polar analytes than non-polar ones when exposed to identical concentrations of polar and non-polar vapour simultaneously which leads to a larger total resistance change resulting in higher sensitivity. It is evident from the literature that methanol (0.762) is only slightly more polar than ethanol (0.654).<sup>34</sup> However, between these two analytes the response of the fabricated sensor towards ethanol was significantly higher due to better pene-

tration of the ethanol molecules through the sensing layer. In addition, the ink is formulated using ethanol and toluene as solvents, and the affinity of the sensing material for ethanol is much higher than that for methanol. Taken together this phenomenon and the higher SA:V ratio of the printed sensor explain both the improved performance compared to a drop cast sensor and the higher sensitivity towards polar *versus* less polar analytes Fig. 9(d).

Fig. 10(a) illustrates the dynamic resistance variations of the printed sensor using ethanol vapour at the parts per million (ppm) level (5 ppm–100 ppm) at room temperature. The printed sensor exhibited good linear response over the lower range of ethanol vapor concentrations (5–30 ppm). Importantly, because of the clamping effect no mechanical deformation was noticed in the printed sensing materials at the lowest concentration of ethanol vapor (5 ppm). The clamp-

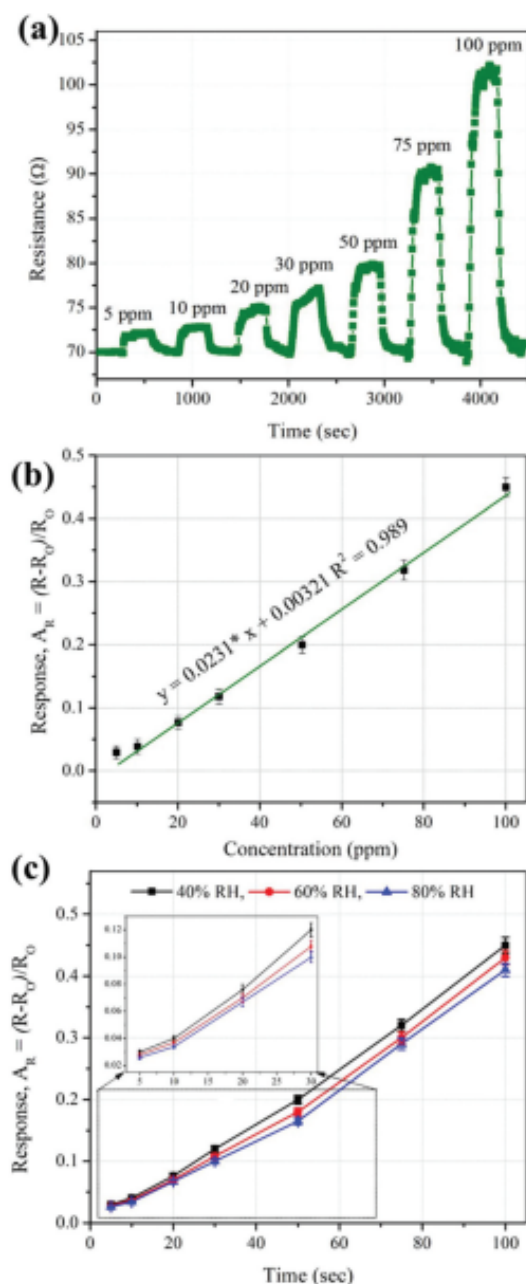


Fig. 10 (a) Transient resistance variation of printed sensors to ethanol vapour at the ppm level at room temperature (20 °C) and (b) linear fitting of ethanol response at the tested ppm level for printed sensors. (c) Transient response of printed sensors to ethanol vapour under different humidity at room temperature (20 °C).

ing effect reveals that the tensile stiffness of a laminate specimen is in inverse relation to the thickness of the specimen.<sup>48</sup> However, due to this phenomenon, at lower ethanol concentrations swelling of polymer encapsulated graphene flakes

occurs, which results in negligible hysteric behaviour and signal to noise ratio (SNR). The linear relationship for the dependency between the response and the concentration of ethanol vapour at the ppm level has been established and is depicted in Fig. 10(b). In real-world applications, the humidity effect is a great concern in the performance evaluation of the sensor, as the adsorption of water molecules decelerates the sensor response significantly. Fig. 10(c) shows the effect of humidity on ethanol vapor sensing performance of the printed sensors at room temperature (20 °C). However, at room temperature no significant degradation in response magnitude was observed with a relative humidity (RH) of up to 80% because of the configuration of specially designed graphene composites. In this composite, EC worked as the host-matrix for graphene encapsulation. There is no cross-linking originating in between graphene and EC. Moreover, because of the lattice structure of graphene, no dangling bonds are present along the external surfaces of the graphene, which therefore gives a reduced chemical activity.<sup>49</sup> Only physisorption interactions can arise when external molecules such as water are adsorbed onto this type of structure. Importantly, Levita *et al.*<sup>49</sup> highlighted in their atomistic simulation that the very reactive edges of the graphene plane (particularly the zigzag edge) can adsorb the fragments of water molecules (-H and -OH) preventing water from intercalating. However, the effects of humidity on methanol and acetone sensing performance of the printed sensor were also investigated (Fig. S2†), and negligible degradation in the response value was observed with a relative humidity of up to 80%. The reliability and durability characteristics of the composite based VOC sensor are also important for real-field applications. In this study approximately the same configurations of the 5 sensors were used, and none of them showed any failure/notable response deviation towards VOC vapour (*e.g.* ethanol). Nevertheless, to check the long-term stability of the as-fabricated sensor, the sensor response along with the baseline resistance was monitored over a fourteen-day period, where each day the as-fabricated sensor was exposed to ethanol vapour at room temperature (20 °C), and at a RH of 40%. Fig. S3(a) and (b)† illustrate the tested sensor response and the effect on its baseline resistance, which demonstrated exceptional durability and stability, suggesting that we have indeed fabricated a high-performance sensor.

## Conclusions

In summary, a 3D extrusion-printing technique for the fabrication of chemo-resistive patterned electrodes was demonstrated using specially designed graphene inks to achieve a larger SA/V aspect ratio and enhanced VOC detection. The new graphene ink combining EC and cyrene provides a facile route to obtain environmentally friendly, sustainable, and low cost sensing devices fabricated by high quality 3D extrusion printing. The graphene ink was printed at high-resolution providing patterned structures with a resistivity as low as 70  $\Omega$  cm after annealing at 250 °C for 30 min. Patterns printed in the form of

lines were used as chemo-resistive sensing devices for VOC detection at room temperature. The results demonstrate that the printed sensors showed high sensitivity to different VOCs (acetone, ethanol, and methanol) when compared with a sensor prepared with the same ink but using a conventional drop casting method. In terms of selectivity, the printed sensors showed higher sensitivity ( $A_R \sim 0.45$ ) towards ethanol due to the polarity and permittivity of the printed ink. The printed sensors also showed a broad detection range of 5–100 ppm with good linearity for ethanol at room temperature. This concept paves a new path towards low cost, environmentally friendly and sustainable printed devices for VOC sensing applications.

## Conflicts of interest

There are no conflicts to declare.

## Acknowledgements

The authors acknowledge financial support from the Australian Research Council (ARC Research Hub for Graphene Enabled Industry Transformation, IH15000003). The authors would like to acknowledge Circa Group Ltd., Australia for the generous gift of Cyrene solvent applied in this research.

## Notes and references

- A. C. Arias, J. D. MacKenzie, I. McCulloch, J. Rivnay and A. Salleo, *Chem. Rev.*, 2010, **110**, 3–24.
- D.-H. Kim, N. Lu, R. Ma, Y.-S. Kim, R.-H. Kim, S. Wang, J. Wu, S. M. Won, H. Tao and A. Islam, *science*, 2011, **333**, 838–843.
- A. M. Gaikwad, G. L. Whiting, D. A. Steingart and A. C. Arias, *Adv. Mater.*, 2011, **23**, 3251–3255.
- J. A. Rogers, Z. Bao, K. Baldwin, A. Dodabalapur, B. Crone, V. Raju, V. Kuck, H. Katz, K. Amundson and J. Ewing, *Proc. Natl. Acad. Sci. U. S. A.*, 2001, **98**, 4835–4840.
- M. Jung, J. Kim, J. Noh, N. Lim, C. Lim, G. Lee, J. Kim, H. Kang, K. Jung and A. D. Leonard, *IEEE Trans. Electron Devices*, 2010, **57**, 571–580.
- T. S. Tran, N. K. Dutta and N. R. Choudhury, *Adv. Colloid Interface Sci.*, 2018, **261**, 41–61.
- G. Hu, J. Kang, L. W. Ng, X. Zhu, R. C. Howe, C. G. Jones, M. C. Hersam and T. Hasan, *Chem. Soc. Rev.*, 2018, **47**, 3265–3300.
- F. Alotaibi, T. T. Tung, M. J. Nine, C. J. Coghlan and D. Losic, *ACS Appl. Nano Mater.*, 2018, **1**, 2249–2260.
- X. Zhou, W. Huang, J. Shi, Z. Zhao, Q. Xia, Y. Li, H. Wang and Z. Li, *J. Mater. Chem. A*, 2014, **2**, 4722–4730.
- C. Piloto, F. Mirri, E. A. Bengio, M. Notarianni, B. Gupta, M. Shafiei, M. Pasquali and N. Motta, *Sens. Actuators, B*, 2016, **227**, 128–134.
- H. Y. Jeong, D.-S. Lee, H. K. Choi, D. H. Lee, J.-E. Kim, J. Y. Lee, W. J. Lee, S. O. Kim and S.-Y. Choi, *Appl. Phys. Lett.*, 2010, **96**, 213105.
- W. Li, F. Li, H. Li, M. Su, M. Gao, Y. Li, D. Su, X. Zhang and Y. Song, *ACS Appl. Mater. Interfaces*, 2016, **8**, 12369–12376.
- X. Huang, T. Leng, X. Zhang, J. C. Chen, K. H. Chang, A. K. Geim, K. S. Novoselov and Z. Hu, *Appl. Phys. Lett.*, 2015, **106**, 203105.
- X. Huang, K. Pan and Z. Hu, *Sci. Rep.*, 2016, **6**, 38197.
- M. Akbari, M. W. A. Khan, M. Hasani, T. Björninen, L. Sydänheimo and L. Ukkonen, *IEEE Antennas Wirel. Propag. Lett.*, 2015, **15**, 1569–1572.
- S. Lim, B. Kang, D. Kwak, W. H. Lee, J. A. Lim and K. Cho, *J. Phys. Chem. C*, 2012, **116**, 7520–7525.
- D. Kong, L. T. Le, Y. Li, J. L. Zunino and W. Lee, *Langmuir*, 2012, **28**, 13467–13472.
- K. Y. Shin, J. Y. Hong and J. Jang, *Adv. Mater.*, 2011, **23**, 2113–2118.
- L. Wang, S. Chen, T. Shu and X. Hu, *ChemSusChem*, 2019, **12**, 1–25.
- D. Dodoo-Arhin, R. C. Howe, G. Hu, Y. Zhang, P. Hiralal, A. Bello, G. Amaratunga and T. Hasan, *Carbon*, 2016, **105**, 33–41.
- M. Hartwig, R. Zichner and Y. Joseph, *Chemosensors*, 2018, **6**, 66.
- A. J. Bandodkar, I. Jeerapan and J. Wang, *ACS Sens.*, 2016, **1**, 464–482.
- M. Li, T. Chen, J. J. Gooding and J. Liu, *ACS Sens.*, 2019, **4**, 1732–1748.
- S. Han, X. Zhuang, W. Shi, X. Yang, L. Li and J. Yu, *Sens. Actuators, B*, 2016, **225**, 10–15.
- L. O. Pères, R. W. Li, E. Y. Yamauchi, R. Lippi and J. Gruber, *Food Chem.*, 2012, **130**, 1105–1107.
- K. Hassan, A. I. Uddin and G.-S. Chung, *Sens. Actuators, B*, 2016, **234**, 435–445.
- K. Hassan and G.-S. Chung, *Sens. Actuators, B*, 2017, **239**, 824–833.
- H. Zhang, Z. Wang, Q. Zhang, F. Wang and Y. Liu, *Biosens. Bioelectron.*, 2019, **124**, 184–190.
- C. Wu, F. Li, W. Wu, W. Chen and T. Guo, *Appl. Phys. Lett.*, 2014, **105**, 243509.
- K. Hassan, M. J. Nine, T. T. Tung, N. Stanley, P. L. Yap, H. Rastin, L. Yu and D. Losic, *Nanoscale*, 2020, **12**, 19007–19042.
- J. W. Hennek, Y. Xia, K. Everaerts, M. C. Hersam, A. Facchetti and T. J. Marks, *ACS Appl. Mater. Interfaces*, 2012, **4**, 1614–1619.
- C. N. Hoth, P. Schilinsky, S. A. Choulis and C. J. Brabec, *Nano Lett.*, 2008, **8**, 2806–2813.
- K. Pan, Y. Fan, T. Leng, J. Li, Z. Xin, J. Zhang, L. Hao, J. Gallop, K. S. Novoselov and Z. Hu, *Nat. Commun.*, 2018, **9**, 5197.
- T. T. Tung, M. T. Tran, J.-F. Feller, M. Castro, T. Van Ngo, K. Hassan, M. J. Nine and D. Losic, *Carbon*, 2020, **159**, 333–344.
- K. S. Novoselov, V. Fal, L. Colombo, P. Gellert, M. Schwab and K. Kim, *Nature*, 2012, **490**, 192.
- K. Pan, Y. Fan, T. Leng, J. Li, Z. Xin, J. Zhang, L. Hao, J. Gallop, K. S. Novoselov and Z. Hu, *Nat. Commun.*, 2018, **9**, 1–10.

[View Article Online](#)

## Paper

## Nanoscale

- 37 M. Singh, H. M. Haverinen, P. Dhagat and G. E. Jabbour, *Adv. Mater.*, 2010, **22**, 673–685.
- 38 J. A. Lim, W. H. Lee, H. S. Lee, J. H. Lee, Y. D. Park and K. Cho, *Adv. Funct. Mater.*, 2008, **18**, 229–234.
- 39 K. Hassan, A. I. Uddin and G.-S. Chung, *Int. J. Hydrogen Energy*, 2016, **41**, 10991–11001.
- 40 K. Hassan and G.-S. Chung, *Sens. Actuators, B*, 2017, **242**, 450–460.
- 41 M. Keiluweit, P. S. Nico, M. G. Johnson and M. Kleber, *Environ. Sci. Technol.*, 2010, **44**, 1247–1253.
- 42 I. Pastorova, R. E. Botto, P. W. Arisz and J. J. Boon, *Carbohydr. Res.*, 1994, **262**, 27–47.
- 43 D. Robinson, *Drug Dev. Ind. Pharm.*, 1989, **15**, 2597–2620.
- 44 O. Leenaerts, B. Partoens and F. Peeters, *Phys. Rev. B: Condens. Matter Mater. Phys.*, 2008, **77**, 125416.
- 45 V. Van Quang, V. N. Hung, V. N. Phan, T. Q. Huy and N. Van Quy, *Thin Solid Films*, 2014, **568**, 6–12.
- 46 T. T. Tung, M. J. Nine, M. Krebsz, T. Pasinszki, C. J. Coghlan, D. N. Tran and D. Losic, *Adv. Funct. Mater.*, 2017, **27**, 1702891.
- 47 P. Wei, H. Leng, Q. Chen, R. C. Advincula and E. B. Pentzer, *ACS Appl. Polym. Mater.*, 2019, **1**, 885–892.
- 48 K. Lundström, M. Shivaraman and C. Svensson, *J. Appl. Phys.*, 1975, **46**, 3876–3881.
- 49 G. Levita, P. Restuccia and M. C. Righi, *Carbon*, 2016, **107**, 878–884.

Electronic Supplementary Material (ESI) for Nanoscale.  
This journal is © The Royal Society of Chemistry 2021

### Supplementary Information

#### Graphene ink for 3D extrusion micro printing of chemo-resistive sensing devices for volatile organic compounds detection

Kamrul Hassan,<sup>a,b</sup> Tran Thanh Tung,<sup>a,b</sup> Nathan Stanley,<sup>a,b</sup>, Pei Lay Yap,<sup>a,b</sup> Farzaneh Farivar,<sup>a,b</sup> Hadi Rastin,<sup>a,b</sup> Md Julker Nine<sup>a,b</sup> and Dusan Losic<sup>a,b\*</sup>

<sup>a</sup>*School of Chemical Engineering and Advanced Materials, The University of Adelaide, Adelaide, SA 5005, Australia*

<sup>b</sup>*ARC Research Hub for Graphene Enabled Industry Transformation, The University of Adelaide, Adelaide, SA 5005, Australia*

**Contact angle measurement:**

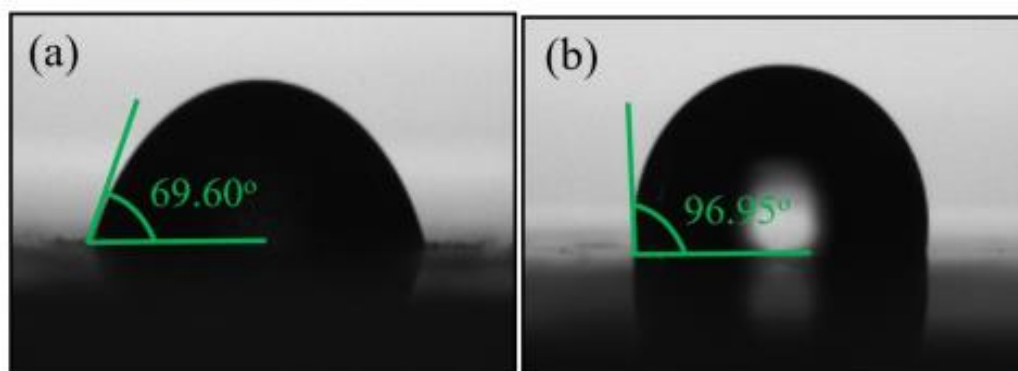


Fig. S1. Contact angle measurement of printed graphene ink (c) before annealing, and (d) after annealing at 250 °C temperature.



Table S1. Contact angles and calculated surface energy of printed graphene ink (a) before annealing and (b) after annealing at 250 °C temperature.

Sample	Contact angle (°)	Owens–Wendt method <sup>25</sup>			Wu method <sup>26</sup>		
		$\gamma_{sv}^D$ (mN/m)	$\gamma_{sv}^D$ (mN/m)	$\gamma_{sv}^P$ (mN/m)	$\gamma_{sv}^D$ (mN/m)	$\gamma_{sv}^D$ (mN/m)	$\gamma_{sv}^P$ (mN/m)
Graphene ink (before annealing)	69.60	97.45	43.58	54.27	108.69	56.83	51.84
Graphene ink (after annealing)	96.95	96.95	0.005	0.005	-3.8	-0.98	-2.05

Table S2. Surface area and surface volume calculation for 3D printed sensor and conventional sensor.

<i>For 3D printed sensor:</i>	<i>For conventional sensor (non-printed):</i>
<p>No of printed line=13,</p> <p>Length (L) =6.60 mm,</p> <p>width (d) = 0.6 mm,</p> <p>average thickness (<math>T_{avg}</math>) = 15 <math>\mu</math>m = 0.015 mm</p> <p>Active area <math>_{eff}</math> (<math>A_{printed\ sensor}</math>)  <math>= N \times (L \times d)</math>  <math>= 13 \times (6.60 \times 0.6)</math>  <math>= 51.48\ mm^2</math></p>	<p>No of spherical curve (drop cast) = 1,</p> <p>radius (r) =2.5 mm,</p> <p>average thickness (<math>T_{avg}</math>) = 145 <math>\mu</math>m = 0.145 mm</p> <p>Active area <math>_{eff}</math> (<math>A_{printed\ sensor}</math>)  <math>= N \times \pi r^2</math>  <math>= 1 \times (3.1415 \times (2.5)^2)</math>  <math>= 19.625\ mm^2</math></p>
<p>Active volume <math>_{eff} = Active\ area\ _{eff} \times T_{Avg}</math>  <math>= 51.48 \times 0.015</math>  <math>= 0.7722\ m^3</math></p>	<p>Active volume <math>_{eff} = Active\ area\ _{eff} \times T_{Avg}</math>  <math>= 19.625 \times 0.145</math>  <math>= 2.845\ m^3</math></p>
<p>SA:V = Active area <math>_{eff}</math> / Active volume <math>_{eff}</math>  <math>= 51.48 / 0.7722 = \mathbf{66.66}</math></p>	<p>SA:V = Active area <math>_{eff}</math> / Active volume <math>_{eff} =</math>  <math>19.625 / 2.845 = \mathbf{6.91}</math></p>

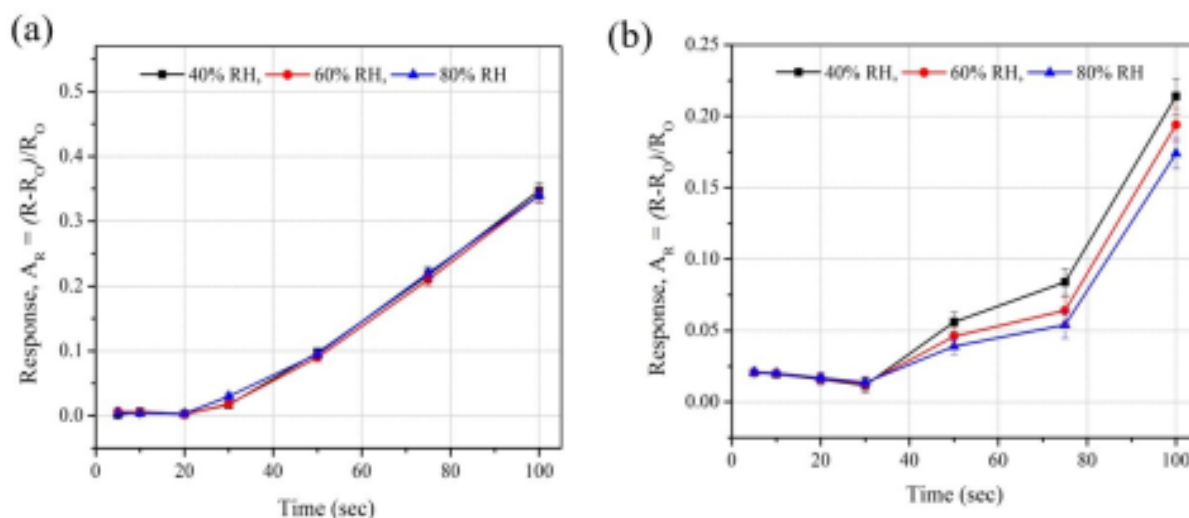
**Humidity effect:**

Fig. S2. Transient response of printed sensors to (a) methanol and (b) acetone vapour under different humidity at room temperature (20 °C).

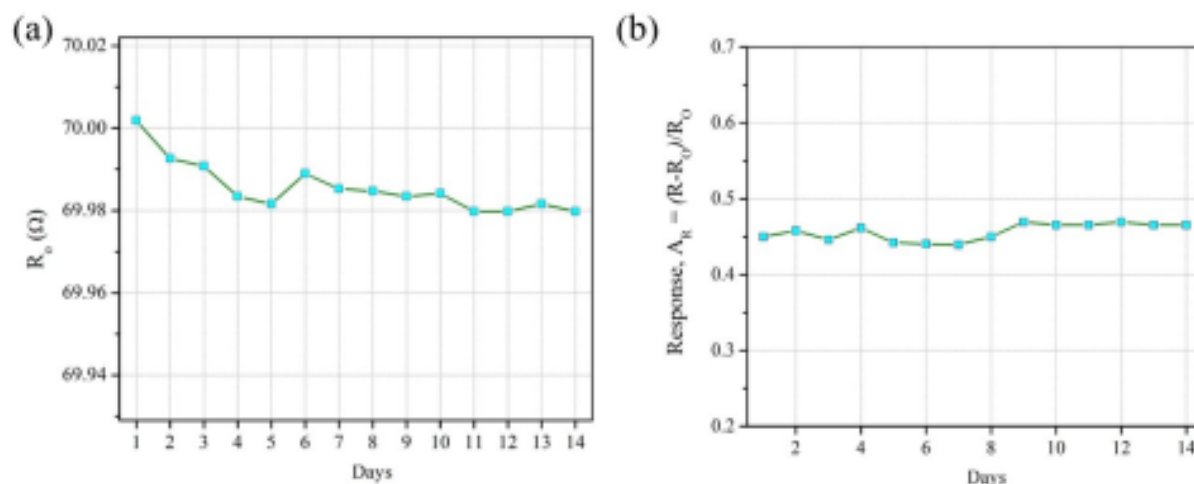
**Sensor stability and durability:**

Fig. S3. Time reliance of the printed sensor (c) baseline resistance value and (d) response value, monitored over a fourteen-day period, where on each day the printed sensor was exposed to saturated ethanol biomarkers at room temperature (20 °C).

# Chapter 4

## Development of fractal designed VOC sensors

In this chapter, fractal designed sensors are presented that is printed by an extrusion process on a flexible substrate (PET) using specially formulated graphene ink as a sensing material, which provided significant enhancement of the active surface area to volume ratio and allowed high-resolution fractal patterning along with a reduced current transportation path. To demonstrate the advantages and influence of fractal geometry on sensor performance, here, three different kinds of sensors were fabricated based on different fractal geometrics and the sensing performance was explored toward different VOC analytes. Among all these fractal-designed sensors including interdigitate sensors, the Hilbert designed printed sensor shows enhanced sensing properties for ethanol at room temperature (20 °C). Moreover, a significant improvement of this sensor performance is observed by applying the mechanical deformation technique. The practical application of this sensor is also successfully demonstrated by monitoring food spoilage using a commercial box of strawberries as a model.

This chapter has been published as research paper in “ACS Sensors” journal as follows:

“**Hassan K**, Tung TT, Yap PL, Rastin H, Stanley N, Nine MJ, Losic D. Fractal Design for Advancing the Performance of Chemoresistive Sensors. *ACS Sensors*. 2021;**13**, 5356-5368”

## Statement of Authorship

Title of Paper	Fractal design for advancing performance of chemo-resistive sensors		
Publication Status	<input checked="" type="checkbox"/> Published	<input type="checkbox"/> Accepted for Publication	
	<input type="checkbox"/> Submitted for Publication	<input type="checkbox"/> Unpublished and Unsubmitted work written in manuscript style	
Publication Details	Hassan K, Tung TT, Yap P.L, Rastin H, Stanley N, Nime MJ, Losic D, Fractal design for advancing performance of chemo-resistive sensors, ACS Sensors, 2021, 6, 3685-3695		

### Principal Author

Name of Principal Author (Candidate)	Kamrul Hassan		
Contribution to the Paper	Prepared, edited and revised the review manuscript.		
Overall percentage (%)	85%		
Certification:	This paper reports on original research I conducted during the period of my Higher Degree by Research candidature and is not subject to any obligations or contractual agreements with a third party that would constrain its inclusion in this thesis. I am the primary author of this paper.		
Signature		Date	19/10/2021

### Co-Author Contributions

By signing the Statement of Authorship, each author certifies that:

- i. the candidate's stated contribution to the publication is accurate (as detailed above);
- ii. permission is granted for the candidate to include the publication in the thesis; and
- iii. the sum of all co-author contributions is equal to 100% less the candidate's stated contribution.

Name of Co-Author	Tran Thanh Tung		
Contribution to the Paper	Co-supervised and revised the manuscript.		
Signature		Date	26/10/2021

Name of Co-Author	Pei Lay Yap		
Contribution to the Paper	Edited and revised the manuscript.		
Signature		Date	26/10/21

Please cut and paste additional co-author panels here as required.

## Statement of Authorship

Title of Paper	Fractal design for advancing performance of chemo-resistive sensors
Publication Status	<input checked="" type="checkbox"/> Published <input type="checkbox"/> Accepted for Publication <input type="checkbox"/> Submitted for Publication <input type="checkbox"/> Unpublished and Unsubmitted work written in manuscript style
Publication Details	Hassan K, Tung TT, Yap P.L, Rastin H, Stanley N, Nire MJ, Losic D. Fractal design for advancing performance of chemo-resistive sensors, ACS Sensors, 2021, 6, 3885-3895

### Principal Author

Name of Principal Author (Candidate)	Kamrul Hassan
Contribution to the Paper	Prepared, edited and revised the review manuscript.
Overall percentage (%)	85%
Certification:	This paper reports on original research I conducted during the period of my Higher Degree by Research candidature and is not subject to any obligations or contractual agreements with a third party that would constrain its inclusion in this thesis. I am the primary author of this paper.
Signature	<div style="border-bottom: 1px solid black; width: 100%;"></div>
Date	19/10/2021

### Co-Author Contributions

By signing the Statement of Authorship, each author certifies that:

- i. the candidate's stated contribution to the publication is accurate (as detailed above);
- ii. permission is granted for the candidate to include the publication in the thesis; and
- iii. the sum of all co-author contributions is equal to 100% less the candidate's stated contribution.

Name of Co-Author	Hadi Rastin
Contribution to the Paper	Edited and revised the manuscript.
Signature	<div style="border-bottom: 1px solid black; width: 100%;"></div>
Date	29.10.2021

Name of Co-Author	Nathan Stanley
Contribution to the Paper	Edited and revised the manuscript.
Signature	<div style="border-bottom: 1px solid black; width: 100%;"></div>
Date	28.10.2021

Please cut and paste additional co-author panels as required.

## Statement of Authorship

Title of Paper	Fractal design for advancing performance of chemo-resistive sensors		
Publication Status	<input checked="" type="checkbox"/> Published	<input type="checkbox"/> Accepted for Publication	
	<input type="checkbox"/> Submitted for Publication	<input type="checkbox"/> Unpublished and Unsubmitted work written in manuscript style	
Publication Details	Hassan K, Tung TT, Yap P.L, Raslin H, Stanley N, Nine MJ, Losic D, Fractal design for advancing performance of chemo-resistive sensors, ACS Sensors, 2021, 6, 3695-3695		

### Principal Author

Name of Principal Author (Candidate)	Kamrul Hassan		
Contribution to the Paper	Prepared, edited and revised the review manuscript.		
Overall percentage (%)	85%		
Certification:	This paper reports on original research I conducted during the period of my Higher Degree by Research candidature and is not subject to any obligations or contractual agreements with a third party that would constrain its inclusion in this thesis. I am the primary author of this paper.		
Signature		Date	19/10/2021

### Co-Author Contributions

By signing the Statement of Authorship, each author certifies that:

- i. the candidate's stated contribution to the publication is accurate (as detailed above);
- ii. permission is granted for the candidate to include the publication in the thesis; and
- iii. the sum of all co-author contributions is equal to 100% less the candidate's stated contribution.

Name of Co-Author	Md Julker Nine		
Contribution to the Paper	Edited and revised the manuscript.		
Signature		Date	01-11-2021

Name of Co-Author	Dusan Losic		
Contribution to the Paper	Supervised the development of work, edited, revised the manuscript and acted as the corresponding author.		
Signature		Date	26 Oct 2021

Please cut and paste additional co-author panels here as required.



pubs.acs.org/acssensors

Article

## Fractal Design for Advancing the Performance of Chemoresistive Sensors

Kamrul Hassan, Tran Thanh Tung, Pei Lay Yap, Hadi Rastin, Nathan Stanley, Md. Julker Nine, and Dusan Losic\*

Cite This: <https://doi.org/10.1021/acssensors.1c01449>

Read Online

ACCESS |

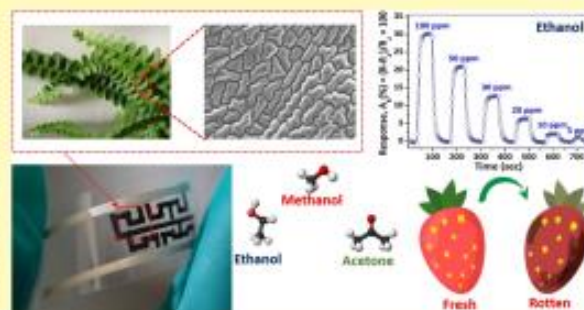
Metrics &amp; More

Article Recommendations

Supporting Information

**ABSTRACT:** The rapid advancement of internet of things (IoT)-enabled applications along with connected automation in sensing technologies is the heart of future intelligent systems. The probable applications have significant implications, from chemical process monitoring to agriculture, mining, space, wearable electronics, industrial manufacturing, smart cities, and point-of-care (PoC) diagnostics. Advancing sensor performance such as sensitivity to detect trace amounts (ppb–ppm) of analytes (gas/VOCs), selectivity, portability, and low cost is critical for many of these applications. These advancements are mainly achieved by selecting and optimizing sensing materials by their surface functionalization and/or structural optimization to achieve favorable transport characteristics or chemical binding/reaction sites. Surprisingly, the sensor geometry, shapes, and patterns were not considered as critical parameters, and most of these sensors were designed by following simple planar and interdigitated electrode geometry. In this study, we introduce a new bioinspired fractal approach to design chemoresistive sensors with fractal geometry, which grasp the architecture of fern leaves represented by the geometric group of space-filling curves of fractal patterns. These fractal sensors were printed by an extrusion process on a flexible substrate (PET) using specially formulated graphene ink as a sensing material, which provided significant enhancement of the active surface area to volume ratio and allowed high-resolution fractal patterning along with a reduced current transportation path. To demonstrate the advantages and influence of fractal geometry on sensor performance, here, three different kinds of sensors were fabricated based on different fractal geometries (Sierpinski, Peano, and Hilbert), and the sensing performance was explored toward different VOC analytes (e.g., ethanol, methanol, and acetone). Among all these fractal-designed sensors including interdigitate sensors, the Hilbert-designed printed sensor shows enhanced sensing properties in terms of fast response time (6 s for 30 ppm), response value (14%), enhanced detection range (5–100 ppm), high selectivity, and low interference to humidity (up to RH 80%) for ethanol at room temperature (20 °C). Moreover, a significant improvement of this sensor performance was observed by applying the mechanical deformation (positive bending) technique. The practical application of this sensor was successfully demonstrated by monitoring food spoilage using a commercial box of strawberries as a model. Based on these presented results, this biofractal biomimetic VOC sensor is demonstrated for a prospective application in food monitoring.

**KEYWORDS:** graphene ink, extrusion printing, bioinspired fractal design, printed sensor, VOC detection, food monitoring



Printed electronics offer a fascinating opportunity for innovative fabrication of large-scale, low-cost, flexible, and portable devices, with micron- to nanoscale dimensions.<sup>1</sup> This technology is applicable to advances in a vast number of varied applications such as energy storage devices (supercapacitors),<sup>2</sup> digital displays,<sup>3</sup> sensors for medical diagnostics, ambient condition monitoring, and food control.<sup>4,5</sup> Printing approaches, including screen, gravure, inkjet, flexographic, and extrusion processes have been fruitfully adopted to convey additive patterning of a functional ink material onto conformable, flexible, and/or rigid substrates that promises high-speed, large-scale, and low-cost production.<sup>6</sup> Key elements of these printing methods are liquid-phase con-

ductive/nonconductive inks having considerably various physical characteristics such as rheological properties (surface tension and viscosity) and concentration of fillers and/or additives. Numerous conductive fillers have been used for formulating the printable ink including carbon particles, carbon nanotubes, metal nanoparticles, metal oxides, conductive

Received: July 8, 2021

Accepted: September 29, 2021

polymers, and graphene.<sup>6</sup> Among them, graphene (Gr) has become a leading contender for printed nonflexible/flexible electronics (e.g., sensors) and a good substitute to metal-based printable inks owing to its exceptional thermal, electrical, and mechanical characteristics with a remarkable carrier mobility ( $2 \times 10^5 \text{ cm}^2 \text{ V}^{-1} \text{ cm}^{-2}$ ).<sup>7–9</sup> Graphene inks with different formulations and characteristics have been reported previously for the fabrication of patterned architectures with various resolutions using screen and gravure printing,<sup>10</sup> spray printing,<sup>11,12</sup> inkjet printing,<sup>13</sup> and flexographic methods. These have been successfully practiced to fabricate several electronic devices including supercapacitors,<sup>14</sup> organic thin-film transistor electrodes,<sup>15</sup> radio frequency identification devices,<sup>16</sup> chemical, temperature, and volatile organic compound (VOC) sensors,<sup>17</sup> and solar cells.<sup>18</sup> Even though a considerable enhancement has been made, the formulation of graphene inks that fulfill the printing and device characteristic criteria for these applications and especially for sensing remains a challenge.

The implementation of chemical vapor (e.g., gas and VOCs) sensors increasing at a growth rate of around 8% per annum is predicted to concur an approximately USD 41 billion market share universally by 2024.<sup>19</sup> The incorporation of gas and VOC sensors with wearable microelectronics will be a primary driving influence in this global market evolution, linked with industry, medical, space, defense, and environmental sectors.<sup>20</sup> Particularly, new-generation VOC sensors are gaining remarkable attention from both academia and the industry sector.

The advancement of lightweight, cheap, and friendly sensors with superior selectivity, sensitivity, stability, reproducibility, and miniaturization features is still in great demand. In order to address these requirements and advance sensing performances, most studies were focused on exploring new sensing materials, in particular using nano/microscale materials with different low-cost fabrication techniques. Nevertheless, there was less focus on designing sensing devices. Until now, several advanced devices have been reported based on nanoscale metal/metal oxides,<sup>21,22</sup> conductive polymers,<sup>23,24</sup> and nanocomposites.<sup>7</sup> Majority of these sensors are fabricated by following simple and inexpensive methods including dip<sup>8</sup> and spin<sup>9,25</sup> coating and drop casting, which offer low-cost and simple, however, sensing variation and possible unrealizable signals as a consequence of the uncontrolled fabrication processes. Most of the chemoresistive sensors were designed as interdigitated or planar electrodes, and surprisingly, there was a limited number of studies exploring to use different patterns and sensing geometries to improve sensing performances. That is why a new approach and paradigm shift for designing more advanced sensing devices considering optimizing their geometries are needed. The best approach toward these goals is to learn and translate nature's concepts with unique hierarchical, morphological, and structural features created to achieve complex properties and biological functions. Fractal geometries of nature introduced Mandelbrot's masterpiece, which has originated a novel epistemological art work for understanding real life along with the natural universe in a way that evades any subjective sight. The fractal geometry could supply a coherent explanation of the design principles underlying living organisms and the function of many organs such as brain, nervous, blood, and bone systems and be used for creating artificial systems and devices. There are several examples of implementing fractal concepts in engineering new devices such as stretchable electronics,<sup>26</sup> optoelectronics,<sup>27</sup> antennas and

supercapacitors,<sup>28</sup> composites, and so forth but surprisingly not in sensing field.

In this study, we demonstrate that the concept of fractal geometry can be successfully exploited in chemical sensors with significant functional consequences in advancing their sensing performances. We used a fractal approach to design and fabricate chemoresistive VOC sensors with several fractal space-filling patterns using a graphene-based ink as a sensing material and extrusion printing technique. To prove the fractal-based concept for advancing sensing performances of chemoresistive sensors, we selected to explore three fractal patterns (Sierpinski, Peano, and Hilbert) schematically presented in Figure 1. The ubiquitous VOC sensor is designed by following

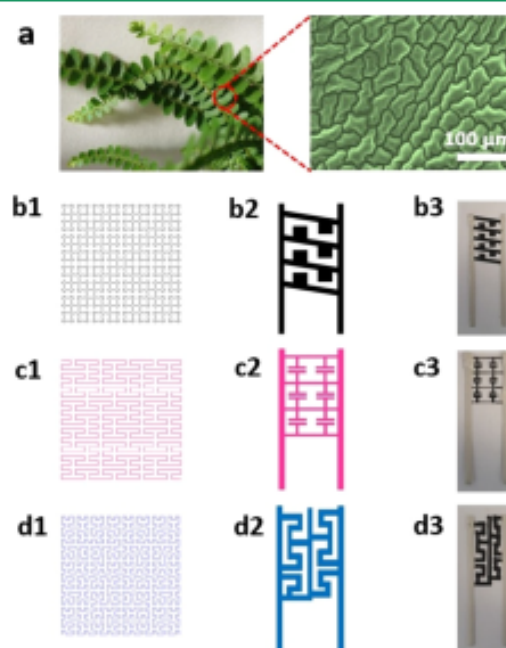


Figure 1. Concept of bio-inspired fractal sensor designs for VOC detection. (a) Optical photograph of fern leaves with the highlighted internal structure by the SEM micrograph. (b1–b3) Sierpinski space-filling design, (c1–c3) Peano space-filling design, and (d1–d3) Hilbert space-filling design. (From the left: the first column shows the space-filling curves,<sup>28</sup> the second column shows the design of the printed sensors, and the third column shows the images of the fabricated extrusion-printed sensors.) Figure (b1,c1,d1) reproduced with permission from ref 28 Copyright (2017) Springer Nature.

the internal structure of fern leaves (*Polystichum munition*), which resembles the fractal space-filling curve patterns.<sup>29</sup> Fractal-based space-filling architectures can be characterized by self-similarity: subdivision into small segments yields sections with mathematical geometries that present wholly, and the active, geometric surface area was also calculated by considering the pore size along with the thickness of the printed pattern. This elevated surface area to volume (SA/V) ratio for a patterned sensor enhanced the relative exposure and pressure of different VOC analytes on the sensing material surface that increases the sensing efficiency. To fabricate these fractal patterns, we used graphene-based ink formulated with a cellulose-derived binder and dihydrolevoglucosenone (Cyrene) through extrusion printing technique, which allows us to fabricate printed 3D structures with a high SA/V aspect ratio.<sup>30</sup> It is worth noting that our formulated graphene ink is



nontoxic, environmentally friendly, sustainable, and nonflammable with controllable viscosity and high conductivity and provides higher graphene ink loading that is suitable for extrusion printing and large-scale production.<sup>31</sup>

Sensing performances of fabricated sensors with different fractal patterns were characterized at room temperatures (20 °C) for VOC detection of several gases including influence of their mechanical deformation (bending). Results from this study showed that the fractal concept can be successfully used to advance sensing performances and open up the window for low-cost, controllable, and scalable fabrication of printed architectures with a higher surface area to volume (SA/V) aspect ratio, higher sensitivity, fast response time, broad detection range, and superior selectivity for real-life applications.

## EXPERIMENTAL SECTION

**Production and Dispersion of Graphene.** Pristine graphene (pG) (600 mg), supplied by First Graphene Ltd. (Australia) with a sheet size of  $\sim 5 \mu\text{m}$ , was dispersed in 4% w/v ethyl cellulose (EC) (Aldrich, viscosity 10 cP) in a mixed volume ratio of 80:20 of toluene: ethanol (600 mL) in a steel beaker. Using a high-shear mixer system (Silverson L5M), the dispersion was mixed for 55 min at 10,000 rpm within an ice bath cooling system. Subsequently, the dispersion was ultrasonicated using a probe sonication system (Fisher Scientific Sonic Dismembrator model 500, 13 mm Branson tip) in an ice bath for 55 min at 80 W. An aqueous solution of sodium chloride (NaCl, 0.08 g/mL, Sigma-Aldrich, >99.5%) was added to this dispersion in a 1:2 volume ratio. The resulting pG/EC solid was washed with deionized (DI) water and separated by centrifugation at 4200 rpm over 35 min to remove the residual NaCl. The resulting pG/EC product was dried in a vacuum oven for 18 h, yielding 350 mg of a fine powdery black product.

**Synthesis of Graphene Ink and Characterization.** The pG/EC ink for 3D extrusion printing was formulated through incorporation of pG into the EC matrix by a combination of sonication and solvent exchange, as reported earlier with slight modification.<sup>30</sup> Briefly, pG and EC powder was dispersed in an 85:15 isopropanol/cyrene solution at a concentration of 0.9 wt % through sonication. Removal of the isopropanol from the isopropanol/Cyrene solution was performed by a solvent exchange procedure via a rotary evaporation system under vacuum. Subsequently, the remaining pG/EC/Cyrene dispersion was collected from the rotary evaporation system. In comparison to the primary isopropanol/Cyrene dispersion, the concentration of pG/EC was about 50 times higher in the final Cyrene dispersion. This pG/EC/Cyrene (concentrated) dispersion was used as a printable ink and directly applied for extrusion printing.

**3D Extrusion Printing of Bioinspired Fractal Patterns and Printed Sensor Fabrication.** Sensing devices for VOC sensing were fabricated by direct 3D extrusion printing of graphene ink onto a PET substrate. The new concepts of nature-inspired fractal-based design including Sierpinski space-filling design, Peano space-filling design, and Hilbert space-filling designs were used to make transducer electrodes to overcome the limitations of conventional ones. Thin traces of silver (Ag) ink (width  $\sim 300 \mu\text{m}$ ) were printed on a PET substrate using a 3D extrusion printer to connect to the negative and positive electrodes. The as-synthesized inks were then printed according to the bioinspired design on the prepatterned Ag using a 3D extrusion printer (V-One) with a three-axis motion control scheme along with  $1 \mu\text{m}$  positioning resolution. A nozzle with  $225 \mu\text{m}$  inner diameter was used to pattern the graphene inks. The speed of the nozzle was set at  $400 \text{ mm min}^{-1}$ , and the nozzle to substrate distance was changed from 50 to  $100 \mu\text{m}$ . Two slips of copper (Cu) tape were attached to the top of the Ag electrodes as connectors to avoid the Ag trace from being scratched by flat wire clamps and to establish electrical connection to the electrochemical workstation for sensor characterizing.

**Material Characterizations.** A scanning electron microscope (SEM-FEI QUANTA 450) operated at 20 kV voltage was used to analyze the morphological characteristics of pure pristine graphene (pG) and composite materials [samples coated with 3 nm sputtered platinum (Pt)]. Transmission electron microscopy (TEM) was conducted on a TECNAI 20 microscope operated at 120 kV. Thermal gravimetric analysis (TGA) was carried out on a TGA/DSC-2 Star system (Mettler Toledo) with a heating rate of  $10 \text{ }^\circ\text{C/min}$  in supplied air. The shear viscosity of the formulated ink was measured using a Physica MCR 302 rheometer equipped with a 50 mm cone and plate geometry at shear rates of  $1\text{--}1000 \text{ s}^{-1}$ . For viscosity measurement, the temperature was maintained using a Peltier plate. Rheological characteristics of the inks were obtained in the oscillation mode by calculating  $G'$  and  $G''$  over time. In this procedure, repetitive strain ranging from 1 to 50% was induced on the ink samples, and the response value of the sample to the induced strain was traced over four cycles. To analyze the electrical properties of the ink, materials (in a film manner) were blade-coated onto glass substrates and annealed in an air oven system with variation of the temperature and annealing time.

**VOC Sensor Characterizations.** For VOC-sensing measurement, each bioinspired designed graphene-based sensor was placed in the center of a U-shaped support stand under ambient conditions (open air). The sidewall of the support stand was moved in the horizontal direction (left and right) to adjust and vary the bending radius (1–5 mm) of the sensor. Using an electrochemical workstation (CH Instruments), the relative resistance response ( $A_R$ ) of the sensor was recorded. To ensure the flow of target VOCs, a narrow tube was placed on the top of the sensor device. The VOC-sensing characteristics of the printed sensors were characterized by recording the chemoresistive response upon exposure to VOC vapor and synthetic air formed through a bubbler system, in which the concentration of the mixture was controlled by varying the synthetic air flow rate from 200 to  $4 \text{ mL min}^{-1}$  through 100% liquid VOCs (e.g., ethanol, methanol, and acetone) at room temperature (20 °C). Using the following equation, the VOC concentration was measured and controlled<sup>32</sup>

$$\text{VOC}_{\text{conc}} (\text{ppm}) = \frac{\text{flow rate}_{\text{voc}} + \text{flow rate}_{\text{air}}}{\text{total flow rate}}$$

All as-fabricated sensors were tested under ambient conditions. The sensor response ( $A_R$ ) was defined by the following equation

$$A_R (\%) = \frac{(R - R_0)}{R_0} \times 100 \quad (1)$$

where  $R_0$  is the initial resistance ( $\Omega$ ) in air and  $R$  is the resistance of the sensing materials when exposed to the analyte (VOC vapor). The response–recovery time characteristics of the bioinspired VOC sensor were calculated as the time to reach 90% of the total resistance change. The relative humidity (RH) of experimental conditions was varied from RH=40% to RH=80% using a water bubbler controller and measured using a hygrometer (Testo-625). An optical photograph of the experimental setup for VOC-sensing characterizations is depicted in Figure S1.

**Demonstration of the Practical Sensor Module.** The core of the sensor module was an analogue comparator module (LM 393) that includes a microcontroller and variable resistor to set the cutoff value to signal through an LED indicator. This sensor module was connected to a printed sensor using two flat clamps. To perform real-time data monitoring, the sensor module including the printed sensor was connected to a sealed plastic box containing  $\sim 250 \text{ g}$  of fresh strawberries (eight in total) and also connected with the electrochemical workstation (CH Instrument). The sensor was placed with positive bending deformation (3 mm bending radius) on the top of one hole of the box and kept for real-time data logging. Cumulative data were collected from day 0 to 7 using this setup to monitor the quality of these strawberries.

C

<https://doi.org/10.1021/acssensors.1c01449>  
ACS Sens. XXXX, XXX, XXX–XXX

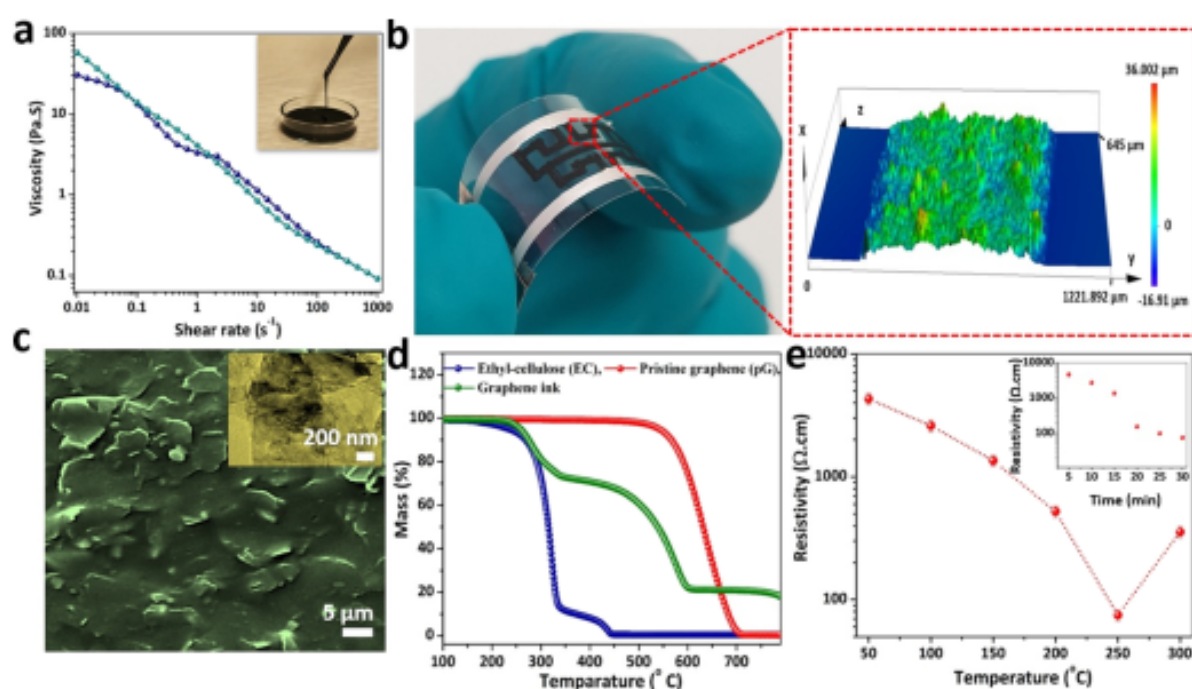


**Figure 2.** (a) Rheological characteristics of graphene inks such as viscosity as a function of shear rate (the inset shows the optical image of the formulated viscous graphene ink). (b) Optical image of the graphene ink-based extrusion printed sensor (the enlarged diagram shows the 3D profile map of the representative printed line). (c) SEM micrograph of graphene ink (the inset shows the TEM micrograph of graphene sheets). (d) TGA analysis of different ingredients of graphene ink. (e) Electrical resistance characteristics of the graphene inks showing resistivity vs annealing temperature of blade-coated films for an annealing time of 30 min (the inset shows the resistivity vs annealing time of the fabricated films at a fixed annealing temperature of 250 °C).

## RESULTS AND DISCUSSION

### Concept of Fractal Design for Chemoresistive VOC

**Sensors.** To demonstrate a concept of fractal design for advancing chemoresistive sensors, we considered several designs, which are good mathematical modeling and used for practical applications such as stretchable electronics,<sup>33</sup> supercapacitors,<sup>28</sup> and so forth. According to its history, the mathematical concept of fractal-designed space-filling curves is mainly generated by the “Cantor set”, designed in 1874 by Henry John Stephen Smith and reported by German mathematician Georg Cantor in 1883, where he defined every curve that passes through each point of an  $n$ -dimensional region.<sup>34</sup> Based on this mathematical concept, in this study, we constructed the space-filling curve by counting a regular function “ $b$ ” from the Cantor space “ $c$ ” onto every unit interval  $\{0, 1\}$ .<sup>34</sup> The outcomes in the formation of regular function “ $B$ ” from the topological product “ $c \times c$ ” onto the entire unit square  $\{0, 1\} \times \{0, 1\}$  by calculating

$$B(x, y) = (b(x), b(y)) \quad (2)$$

where the Cantor space is denoted as  $2^N$  and the base “2” represents the 2-elemental set of  $\{0, 1\}$ . It also defines the infinite topological product of the discrete 2-point space  $\{0, 1\}$ . Among several most popular cases of the space-filling curve family, we selected three cases such as Hilbert fractals<sup>35</sup> (Figure 1b), Peano fractals<sup>36</sup> (Figure 1c), and Sierpinski fractals<sup>37</sup> (Figure 1d) for this study and proved the proposed concept of using fractal design for advancing chemoresistive sensor performances. Initially, we explored the active sensing area mathematically by counting the dimension of the space-filling curves and later characterized by calculation of their

Hausdorff dimension in order to reveal their key geometric, surface area, and SA/V aspect ratio features.<sup>38</sup>

Theoretically, these designs are based on the linear equations in the iteration method with a dimensionality denoted by the Hausdorff dimension ( $D$ ), which is the measure of the local size of a set of numbers, and calculated by the box-counting method.<sup>39,40</sup> The relationship between the linear scaling ( $L$ ), the Hausdorff dimension ( $D$ ), and the resulting size ( $S$ ) for a 2D object plane having generalized as width, length, and height can be described by the following equation

$$D = \lim_{L \rightarrow 0} \log(S)/\log(L) \quad (3)$$

From the iteration of eq 3, we found that among the three designed fractals, the Hilbert fractal design has the highest dimension of 1.73, which is closest to the dimension found in the structure of fern leaves (Figure S2). Inspired by these space-filling fractal patterns, we designed fractal chemoresistive sensors for VOC biomarker detection and compared their performance with conventional interdigitated geometry.

### Optimization of Graphene Inks for Extrusion Printing

**of Fractal Sensors.** Figure 2a demonstrates the viscosity as a function of the shear rate for the formulated graphene ink, which was measured at room temperature (20 °C). It was evident that the ink formulation for extrusion printing is driven by the rheological property of the printable ink such as surface tension and viscosity.<sup>41</sup> The viscous ink was successfully dispersed in Cyrene with a final viscosity of 50–60 Pa·s, which is within the common viscosity region (10–100 Pa·s) suitable for the technology of extrusion printing. Moreover, the storage modulus ( $G'$ ) of the graphene ink was lower than the loss

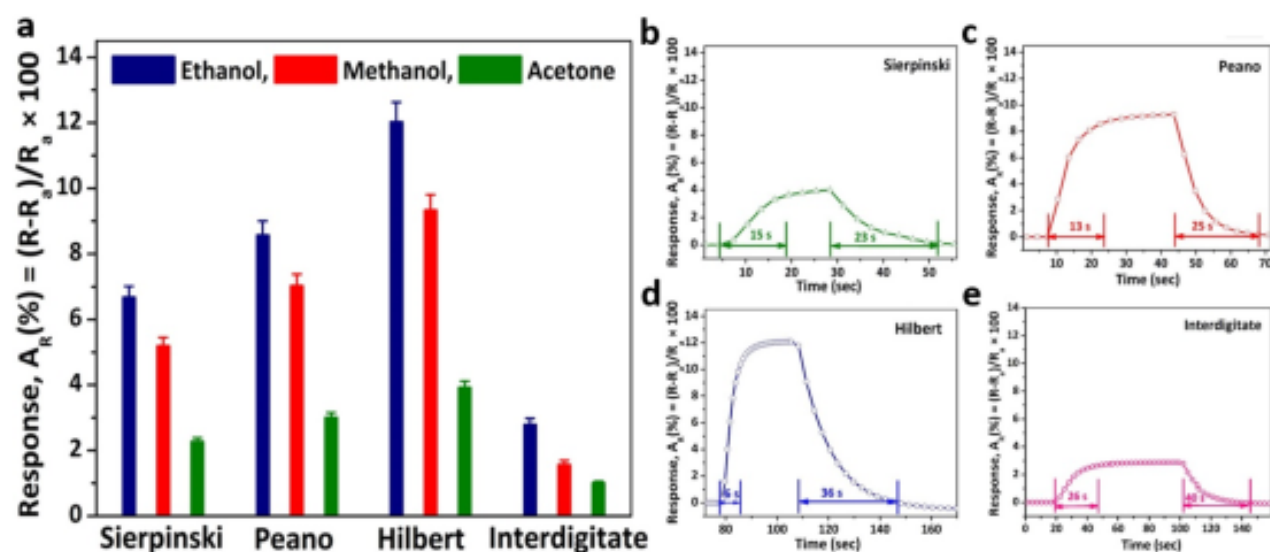


Figure 3. (a) Comparative transient response  $A_R$  (%) of bioinspired fractal-designed printed sensors exposed to 30 ppm VOC analytes at RT (20 °C). Response–recovery time characteristics of (b) Sierpinski, (c) Peano, (d) Hilbert, and (e) conventional interdigitate sensors to 30 ppm ethanol vapor at RT.

modulus ( $G''$ ), confirming the fluidic state of the ink at both low and high strain (Figure S3). The thixotropic characteristics including the storage modulus ( $G'$ ) and loss modulus ( $G''$ ) decreased rapidly and returned to their initial states after removing the additional load. This indicates the recovery characteristics of the printable graphene ink, which was successfully demonstrated to print the proposed fractal on a PET substrate via an extrusion printer nozzle and the speed of printing.

Figure 2b illustrates that the extrusion printing of Hilbert-designed graphene ink patterns on PET yielded a line width of  $\sim 760.6 \mu\text{m}$ . The uniform 3D dome-shaped cross-sectional profile across the printed pass marked the successful ink formulation of graphene ink for the 3D extrusion printer, which was observed for all printed patterns with a thickness (average) of  $20 \mu\text{m}$  (Figure S4). This dome morphology of the printed passes was attributed to the solvent evaporation during the annealing process, which causes inward Marangoni flow recognized by the surface tension gradient.<sup>42</sup> Moreover, the coffee ring effect was suppressed over the printed patterns due to the Marangoni flow that also homogenizes the droplet compositions.<sup>42,43</sup> In addition, the  $sp^2$  bonding along with the small lateral size of the graphene flakes ( $\sim 5 \mu\text{m}$ ) restricts the folding and/or buckling of the printed flakes that stimulates low surface roughness and flake to flake contacts.

Morphological features of Cyrene-based graphene ink were characterized using scanning electron microscopy (SEM) and TEM (Figure 2c). From Figure 2c, the surface of the graphene flakes is smooth due to the encapsulated graphene flakes within the polymeric binder (EC) and Cyrene. Ordinarily, bare pG tends to curl up easily along with the poor adhesion between the flakes due to the random flake to flake stacking. Subsequently, gaps (appearing as dark holes) can be observed in between the flakes, which causes relatively large sheet resistance due to the emergence of electron flow between the tips and edges of the flakes. Consequently, the use of a polymeric binder (EC) is a very effective way to reduce the sheet resistance between the flakes and avoid the degradation of contact quality (Figure S5a). Moreover, polymeric binder

(EC) also reduces the sheet resistance between the graphene flakes by eliminating the gaps via formation of a condensed structure (Figure S5b). However, the elliptical spots (black hole) still remained because of the condensed pG and EC structure, which was further overcome in the final ink formation by addition of Cyrene. This environmentally friendly solvent helps encapsulated graphene flakes (inset of Figure 2c) to pile sequentially with face to face contacts that reduced the total sheet resistance.

Figure 2d displays the TGA of bare pG, EC, and graphene ink, indicating the thermal decomposition of EC initiated at 200 °C with no residue found above 400 °C. On the other hand, pG fully decomposed above 700 °C. For graphene ink, it is notable that EC decomposition occurred in two stages: first, charring begins at  $>250$  °C, and second, the intermediates are volatilized with the removal of all residues at  $\geq 400$  °C. In graphene ink, the decomposition threshold of EC shifted from lower to higher temperatures due to the presence of graphene flakes. This examination coupled with the electrical conductivity characterized after annealing at temperatures of 250–350 °C suggested that the primary decomposition of EC progresses the graphene flake to flake contact that permits efficient charge transport via the graphene network.

Figure 2e illustrates that films annealed at a temperature of 250 °C for 30 min illustrated high electrical conductivity compared with other tested annealing temperatures. Besides, resistivity was increased for coated films at above 300 °C due to the initial vaporization of EC, which causes the elliptical spots in between the graphene network. At 250 °C, annealing for just 30 min was optimal to acquire low resistivity (inset of Figure 2e) because of the initial decomposition of EC (not initiated by the vaporization), which improves the contact between the graphene flakes and enhanced the charge transport mobility. Another explanation behind this phenomenon is that the thermal decomposition of cellulose derivatives can form aromatic species by  $\pi$ – $\pi$  stacking in between the polymer residues and the graphene flakes. This results in a graphene composite with comparatively effective charge transport properties.<sup>44,45</sup> Hence, the annealing conditions of

250 °C for 30 min were acknowledged as optimum to gain highly electrically conductive properties for printing and sensing applications.

**Characterization of Bioinspired Fractal-Designed Chemoresistive VOC Sensors.** To characterize performance of fabricated sensors with fractal geometry compared with the control (interdigitated electrode), we performed time response characterization of designed sensors using three typical VOCs (ethanol, methanol, and acetone) with 30 ppm concentration, of which results are presented in Figure 3. From Figure 3a, it was observed that bioinspired fractal-designed sensors possessed superior sensitivity toward more polar analytes (methanol and ethanol) rather than for less-polar analytes (acetone) and considerably higher response compared with control geometry. These results clearly showed significant difference between fractal and conventional geometries, showing enhancement of response for these VOCs. Selectivity behavior toward polar VOC analytes was explained by considering that both the defect sites on the graphene surface and EC are polar regions, which can interact more proficiently with highly polar analytes in comparison with less-polar analytes.<sup>36–48</sup>

Furthermore, based on this sensing phenomenon, the composite material volume was expanded by the adsorption of vapor analytes, which increases the distance between the neighboring graphene flakes in the graphene network. As a result, the resistance and the carrier tunneling barrier of the sensor also increased.<sup>49</sup> The printed sensor adsorbs additional polar analytes than nonpolar analytes when it was exposed to nonpolar and polar analytes with the same concentration, which leads to a higher resistance variation and thus higher sensitivity. It is evident from the literature that methanol (0.762) is slightly more polar than ethanol (0.654).<sup>30</sup> Nevertheless, among these two gas analytes, the response of the printed sensor toward ethanol was significantly higher because of the improved penetration capability of ethanol molecules through the EC-encapsulated graphene sensing layer since the ink was formulated using ethanol and toluene as solvents, and the affinity of the sensing material for ethanol is much higher than that for methanol.

Further analysis of sensor performance for different fractal designs was performed by comparing response–recovery time characteristics for ethanol (30 ppm), of which results are presented in Figure 3b–e. These results showed considerable difference in response and recovery time characteristics between four tested geometries. The Hilbert-designed sensor showed a fast response time (6 s) toward ethanol at RT than Sierpinski (15 s), Peano (13 s), and conventional interdigitate ones (26 s) (Figure 3b–e). On the other hand, it was significant that the recovery time for the Hilbert-designed sensor (36 s) was higher than that of Sierpinski (23 s) and Peano (25 s) but lower than that of the conventional interdigitate-designed sensor (40 s). These results are explained by two physical mechanisms. The first physical mechanism behind this elevated sensing performance (response time and response value) was an enhanced effectively sensing area, which is illustrated by two electrode widths  $d_1$  and  $d_2$ .

A geometric active surface area ( $SA_{geo}$ ) was calculated for all these fractal-designed sensors within a total area of  $2 \times 1.5 \text{ cm}^2$ , and it was found that the ratio of the  $SA_{geo}$  between the two electrodes is the highest for Hilbert fractals (36% improvement) compared with that for other two fractal-

designed sensors and interdigitated sensors (Figure S6a). The active SA/V ratio for different designed sensors fabricated in this work was calculated by considering the pore size (13.73 nm; Figure S6b) and thickness ( $t_{avg} \sim 20 \text{ }\mu\text{m}$ , Figure S4a). From the calculation, it was found that the SA/V ratio for the Hilbert-designed sensor increased 10 times higher than that of interdigitate sensors and also higher than that of other fractal-designed sensors (Sierpinski and Peano). This elevated SA/V ratio for the Hilbert-designed sensor enhanced the relative exposure and pressure of different VOC analytes on the sensing material surface that increases the sensing efficiency. The second mechanism for these enhanced sensing capabilities of the Hilbert-designed sensor is the diverse adsorption capabilities of VOC analytes that was explained earlier. Importantly, the response–recovery time characteristics for this Hilbert-designed printed sensor toward ethanol are 6/36 s, which are faster than earlier reported sensors composed of graphene composites, as listed in Table 1.

**Table 1.** Figure of Merits of Graphene Composite-Based VOC Sensors

target VOC	response time (s)	recovery time (s)	detection limit (ppm)	working temperature (°C)	references
methanol	300	300	2.5	25	50
acetone	10	10	100	25	51
acetone	13	>20	2.5	350	52
ethanol			2.5	350	52
acetone	12	32	5	25	53
ethanol			5	25	53
ethanol	6	36	5	20	this study

From the experimental analysis, it was evident that without any external parameters (e.g., temperature and/or mechanical deformation), it was difficult to enhance the recovery time of the as-fabricated sensor. However, taken together, these two mechanisms of the bioinspired fractal-designed printed sensor explain both the improved performance of the Hilbert-designed sensor and the higher sensitivity toward polar versus less-polar analytes.

Figure 4a demonstrates the dynamic response variations of the Hilbert-designed sensor using ethanol vapor at ppm concentration at RT. The Hilbert-designed sensor shows good linear response behavior over the lower range of ethanol concentrations (5–100 ppm). It is noteworthy that the as-fabricated sensor did not show any mechanical deformation at the minimum concentration of ethanol vapor (5 ppm) because of the clamping effect, which justified the statement for tensile stiffness of a laminate specimen.<sup>54</sup> Owing to this characteristic, at minimum ethanol vapor concentrations, swelling of the EC-encapsulated graphene flakes originated, which resulted in a high signal to noise ratio (SNR) along with negligible hysteretic behavior. Based on the response value and noise of the sensor, we characterized the SNR of each sensor toward ethanol vapor. Figure S7a illustrates the SNR characteristics for the Hilbert-designed sensor toward different concentrations of ethanol vapor. Figure S7b displays the SNR values of interdigitate-, Sierpinski-, Peano-, and Hilbert-designed sensors upon introducing to 5 ppm ethanol. For ethanol, the Hilbert-designed sensor displayed a SNR of 35.56, which was five times higher than that of the interdigitate-designed sensor. By observing the trend of gas response and the SNR for different

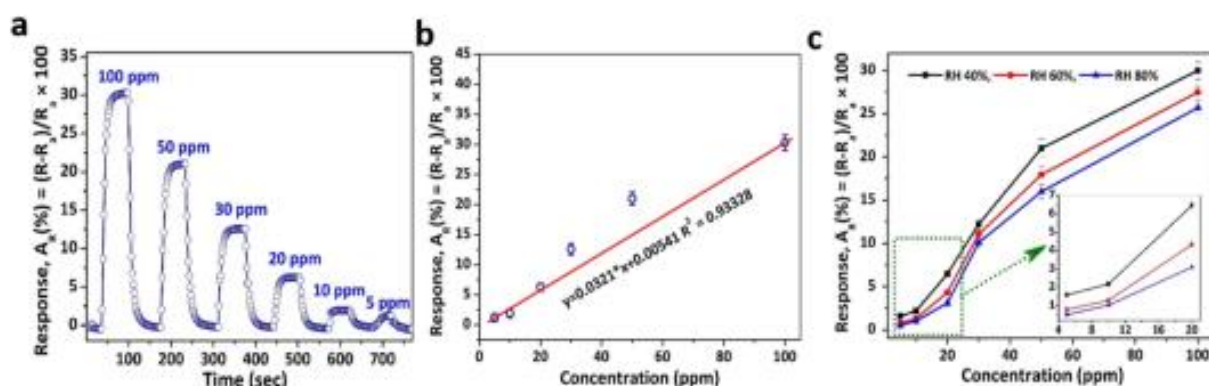


Figure 4. (a) Dynamic response and (b) linear correlation characteristics of the Hilbert-designed printed sensor toward different concentrations of ethanol vapor at RT (20 °C). (c) Transient response variations under different humidity conditions of the Hilbert-designed printed sensor toward different concentrations of ethanol vapor at RT.

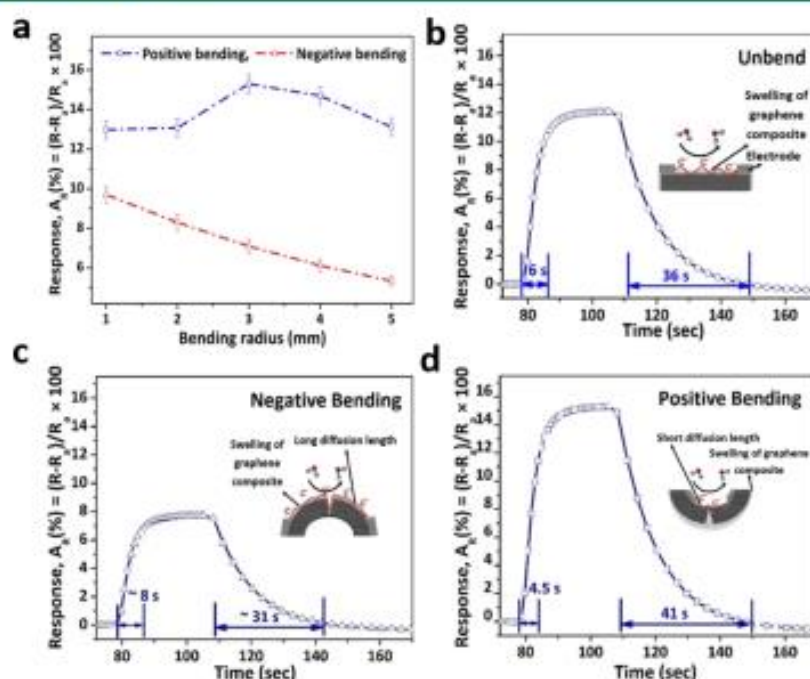


Figure 5. (a) Response variations to 30 ppm ethanol vapor as a function of the bending radius of the Hilbert-designed printed sensor under different bending conditions at RT (20 °C). Response–recovery time characteristics of the Hilbert-designed printed sensor to 30 ppm ethanol vapor at RT (20 °C) for (b) unbend, (c) negative bend, and (d) positive bend conditions.

fractal-designed sensors, our results directly show that the Hilbert-designed sensor is up to 2 orders of higher magnitude than other printed sensors.

The linear relationship for the dependency between the response and the concentration of ethanol at ppm levels at RT has been established, as illustrated in Figure 4b. Figure 4c illustrates the humidity effect on the Hilbert-designed sensor to ethanol at RT. It was observed that there was no significant degradation in the response magnitude at RT with the presence of a RH of up to 80% due to the specially configured graphene flake network in the composite. In this network, EC acted as the host matrix for encapsulation of graphene without any crosslinking origination. In addition, due to the lattice structure of graphene, no dangling bonds were present along the external surfaces of the graphene, which therefore showed the less chemical activity.<sup>55</sup> As a result, only physisorption

interactions were attributed when adsorbing external molecules (e.g., water) except for ethanol on this network. Levita et al.<sup>55</sup> reported in their atomistic simulation that the highly reactive edges of the graphene plane (particularly the zigzag edge) can adsorb fragments of water molecules (–H and –OH), preventing water from intercalating, which was also applicable for this configured graphene network synthesized as a printable ink.

To prove the stability and reproducibility, in this study, the same configuration in five sensors (Hilbert) was used, and none of them demonstrated an open-circuit failure even upon exposure to ethanol vapor severally. In fact, these Hilbert-designed sensors have shown quite robust behavior. For further assessment, five similarly configured Hilbert-designed sensors were exposed to 30 ppm concentration of ethanol vapor over a 14-day period. Figure S8a,b illustrates the tested

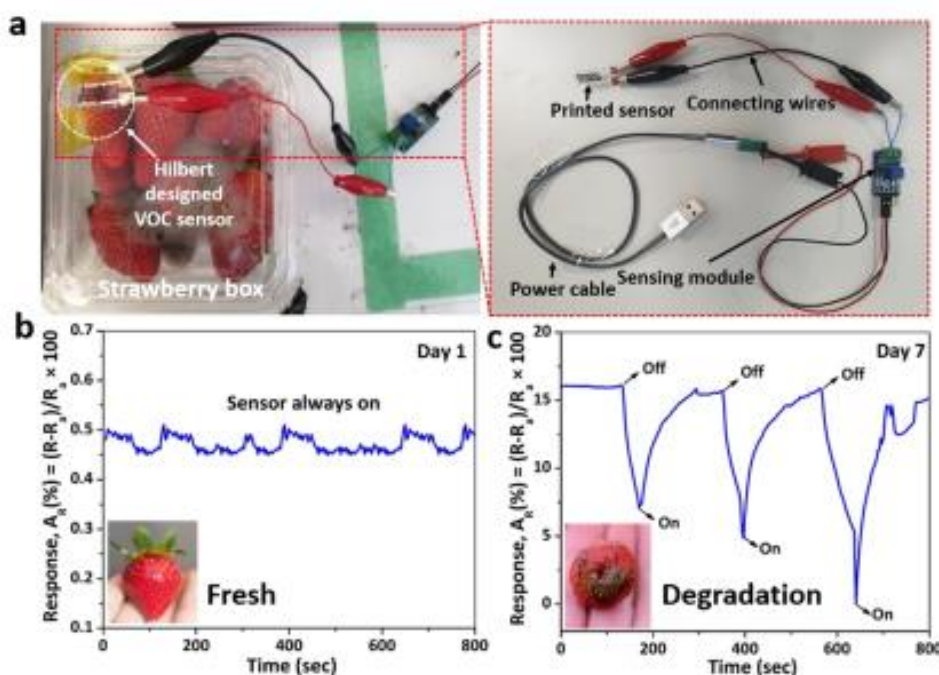


Figure 6. (a) Optical image of the Hilbert sensor on the strawberry box connected to a sensor module (the enlarged picture shows the configuration of the sensor module). Real-time monitoring of VOCs emitting from the strawberry during (b) day 1 (fresh strawberry) and (c) day 7 (rotten strawberry) using the Hilbert-designed printed sensor.

sensor response and the effect on its baseline resistance, which demonstrated exceptional durability, stability, and reproducibility.

**Influence of Mechanical Deformation on Bioinspired Fractal-Printed Sensors.** For real-field applications such as wearable sensors, food packaging sensors, and so forth, it is critical to explore the influence of mechanical deformation on their sensing performances. Preliminary mechanical bending treatments were performed with the Hilbert-designed graphene-printed VOC sensor on a PET substrate, as shown in Figure S1. The base resistance was increased from  $\sim 70$  to  $\sim 111.6 \Omega$  (Figure S8) when the sensor was bended negatively with a bending radius of 3 mm. Inversely, when the sensor was bended positively, the base resistance was reduced to  $\sim 50.5 \Omega$  (Figure S9). Changes in the base resistance have an influential effect on the sensor response at RT, as presented in Figure 5a. It shows that the response value of the negative bending of the Hilbert-designed sensor was decreased gradually with an increased bending radius (1–5 mm); meanwhile, the response value increased steadily with the rise of the bending radius (1–5 mm) during positive deformation. This change in response variation for the Hilbert-designed sensor happened due to the tensile stresses which were originating from the mechanical bending deformation. During the mechanical bending deformation of a sensor, a stress distribution originated across its sensing area that varied from a maximum compressive stress (concave surface) to a point of zero stress (neutral axis) and then to a maximum tensile stress (convex surface) (Figure S10). As a result, when the process ended, the concave surface was significantly shortened, while the convex surface was lengthened.

In contrast with positive deformation, the compressive stress in the negative bending case implied on the opposite portion of the sensing layer. The actual stress occurred in two-layer

sensor devices (graphene ink/PET) that are expected to deviate somewhat from this ideal one-layer scenario, which was dominated by the PET substrate due to its thickness along with high yield strength. However, when the bending moment ( $M$ ) was applied on the PET substrate, the substrate was yielded elastically followed by being yielded plastically. When the force was unloaded from the substrate, partial springback originated throughout the substrate because of the elastic strain recovery characteristics, which created gaps between sequentially piled encapsulated graphene flakes (from Figure 2c). During positive bending, compressive stress applied on the sensing layer reduced the nanogaps between the encapsulated graphene networks by compressing the polymeric surface. Interestingly, with the bending radius of  $>3$  mm, the response value of the Hilbert-designed sensor toward ethanol vapor decreased. This phenomenon could be explained by the shortened gaps between the encapsulated graphene networks, which implied that the additional force during bending disturbed the swelling process throughout the sensing progression. Moreover, this bending mechanism also enhanced the response–recovery time characteristics upon exposure to an ethanol concentration of 30 ppm with respect to the resistance at  $\sim 3$  mm bending radius.

From the experimental analysis, it was evident that positive bending deformation can enhance the response time ( $\sim 4$  s), whereas negative bending enhanced the recovery time ( $\sim 31$  s) compared with the unbend sensor (Figure 5b–d). The fast response time during positive bending could be described by the current path mechanism throughout the graphene network, which was activated by contacting neighboring encapsulated graphene flakes. Because of this shortened diffusion path, after ethanol absorption, electron scattering was reduced and led to abrupt resistance variation. In contrast, during negative bending, the electron scattering was increased due to the

longest current path along with slow resistance variation. Nevertheless, in terms of the recovery time, negative bending was more efficient than positive bending because of voids between the graphene networks, which helped to expel the ethanol analytes at RT.

**Demonstration of the Fractal Sensor for Real-Time VOC Monitoring.** Among different fractal-designed VOC sensors, the sensor with the Hilbert fractal design showed the best performance, which was further used to demonstrate the scalability of its practical application for monitoring of food spoilage (strawberry). From the literature, it was evident that anthracnose is one of the diseases affecting strawberries easily. It was caused by several *Colletotrichum* fungal species including *Colletotrichum fragariae*, *C. acutatum*, and *C. gloeosporioides* (Feliziani and Romanazzi, 2016; Jayawardena et al., 2016). It was reported that when the strawberry was affected by this fungal disease, at that time, it was rotten very easily and released several kinds of VOC biomarkers (e.g., 2-methyl propyl ester (28.5%), ethanol (19%), 2-methyl acetates (15.6%), etc. at 21 °C) along with CO<sub>2</sub> gas (16%).<sup>56,57</sup> Among these biomarkers, ethanol is one of the key VOC biomarkers with its extremely high concentration (ppm, depends on the number/weight of strawberries).<sup>56,57</sup>

To control the quality of the strawberry, it is important to monitor the presence of VOC biomarkers inside the fruit box. The Hilbert-designed sensor with enhanced characteristics of fast response–recovery time, a higher response value, strong water resistance, and durability was used to demonstrate a concept as a strawberry fruit quality-monitoring device. To check its potential real-field applicability, the Hilbert-designed sensor under positive bending conditions was installed on the top of the strawberry box (eight strawberries/box, ~250 g) with a sensor module device (part no: LM393) and was externally placed at 20 °C (Figure 6a). This sensor module was connected to a CH instrument through a connector to monitor the real-time resistance variation. From Figure 6b, it was observed that at day 1, when the strawberry was still fresh, the sensor did not exhibit any response as a resistance variation, while at day 7, when the strawberry was rotten, the sensor responded with a high resistance variation (Figure 6c). Our fabricated Hilbert-designed printed sensor developed in this work successfully detected the presence of ethanol in the rotten strawberry at RT efficiently, which paves a promising pathway for food (strawberry) industries as a quality control and monitoring practice to gauge the food conditions in ensuring food quality and safety globally.

## CONCLUSIONS

This work presents the development of bioinspired fractal-designed VOC sensors, fabricated by the extrusion printing process. The fabrication of three fractal-designed sensors such as Sierpinski, Peano, and Hilbert was done using specially formulated graphene ink using the extrusion printing technique to achieve stable structures of fabricated patterns with a high SA/V aspect ratio. The graphene ink formulated by combining EC and Cyrene provides a facile route to achieve sustainable, environmentally friendly, and low-cost sensing modules. This graphene ink was successfully used for printing at high-resolution biomimetic fractal-patterned architectures with a resistivity as low as 70 Ω cm after annealing at 250 °C for 30 min as a chemoresistive sensing device for VOC detection at room temperature. Performance characteristics evaluated for the Hilbert-designed sensor to ethanol vapor showed a fast

response time (~6 s @ 30 ppm), high response value (14% @ 30 ppm), broad detection limit (5–100 ppm), and high selectivity to ethanol vapor at room temperature (20 °C) among a set of VOCs (ethanol, methanol, and acetone), which was prominent than Sierpinski-, Peano-, and conventional interdigitate-designed VOC sensor characteristics. Furthermore, the as-fabricated sensor exhibited sensitivity to mechanical deformation and illustrated an enhanced response time (~4.5 s @ 30 ppm) to ethanol vapor at room temperature for positive bending. Eventually, in a practical application experiment, real-time monitoring of ethanol evolved from the rotten strawberry confirmed the concept and the feasibility of our developed sensing device for real-life applications. In summary, sensors with bioinspired fractal design using specially composed graphene ink with enhanced sensing performance by mechanical deformation have been demonstrated to be useful for VOC sensing, which paves a new path toward sustainable, low-cost, and environmentally friendly printable devices for food monitoring and/or tracking applications.

## ASSOCIATED CONTENT

### Supporting Information

The Supporting Information is available free of charge at <https://pubs.acs.org/doi/10.1021/acssensors.1c01449>.

Optical photograph of the experimental setup, calculated Hausdorff dimensions for biomimetic sensor design, storage and loss modulus as a function of time for graphene ink, 3D profile measurements of the printed pattern, FESEM micrographs, BET analysis of graphene ink, and *I*–*V* characteristic curve for the Hilbert sensor under different bending conditions (PDF)

## AUTHOR INFORMATION

### Corresponding Author

Dusan Losic – School of Chemical Engineering and Advanced Materials and ARC Research Hub for Graphene Enabled Industry Transformation, The University of Adelaide, Adelaide, South Australia 5005, Australia; [orcid.org/0000-0002-1930-072X](https://orcid.org/0000-0002-1930-072X); Email: [dusan.losic@adelaide.edu.au](mailto:dusan.losic@adelaide.edu.au)

### Authors

Kamrul Hassan – School of Chemical Engineering and Advanced Materials and ARC Research Hub for Graphene Enabled Industry Transformation, The University of Adelaide, Adelaide, South Australia 5005, Australia

Tran Thanh Tung – School of Chemical Engineering and Advanced Materials and ARC Research Hub for Graphene Enabled Industry Transformation, The University of Adelaide, Adelaide, South Australia 5005, Australia

Pei Lay Yap – School of Chemical Engineering and Advanced Materials and ARC Research Hub for Graphene Enabled Industry Transformation, The University of Adelaide, Adelaide, South Australia 5005, Australia

Hadi Rastin – School of Chemical Engineering and Advanced Materials and ARC Research Hub for Graphene Enabled Industry Transformation, The University of Adelaide, Adelaide, South Australia 5005, Australia

Nathan Stanley – School of Chemical Engineering and Advanced Materials and ARC Research Hub for Graphene

Enabled Industry Transformation, The University of Adelaide, Adelaide, South Australia 5005, Australia  
 Md. Julker Nine – School of Chemical Engineering and Advanced Materials and ARC Research Hub for Graphene Enabled Industry Transformation, The University of Adelaide, Adelaide, South Australia 5005, Australia;  
 ● [orcid.org/0000-0002-5740-8627](https://orcid.org/0000-0002-5740-8627)

Complete contact information is available at:  
<https://pubs.acs.org/10.1021/acssensors.1c01449>

### Author Contributions

The manuscript was written through contributions of all authors. All authors have given approval to the final version of the manuscript.

### Notes

The authors declare no competing financial interest.

### ACKNOWLEDGMENTS

The authors acknowledge financial support from the Australian Research Council Research Hub for Graphene Enabled Industry Transformation (IH150100003)ARC NS 210100245 and the University of Adelaide.

### REFERENCES

- (1) Arias, A. C.; MacKenzie, J. D.; McCulloch, I.; Rivnay, J.; Salleo, A. Materials and applications for large area electronics: solution-based approaches. *Chem. Rev.* 2010, 110, 3–24.
- (2) Gaikwad, A. M.; Whiting, G. L.; Steingart, D. A.; Arias, A. C. Highly flexible, printed alkaline batteries based on mesh-embedded electrodes. *Adv. Mater.* 2011, 23, 3251–3255.
- (3) Rogers, J. A.; Bao, Z.; Baldwin, K.; Dodabalapur, A.; Crone, B.; Raju, V. R.; Kuck, V.; Katz, H.; Amundson, K.; Ewing, J.; Drzaic, P. Paper-like electronic displays: Large-area rubber-stamped plastic sheets of electronics and microencapsulated electrophoretic inks. *Proc. Natl. Acad. Sci. U. S. A.* 2001, 98, 4835–4840.
- (4) Kim, D.-H.; Lu, N.; Ma, R.; Kim, Y.-S.; Kim, R.-H.; Wang, S.; Wu, J.; Won, S. M.; Tao, H.; Islam, A.; Yu, K. J.; Kim, T.-i.; Chowdhury, R.; Ying, M.; Xu, L.; Li, M.; Chung, H.-J.; Keum, H.; McCormick, M.; Liu, P.; Zhang, Y.-W.; Omenetto, F. G.; Huang, Y.; Coleman, T.; Rogers, J. A. Epidermal electronics. *science* 2011, 333, 838–843.
- (5) Jung, M.; Kim, J.; Noh, J.; Lim, N.; Lim, C.; Lee, G.; Kim, J.; Kang, H.; Jung, K.; Leonard, A. D.; Tour, J. M.; Cho, G. All-printed and roll-to-roll-printable 13.56-MHz-operated 1-bit RF tag on plastic foils. *IEEE Trans. Electron Devices* 2010, 57, 571–580.
- (6) Tran, T. S.; Dutta, N. K.; Choudhury, N. R. Graphene inks for printed flexible electronics: graphene dispersions, ink formulations, printing techniques and applications. *Adv. Colloid Interface Sci.* 2018, 261, 41–61.
- (7) Zhou, X.; Huang, W.; Shi, J.; Zhao, Z.; Xia, Q.; Li, Y.; Wang, H.; Li, Z. A novel MOF/graphene oxide composite GrO@MIL-101 with high adsorption capacity for acetone. *J. Mater. Chem. A* 2014, 2, 4722–4730.
- (8) Piloto, C.; Mirri, F.; Bengio, E. A.; Notarianni, M.; Gupta, B.; Shafiei, M.; Pasquali, M.; Motta, N. Room temperature gas sensing properties of ultrathin carbon nanotube films by surfactant-free dip coating. *Sens. Actuators, B* 2016, 227, 128–134.
- (9) Jeong, H. Y.; Lee, D.-S.; Choi, H. K.; Lee, D. H.; Kim, J.-E.; Lee, J. Y.; Lee, W. J.; Kim, S. O.; Choi, S.-Y. Flexible room-temperature NO<sub>2</sub> gas sensors based on carbon nanotubes/reduced graphene hybrid films. *Appl. Phys. Lett.* 2010, 96, 213105.
- (10) Huang, X.; Leng, T.; Zhang, X.; Chen, J. C.; Chang, K. H.; Geim, A. K.; Novoselov, K. S.; Hu, Z. Binder-free highly conductive graphene laminate for low cost printed radio frequency applications. *Appl. Phys. Lett.* 2015, 106, 203105.
- (11) Huang, X.; Pan, K.; Hu, Z. Experimental demonstration of printed graphene nano-flakes enabled flexible and conformable wideband radar absorbers. *Sci. Rep.* 2016, 6, 38197.
- (12) Akbari, M.; Khan, M. W. A.; Hasani, M.; Björninen, T.; Sydänheimo, L.; Ukkonen, L. Fabrication and characterization of graphene antenna for low-cost and environmentally friendly RFID tags. *IEEE Antenn. Wireless Propag. Lett.* 2016, 15, 1569–1572.
- (13) Li, W.; Li, F.; Li, H.; Su, M.; Gao, M.; Li, Y.; Su, D.; Zhang, X.; Song, Y. Flexible circuits and soft actuators by printing assembly of graphene. *ACS Appl. Mater. Interfaces* 2016, 8, 12369–12376.
- (14) Wang, L.; Chen, S.; Shu, T.; Hu, X. Functional Inks for Printable Energy Storage Applications based on 2 D Materials. *ChemSusChem* 2020, 13, 1330.
- (15) Lim, S.; Kang, B.; Kwak, D.; Lee, W. H.; Lim, J. A.; Cho, K. Inkjet-printed reduced graphene oxide/poly (vinyl alcohol) composite electrodes for flexible transparent organic field-effect transistors. *J. Phys. Chem. C* 2012, 116, 7520–7525.
- (16) Shin, K.-Y.; Hong, J.-Y.; Jang, J. Micropatterning of Graphene Sheets by Inkjet Printing and Its Wideband Dipole-Antenna Application. *Adv. Mater.* 2011, 23, 2113–2118.
- (17) Kong, D.; Le, L. T.; Li, Y.; Zunino, J. L.; Lee, W. Temperature-dependent electrical properties of graphene inkjet-printed on flexible materials. *Langmuir* 2012, 28, 13467–13472.
- (18) Dodoo-Arhin, D.; Howe, R. C. T.; Hu, G.; Zhang, Y.; Hiralal, P.; Bello, A.; Amarantunga, G.; Hasan, T. Inkjet-printed graphene electrodes for dye-sensitized solar cells. *Carbon* 2016, 105, 33–41.
- (19) Hartwig, M.; Zichner, R.; Joseph, Y. Inkjet-printed wireless chemiresistive sensors—a review. *Chemosensors* 2018, 6, 66.
- (20) Bandodkar, A. J.; Jeeranpan, I.; Wang, J. Wearable chemical sensors: Present challenges and future prospects. *ACS Sens.* 2016, 1, 464–482.
- (21) Hassan, K.; Iftekhar Uddin, A. S. M.; Chung, G.-S. Fast-response hydrogen sensors based on discrete Pt/Pd bimetallic ultrathin films. *Sens. Actuators, B* 2016, 234, 435–445.
- (22) Hassan, K.; Chung, G.-S. Catalytically activated quantum-size Pt/Pd bimetallic core-shell nanoparticles decorated on ZnO nanorod clusters for accelerated hydrogen gas detection. *Sens. Actuators, B* 2017, 239, 824–833.
- (23) Han, S.; Zhuang, X.; Shi, W.; Yang, X.; Li, L.; Yu, J. Poly(3-hexylthiophene)/polystyrene (P3HT/PS) blends based organic field-effect transistor ammonia gas sensor. *Sens. Actuators, B* 2016, 225, 10–15.
- (24) Péres, L. O.; Li, R. W. C.; Yamauchi, E. Y.; Lippi, R.; Gruber, J. Conductive polymer gas sensor for quantitative detection of methanol in Brazilian sugar-cane spirit. *Food Chem.* 2012, 130, 1105–1107.
- (25) Wu, C.; Li, F.; Wu, W.; Chen, W.; Guo, T. Liquid-phase exfoliation of chemical vapor deposition-grown single layer graphene and its application in solution-processed transparent electrodes for flexible organic light-emitting devices. *Appl. Phys. Lett.* 2014, 105, 243509.
- (26) Yeo, W.-H.; Kim, Y.-S.; Lee, J.; Ameen, A.; Shi, L.; Li, M.; Wang, S.; Ma, R.; Jin, S. H.; Kang, Z.; Huang, Y.; Rogers, J. A. Multifunctional epidermal electronics printed directly onto the skin. *Adv. Mater.* 2013, 25, 2773–2778.
- (27) Jeong, J.-W.; Yeo, W.-H.; Akhtar, A.; Norton, J. J. S.; Kwack, Y.-J.; Li, S.; Jung, S.-Y.; Su, Y.; Lee, W.; Xia, J.; Cheng, H.; Huang, Y.; Choi, W.-S.; Bretl, T.; Rogers, J. A. Materials and Optimized Designs for Human-Machine Interfaces Via Epidermal Electronics. *Adv. Mater.* 2013, 25, 6839–6846.
- (28) Thekkekara, L. V.; Gu, M. Bioinspired fractal electrodes for solar energy storages. *Sci. Rep.* 2017, 7, 45585.
- (29) Falconer, K. J. *The Geometry of Fractal Sets*; Cambridge University Press, 1986; Vol. 85.
- (30) Hassan, K.; Tung, T. T.; Stanley, N.; Yap, P. L.; Farivar, F.; Rastin, H.; Nine, M. J.; Losic, D. Graphene inks for extrusion-based 3D micro printing of chemo-resistive sensing devices for volatile organic compounds (VOCs) detection. *Nanoscale* 2021, 13, 5356–5368.



- (31) Pan, K.; Fan, Y.; Leng, T.; Li, J.; Xin, Z.; Zhang, J.; Hao, L.; Gallop, J.; Novoselov, K. S.; Hu, Z. Sustainable production of highly conductive multilayer graphene ink for wireless connectivity and IoT applications. *Nat. Commun.* 2018, 9, 5197.
- (32) Hassan, K.; Uddin, A. S. M. L.; Chung, G.-S. Hydrogen sensing properties of Pt/Pd bimetal decorated on highly hydrophobic Si nanowires. *Int. J. Hydrogen Energy* 2016, 41, 10991–11001.
- (33) Fan, J. A.; Yeo, W.-H.; Su, Y.; Hattori, Y.; Lee, W.; Jung, S.-Y.; Zhang, Y.; Liu, Z.; Cheng, H.; Falgout, L. Fractal design concepts for stretchable electronics. *Nat. Commun.* 2014, 5, 3266.
- (34) Smith, H. J. S. On the integration of discontinuous functions. *Proc. Lond. Math. Soc.* 1874, 1–6, 140–153.
- (35) Hilbert, D. Über die stetige Abbildung einer Linie auf ein Flächenstück. *Dritter Band: Analysis Grundlagen der Mathematik Physik Verschiedenes*; Springer, 1935; pp 1–2.
- (36) Peano, G. Sur une courbe, qui remplit toute une aire plane. *Math. Ann.* 1890, 36, 157–160.
- (37) Platzman, L. K.; Bartholdi, J. J., III Spacefilling curves and the planar travelling salesman problem. *J. ACM* 1989, 36, 719–737.
- (38) Sagan, H. Hilbert's Space-Filling Curve. *Space-filling Curves*; Springer, 1994; pp 9–30.
- (39) Foroutan-pour, K.; Dutilleul, P.; Smith, D. L. Advances in the implementation of the box-counting method of fractal dimension estimation. *Appl. Math. Comput.* 1999, 105, 195–210.
- (40) Smith, T. G., Jr.; Lange, G. D.; Marks, W. B. Fractal methods and results in cellular morphology—dimensions, lacunarity and multifractals. *J. Neurosci. Methods* 1996, 69, 123–136.
- (41) Hassan, K.; Nine, M. J.; Tung, T. T.; Stanley, N.; Yap, P. L.; Rastin, H.; Yu, L.; Losic, D. Functional inks and extrusion-based 3D printing of 2D materials: a review of current research and applications. *Nanoscale* 2020, 12, 19007–19042.
- (42) Singh, M.; Haverinen, H. M.; Dhagat, P.; Jabbour, G. E. Inkjet printing—process and its applications. *Adv. Mater.* 2010, 22, 673–685.
- (43) Lim, J. A.; Lee, W. H.; Lee, H. S.; Lee, J. H.; Park, Y. D.; Cho, K. Self-Organization of Ink-jet-Printed Triisopropylsilyl ethynyl Pentacene via Evaporation-Induced Flows in a Drying Droplet. *Adv. Funct. Mater.* 2008, 18, 229–234.
- (44) Keiluweit, M.; Nico, P. S.; Johnson, M. G.; Kleber, M. Dynamic molecular structure of plant biomass-derived black carbon (biochar). *Environ. Sci. Technol.* 2010, 44, 1247–1253.
- (45) Pastorova, I.; Botto, R. E.; Arisz, P. W.; Boon, J. J. Cellulose char structure: a combined analytical Py-GC-MS, FTIR, and NMR study. *Carbohydr. Res.* 1994, 262, 27–47.
- (46) Tung, T. T.; Tran, M. T.; Feller, J.-F.; Castro, M.; Van Ngo, T.; Hassan, K.; Nine, M. J.; Losic, D. Graphene and metal organic frameworks (MOFs) hybridization for tunable chemoresistive sensors for detection of volatile organic compounds (VOCs) biomarkers. *Carbon* 2020, 159, 333–344.
- (47) Robinson, D. H. Ethyl cellulose-solvent phase relationships relevant to coacervation microencapsulation processes. *Drug Dev. Ind. Pharm.* 1989, 15, 2597–2620.
- (48) Leenaerts, O.; Partoens, B.; Peeters, F. M. Adsorption of H<sub>2</sub>O, NH<sub>3</sub>, CO, NO<sub>2</sub>, and NO on graphene: A first-principles study. *Phys. Rev. B: Condens. Matter Mater. Phys.* 2008, 77, 125416.
- (49) Tung, T. T.; Nine, M. J.; Krebsz, M.; Pasinszki, T.; Coghlan, C. J.; Tran, D. N. H.; Losic, D. Recent advances in sensing applications of graphene assemblies and their composites. *Adv. Funct. Mater.* 2017, 27, 1702891.
- (50) Tung, T. T.; Castro, M.; Pillin, I.; Kim, T. Y.; Suh, K. S.; Feller, J.-F. Graphene-Fe<sub>3</sub>O<sub>4</sub>/PIL-PEDOT for the design of sensitive and stable quantum chemo-resistive VOC sensors. *Carbon* 2014, 74, 104–112.
- (51) Zhang, Q.; An, C.; Fan, S.; Shi, S.; Zhang, R.; Zhang, J.; Li, Q.; Zhang, D.; Hu, X.; Liu, J. Flexible gas sensor based on graphene/ethyl cellulose nanocomposite with ultra-low strain response for volatile organic compounds rapid detection. *Nanotechnology* 2018, 29, 285501.
- (52) Singkammo, S.; Wisitsoraat, A.; Sriprachuabwong, C.; Tuantranont, A.; Phanichphant, S.; Liawhiran, C. Electrolytically exfoliated graphene-loaded flame-made Ni-doped SnO<sub>2</sub> composite film for acetone sensing. *ACS Appl. Mater. Interfaces* 2015, 7, 3077–3092.
- (53) Gavvani, J. N.; Dehsari, H. S.; Hasani, A.; Mahyari, M.; Shalamzari, E. K.; Salehi, A.; Taromi, F. A. A room temperature volatile organic compound sensor with enhanced performance, fast response and recovery based on N-doped graphene quantum dots and poly (3, 4-ethylenedioxythiophene)-poly (styrenesulfonate) nano-composite. *RSC Adv.* 2015, 5, 57559–57567.
- (54) Lundström, K. L.; Shivaraman, M. S.; Svensson, C. M. A hydrogen-sensitive Pd-gate MOS transistor. *J. Appl. Phys.* 1975, 46, 3876–3881.
- (55) Levita, G.; Restuccia, P.; Righi, M. C. Graphene and MoS<sub>2</sub> interacting with water: A comparison by ab initio calculations. *Carbon* 2016, 107, 878–884.
- (56) Pesis, E. The role of the anaerobic metabolites, acetaldehyde and ethanol, in fruit ripening, enhancement of fruit quality and fruit deterioration. *Postharvest Biol. Technol.* 2005, 37, 1–19.
- (57) Rojas-Flores, C.; Ventura-Aguilar, R. I.; Bautista-Baños, S.; Revah, S.; Saucedo-Lucero, J. O. Estimating CO<sub>2</sub> and VOCs production of *Colletotrichum fragariae* and *Rhizopus stolonifer* grown in cold stored strawberry fruit. *Microbiol. Res.* 2019, 228, 126327.

## Fractal design for advancing performance of chemo-resistive sensors

Kamrul Hassan<sup>1,2</sup>, Tran Thanh Tung<sup>1,2</sup>, Pei Lay Yap<sup>1,2</sup>, Hadi Rastin<sup>1,2</sup>, Nathan Stanley<sup>1,2</sup>, Md. Julker Nine<sup>1,2</sup>, Dusan Losic<sup>1,2\*</sup>

<sup>1</sup>School of Chemical Engineering and Advanced Materials, The University of Adelaide, SA 5005, Australia

<sup>2</sup>ARC Research Hub for Graphene Enabled Industry Transformation, The University of Adelaide, SA 5005, Australia

Corresponding author: Prof. Dusan Losic (email: dusan.losic@adelaide.edu.au)

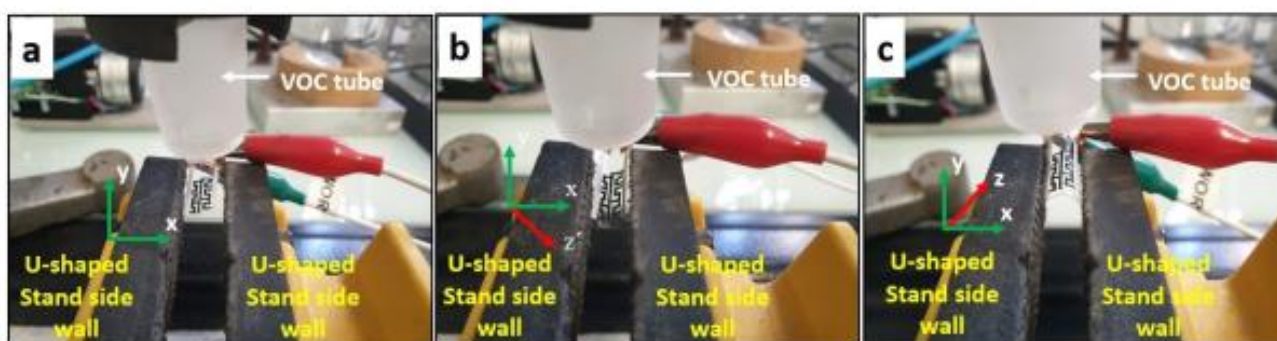


Figure S1. Optical photographs of the experimental setup for (a) flat, (b) positive bending, and (c) negative bending conditions.

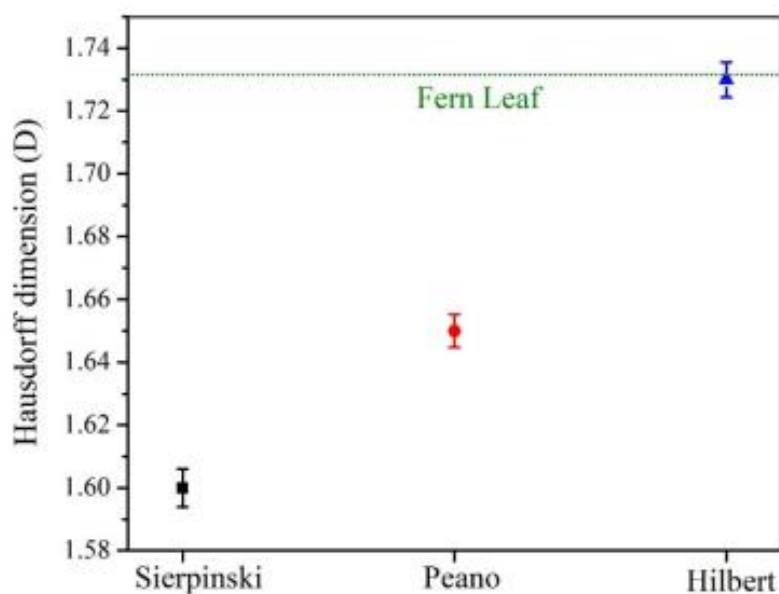


Figure S2. Calculated Hausdorff dimensions for bio-inspired fractal sensor design.

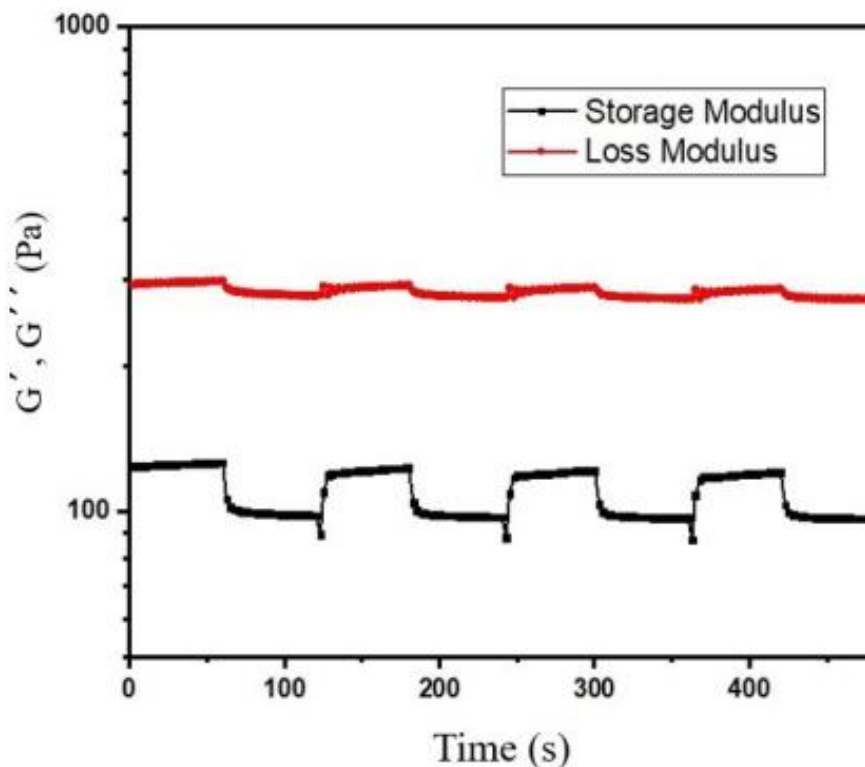


Figure S3. Storage and loss modulus as a function of time; at room temperature relevant for extrusion printing.

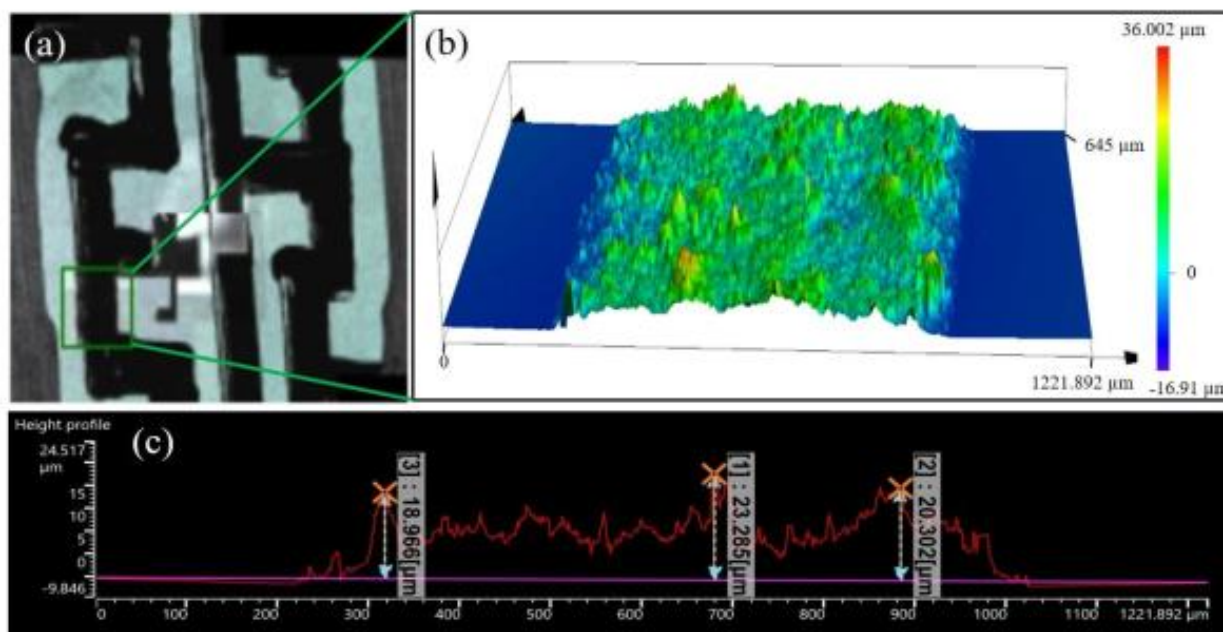


Figure S4. Results of 3D profile measurements of printed inks by 3D optical profilometer. (a) 2D image of printed patterns on PET, (b) 3D profile map of representative printed line and (c) averaged cross-sectional profiles of printed lines for selected region.

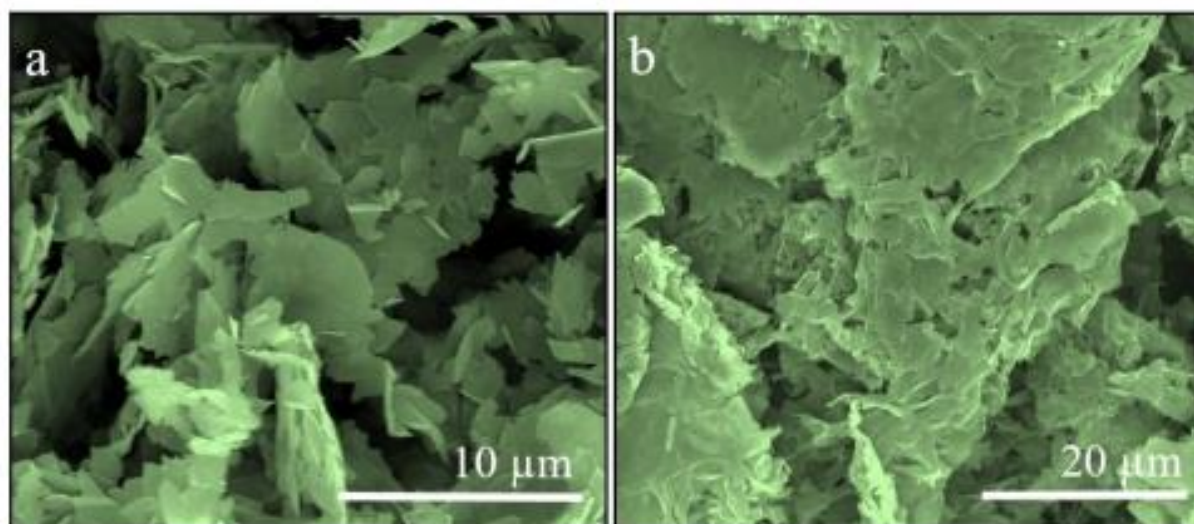


Figure S5. FESEM of (a) pristine graphene (pG), and (b) pristine graphene/ethyl-cellulose (pG/EC) powder.

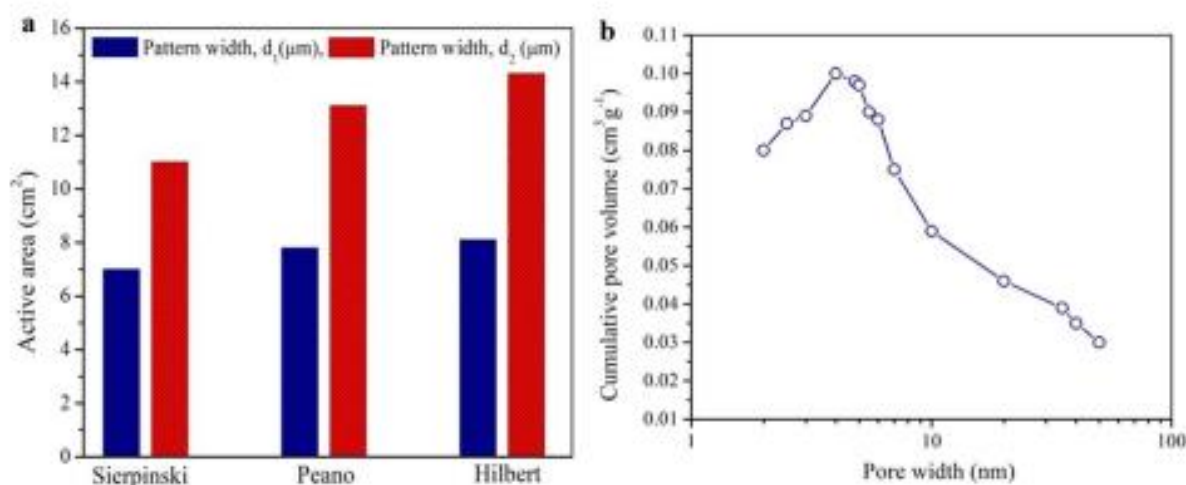


Figure S6. (a) Geometric surface active area calculated for different fractal designs for pattern widths  $d_1$  and  $d_2$ , (b) Porous analysis of as-synthesized graphene ink by the BJH method. The pore size distributions vary from 2 to 48 nm.

#### Calculation procedure of SA:V ratio for patterned sensors:

The performance of the bio-fractal designed sensors was enhanced due to the patterned structure compared to sensors prepared by interdigitate design methods. The mechanism is mainly based on the surface to volume enhancement of the effective sensing materials. To calculate the ratio of the active surface area to volume (SA:V) of four different sensors, thickness ( $T$ ) and width ( $d$ ) of the sensing materials was obtained from the optical profilometer measurement.

The active area of the printed sensing material was calculated by this equation:

$$\text{Active area}_{\text{eff}} (A_{\text{printed}}) = N \times (L \times d) \quad (1)$$

where  $N$  is the number of printed lines,  $L$  is the length and  $d$  is the width of one printed line.

Based on this calculation the effective volume for sensing materials can be further calculated by taking into account the average thickness:

$$\text{Active volume}_{\text{eff}} = \text{Active area}_{\text{eff}} \times T_{\text{Avg}} \quad (2)$$

The ratio of the surface area to volume is calculated as follows:

$$\text{SA:V} = \text{Active area}_{\text{eff}} / \text{Active volume}_{\text{eff}} \quad (3).$$

**Signal to Noise ratio (SNR) calculation for patterned sensors:**

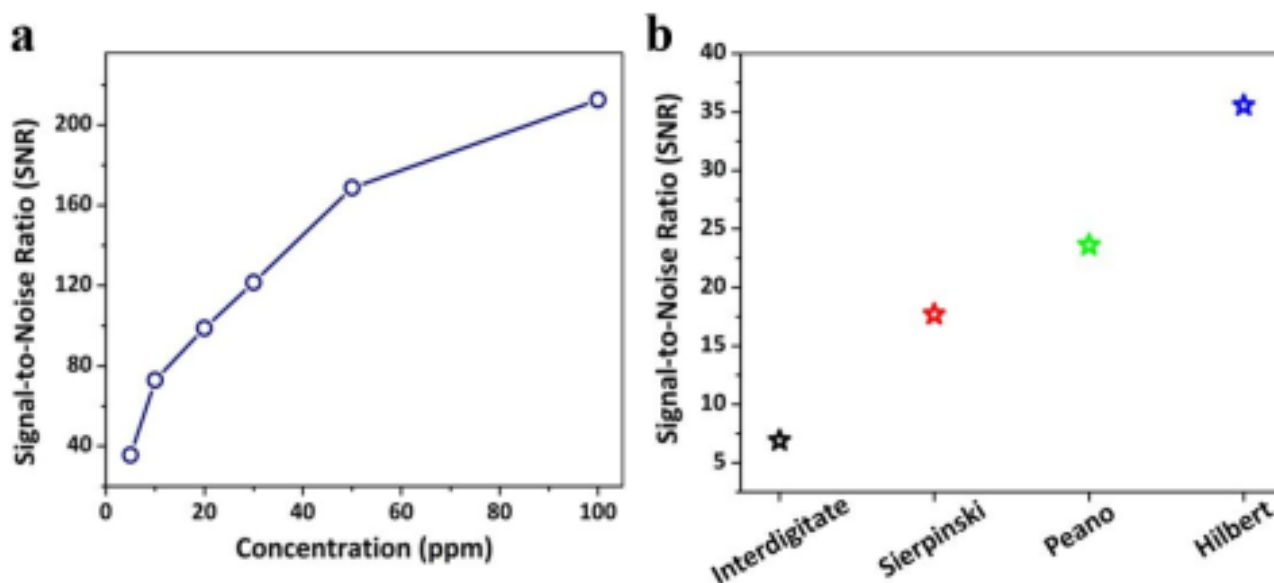


Figure S7. (a) Signal-to-Noise ratio (SNR) of Hilbert designed sensor upon exposure to ppm concentration (5-100 ppm) of ethanol at RT. (b) SNR values of different printed sensors upon exposure to 5 ppm of ethanol.

Hilbert designed sensors has the largest signal-to-noise ratio compare with the other patterned sensors because of the two physical mechanism. One is effective surface area and the active surface area to volume ratio (SA:V), and another one is diverse adsorption capabilities of VOC analytes. The active surface area to volume (SA:V) ratio for different designed sensors fabricated in this work was calculated by considering the pore size (13.73 nm; Figure S6 (b)) and thickness ( $t_{\text{avg}} \sim 20 \mu\text{m}$ , Figure S4 (c)). From the calculation, it was found that the SA:V ratio for Hilbert designed increased 10 times compare with the Interdigitate sensors. This elevated SA:V ratio for Hilbert designed sensor enhanced the relative exposure and pressure of different VOC analytes on the sensing material surface that increases the sensing efficiency.

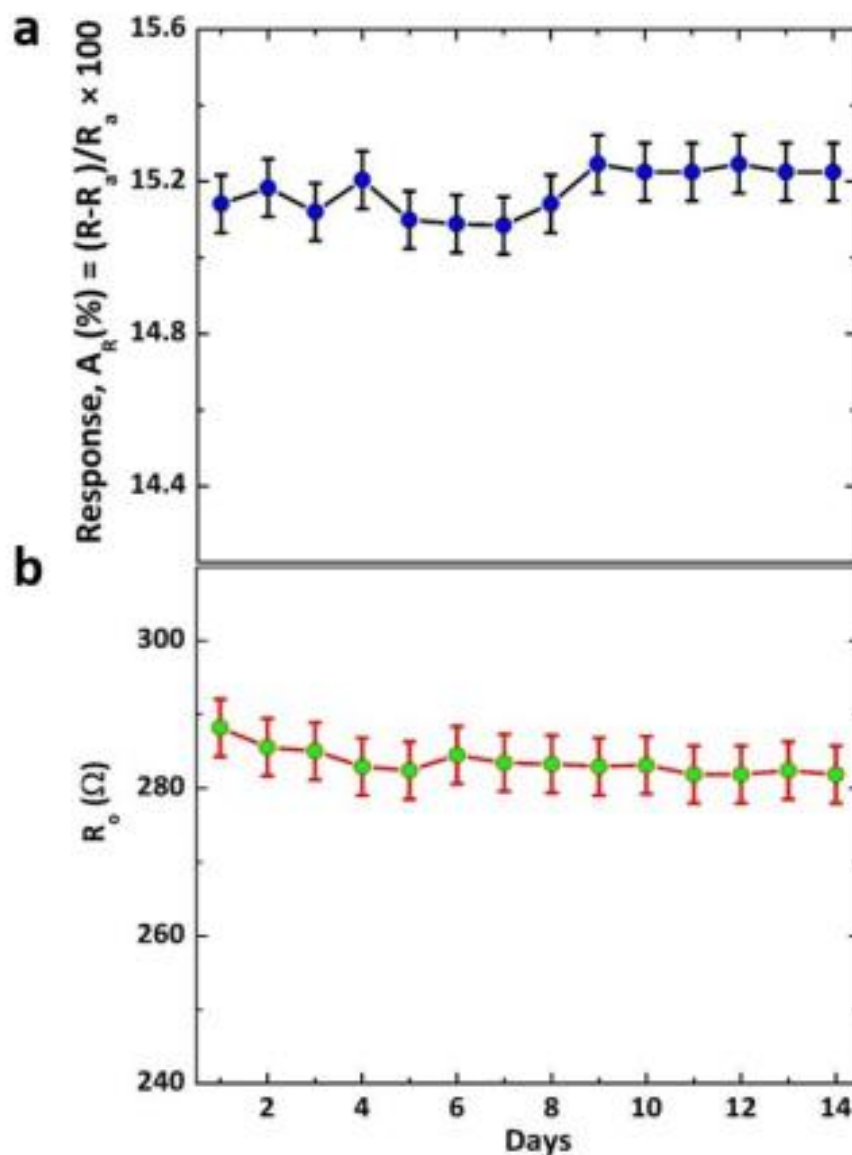


Figure S8. Time reliance of the Hilbert designed sensors (5 sensor) (a) response value and (b) baseline resistance value, monitored over a fourteen-day period, where on each day each sensor was exposed to 30 ppm of ethanol vapour at 20 °C.

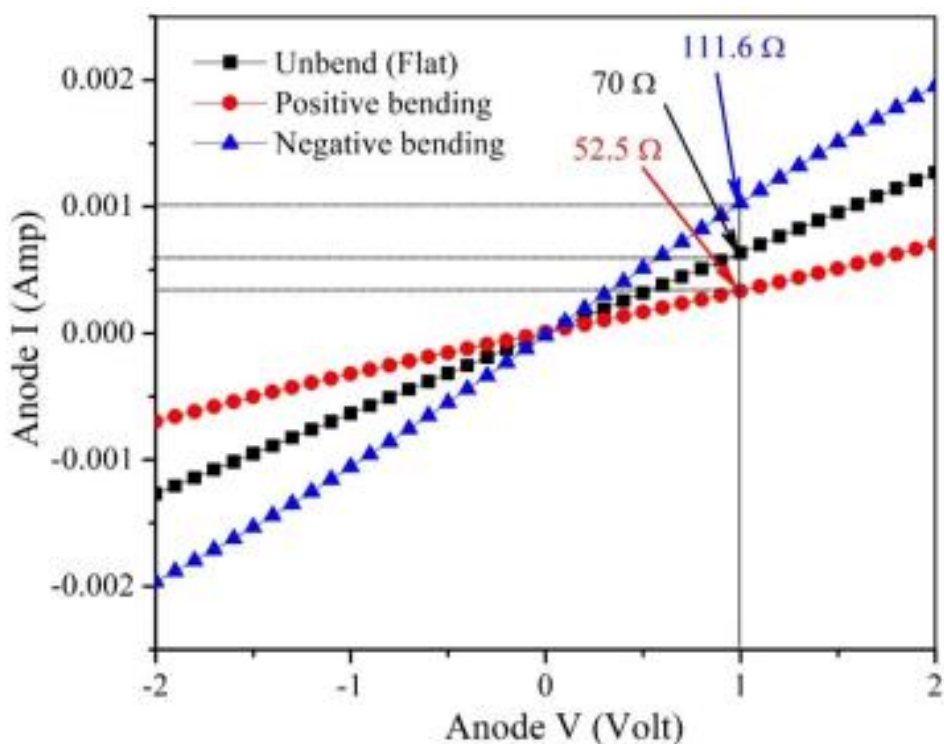


Figure S9. I-V characteristics curve for Hilbert designed printed sensor at different bending conditions.

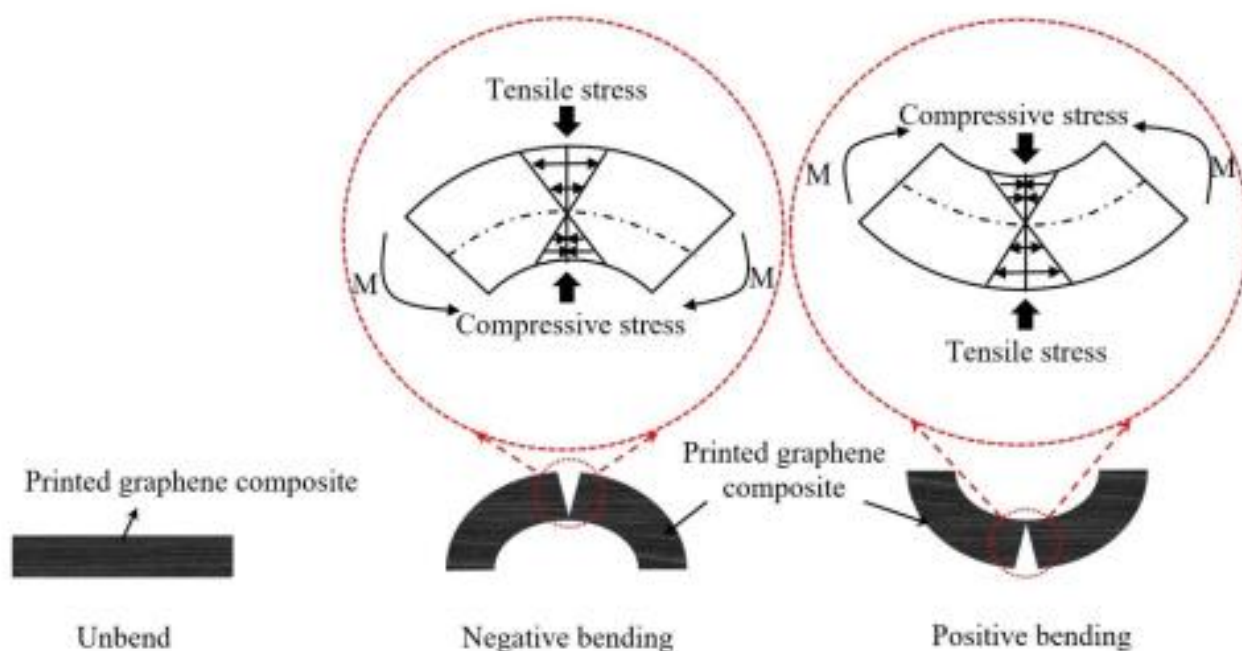


Figure S10. Schematic showing the stress distributions occurring when a bending moment ( $M$ ) is applied to the ends of a sensor for positive and negative bending condition.

## Chapter 5

# Development of CNT-graphene sensor array with embedded MXene heater for NO<sub>2</sub> sensing

In this chapter, development of a hybrid sensing material of one-dimensional CNTs and two-dimensional graphene and formulated a conductive ink, which is applied for fabricating an NO<sub>2</sub> gas sensor array within a compact design utilizing extrusion printing is presented. To improve NO<sub>2</sub> sensing performance, a reverse-side layer is designed that functions as a Joule heater. Challenges of integrating a heater on a flexible substrate for heating the sensor to optimal operating temperature is overcome by controlling the loading of MXene and PEDOT:PSS. The printed CNT-graphene-based sensor with embedded MXene/PEDOT:PSS heater is capable of detecting trace amount of NO<sub>2</sub> gas (1 ppm) at 65 °C. The sensor is able to distinguish between various gases/VOCs and target NO<sub>2</sub> gas based on their chemical affinities. The printed CNT-graphene sensor array also demonstrate a high-level of recoverability (2.9 min), promising stability, durability as well as reproducibility, which renders this sensor suitable candidate for practical applications.

This chapter has been published in “Advanced Materials Interfaces” journal as follows:

“**Hassan K**, Stanley N, Tung TT, Yap PL, Rastin H, Yu L, Losic D. Extrusion-Printed CNT-Graphene Sensor array with Embedded MXene/PEDOT:PSS Heater for Enhanced NO<sub>2</sub> Sensing at Low Temperature. **Advanced Materials Interfaces**, 1138 (2020), 49-58.”



## Statement of Authorship

Title of Paper	Extrusion printed CNT-graphene sensor array with embedded MXene/PEDOT:PSS heater for enhanced NO <sub>2</sub> sensing at low temperature
Publication Status	<input checked="" type="checkbox"/> Published <input type="checkbox"/> Accepted for Publication <input type="checkbox"/> Submitted for Publication <input type="checkbox"/> Unpublished and Unsubmitted work written in manuscript style
Publication Details	Hassan K, Tung TT, Yap PL, Nino MJ, Kim HC, Losic D. Extrusion printed CNT-graphene sensor array with embedded MXene/PEDOT:PSS heater for enhanced NO <sub>2</sub> sensing at low temperature. Advanced Materials Interfaces.

### Principal Author

Name of Principal Author (Candidate)	Kamrul Hassan			
Contribution to the Paper	Prepared, edited and revised the review manuscript.			
Overall percentage (%)	85%			
Certification:	This paper reports on original research I conducted during the period of my Higher Degree by Research candidature and is not subject to any obligations or contractual agreements with a third party that would constrain its inclusion in this thesis. I am the primary author of this paper.			
Signature	<table border="1" style="width: 100%;"> <tr> <td style="width: 80%;"></td> <td style="width: 20%;">Date</td> <td>19/10/2021</td> </tr> </table>		Date	19/10/2021
	Date	19/10/2021		

### Co-Author Contributions

By signing the Statement of Authorship, each author certifies that:

- i. the candidate's stated contribution to the publication is accurate (as detailed above);
- ii. permission is granted for the candidate to include the publication in the thesis; and
- iii. the sum of all co-author contributions is equal to 100% less the candidate's stated contribution.

Name of Co-Author	Nathan Stanley			
Contribution to the Paper	Edited and revised the manuscript.			
Signature	<table border="1" style="width: 100%;"> <tr> <td style="width: 80%;"></td> <td style="width: 20%;">Date</td> <td>28.10.2021</td> </tr> </table>		Date	28.10.2021
	Date	28.10.2021		

Name of Co-Author	Tran Thanh Tung			
Contribution to the Paper	Co-supervised and revised the manuscript.			
Signature	<table border="1" style="width: 100%;"> <tr> <td style="width: 80%;"></td> <td style="width: 20%;">Date</td> <td>26/10/2021</td> </tr> </table>		Date	26/10/2021
	Date	26/10/2021		

Please cut and paste additional co-author panels here as required.

## Statement of Authorship

Title of Paper	Extrusion printed CNT-graphene sensor array with embedded MXene/PEDOT:PSS heater for enhanced NO <sub>2</sub> sensing at low temperature		
Publication Status	<input checked="" type="checkbox"/> Published	<input type="checkbox"/> Accepted for Publication	
	<input type="checkbox"/> Submitted for Publication	<input type="checkbox"/> Unpublished and Unsubmitted work written in manuscript style	
Publication Details	Hassan K, Tung TT, Yap PL, Nire MJ, Kim HC, Losic D. Extrusion printed CNT-graphene sensor array with embedded MXene/PEDOT:PSS heater for enhanced NO <sub>2</sub> sensing at low temperature. Advanced Materials Interfaces		

### Principal Author

Name of Principal Author (Candidate)	Kamrul Hassan		
Contribution to the Paper	Prepared, edited and revised the review manuscript.		
Overall percentage (%)	85%		
Certification:	This paper reports on original research I conducted during the period of my Higher Degree by Research candidature and is not subject to any obligations or contractual agreements with a third party that would constrain its inclusion in this thesis. I am the primary author of this paper.		
Signature		Date	19/10/2021

### Co-Author Contributions

By signing the Statement of Authorship, each author certifies that:

- the candidate's stated contribution to the publication is accurate (as detailed above);
- permission is granted for the candidate to include the publication in the thesis; and
- the sum of all co-author contributions is equal to 100% less the candidate's stated contribution.

Name of Co-Author	Pei Lay Yap		
Contribution to the Paper	Edited and revised the manuscript.		
Signature		Date	26/10/21

Name of Co-Author	Hadi Rastin		
Contribution to the Paper	Co-supervised and revised the manuscript.		
Signature		Date	29.10.2021

Please cut and paste additional co-author panels here as required.

## Statement of Authorship

Title of Paper	Extrusion printed CNT-graphene sensor array with embedded MXene/PEDOT/PSS heater for enhanced NO <sub>2</sub> sensing at low temperature
Publication Status	<input checked="" type="checkbox"/> Published <input type="checkbox"/> Accepted for Publication <input type="checkbox"/> Submitted for Publication <input type="checkbox"/> Unpublished and Unsubmitted work written in manuscript style
Publication Details	Hassan K, Tung TT, Yap PL, Nino MJ, Kim HC, Losic D. Extrusion printed CNT-graphene sensor array with embedded MXene/PEDOT/PSS heater for enhanced NO <sub>2</sub> sensing at low temperature. <i>Advanced Materials Interfaces</i> .

### Principal Author

Name of Principal Author (Candidate)	Kamrul Hassan
Contribution to the Paper	Prepared, edited and revised the review manuscript.
Overall percentage (%)	85%
Certification:	This paper reports on original research I conducted during the period of my Higher Degree by Research candidature and is not subject to any obligations or contractual agreements with a third party that would constrain its inclusion in this thesis. I am the primary author of this paper.
Signature	Date 19/10/2021

### Co-Author Contributions

By signing the Statement of Authorship, each author certifies that:

- the candidate's stated contribution to the publication is accurate (as detailed above);
- permission is granted for the candidate to include the publication in the thesis; and
- the sum of all co-author contributions is equal to 100% less the candidate's stated contribution.

Name of Co-Author	Le Yu
Contribution to the Paper	Edited and revised the manuscript.
Signature	Date 26/10/2021

Name of Co-Author	Dusan Losic
Contribution to the Paper	Supervised the development of work, edited, revised the manuscript and acted as the corresponding author.
Signature	Date 28 Oct 2021

Please cut and paste additional co-author panels here as required.

## RESEARCH ARTICLE

# Extrusion-Printed CNT–Graphene Sensor Array with Embedded MXene/PEDOT:PSS Heater for Enhanced NO<sub>2</sub> Sensing at Low Temperature

Kamrul Hassan, Nathan Stanley, Tran Thanh Tung, Pei Lay Yap, Hadi Rastin, Le Yu, and Dusan Losic\*


Wearable sensors are currently one of the top emerging areas with enormous growth potential. Low-cost fabrication techniques using simple and scalable printing technologies are making a significant impact on their development. Recent advances in high-performance gas/vapor sensors based on carbon nanomaterials have shown potential applications ranging from disease diagnostics to environmental monitoring and defences. Herein, a hybrid sensing material of 1D carbon nanotubes (CNTs) and 2D graphene is developed, and a conductive ink is formulated, which is applied for fabricating a nitrogen dioxide (NO<sub>2</sub>) gas sensor array within a compact design utilizing extrusion printing. To improve NO<sub>2</sub>-sensing performance and optimal operating temperature, a reverse-side layer is designed, which combines MXene and poly(3,4-ethylenedioxythiophene)-doped poly(styrene sulfonate) (PEDOT:PSS), and functions as a Joule heater. The printed CNT–graphene-based sensor with an embedded MXene/PEDOT:PSS heater is capable of detecting trace amounts of NO<sub>2</sub> gas (1 ppm) at 65 °C. The sensor is able to distinguish between various gases/volatile organic compounds and target NO<sub>2</sub> gas based on their chemical affinities. The printed CNT–graphene sensor array also demonstrates a high-level of recoverability, satisfied stability, durability, and reproducibility, which render this sensor a suitable candidate for practical applications.

## 1. Introduction

The rise of Internet-of-things (IoT) has contributed enormously to heightened printed electronics research.<sup>[1]</sup> To develop a smarter electronics ecosystem, various types of sensors and operational systems are being developed, which show potential increased security and quality of life.<sup>[2,3]</sup> Nevertheless, in order

K. Hassan, N. Stanley, T. T. Tung, P. L. Yap, H. Rastin, L. Yu, D. Losic  
School of Chemical Engineering and Advanced Materials  
The University of Adelaide  
Adelaide, SA 5005, Australia  
E-mail: dusan.losic@adelaide.edu.au

K. Hassan, N. Stanley, T. T. Tung, P. L. Yap, H. Rastin, L. Yu, D. Losic  
ARC Research Hub for Graphene Enabled Industry Transformation  
The University of Adelaide  
Adelaide, SA 5005, Australia

 The ORCID identification number(s) for the author(s) of this article can be found under <https://doi.org/10.1002/admi.202101175>.

DOI: 10.1002/admi.202101175

to be ubiquitous, the sensor system should be cost-effective, and in many cases, have a flexible footprint, which is inaccessible by conventional electronics.<sup>[4,5]</sup> Printed electronics are ideal for meeting these demands. First, printing processes are inherently low cost, as they often utilize additive manufacturing methods, which do not require vacuum systems or high temperatures.<sup>[6,7]</sup> Second, printed electronics are adaptable to a broad variety of substrates that can enable both large-area and flexible systems.<sup>[8]</sup> Sensors fabricated via printing methods have been demonstrated as applicable for fabrication of a wide range of devices including gas/volatile organic compound (VOC) sensing,<sup>[9,10]</sup> biosensing,<sup>[10]</sup> pressure sensing,<sup>[7,11]</sup> and temperature sensing.<sup>[12,13]</sup>

Printing approaches including screen, gravure, inkjet, flexographic, and extrusion processes have been fruitfully adopted for additive patterning of functional ink materials onto conformable, flexible, and/or rigid substrates that promise high-speed, large-scale, and low-cost production.<sup>[14]</sup>

The key elements of these printing technologies are liquid-phase conductive and nonconductive inks having variable physical characteristics such as rheological properties (surface tension and viscosity) and the concentration of fillers and/or additives. Numerous conductive fillers have been used for formulating printable inks including carbon particles, carbon nanotubes (CNTs), metal nanoparticles, metal oxide particles, conductive polymers, graphene (Gr), and other 2D materials.<sup>[14,15]</sup> Among them, Gr has become a leading contender for printed nonflexible/flexible electronics (e.g., sensors) as well as a good substitute to metal-based printable inks owing to its exceptional thermal, electrical, and mechanical characteristics with a remarkable carrier mobility ( $2 \times 10^5 \text{ cm}^2 \text{ V}^{-1} \text{ cm}^{-2}$ ).<sup>[9,16]</sup> Graphene inks with different formulations and characteristics have been reported previously for fabrication of patterned architectures with various resolution using screen and gravure printing,<sup>[17]</sup> spray printing,<sup>[18]</sup> inkjet printing,<sup>[19]</sup> and flexographic methods. These have been successfully applied to fabrication of electronic devices such as supercapacitors,<sup>[20]</sup> organic thin-film transistor electrodes,<sup>[21]</sup> radio frequency identification (RFID) devices,<sup>[22]</sup> chemical, temperature, and VOC sensors,<sup>[9]</sup>

as well as solar cells.<sup>[23]</sup> In contrast, CNTs also have flexibility, high on/off ratio, high mobility, and small operating voltage, which make this material viable for printed electronics.<sup>[23,24]</sup> Until now, the use of CNT has been advanced for fabrication of printed thin-film transistor (TFT) as flexible transistor devices with superior performance compared with other reported TFTs.<sup>[25,26]</sup> Even though considerable advancement has been made in graphene and CNT ink formulations, the formulation of hybrid inks, which include both 1D and 2D graphene for high-throughput printing technology, still needs efforts to develop. For example, uncontrollable entanglement and bundling mechanism of CNTs in ink formulations results in poor printability, and droplet ejection velocity can have an impact on the electrical conductivity of the ink. In particular, the formulation of hybrid inks from 1D and 2D materials that fulfill the printing characteristic (e.g., ejection of droplet, impact of the droplet on the substrate, and ink drying) criteria for printed gas-sensing applications still remains a challenge that needs to be tackled.

Nitrogen dioxide (NO<sub>2</sub>) is a reddish-brown, poisonous, oxidizing, and nonflammable gas with an irritating odor, which usually originates from the combustion of fossil fuel. This gas is extremely harmful to humankind and also threatens the environment, causing acid rain by increasing the ozone (O<sub>3</sub>) layer and global warming.<sup>[27]</sup> There is a strong demand to develop simple, cost-effective, selective, and sensitive devices to detect trace amounts of NO<sub>2</sub> gas in the air to improve human health and protect the environment.<sup>[27]</sup> Among several other sensing materials, carbon materials such as graphene and CNTs have attracted considerable research interest because of their excellent NO<sub>2</sub> gas-sensing properties attributed to high surface area and superior charge carrier mobility.<sup>[28]</sup> In addition, graphene and CNTs have excellent mechanical flexibility and robustness, which make these materials highly suitable for a flexible NO<sub>2</sub> sensor.<sup>[29]</sup> Printing technology is emerging as a fantastic tool for designing and fabricating precision flexible sensor arrays at low cost.<sup>[9,30]</sup> To date, the formulation of graphene and CNT inks to fabricate printed NO<sub>2</sub> sensors is still in its early stages.<sup>[30,31]</sup> For the development of printed flexible sensors, researchers have a particular concern regarding limit of detection (LOD) for NO<sub>2</sub> sensor's sensitivity and recovery. From the literature, it is evident that stability in a flexible medium, recoverability, selectivity, lower LOD, and synthesis-process complexity are still great challenges.<sup>[30,32]</sup> One way to overcome some of these challenges is to embed heating elements within the sensor devices. While integrated heating elements can resolve the stability, selectivity, and recoverability problems associated with NO<sub>2</sub> sensors, they have high power requirements, which remain a major obstacle. Moreover, integration of heaters within the flexible substrate (e.g., polyethylene terephthalate (PET), Kapton, and polyimide (PI)) is also challenging due to possible degradation or deformation of the flexible substrates at the operating temperatures of sensors. Thus, the advancement of printed NO<sub>2</sub> sensors on flexible substrates for overcoming the operation temperature restriction remains an inevitable challenge waiting to be addressed.

Herein, to address above-noted problems, threefold solution was taken whereas we formulated a CNT-graphene ink for extrusion printing to fabricate a printed sensor array with embedded MXene/poly(3,4-ethylenedioxythiophene)-doped

poly(styrene sulfonate) (PEDOT:PSS) heater for detecting trace amounts of NO<sub>2</sub> at low temperature. First, we present the development of the printable ink composed of 1D–2D hybrid carbon nanomaterials (CNT and graphene) dispersed within an environmentally friendly ethanol/Cyrene-based formulation for extrusion printing (Figure 1a). The CNT–graphene ink characteristics were specifically formulated to take advantage of the synergetic effect between the 1D and 2D hybrid carbon nanomaterials. Solvothermal graphene, which contains a high percentage of oxygen functionality, was selected and expected to provide excellent NO<sub>2</sub> sensing characteristics coupled with CNT-connected network, which ensures good electrical conductivity. It is worthy to note that the hybrid CNT–graphene-based chemical/gas sensor has a number of shortcomings including low absorption energy with poor recoverability and poor selectivity, which is possible to overcome by doping of heteroatom into the hexagonal carbon structure of graphene.<sup>[33,34]</sup> Nevertheless, this doping procedure into the hexagonal structure of graphene is hazardous, complex, as well as expensive that limits its applicability.<sup>[33]</sup> By using solvothermal graphene with high percentage of oxygen functionality overcomes the challenges of doping for functionalizing hybrid CNT–graphene materials. Besides, a heater was fabricated by spray-coating technique for embedding within the sensor. The heater was implemented as a Joule heater (low power heater) and fabricated with MXene nanosheets and PEDOT:PSS dispersed in dimethyl sulfoxide (DMSO) for spray coating onto a Kapton substrate (Figure 1b). To enhance the NO<sub>2</sub>-sensing performance, sensor design is also critical. We design sensor array (composed of five individual sensors) by following a parent and subordinate manner within a small area by extrusion printing to make compatible for IoT application with a purpose to maximize the active surface area on the back of the MXene/PEDOT:PSS heater (Figure 1c). Herein, the MXene/PEDOT:PSS heater property at low voltage was evaluated by controlling the loading of PEDOT:PSS to generate low-temperature heating for enhanced sensing. In the next step, the printability of the optimized CNT–graphene ink was fully investigated by rheological analysis, followed by extrusion printing of the sensor array on the back side of the MXene heater to demonstrate its printing performance. Finally, the sensing performance of the CNT–graphene ink at elevated temperature generated by the embedded MXene/PEDOT:PSS heater was characterized by exposure to low concentration of NO<sub>2</sub> gas to the designed printing sensor array (Figure 1d).

## 2. Results and Discussion

### 2.1. Characterization of Hybrid CNT–Graphene Inks and Extrusion-Printed Sensor Patterns

Morphological features of CNT–graphene ink and formulation components were characterized using SEM and TEM (Figure 2a–e). From Figure 2a, the CNT chains are fully wrapped by the graphene flakes and piled sequentially, whereas the surface of the graphene flakes is smooth because of the fused sheet structures of graphene. Moreover, the binder solution of polymeric EC binder and Cyrene helps to enhance the adhesion between the graphene flakes and distributed CNTs.

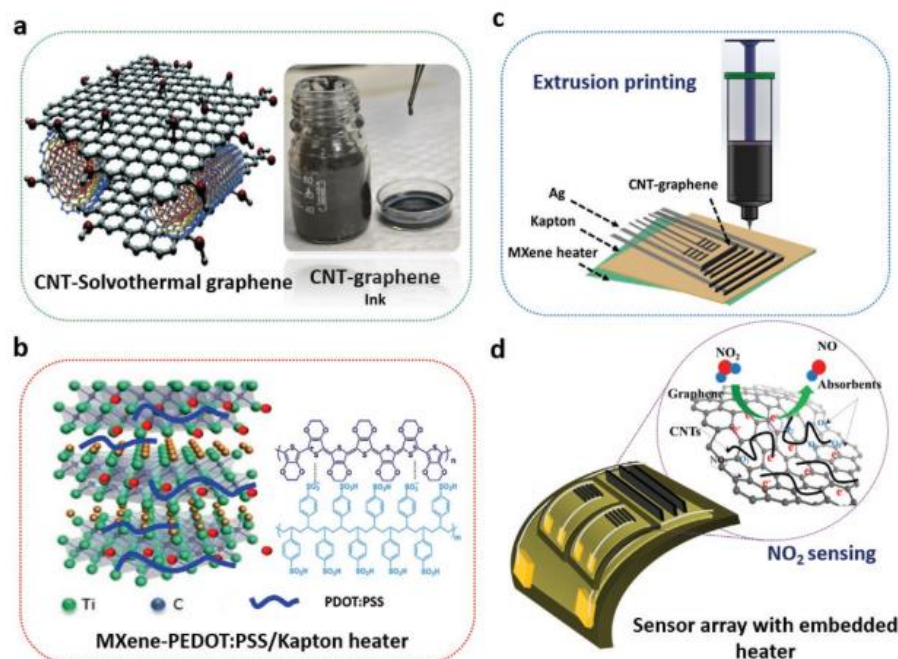


**Figure 1.** a–d) Schematic illustration of the fabrication process of extrusion-printed CNT–graphene ink-based sensor array with an embedded MXene/PEDOT:PSS thin-film heater for NO<sub>2</sub> gas sensing. MXene in (b): Reproduced with permission.<sup>[35]</sup> Copyright 2018, Wiley-VCH.

To illustrate the interconnection between CNT and graphene sheets, higher-magnification SEM and TEM analyses were performed and presented in Figure 2b and Figure 2c, respectively. Ordinarily, bare CNTs tend to form bundles because of the long-chain structure of individual CNT, which readily curl up into bundled structures (Figure 2d).

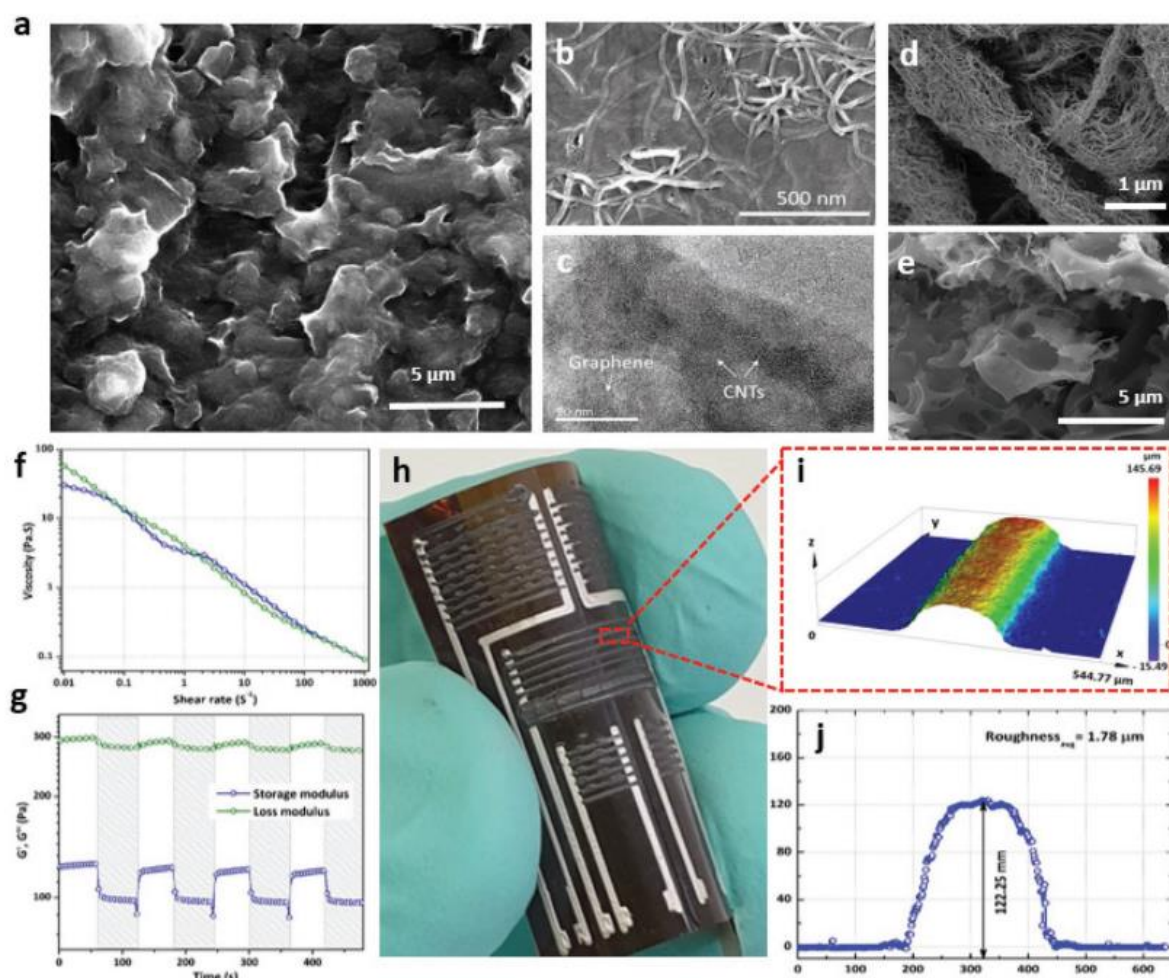
In this work, we used the solvothermal graphene in which graphene sheets have numerous cavities or holes that give this graphene material a foam-like structure consisting of weakly bonded fused graphene flakes (Figure 2e).<sup>[36]</sup> Before formulating the CNT–graphene ink, the solvothermal graphene was sonicated in ethanol for 15 min to break down the foam structure and obtain separated graphene flakes. Due to the solvothermal graphene morphology, cavities or holes still appear in the final formulated ink (Figure 2a), which increases the porosity of ink materials and enhanced the total surface area to volume aspect ratio of the material, which has advantage for enhancing NO<sub>2</sub> sensing.

Figure 2f illustrates the viscosity characteristics for the formulated CNT–graphene ink as a function of shear rate, which was recorded at a temperature of 20 °C. It is well known that the formulation of printable ink for extrusion printing depends on the rheological characteristics of the formulated printable ink (e.g., viscosity and surface tension).<sup>[9,23]</sup> Herein, the formulated CNT–graphene composites were well dispersed in Cyrene followed by ethanol evaporation with a resultant viscosity of ≈55 Pa s, which is within the viscosity range of 10–100 Pa s compatible with extrusion printing. Figure 2g demonstrates the storage and loss moduli of the CNT–graphene ink and shows that the storage modulus ( $G'$ ) of the formulated ink was lower than the loss modulus ( $G''$ ), which further confirms the fluidic

properties of the formulated ink at both high and low applied strains. In observation of these properties, the storage modulus ( $G'$ ) and loss modulus ( $G''$ ) decreased abruptly, which returned to their preliminary states after eliminating the added load. The recovery properties of the CNT–graphene ink exhibited thixotropic behavior, which allowed successful printing of the sensor array on a Kapton substrate via a printer nozzle.

Figure 2h shows the extrusion printing of CNT–graphene ink patterns as an array on Kapton yielded a line width of 256 μm. The cross-sectional 3D profile of the printed traces exhibited a constant 3D dome shape, marking the efficient formulation of the CNT–graphene ink for 3D extrusion printing, which was noted for all printed traces with an average thickness and roughness of 122.25 and 1.78 μm, respectively (Figure 2j). The dome morphology of the printed traces was attributed to solvent evaporation during annealing, which results from inward Marangoni flow caused by the surface tension gradient.<sup>[37]</sup> The Marangoni flow also helps to homogenize the ink droplet composition, which suppresses the coffee-ring effect over the printed traces.<sup>[9,37]</sup> In addition, the chain and layered structure of CNT along with sp<sup>2</sup>/sp<sup>3</sup> bonding in between graphene sheets with small lateral dimensions also reduces the folding and/or buckling of the printed flakes, which results in low surface roughness and good flake to flake contact. A short video of this rapid and sequential extrusion printing process can be found in Video SV1 (Supporting Information).

To confirm the elements on the surface of CNT–graphene ink and requisite ink formulation components, a performed XPS survey scan with two characteristic peaks for C1s and O1s at around 284.5 and 531.5 respectively, was observed (Figure S2, Supporting Information). Notably, results from the



**Figure 2.** a) SEM, b) high-magnification SEM, and c) TEM image of the CNT–graphene hybrid. SEM image of d) bare CNT and e) solvothermal graphene. Rheological characteristics of CNT–graphene inks, f) viscosity as a function of shear rate, and g) storage and loss moduli as a function of time at 20 °C. h) An optical photograph of extrusion-printed CNT–graphene ink-based sensor array. Characteristics analysis of 3D profile measurements of printed CNT–graphene ink measured by a 3D optical profilometer, i) 3D profile map of the represented printed trace, and j) cross-sectional profile (average) of printed trace for the selected area.

scan (Table S1, Supporting Information) illustrate that the surface of the CNT–graphene ink and its components (EC, CNT, and graphene) consisted of solely carbon and oxygen elements, and there was no evidence of other elements. From Table S1 (Supporting Information), both solvothermal graphene and CNT–graphene ink recorded high concentration of oxygen (14.86 and 28.09 at%, respectively), indicating that these two materials were enriched with oxygen functional groups, which was further confirmed by the elemental mapping of these materials (Figure S3, Supporting Information). The peak fitting of the high-resolution scan for the C1s core level of CNT–graphene ink and its components is shown in Figure 3a. From the figure it was observed that the total number of five peaks positioned at 284.8, 285.5, 286.5, 287.4, and 289.2 eV corresponding to C=C, C–C/C–H, C–O, C–O–C, and O–C–O, respectively, for CNT–graphene ink. Importantly, the intensity

of the C=C ( $sp^2$ ) peak was very low for the formulated ink due to the presence of EC in inks, whereas it was very high in bare CNT and graphene. Besides the C=C peak, the C–O–C peak was attributed in the CNT–graphene ink with high intensity, which was absent in other ingredients. The results from these deconvolution peak analysis from core C1s scanning suggests that the peaks attributed as C–O, C–O–C, and O–C–O from the fitting worked as active sites in between the CNT–graphene ink for elevated NO<sub>2</sub> sensing.

Raman spectroscopy and FTIR were used to characterize the associated functional groups in CNT–graphene ink and its components. Figure 3b shows the Raman spectra of bare CNT, solvothermal graphene, and CNT–graphene composite. The figure shows that the  $E_{2g}$  vibration mode or breathing mode of  $sp^2$  carbon atoms at D band ( $1354\text{ cm}^{-1}$ ), G band ( $1582\text{ cm}^{-1}$ ), and a highly broadened and low-intense 2D band (at  $2697\text{ cm}^{-1}$ )

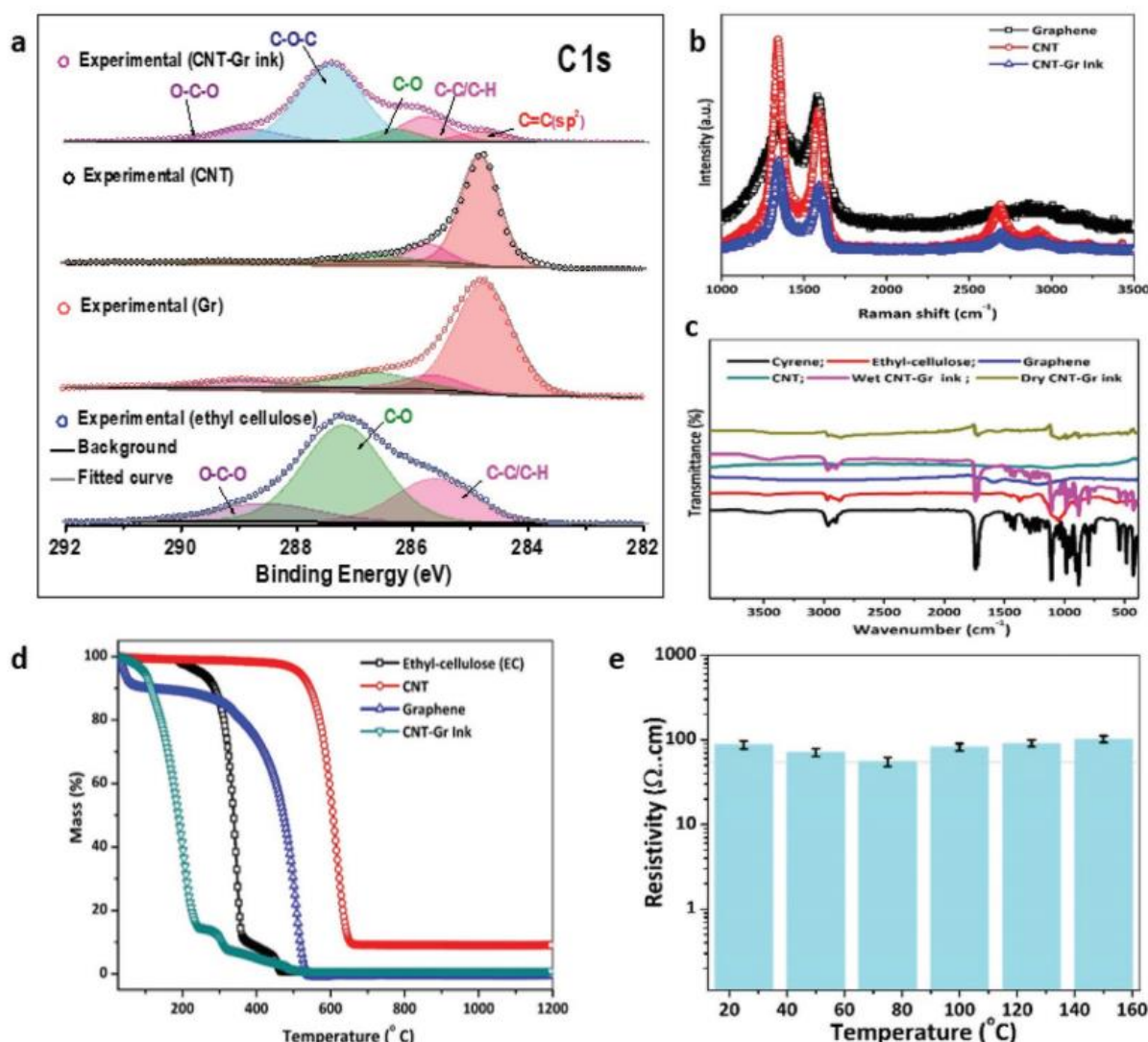


**Figure 3.** a) XPS, high-resolution spectra of C1s for CNT–graphene ink, and its ingredients. b) Raman and c) FTIR spectra of CNT–graphene ink and formulation components. d) TGA analysis of CNT–graphene ink and its ingredients. e) Resistivity characterization of CNT–graphene ink versus annealing temperature of blade-coated materials to anneal for 30 min.

because of double resonance transition resulting from two opposite phonon momentums for solvothermal graphene. This 2D band is very sharp for CNT and almost flattened down for the CNT–graphene composite.<sup>[36,38]</sup> Figure S4 (Supporting Information) shows the 3D Raman mapping with the ratio of  $I_D/I_G$  for CNT, solvothermal graphene, and CNT–graphene composite. The results illustrate that, for CNT–graphene composite, the  $I_D/I_G$  ratio is 0.95, which is lower than CNT (1.4) and higher than solvothermal graphene (0.8). This low aspect ratio of  $I_D/I_G$  ratio for CNT–graphene composite suggests low level of defects on solvothermal graphene flakes as well as CNT chain, which is significant for electron flow during the sensing mechanism.

Besides, these results appeared from Raman characteristics indicate no structural changes to the graphene flakes and CNT chains within the CNT–graphene ink. Figure 3c illustrates

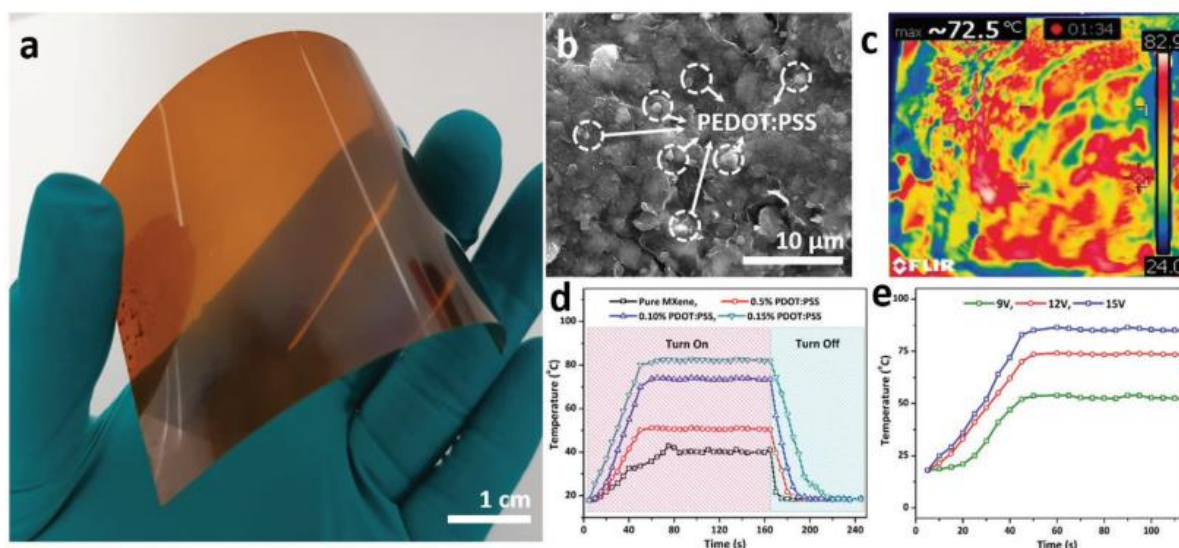
the FTIR spectra of Cyrene, EC, CNT, solvothermal graphene, CNT–graphene ink before and after annealing at 70 °C. It shows that EC had broad –OH absorption peak located at 1053 cm<sup>-1</sup> due to the polymeric structure (brown line). Nevertheless, no peaks associated with –OH (1340 cm<sup>-1</sup>) and –COOH (1710–1720 cm<sup>-1</sup>) groups were detected (blue line) for solvothermal graphene, which was an evidence of graphene formation not graphene oxide.<sup>[32]</sup> Before annealing, a peak of –OH at 1053 cm<sup>-1</sup> for EC was reduced in CNT–graphene composites, which was reduced in terms of intensity after annealing and appeared the peaks (2028–2159 cm<sup>-1</sup>) associated with graphene. These results suggest that after annealing, oxygen molecules associated with the polymeric binder were volatilized and the binder was partially decomposed, which decrease the mass of binder in the annealed ink.



Figure 3d illustrates the TGA of bare solvothermal graphene, CNT, EC, and CNT-graphene ink. It displays that the thermal decomposition of EC initiated at 200 and 400 °C, and no residues of EC remained. In the case of solvothermal graphene, thermal decomposition occurred in two stages: i) moisture from the solvothermal graphene was vaporized at <100 °C, and ii) the intermediates were volatilized with removal of all residues at ≥450 °C. By comparison, decomposition of bare CNT was initiated at 600 °C and fully volatilized at a temperature close to 650 °C. In CNT-graphene ink, the decomposition threshold for this composite material initiated at a temperature of about 70 °C, and the major decomposition occurred when the temperature reached 210 °C and fully volatilized at 250 °C. These results coupled with the resistivity examined after annealing in the range of 25–150 °C, suggesting that the primary evaporation of moisture from the composite material progresses through a contact in between the graphene flakes, and thus facilitates efficient charge transport via the CNT-graphene network. Figure 3e displays the films annealed at a temperature of 70 °C for 30 min showing high electrical conductivity (lower resistivity) compared with other tested annealing temperatures. Moreover, the resistivity increased for coated films above 100 °C due to the initial vaporization of moisture from EC, which causes the formation of elliptical spots between the graphene networks. It is noteworthy that, in the CNT-graphene ink, the decomposition threshold of EC shifted from higher to lower temperatures due to the presence of solvothermal graphene, which enhanced the ratio of oxygen molecules within the composite material. At 70 °C, annealing for just 30 min was optimal to obtain low resistivity for this CNT-graphene ink due to the effective charge-transport characteristics. Hence, an annealing condition of 70 °C for 30 min suggested good enough gaining the highly electrically conductive properties of the printed structures for sensing applications.

## 2.2. Characterizations of the MXene/PEDOT:PSS Thin-Film Heater

The electrochemical heater should be compatible with various substrates and applicable to various devices. In this study, a uniform MXene/PEDOT:PSS thin film was coated by the spray-coating method onto the Kapton substrate (Figure 4a). This example of heater fabrication demonstrates the feasibility of combining the thin-film heater fabrication with sensor and/or nano-electromechanical system (NEMS) technique. The morphological and microscopic properties of this MXene/PEDOT:PSS thin-film heater was characterized by SEM and Raman techniques. Figure 4b illustrates the morphology of the PEDOT:PSS-loaded MXene thin film. It shows that the PEDOT:PSS particles were distributed throughout the MXene surface randomly, where some of the PEDOT:PSS particles were encapsulated by the MXene sheets. This random distribution of non/encapsulated PEDOT:PSS particles on MXene sheets demonstrates the uniform characteristics of the thin film. Figure S5 (Supporting Information) illustrates the cross-sectional SEM image of MXene/PEDOT:PSS thin film and found the uniform thickness of 12 μm. Moreover, in the planar direction, PEDOT:PSS particles were distributed without creating any agglomeration, which may cause temperature fluctuations at the time of electrothermal measurement. Besides, to confirm the formation of MXene from MAX-phase, energy-dispersive X-ray spectroscopy (EDX) is analyzed, which shows the absence of Al component in the MXene spectrum (Figure S6, Supporting Information). In the Raman spectra of the MXene/PEDOT:PSS thin film, a highly broadened D band at around 1345 cm<sup>-1</sup> and a G band at around 1590 cm<sup>-1</sup> are observed, as shown in Figure S7 (Supporting Information), which are normally found in the characteristics of MXene.<sup>[39]</sup> For the electrothermal test, MXene combined with 0.05%, 0.1%, or 0.15% (wt%) of PEDOT:PSS particles



**Figure 4.** a) A photograph of MXene/PEDOT:PSS-based flexible heater, spray-coated on Kapton substrate. b) SEM image of MXene/PEDOT:PSS composites. c) The thermal image of MXene/PEDOT:PSS-0.10% heater. Time-dependent temperature profiles of d) the heater with various loading concentrations of PEDOT:PSS under the supplied voltage of 12 V and e) an MXene/PEDOT:PSS-0.10% heater under various voltage loads.

was prepared, and represented as MXene/PEDOT:PSS-0.05%, MXene/PEDOT:PSS-0.10%, and MXene/PEDOT:PSS-0.15%, respectively. Initially, the Kapton was fully insulative, and with the spray coating of MXene/PEDOT:PSS the resistance was measured in the range of several Ohms (Video SV2, Supporting Information). The sheet resistance of the thin-film heater with different loading of PEDOT:PSS particles is illustrated in Figure S8 (Supporting Information). It is well known that in the Joule heating system electrical power is defined by Equation (1)

$$P = U^2/R \quad (1)$$

For this Joule heating in the electrothermal measurement, it is worthy to note that a reduction of driving voltage occurred due to the decline of resistance for the same power input. In this study, direct current power was supplied to the thin-film heater and the elevated temperature was recorded with an infrared camera (Figure 4c). Here, for the electrothermal test, a driving voltage of 12 V was supplied and it was found that the temperature of the MXene/PEDOT:PSS thin-film heater increased gradually as a function of time until a steady state of temperature was reached (Video SV3, Supporting Information). After the power supply is turned off, the generated temperature decreased down to room temperature gradually following the trend of heating curve.

Figure 4d exhibits the time-dependent temperature profile of different PEDOT:PSS-loaded MXene film heaters, and it shows that the steady-state temperature increased proportionately with the concentration of PEDOT:PSS particles in the film. In the film heater content with 0.15% of PEDOT:PSS, the steady-state temperature was almost double (81 °C) compared with the pure MXene film heater (40 °C). This result reveals that the pure MXene heater required more than 30% of driving voltage to reach the saturated temperature generated by the 0.15% PEDOT:PSS-loaded MXene heater, which satisfied the electrical power formula. Importantly, a higher driving voltage is considered as a potential threat for the human body, which creates challenges for wearable electronics. For this reason, in applications related to human body contact, high driving voltages above the secure voltage suitable for human body (36 V) should be avoided.<sup>[40]</sup> Further Sui et al.<sup>[40]</sup> reported that the lower sheet resistance of a film heater for the Joule heating phenomenon causes higher transduction efficiency of the electric energy. However, this analysis indicates that the loading of PEDOT:PSS efficiently increases the electrothermal characteristics of the MXene film heater. Figure 4e exhibits the electrothermal response of 0.10% loading of PEDOT:PSS on MXene under voltage ratings of 9, 12, and 15 V, and found that the film heater illustrated a saturated temperature value of 72.5 °C with a heating rate of 1.31 °C s<sup>-1</sup> with a voltage power supply of 12 V. Literature reveals that the maximum achieved temperature for the carbon-based flexible heater was reached 200 °C under the supplied voltage of <30 V due to the restriction on the minimum resistance of the materials.<sup>[41–43]</sup> However, the calculated response time for this MXene/PEDOT:PSS thin-film heater was 42 s, where recovery time was 27 s. These elevated temperature characteristics of the PEDOT:PSS-loaded MXene-based thin-film heater make them suitable for integrated electronics (e.g., sensors, NEMS and micro-electromechanical systems)

competing with other existing flexible heaters. This enable us to fabricate a PEDOT:PSS/MXene-based thin-film flexible heater on one side of Kapton, where on the other side of the Kapton, we printed a sensor array for elevated NO<sub>2</sub> sensing from human breath at low temperature.

### 2.3. Characterization of Printed CNT–Graphene Sensor Array with the Embedded Heater for NO<sub>2</sub> Sensing

The sensing mechanism of chemoresistive sensors is mainly dependent on the change in conductance of the sensing materials after interaction with molecules of the target gas, corresponding to the characteristics of the exposed gas.<sup>[27]</sup> For the sensing of NO<sub>2</sub> gas molecules, it is worthy to note that NO<sub>2</sub> is an oxidizing gas, which traps free electrons at the time of gas exposure and, as a result, changes the conductance of the sensing materials. The mechanism of NO<sub>2</sub> sensing of CNT–graphene-based sensor array is shown in Figure 5a. Figure 5a1,a2,b1,b2 illustrates the sensing mechanism of pure CNT and CNT–graphene materials, respectively. In an open-air environment, generally oxygen molecules come to the sensing layer and trap electrons, which creates oxygen adsorbents (O<sub>2</sub>(ads)) on the sensing layer (Equation (2))



After exposure to NO<sub>2</sub> gas, the NO<sub>2</sub> gas molecules collect the electrons from the CNT surface and dissociated as NO, which creates more oxygen adsorbents (O<sup>2-</sup>) (Equation (3))



Subsequently, oxygen adsorbents (O<sup>2-</sup>) behave as anions (Equation (4)), which play a role as active sites to adsorb NO<sub>2</sub> molecules



Following this, with the reaction of half of the oxygen molecules, dissociated NO can convert into NO<sub>2</sub> molecules once again (Equation (5))



The CNT–graphene composite material functions as a p–n heterojunction due to configuration of p-type CNT and n-type graphene, which creates a depletion layer in the sensing materials (Figure 5a,b2). This depletion layer plays a vital role in the NO<sub>2</sub>-adsorption mechanism by providing more oxygen adsorbents (active sites), where NO<sub>2</sub> molecules can interact with the graphene sheets and withdraw more electrons from the heterojunction (Figure 5a,b2). As a consequence, the CNT–graphene-sensing material becomes destabilized. The system reacts to regain stability by electron movement from the CNT surface to the graphene sheets, which fills the electron vacancies, thus decreasing the sensor resistance. Moreover, the graphene sheets provide an efficient pathway to transfer charges from the CNT to the NO<sub>2</sub> molecules through the heterojunction, which

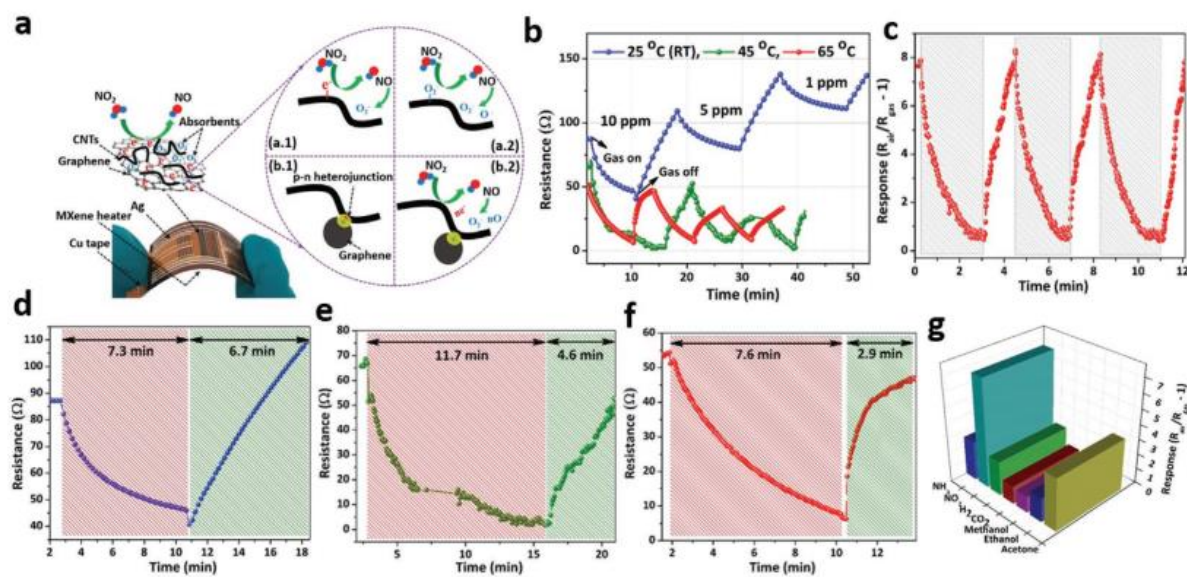


**Figure 5.** a) Schematic presentation of NO<sub>2</sub>-sensing mechanism of a1,a2) CNT and b1,b2) CNT–graphene composites. b) Dynamic resistance variation of the CNT–graphene printed sensor to various concentrations of NO<sub>2</sub> gas at different temperatures originated from an embedded MXene/PEDOT:PSS heater. c) Periodic exposure and response of a CNT–graphene-based printed sensor to 5 ppm concentrated NO<sub>2</sub> gas at 65 °C. Response–recovery time properties for the CNT–graphene-printed sensor to 5 ppm concentrated NO<sub>2</sub> gas at temperature of d) 25 °C, e) 45 °C, and f) 65 °C. g) Selectivity histogram of a CNT–graphene-based printed sensor to 5 ppm NO<sub>2</sub> gas; NH<sub>3</sub> gas; 1000 ppm of H<sub>2</sub> and CO<sub>2</sub> gases; and 100 ppm of acetone, ethanol, and methanol at a temperature of 65 °C.

accelerates the creation of more active sites on the sensing layer surface at the time of NO<sub>2</sub> dissociation (Equation (6))<sup>[27]</sup>



This process occurs continuously within the CNT–graphene material throughout the NO<sub>2</sub> exposure, which causes remarkable enhancement of the sensor response. Figure 5b illustrates the real-time resistance variation of the CNT–graphene sensor array in terms of different NO<sub>2</sub> gas concentrations at different temperatures. As the temperature increases, the total resistance for the sensor array decreased due to material decomposition (refer to Figure 3d), which also affects the sensor response value (Figure S9, Supporting Information; *I*–*V* curve). At room temperature, the sensor array exhibited a drift of baseline resistance over time, most likely due to the slower decomposition of oxygen molecules and reduced number of active sites. In contrast, increasing the temperature of the sensing materials enhances the decomposition rate of oxygen molecules due to faster charge transfer between the heterojunctions. As a result, the electrochemical reaction at the surface of the sensing material after exposure to NO<sub>2</sub> molecules becomes highly efficient, thus maximizing the change in resistance by reducing baseline steady-state resistance.

Analysis of the CNT–graphene ink-based sensor array indicated an excellent detection of NO<sub>2</sub> gas in the range from 1 to 10 ppm at the temperature of 65 °C (sensor temperature maintained by an embedded MXene heater). The as-fabricated sensor array displayed enhanced sensitivity ( $A_R$  8) with good repeatability to NO<sub>2</sub> gas at 65 °C (Figure 5c). The response values for each individual sensor within the array also increased at the

elevated temperatures, which improved the resistive response values for the entire sensor array (Figure S10, Supporting Information). The enhancement of response is due to a higher number of p–n heterojunctions, which create more active sites for adsorption of a higher proportion of NO<sub>2</sub> gas molecules. Along with the response values, the increased temperature also enhanced the recovery time (6.5 min at 25 °C, 4.6 min at 45 °C, and 2.9 min at 65 °C), whereas the response time was not noticeably affected (Figure 5d–f). In this study, sensor response was measured in an open-air environment; thus, the supplied NO<sub>2</sub> gas would be mixed to a small extent with the surrounding air, reducing the concentration of NO<sub>2</sub> and causing slightly increased response time. Nevertheless, the recovery time characteristics for the sensor array were enhanced through the CNT–graphene composites, which delivered an efficient charge-transfer pathway between CNTs and NO<sub>2</sub> gas molecules with low binding energy.<sup>[44]</sup> Moreover, in an open-air environment, the possibility of NO<sub>2</sub> gas elimination from the sensing surface is much higher than in a closed chamber, which also facilitated recovery of the sensor array toward its initial state.

Previous studies reveal that human breath consists of hundred types of VOCs, gases, and moisture.<sup>[45]</sup> For this study, selectivity was characterized at 5 ppm NO<sub>2</sub> and 1000 ppm of H<sub>2</sub>, CO<sub>2</sub>, and 100 ppm of acetone, ethanol, and methanol; these VOCs are normally present in human breath.<sup>[45]</sup> Figure 5g presents the response values of the as-fabricated sensor array under exposure to various tested gases and VOCs, and it was found that the fabricated sensor array exhibited superior selectivity characteristics toward NO<sub>2</sub> due to the preferable adsorption capability of carbon materials toward NO<sub>2</sub> molecules. The as-fabricated sensor array can be effective for

**Table 1.** A comparative study of the chemoresistive sensor for NO<sub>2</sub> gas detection.

NO <sub>2</sub> -sensing material	NO <sub>2</sub> detection range [ppm]	Sensor response, $A_R = \frac{R_0 - R}{R_0}$	Response/recovery time	Ref.
Based on carbon composites				
Al/reduced graphene oxide (rGO)/PI	1.2–5	0.02 at 1.2 ppm	>5 min/35 min	[48]
rGO/PET	1–20	0.115 at 5 ppm	7 min/28 min	[49]
Ag/S/rGO	0.2–5	0.387 at 5 ppm	30 min/NA	[30]
CNTs/rGO/PI	0.5–10	0.13 at 5 ppm	60 min/60 min	[50]
Multi-wall carbon nanotubes (MWCNTs)/PET	1–15	0.19 at 15 ppm	≈12 min/42 min	[51]
WO <sub>3</sub> /MWCNTs	0.1–10	0.14 at 5 ppm	10 min/27 min	[28]
ZnO/rGO/sodium alginate	0.1–10	0.176 at 5 ppm	13.15 min/7.7 min	[27]
Based on metal oxides				
SnO <sub>2</sub> /ZnO/Cr <sub>2</sub> O <sub>3</sub>	2–10	17.5 at 2 ppm	9.1 min/1.67 min	[52]
Ga <sub>2</sub> O <sub>3</sub> /ZnO	10–200	NA	14 min/6.67 min	[53]
In <sub>2</sub> O <sub>3</sub>	0.05–0.25	10.5 at 0.05 ppm	2 min/2.5 min	[54]
ZnO/CuO	1–100	17.5 at 100 ppm	0.14 min/3.28 min	[55]
CNT–Gr ink	1–10	8 at 5 ppm	7.6 min/2.9 min	This study

the selective analysis of target gases due to the highly selective absorption of NO<sub>2</sub> by the 1D CNT and 2D graphene. When the CNT–graphene sensor is exposed to air, it adsorbs more oxygen on the CNT–graphene hybrid material and captures more free electrons to form oxygen adsorbents. At the optimal operating temperature of 65 °C, the catalytic activity of the CNT–graphene toward NO<sub>2</sub> decomposition might be strongly facilitated. At this stage, the reaction (between CNT–graphene and NO<sub>2</sub> at a certain temperature) might be an exothermic and spontaneous process, providing sufficient surface energy to overcome the bond energy of NO<sub>2</sub> (312.7 kJ mol<sup>-1</sup>). In addition, due to the higher bond energies compared to NO<sub>2</sub> resulted in less sensitivity toward H<sub>2</sub> (436 kJ mol<sup>-1</sup>) and CO<sub>2</sub> (1498 kJ mol<sup>-1</sup>). However, the reactions between CNT–graphene and other test gases are endothermic and cannot be spontaneous, resulting in reduced sensor responses. Moreover, the effect of humidity on the sensor was investigated. Humidity is one of the influencing factors on gas-sensing properties.<sup>[46]</sup> It was reported that specifically, for NO<sub>2</sub> sensing, both water and NO<sub>2</sub> molecules behave as oxidizing agents, and consequently, result in an increase in sensor response.<sup>[47]</sup> Nevertheless, because of the elevated temperature (65 °C) originated from the embedded MXene/PEDOT:PSS heater, the as-fabricated sensor array showed a negligible change in sensitivity due to changes in humidity up to RH = 80% during exposure to NO<sub>2</sub> gases (Figure S11, Supporting Information).

To prove the stability and reproducibility, in this study, five similarly configured sensor arrays were used, and none of them demonstrated an open-circuit failure even upon exposure to NO<sub>2</sub> gas severally. In fact, these as-fabricated sensor arrays have shown quite robust behavior. For further assessment, another five similarly configured sensor arrays were exposed to 5 ppm concentration of NO<sub>2</sub> gas over a 14 day period. Figure S12a,b (Supporting Information) illustrates the tested sensor arrays' response as well the effect on its baseline resistance, which demonstrated exceptional durability, stability, and reproducibility. In addition, the extrusion-printed CNT–graphene sensor

array with the embedded MXene/PEDOT:PSS heater demonstrated a low limit of detection, high response, enhanced recovery time characteristics, and excellent durability and stability to NO<sub>2</sub> gas at moderate temperature, compared to earlier reported sensing devices (Table 1).

### 3. Conclusion

This work describes the advancement of a CNT–graphene-based sensor array with an embedded MXene heater, fabricated by an extrusion printing technique for detecting trace amounts of NO<sub>2</sub> gas. The development of a new embedded MXene heater prepared by spray coating on the back of the printed sensor array is demonstrated, which nicely overcomes the challenge of integrating a heater within the sensor system to achieve the optimal operating temperature with low power consumption for selective detection of NO<sub>2</sub> gas. The specially designed hybrid ink was formulated by combining 1D CNT and 2D graphene with Cyrene as a solvent to provide a facile route to achieve sustainable, environmentally friendly, low-cost sensor's fabrication. The new CNT–graphene ink was successfully used for printing at high-resolution compact, array-patterned architectures with a resistivity as low as 70 Ω cm<sup>-1</sup> after annealing at 70 °C for 30 min, as a chemoresistive sensing device for NO<sub>2</sub> detection. By controlling the loading of MXene nanosheets and PEDOT:PSS, the embedded heater in the sensor systems achieved a temperature of up to 73 °C within <45 s from a 12 V voltage supply at a power of 2 W. Excellent performance characteristics were demonstrated for the sensor array toward NO<sub>2</sub> gas as highlighted by fast recovery time (2.9 min at 5 ppm), good response time (7.6 min at 5 ppm), high response value (8 at 5 ppm), a detection limit of 1 ppm, excellent stability, and reproducibility with high selectivity toward NO<sub>2</sub> gas at temperature (65 °C) in the presence of various gases (H<sub>2</sub> and CO<sub>2</sub>), and a set of VOCs (ethanol, methanol, and acetone). Overall, this study demonstrates a simple, affordable, low-cost, and valuable

technique for fabrication of a sensor array utilizing extrusion-printed CNT-graphene ink as the sensing material, and a spray-coated MXene heater embedded into the sensor device that overcomes the challenge of heater integration. The new device capable of detecting trace amounts of NO<sub>2</sub> gas, paves a new path toward sustainable, low-cost, and environmentally friendly printable devices for human health monitoring and/or tracking applications.

#### 4. Experimental Section

**Preparation of CNT-Graphene Ink:** The formulation of CNT-graphene ink for extrusion printing was initiated by preparing the binder solution. A slurry of ethyl cellulose (EC; 2 wt%, 15.8 mg mL<sup>-1</sup>) was prepared by the addition of ethyl cellulose (0.25 g) into ethanol (10 mL) and bath ultrasonication until all solids were dispersed. The slurry was stored in a sealed glass container at ambient temperature and ultrasonicated just prior to use. For ink formulation, multiwalled carbon nanotubes (86 mg) (NC7000, Nanocyl, Belgium, with a diameter of 8–10 nm and a length of 5–10 μm) and solvothermal graphene (50 mg) (GRAPH-001, Carbon Allotropes) were added into the binder solution (2.6 mL, 105 mg equiv.), followed by additional ethanol (10 mL). The mixture was subjected to probe sonication (Branson) in an ice bath for 3 h. Subsequently, Cyrene (0.50 g, 0.80 mL) was added into the mixture solution for stable dispersion of CNT and graphene materials. To increase the viscosity of this dispersion, removal of the ethanol from the ethanol/Cyrene solution was conducted by the solvent-exchange method via a rotary evaporation system under vacuum (100 mbar, 30 °C, water bath). Finally, the remaining CNT-graphene viscous dispersion was collected from the rotary evaporation system for using as a printable ink for extrusion printing to fabricate the sensor array.

**Preparation of MXene Nanosheets:** Titanium carbide (Ti<sub>3</sub>C<sub>2</sub>) MXene was synthesized by selective etching of the aluminum (Al) layers from the MAX phase of Ti<sub>3</sub>AlC<sub>2</sub> as reported in an earlier study with slight modification.<sup>[38]</sup> In brief, etchant solution for MXene nanosheet preparation was first synthesized by dissolving lithium fluoride (500 mg) in 9 M HCl (10 mL) under ambient conditions (20 °C) with mild stirring for 15 min. Following this MAX-phase rock (0.5 g) was supplied by Carbon (Ukraine), which was ground into fine powder with a particle size of 25 μm and added carefully to the etchant solution at 35 °C, and left to react overnight. Subsequently, the as-synthesized product was washed numerous times with deionized (DI) water with centrifugation (3500 rpm) until the pH of the supernatant reached ≈6. Finally, the sedimentation of etched Ti<sub>3</sub>C<sub>2</sub> MAX was subjected to sonication for 2 h followed by centrifugation (4200 rpm) for a further 2 h to obtain Ti<sub>3</sub>C<sub>2</sub> MXene nanosheets.

**Fabrication of the MXene/PEDOT:PSS-Based Thin-Film Heater:** In comparison with other reported electrothermal devices, the MXene/PEDOT:PSS thin-film heater had a relatively simple fabrication process as follows. First, Ti<sub>3</sub>C<sub>2</sub> MXene nanosheets were dispersed in DI water with a concentration of 5 mg mL<sup>-1</sup>. Next, different concentrations (0.5, 0.10, and 0.15 wt%) of PEDOT:PSS (Clevios PH 1000, Heraeus, Germany) were mixed with 5 wt% DMSO (Chem-Supply) under mild stirring at 20 °C. The MXene suspension and PEDOT:PSS solution were mixed and subjected to probe sonication for 30 min in an ice bath to produce a homogeneous suspension. The mixed suspension was spray-coated onto Kapton film (20 × 20 cm) with a fixed coating rate of 0.1 mL cm<sup>-2</sup> to fabricate a thin-film heater. The as-fabricated film was dried in air at room temperature (20 °C) for 24 h. Finally, copper (Cu) tape was attached on the edges of the thin film as a pair of electrodes to supply current to power the MXene thin-film heater.

**Characterization of the MXene/PEDOT:PSS-Based Thin-Film Heater:** Electrical testing of the MXene/PEDOT:PSS-based thin-film heater was carried out using a Keithley power supply (SourceMeter 2400) by varying the voltage from 9 to 12 V, and up to 15 V. A direct current power was

applied to the heater, and the response was recorded by an infrared-thermal camera (FLIR E60 series, FLIR system, Estonia).

**Extrusion Printing of CNT-Graphene Ink and Fabrication of Sensor Array with an Embedded MXene/PEDOT:PSS Heater:** A sensor array for detection of NO<sub>2</sub> gas was fabricated by direct extrusion printing of CNT-graphene ink onto the opposite side of the MXene thin-film heater. Initially, the sensor array was designed using EAGLE design software (Autodesk) and converted to Gerber file format suitable for 3D extrusion printing (Voltera, V-One). Subsequently, thin traces of flexible silver (Ag) ink (line width = 200 μm) were printed on the opposite side of the MXene thin-film heater by using the 3D extrusion printer for connecting the pair electrodes. The CNT-graphene inks were then printed according to the array design on the prepatterned Ag with a three-axis (x–y–z) motion control system along with 1 μm positioning resolution. A nozzle with 225 μm inner diameter was used to pattern the CNT-graphene inks. The speed of the nozzle was set at 400 mm min<sup>-1</sup> and the nozzle-to-substrate distance was changed from 50 to 100 μm. In order to fabricate the sensor, small pieces of copper tapes were connected to the Ag electrodes using Ag paste to establish electrical connection to the electrochemical workstation for sensor characterization.

**Materials' Characterization:** The morphology, element mapping, and EDX analysis of the materials were studied using scanning electron microscope (SEM) equipped with EDX silicon drift Detectors (field emission scanning electron microscopes, Quanta 450 FEG, FEI, USA, EDX, Ultim Max 170 mm SDD, Oxford Instruments, UK) at 10–15 kV (operating voltage).

Bright-field transmission electron microscopy (TEM) images of CNT-graphene hybrid ink were acquired using an FEI Titan Themis.

The functional groups in the samples were identified by Fourier transform infrared spectroscopy (FTIR, Nicolet 6700, Thermo Fisher) in the range of 500–4000 cm<sup>-1</sup>. X-ray diffraction (XRD) with Cu X-ray tube (600 Miniflex, Rigaku, Japan) was performed under 40 kV and 15 mA with 10° min<sup>-1</sup> scan speed at 2θ = 5°–80° to probe the bulk-phase identification.

Thermal properties of the materials were investigated using thermal gravimetric analysis (TGA)/DSC 2, STare System (Mettler Toledo, Switzerland) under air atmosphere with the samples being heated in an alumina crucible to 1000 °C at a 10 °C min<sup>-1</sup> heating rate.

The surface elemental composition and chemical species of the materials were studied using X-ray photoelectron spectroscopy (XPS; AXIS Ultra\_DLD, Kratos, UK) equipped with a monochromatic Al Kα radiation source (hν = 1486.7 eV) at 225 W, 15 kV, and 15 mA. XPS wide scans were recorded at 0.5 eV step size from –10 to 1100 eV at the pass energy of 160 eV, while the narrow scans were collected at a 0.1 eV step size and a pass energy of 20 eV. The peak fitting and deconvolution were analyzed using Casa XPS software with the core-level spectra involved calibrated to the primary peak (C–C/C–H peak) of adventitious carbon at 284.8 eV. The full width at half maximum (fwhm) for all corresponding components was constrained with the difference of 0.2 eV.

Raman spectra were obtained using a Horiba XploRA Raman microscope equipped with a 532 nm laser. Measurements for the sensor-array-printed pattern thickness were collected on extrusion-printed films on Kapton using a Dektak 150 Stylus surface profiler.

The shear viscosity of the formulated ink was measured using the Physica MCR 302 rheometer equipped with a 50 mm cone and plate geometry at shear rates of 1–1000 s<sup>-1</sup>, and the temperature for the measurements was maintained by a Peltier plate. Rheological properties of the as-synthesized inks were achieved in oscillation mode by calculating storage modulus (G') and loss modulus (G'') over time. In this method, repetitive strain ranging from 1% to 50% was applied on the ink samples, and the response value of the sample to the applied strain was traced over four cycles.

To characterize the electrical properties of the ink, sheet resistance was measured for the conductive film using the four-point probe system (CMT series JANDEL four-point probe), where ink materials were blade-coated onto glass substrates and annealed in an air oven system with variation of the temperature.

**Characterizations of Sensor Array with an Embedded Heater.** For NO<sub>2</sub>-sensing measurement, the CNT–graphene-based sensor array with an embedded heater was placed in the center of a U-shaped support-stand under ambient conditions (open air). Using an electrochemical workstation (CH Instruments), the relative response ( $A_R$ ) of the sensor was recorded. To ensure the flow of target NO<sub>2</sub> gas, a narrow tube was placed on the top of the sensor device. The NO<sub>2</sub>-sensing characteristics of the printed sensors were characterized by recording the chemoelectrical response upon exposure to NO<sub>2</sub> gas and synthetic air, in which the concentration of the mixture was controlled by varying the synthetic air flow rate from 200 to 4 mL min<sup>-1</sup> through NO<sub>2</sub> gas at room temperature (20 °C). All as-fabricated sensors were tested under ambient conditions at a fixed temperature supplied by the embedded MXene/PEDOT:PSS thin-film heater. The sensor response ( $A_R$ ) is defined by Equation (7)

$$A_R = \frac{R_0 - R}{R_0} \quad (7)$$

where  $R_0$  is the initial resistance ( $\Omega$ ) and  $R$  is the resistance ( $\Omega$ ) of the sensing materials when exposed to the NO<sub>2</sub> gas. The response-recovery time characteristics of the sensor array were calculated as the time to reach 90% of the total resistance change. The relative humidity (RH) of experimental condition was varied from RH-40% to RH-80% using a water bubbler controller and measured by a hygrometer (Testo-625).

## Supporting Information

Supporting Information is available from the Wiley Online Library or from the author.

## Acknowledgements

The authors acknowledge financial support from the Australian Research Council (ARC Research Hub for Graphene Enabled Industry Transformation, IH15010003 and ARC NS210100255). The authors would like to acknowledge Circa Group Ltd., Australia for the generous gift of Cyrene solvent applied in this research.

## Conflict of Interest

The authors declare no conflict of interest.

## Data Availability Statement

Research data are not shared.

## Keywords

CNT–graphene ink, extrusion printing, MXene heater, NO<sub>2</sub> sensing, sensor array

Received: July 8, 2021  
Revised: September 2, 2021  
Published online: November 15, 2021

- [1] Y. Zhan, Y. Mei, L. Zheng, *J. Mater. Chem. C* **2014**, *2*, 1220.  
[2] A. Zanella, N. Bui, A. Castellani, L. Vangelista, M. Zorzi, *IEEE Internet Things J.* **2014**, *1*, 22.  
[3] A. C. Marques, A. R. Cardoso, R. Martins, M. G. F. Sales, E. Fortunato, *ACS Appl. Nano Mater.* **2020**, *3*, 2795.

- [4] J. Guo, R. Wen, Y. Liu, K. Zhang, J. Kou, J. Zhai, Z. L. Wang, *ACS Appl. Mater. Interfaces* **2018**, *10*, 8110.  
[5] B. Kulyk, B. F. Silva, A. F. Carvalho, S. Silvestre, A. J. Fernandes, R. Martins, E. Fortunato, F. M. Costa, *ACS Appl. Mater. Interfaces* **2021**, *13*, 10210.  
[6] S. R. Forrest, *Nature* **2004**, *428*, 911.  
[7] J. B. Andrews, J. A. Cardenas, C. J. Lim, S. G. Noyce, J. Mullett, A. D. Franklin, *IEEE Sens. J.* **2018**, *18*, 7875.  
[8] S. Khan, L. Lorenzelli, R. S. Dahiya, *IEEE Sens. J.* **2014**, *15*, 3164.  
[9] K. Hassan, T. T. Tung, N. J. Stanley, P. L. Yap, F. Farivar, H. Rastin, M. J. Nine, D. Losic, *Nanoscale* **2021**, *13*, 5356.  
[10] L. Li, L. Pan, Z. Ma, K. Yan, W. Cheng, Y. Shi, G. Yu, *Nano Lett.* **2018**, *18*, 3322.  
[11] A. F. Carvalho, A. J. Fernandes, C. Leitão, J. Deuermeier, A. C. Marques, R. Martins, E. Fortunato, F. M. Costa, *Adv. Funct. Mater.* **2018**, *28*, 1805271.  
[12] S. Harada, W. Honda, T. Arie, S. Akita, K. Takei, *ACS Nano* **2014**, *8*, 3921.  
[13] Y. Yamamoto, S. Harada, D. Yamamoto, W. Honda, T. Arie, S. Akita, K. Takei, *Sci. Adv.* **2016**, *2*, e1601473.  
[14] T. S. Tran, N. K. Dutta, N. R. Choudhury, *Adv. Colloid Interface Sci.* **2018**, *261*, 41.  
[15] A. T. Vicente, A. Araújo, M. J. Mendes, D. Nunes, M. J. Oliveira, O. Sanchez-Sobrado, M. P. Ferreira, H. Águas, E. Fortunato, R. Martins, *J. Mater. Chem. C* **2018**, *6*, 3143.  
[16] Z. Yang, R. Gao, N. Hu, J. Chai, Y. Cheng, L. Zhang, H. Wei, E. S.-W. Kong, Y. Zhang, *Nano-Micro Letters* **2012**, *4*, 1.  
[17] X. Huang, T. Leng, X. Zhang, J. C. Chen, K. H. Chang, A. K. Geim, K. S. Novoselov, Z. Hu, *Appl. Phys. Lett.* **2015**, *106*, 1.  
[18] X. Huang, K. Pan, Z. Hu, *Sci. Rep.* **2016**, *6*, 38197.  
[19] W. Li, F. Li, H. Li, M. Su, M. Gao, Y. Li, D. Su, X. Zhang, Y. Song, *ACS Appl. Mater. Interfaces* **2016**, *8*, 12369.  
[20] L. Wang, S. Chen, T. Shu, X. Hu, *ChemSusChem* **2020**, *13*, 1330.  
[21] S. Lim, B. Kang, D. Kwak, W. H. Lee, J. A. Lim, K. Cho, *J. Phys. Chem. C* **2012**, *116*, 7520.  
[22] K. Y. Shin, J. Y. Hong, J. Jang, *Adv. Mater.* **2011**, *23*, 2113.  
[23] K. Hassan, M. J. Nine, T. T. Tung, N. Stanley, P. L. Yap, H. Rastin, L. Yu, D. Losic, *Nanoscale* **2020**, *12*, 19007.  
[24] A. Javey, J. Guo, Q. Wang, M. Lundstrom, H. Dai, *Nature* **2003**, *424*, 654.  
[25] C. Cao, J. B. Andrews, A. Kumar, A. D. Franklin, *ACS Nano* **2016**, *10*, 5221.  
[26] M. Ha, Y. Xia, A. A. Green, W. Zhang, M. J. Renn, C. H. Kim, M. C. Hersam, C. D. Frisbie, *ACS Nano* **2010**, *4*, 4388.  
[27] K. Hassan, R. Hossain, V. Sahajwalla, *Sens. Actuators, B* **2021**, *330*, 129278.  
[28] U. Yaqoob, D.-T. Phan, A. I. Uddin, G.-S. Chung, *Sens. Actuators, B* **2015**, *221*, 760.  
[29] W. Yang, K. R. Ratnac, S. P. Ringer, P. Thordarson, J. J. Gooding, F. Braet, *Angew. Chem., Int. Ed.* **2010**, *49*, 2114.  
[30] L. Huang, Z. Wang, J. Zhang, J. Pu, Y. Lin, S. Xu, L. Shen, Q. Chen, W. Shi, *ACS Appl. Mater. Interfaces* **2014**, *6*, 7426.  
[31] K. A. Mirica, J. M. Azzarelli, J. G. Weis, J. M. Schnorr, T. M. Swager, *Proc. Natl. Acad. Sci. USA* **2013**, *110*, E3265.  
[32] Y. Jian, W. Hu, Z. Zhao, P. Cheng, H. Haick, M. Yao, W. Wu, *Nano-Micro Lett.* **2020**, *12*, 71.  
[33] U. Yaqoob, A. I. Uddin, G.-S. Chung, *Sens. Actuators, B* **2016**, *224*, 738.  
[34] T. T. Tung, C. Pham-Huu, I. Janowska, T. Kim, M. Castro, J. F. Feller, *Small* **2015**, *11*, 3485.  
[35] S. Yang, P. Zhang, F. Wang, A. G. Ricciardulli, M. R. Lohe, P. W. M. Blom, X. Feng, *Angewandte Chemie* **2018**, *57*, 15491.  
[36] M. Choucair, P. Thordarson, J. A. Stride, *Nat. Nanotechnol.* **2009**, *4*, 30.  
[37] M. Singh, H. M. Haverinen, P. Dhagat, G. E. Jabbour, *Adv. Mater.* **2010**, *22*, 673.

- [38] K. Pan, Y. Fan, T. Leng, J. Li, Z. Xin, J. Zhang, L. Hao, J. Gallop, K. S. Novoselov, Z. Hu, *Nat. Commun.* **2018**, *9*, 5197.
- [39] H. Rastin, B. Zhang, A. Mazinani, K. Hassan, J. Bi, T. T. Tung, D. Losic, *Nanoscale* **2020**, *12*, 16069.
- [40] S.-Y. Lin, T.-Y. Zhang, Q. Lu, D.-Y. Wang, Y. Yang, X.-M. Wu, T.-L. Ren, *RSC Adv.* **2017**, *7*, 27001.
- [41] D. Sui, Y. Huang, L. Huang, J. Liang, Y. Ma, Y. Chen, *Small* **2011**, *7*, 3186.
- [42] C. Li, Y.-T. Xu, B. Zhao, L. Jiang, S.-G. Chen, J.-B. Xu, X.-Z. Fu, R. Sun, C.-P. Wong, *J. Mater. Sci.* **2016**, *51*, 1043.
- [43] Y. H. Yoon, J. W. Song, D. Kim, J. Kim, J. K. Park, S. K. Oh, C. S. Han, *Adv. Mater.* **2007**, *19*, 4284.
- [44] J. Hodkiewicz, *Characterizing Carbon Materials with Raman Spectroscopy, Application Note: 51901*, ThermoFisher Scientific, Madison, WI **2010**.
- [45] T. T. Tung, M. T. Tran, J.-F. Feller, M. Castro, T. Van Ngo, K. Hassan, M. J. Nine, D. Losic, *Carbon* **2020**, *159*, 333.
- [46] E. Traversa, *Sens. Actuators, B* **1995**, *23*, 135.
- [47] W. Yuan, G. Shi, *J. Mater. Chem. A* **2013**, *1*, 10078.
- [48] B. Cho, J. Yoon, M. G. Hahm, D.-H. Kim, A. R. Kim, Y. H. Kahng, S.-W. Park, Y.-J. Lee, S.-G. Park, J.-D. Kwon, *J. Mater. Chem. C* **2014**, *2*, 5280.
- [49] P.-G. Su, H.-C. Shieh, *Sens. Actuators, B* **2014**, *190*, 865.
- [50] H. Y. Jeong, D.-S. Lee, H. K. Choi, D. H. Lee, J.-E. Kim, J. Y. Lee, W. J. Lee, S. O. Kim, S.-Y. Choi, *Appl. Phys. Lett.* **2010**, *96*, 213105.
- [51] P.-G. Su, C.-T. Lee, C.-Y. Chou, K.-H. Cheng, Y.-S. Chuang, *Sens. Actuators, B* **2009**, *139*, 488.
- [52] Y. J. Kwon, S. Y. Kang, A. Mirzaei, M. S. Choi, J. H. Bang, S. S. Kim, H. W. Kim, *Sens. Actuators, B* **2017**, *249*, 656.
- [53] C. Jin, S. Park, H. Kim, C. Lee, *Sens. Actuators, B* **2012**, *161*, 223.
- [54] Y. Ren, X. Zhou, W. Luo, P. Xu, Y. Zhu, X. Li, X. Cheng, Y. Deng, D. Zhao, *Chem. Mater.* **2016**, *28*, 7997.
- [55] Y. Navale, S. Navale, F. Stadler, N. Ramgir, V. Patil, *Ceram. Int.* **2019**, *45*, 1513.
- [56] T. Wang, D. Huang, Z. Yang, S. Xu, G. He, X. Li, N. Hu, G. Yin, D. He, L. Zhang, *Nano-Micro Lett.* **2016**, *8*, 95.

**Supporting information****Extrusion printed CNT-graphene sensor array with embedded MXene/PEDOT:PSS heater for enhanced NO<sub>2</sub> sensing at low temperature**

*Kamrul Hassan<sup>1,2</sup>, Nathan Stanley<sup>1,2</sup>, Tran Thanh Tung<sup>1,2</sup>, Pei Lay Yap<sup>1,2</sup>, Hadi Rastin<sup>1,2</sup>, Le Yu<sup>1,2</sup>, Dusan Losic<sup>1,2\*</sup>*

*<sup>1</sup>School of Chemical Engineering and Advanced Materials, The University of Adelaide, Adelaide, SA 5005, Australia*

*<sup>2</sup>ARC Research Hub for Graphene Enabled Industry Transformation, The University of Adelaide, Adelaide, SA 5005, Australia*

*Email: [Dusan.losic@adelaide.edu.au](mailto:Dusan.losic@adelaide.edu.au)*

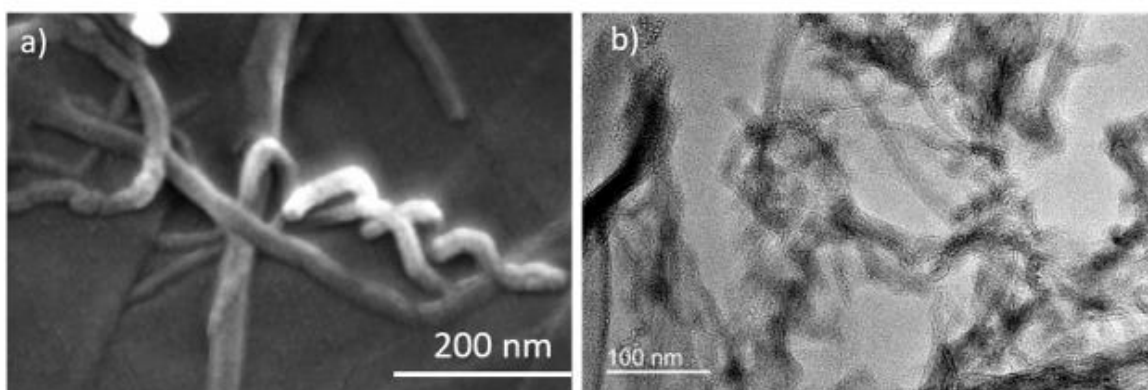


**Figure S1.** (a) High resolution SEM micrographs and (b) TEM micrographs of 1D CNT-2D graphene ink.



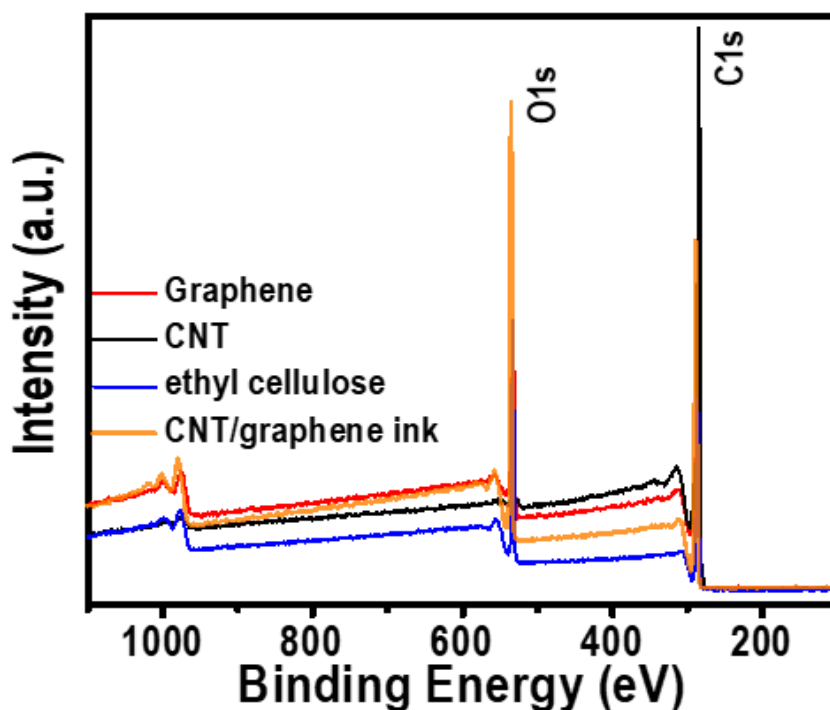
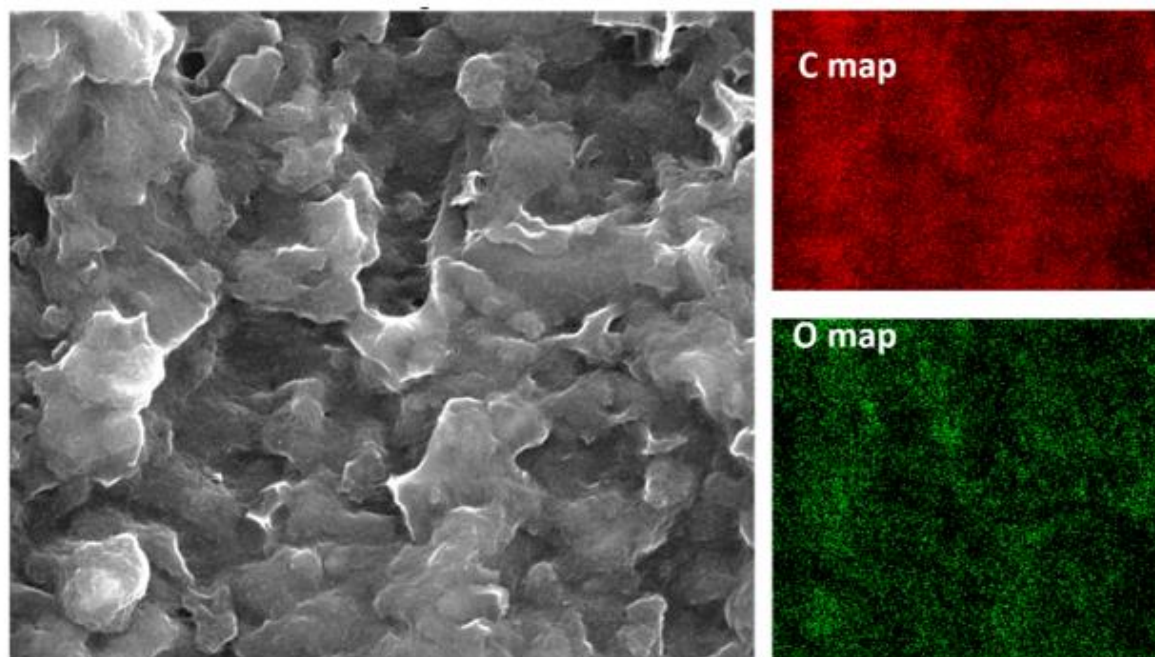


Figure S2. XPS, survey scan of C1s for CNT-graphene ink and formulation components.

Table S1. Elemental composition (XPS) of CNT-graphene ink and formulation components.

Sample	Binding energy (eV) Atomic %		
	C	O	Al
CNT-graphene ink	286.41eV 71.91%	533.41eV 28.09%	-
Graphene	285.03eV 85.14%	532.03eV 14.86%	-
CNT	284.56eV 96.56%	532.56eV 3.42%	0.02
Ethyl cellulose	286.42 eV 71.16%	532.42eV 28.84%	



Element	Line Type	Apparent Concentration	k Ratio	Wt%	Wt% Sigma	Standard Label	Factory Standard
C	K series	1.84	0.01843	77.74	0.19	C Vit	Yes
O	K series	0.31	0.00123	22.26	0.3	SiO <sub>2</sub>	Yes
<b>Total:</b>				<b>100.0</b>			

**Figure S3** EDX mapping and elemental composition (EDX) of CNT-graphene composites.

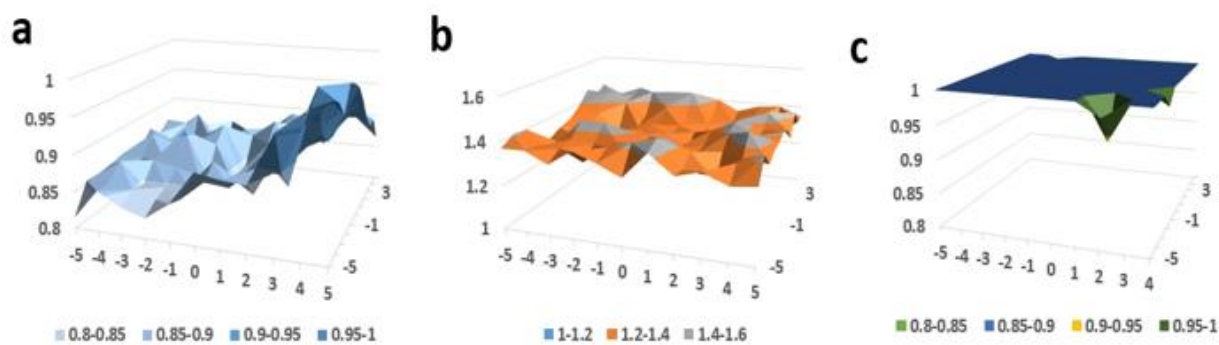


**Figure S4.** Raman 3D mapping with the calculated ID/IG ratio for (a) solvothermal graphene, (b) bare CNT, and (c) CNT-graphene composites.

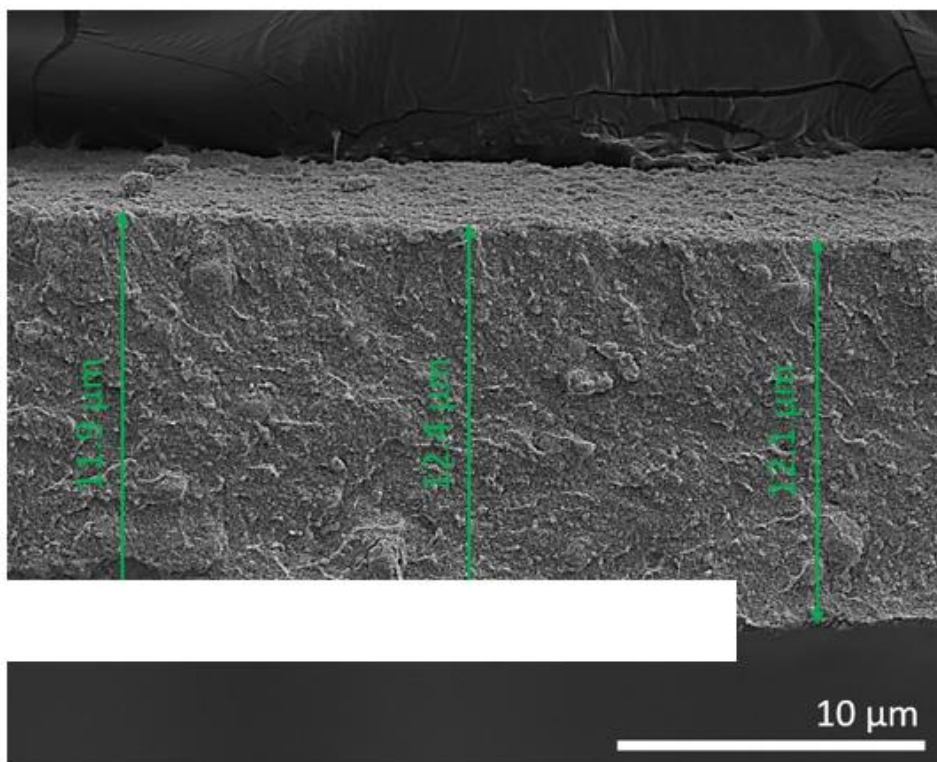


**Figure S5.** Cross-section SEM micrograph of MXene/PEDOT:PSS thin film.

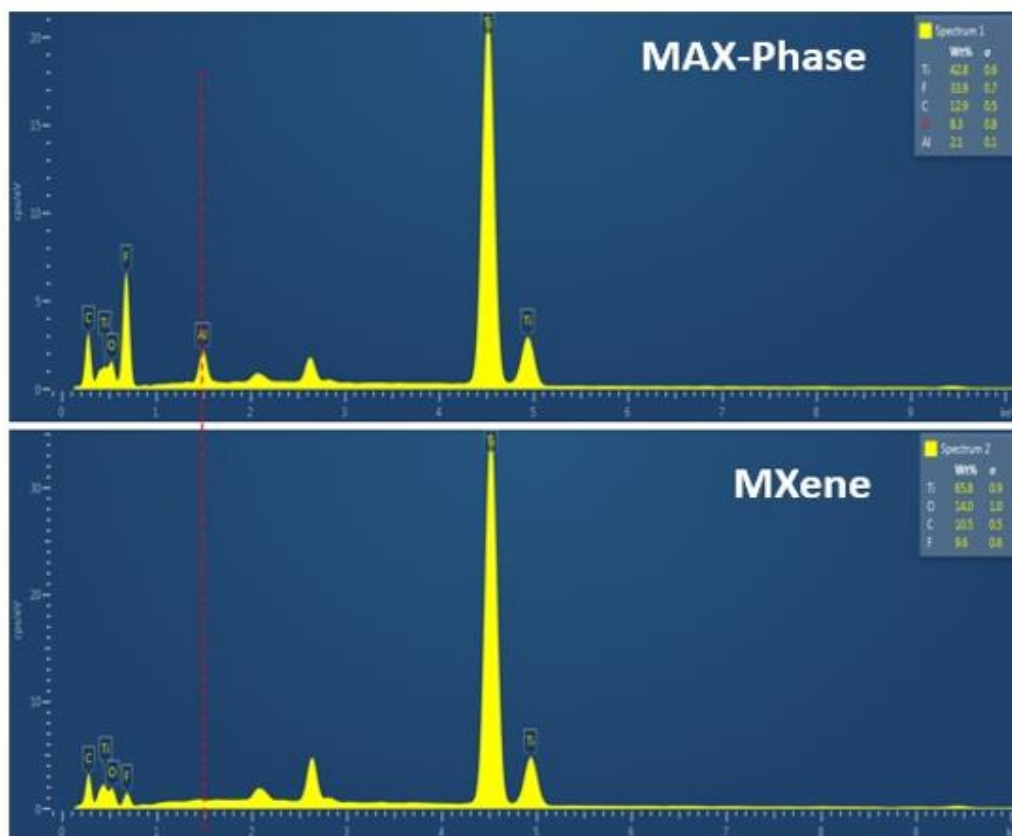


Figure S6. EDS spectrum of MAX-phase and MXene.

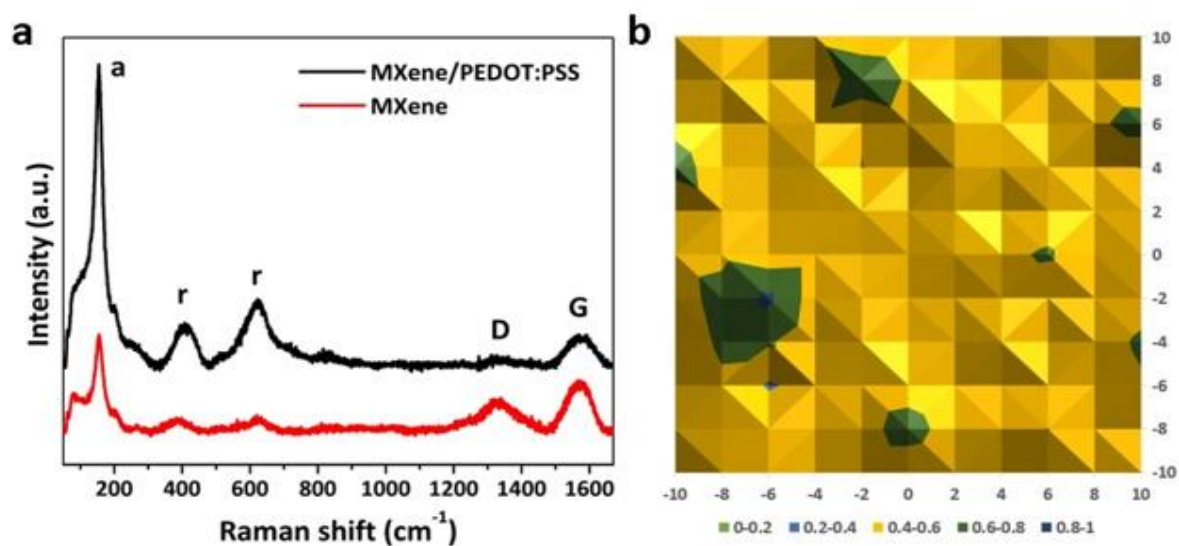


Figure S7 (a) Raman spectra and (b) 3D mapping with the calculated I<sub>D</sub>/I<sub>G</sub> ratio for MXene/PEDOT:PSS composites.

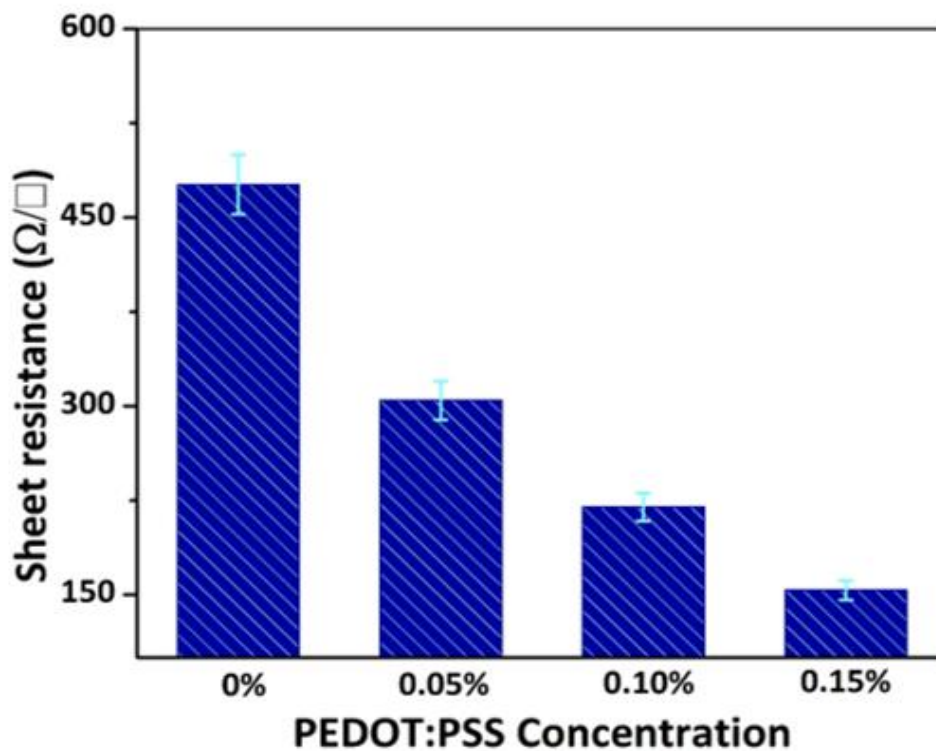


Figure S8. Sheet resistance of the MXene thin film heater with different loading of PEDOT:PSS.

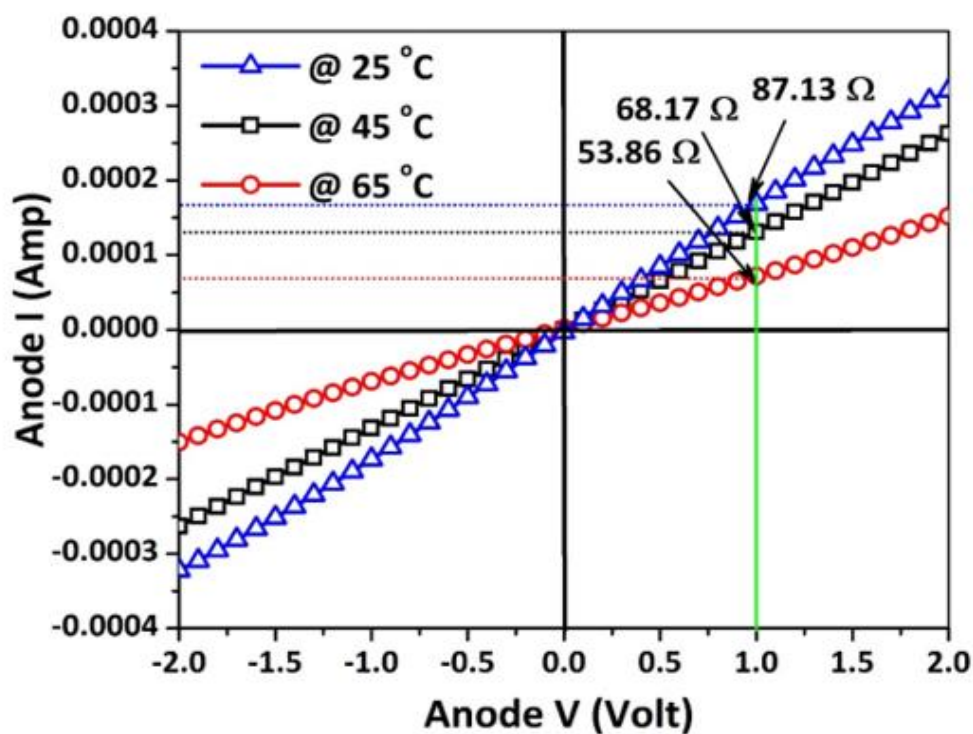
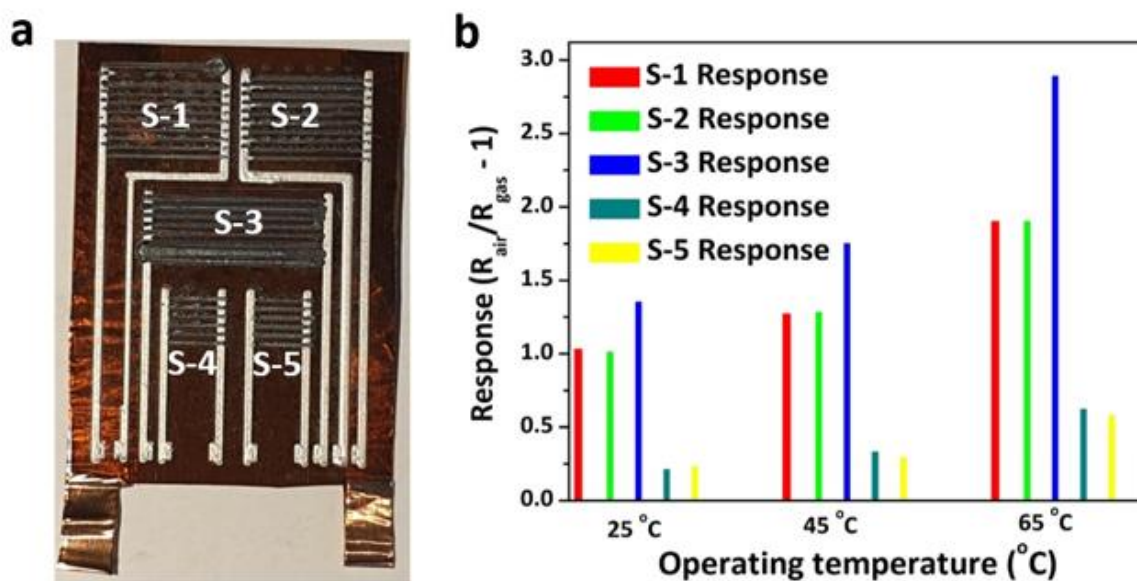
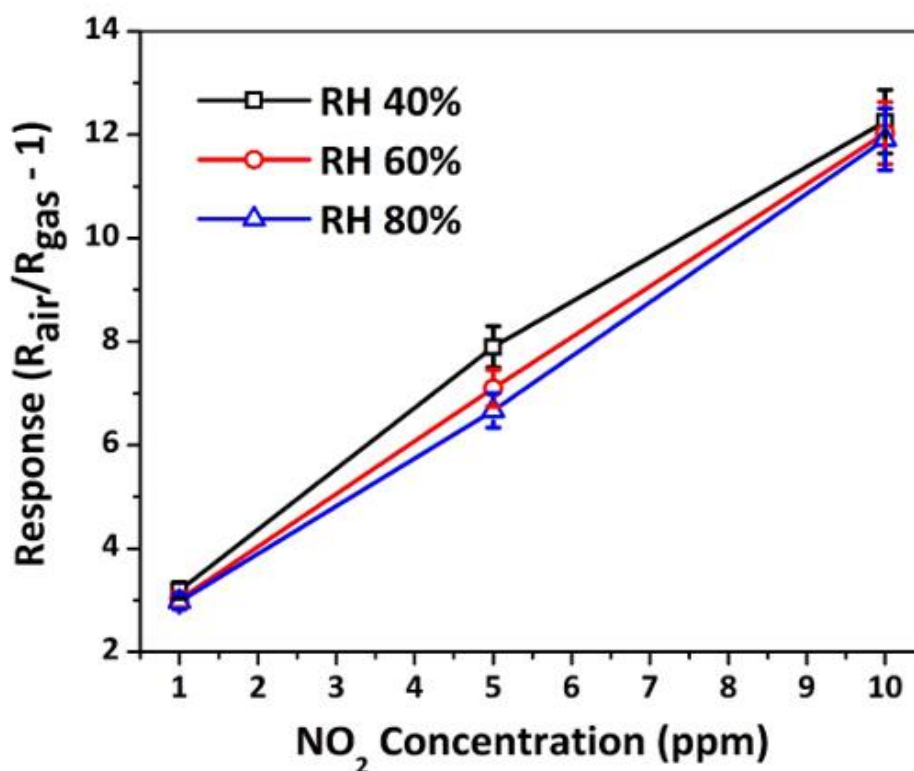


Figure S9. I-V characteristics curve of CNT-graphene sensor array at different temperature.



**Figure S10.** (a) An optical photograph of CNT-graphene sensor array composed of 5 different sensors. (b) Sensor response of each individual sensor within sensor array to 5 ppm NO<sub>2</sub> gas at 65 °C temperature.



**Figure. S11.** Transient response of CNT-graphene sensor array to NO<sub>2</sub> gas under different humidity at 65 °C temperature.

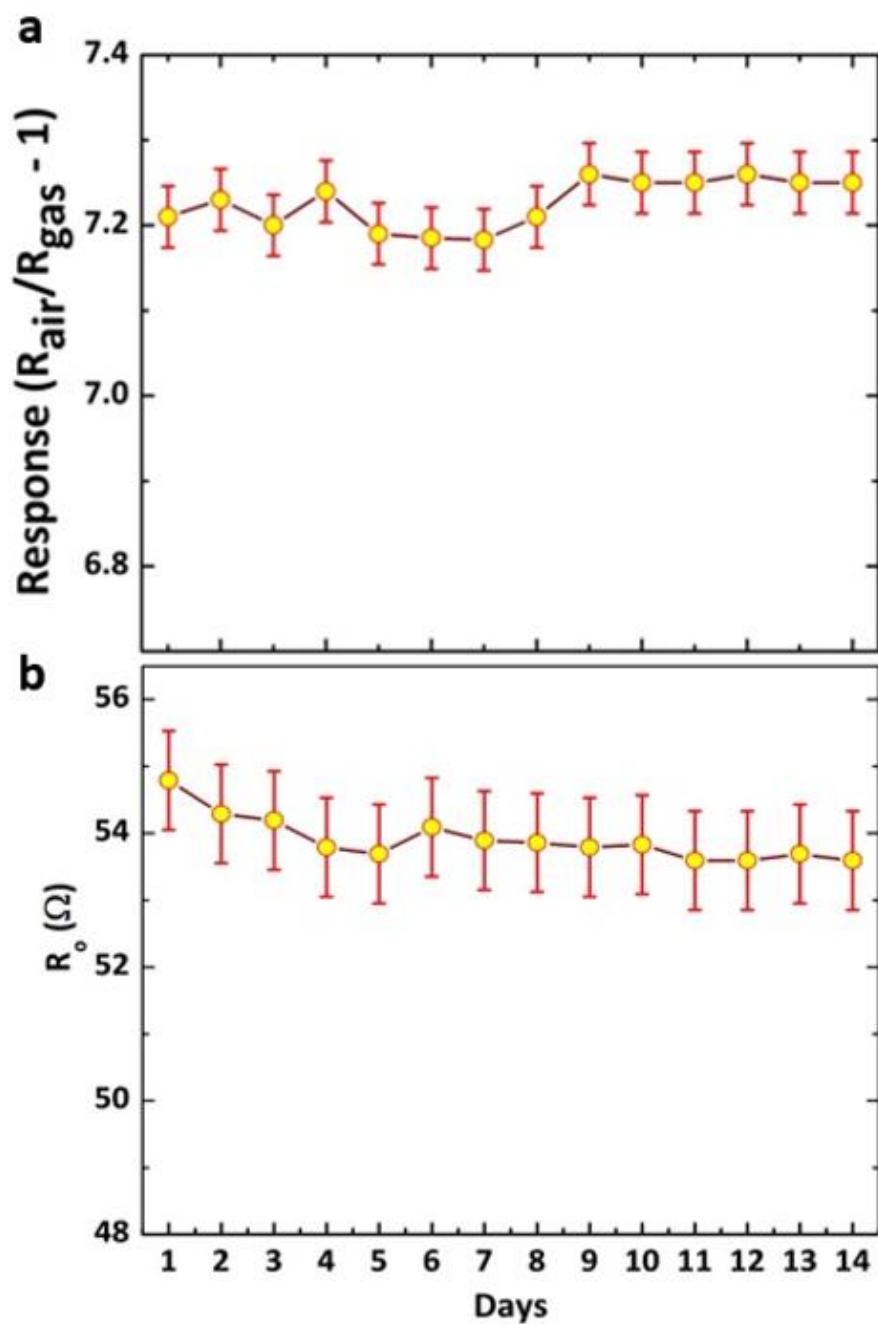


**Figure S12.** Time reliance of the CNT-graphene sensor arrays (5 sensor array) (c) response value and (d) baseline resistance value, monitored over a fourteen-day period, where on each day the each sensor was exposed to 5 ppm of NO<sub>2</sub> at 65 °C.

## Chapter 6

# Development of Pd/Cr nanogap for H<sub>2</sub> sensing

In this chapter a new concept of hydrogen sensors based on Pd/Cr nanogaps created by using a simple mechanical bending deformation technique is presented. These nanogap sensors can selectively detect the H<sub>2</sub> gas based on transduction of the volume expansion after H<sub>2</sub> uptake into an electrical signal by palladium-based metal-hydrides that allows closure of nanogap for electrons flowing or tunnelling. Based on the computational modelling outcome, the size of the nanogaps can be investigated in order to optimize the fabrication conditions. Indeed, a single nanogap with optimum width (15 nm) acts as an on-off switch for best performing hydrogen detection. Moreover, with the unique design of Pd/Cr nanogap, the developed sensing device meets major requirement of advanced H<sub>2</sub> gas sensor including room temperature (25 °C) operation, detection of trace amounts (10-40,000 ppm), good linearity, ultra-fast response-recovery time (3/4.5 sec) and high selectivity. The presented economical lithography-free fabrication method has simple circuitry, low power consumption, recyclability, and favorable aging properties that promises great potential to be used for many practical applications of H<sub>2</sub> detection.

This chapter has been published in “Analytica Chimica Acta” journal as follows:

“**Hassan K**, Tung TT, Yap PL, Nine MJ, Kim HC, Losic D. Fast response hydrogen gas sensor based on Pd/Cr nanogaps fabricated by a single-step bending deformation. *Analytica Chimica Acta*, 1138 (2020), 49-58.”



## Statement of Authorship

Title of Paper	Fast response hydrogen gas sensor based on Pd/Cr nanogaps fabricated by a single-step bending deformation.
Publication Status	<input checked="" type="checkbox"/> Published <input type="checkbox"/> Accepted for Publication <input type="checkbox"/> Submitted for Publication <input type="checkbox"/> Unpublished and Unsubmitted work written in manuscript style
Publication Details	Hassan K, Tung TT, Yap PL, Nire MJ, Kim HC, Losic D. Fast response hydrogen gas sensor based on Pd/Cr nanogaps fabricated by a single-step bending deformation. <i>Analytica Chimica Acta</i> , 1138 (2020), 49-58

### Principal Author

Name of Principal Author (Candidate)	Kamrul Hassan
Contribution to the Paper	Prepared, edited and revised the review manuscript.
Overall percentage (%)	85%
Certification:	This paper reports on original research I conducted during the period of my Higher Degree by Research candidature and is not subject to any obligations or contractual agreements with a third party that would constrain its inclusion in this thesis. I am the primary author of this paper.
Signature	Date 19/10/2021

### Co-Author Contributions

By signing the Statement of Authorship, each author certifies that:

- the candidate's stated contribution to the publication is accurate (as detailed above);
- permission is granted for the candidate to include the publication in the thesis; and
- the sum of all co-author contributions is equal to 100% less the candidate's stated contribution.

Name of Co-Author	Tran Thanh Tung
Contribution to the Paper	Co-supervised and revised the manuscript.
Signature	Date 26/10/2021

Name of Co-Author	Pei Lay Yap
Contribution to the Paper	Edited and revised the manuscript.
Signature	Date 26/10/21

Please cut and paste additional co-author panels here as required.

## Statement of Authorship

Title of Paper	Fast response hydrogen gas sensor based on Pd/Cr nanogaps fabricated by a single-step bending deformation.
Publication Status	<input checked="" type="checkbox"/> Published <input type="checkbox"/> Accepted for Publication <input type="checkbox"/> Submitted for Publication <input type="checkbox"/> Unpublished and Unsubmitted work written in manuscript style
Publication Details	Hassan K, Tung TT, Yap PL, Nino MJ, Kim HC, Losic D. Fast response hydrogen gas sensor based on Pd/Cr nanogaps fabricated by a single-step bending deformation. <i>Analytica Chimica Acta</i> , 1138 (2020), 49-58

### Principal Author

Name of Principal Author (Candidate)	Kamrul Hassan
Contribution to the Paper	Prepared, edited and revised the review manuscript.
Overall percentage (%)	85%
Certification:	This paper reports on original research I conducted during the period of my Higher Degree by Research candidature and is not subject to any obligations or contractual agreements with a third party that would constrain its inclusion in this thesis. I am the primary author of this paper.
Signature	<div style="border-bottom: 1px solid black; width: 100%;"></div> <div style="display: flex; justify-content: space-between;"> <span>Date</span> <span>19/10/2021</span> </div>

### Co-Author Contributions

By signing the Statement of Authorship, each author certifies that:

- i. the candidate's stated contribution to the publication is accurate (as detailed above);
- ii. permission is granted for the candidate to include the publication in the thesis; and
- iii. the sum of all co-author contributions is equal to 100% less the candidate's stated contribution.

Name of Co-Author	Md Jaker Nino
Contribution to the Paper	Edited and revised the manuscript.
Signature	<div style="border-bottom: 1px solid black; width: 100%;"></div> <div style="display: flex; justify-content: space-between;"> <span>Date</span> <span>01-11-2021</span> </div>

Name of Co-Author	Hyeon Cheol Kim
Contribution to the Paper	Edited and revised the manuscript.
Signature	<div style="border-bottom: 1px solid black; width: 100%;"></div> <div style="display: flex; justify-content: space-between;"> <span>Date</span> <span>21/10/2021</span> </div>

Please cut and paste additional co-author panels here as required.

## Statement of Authorship

Title of Paper	Fast response hydrogen gas sensor based on Pd/Cr nanogaps fabricated by a single-step bending deformation.
Publication Status	<input checked="" type="checkbox"/> Published <input type="checkbox"/> Accepted for Publication <input type="checkbox"/> Submitted for Publication <input type="checkbox"/> Unpublished and Unsubmitted work written in manuscript style
Publication Details	Hassan K, Tung TT, Yap PL, Nine MJ, Kim HC, Lolic D. Fast response hydrogen gas sensor based on Pd/Cr nanogaps fabricated by a single-step bending deformation. <i>Analytica Chimica Acta</i> , 1138 (2020), 49-58

### Principal Author

Name of Principal Author (Candidate)	Kamrul Hassan			
Contribution to the Paper	Prepared, edited and revised the review manuscript.			
Overall percentage (%)	85%			
Certification:	This paper reports on original research I conducted during the period of my Higher Degree by Research candidature and is not subject to any obligations or contractual agreements with a third party that would constrain its inclusion in this thesis. I am the primary author of this paper.			
Signature	<table border="1" style="width: 100%;"> <tr> <td style="width: 80%;"></td> <td style="width: 20%;">Date</td> <td>19/10/2021</td> </tr> </table>		Date	19/10/2021
	Date	19/10/2021		

### Co-Author Contributions

By signing the Statement of Authorship, each author certifies that:

- i. the candidate's stated contribution to the publication is accurate (as detailed above);
- ii. permission is granted for the candidate to include the publication in the thesis; and
- iii. the sum of all co-author contributions is equal to 100% less the candidate's stated contribution.

Name of Co-Author	Md Julker Nine			
Contribution to the Paper	Edited and revised the manuscript.			
Signature	<table border="1" style="width: 100%;"> <tr> <td style="width: 80%;"></td> <td style="width: 20%;">Date</td> <td>01-11-2021</td> </tr> </table>		Date	01-11-2021
	Date	01-11-2021		

Name of Co-Author	Dusan Lolic			
Contribution to the Paper	Supervised the development of work, edited, revised the manuscript and acted as the corresponding author.			
Signature	<table border="1" style="width: 100%;"> <tr> <td style="width: 80%;"></td> <td style="width: 20%;">Date</td> <td>26 Oct 21</td> </tr> </table>		Date	26 Oct 21
	Date	26 Oct 21		

Please cut and paste additional co-author panels here as required.



Contents lists available at ScienceDirect

Analytica Chimica Acta

journal homepage: [www.elsevier.com/locate/aca](http://www.elsevier.com/locate/aca)

## Fast response hydrogen gas sensor based on Pd/Cr nanogaps fabricated by a single-step bending deformation

Kamrul Hassan<sup>a, b</sup>, Tran Thanh Tung<sup>a, b</sup>, Pei Lay Yap<sup>a, b</sup>, Md J. Nine<sup>a, b</sup>, Hyeon C. Kim<sup>c</sup>, Dusan Losic<sup>a, b, \*</sup>

<sup>a</sup> School of Chemical Engineering and Advanced Materials, The University of Adelaide, SA 5005, Australia

<sup>b</sup> ARC Research Hub for Graphene Enabled Industry Transformation, The University of Adelaide, SA 5005, Australia

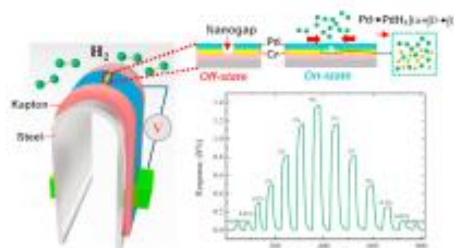
<sup>c</sup> School of Electrical Engineering, University of Ulsan, 93 Daehak-ro, Nam-gu, Ulsan 680-749, Republic of Korea



### HIGHLIGHTS

- Fabrication and sensing performances of Pd/Cr nanogap hydrogen gas sensors is presented.
- Fabrication is performed by single step bending deformation process.
- Computational modelling confirms the optimal deformation conditions and gap of 15 nm.
- High hydrogen sensitivity in range of 10–40,000 ppm and response time of 3–4 s is confirmed achieved.

### GRAPHICAL ABSTRACT



### ARTICLE INFO

#### Article history:

Received 26 May 2020

Received in revised form

31 August 2020

Accepted 5 September 2020

Available online 8 September 2020

#### Keywords:

Gas sensor

Hydrogen sensor

Nanogap sensor

Pd/Cr nanogap

Mechanical deformation

### ABSTRACT

The development of low-cost and high performing hydrogen gas sensors is important across many sectors, including mining, energy and defense using hydrogen (H<sub>2</sub>) gas. Herein, we demonstrate a new concept of H<sub>2</sub> sensors based on Pd/Cr nanogaps created by using a simple mechanical bending deformation technique. These nanogap sensors can selectively detect the H<sub>2</sub> gas based on transduction of the volume expansion after H<sub>2</sub> uptake into an electrical signal by palladium-based metal-hydrides that allows closure of nanogaps for electrons flowing or tunneling. While this break-junction architecture, according to literature, can provide several advantages with research gaps in terms of fabricating nanogap sensors with ultra-fast response ( $\leq 4$  s), the size of nanogap ( $\leq 20$  nm) and their relationship with time response and recovery as addressed in this paper. Based on the computational modelling outcome, the size of the nanogaps can be investigated in order to optimize the fabrication conditions. Indeed, a single nanogap with optimum width (15 nm) acts as an on-off switch for best performing hydrogen detection. Moreover, with the unique design of Pd/Cr nanogap, the developed sensing device meets major requirement of advanced H<sub>2</sub> gas sensor including room temperature (25 °C) operation, detection of trace amounts (10–40,000 ppm), good linearity, ultra-fast response-recovery time (3/4.5 s) and high selectivity. The presented economical lithography-free fabrication method has simple circuitry, low power consumption, recyclability, and favorable aging properties that promises great potential to be used for many practical applications of H<sub>2</sub> detection.

© 2020 Elsevier B.V. All rights reserved.

\* Corresponding author. , School of Chemical Engineering and Advanced Materials, The University of Adelaide, SA 5005, Australia.  
E-mail address: [dusan.losic@adelaide.edu.au](mailto:dusan.losic@adelaide.edu.au) (D. Losic).

<https://doi.org/10.1016/j.aca.2020.09.012>

0003-2670/© 2020 Elsevier B.V. All rights reserved.

## 1. Introduction

Hydrogen (H<sub>2</sub>) has recently gained the top of global research impact as future energy solution for sustainable and renewable energy arrangements [1]. Due to its high-power conversion efficiency, H<sub>2</sub> is the primary propellant in spaceships, commercial- and military-launched vehicles, and is used across many industrial sectors in the production of steel, glass, and the refining of petroleum products [1]. In 2003, the U.S. Department of Energy inaugurated H<sub>2</sub> program to develop the technology required for commercially feasible hydrogen-powered fuel cells to power vehicles, homes, and businesses to control the worsening pollution issue with the effort to lower the greenhouse gas emissions significantly through cutting down the dependence on fossil fuels burning [2]. This H<sub>2</sub> gas as fuel is highly flammable and explosive in air over a broad range of concentrations (4%–75%) with very low energy needed to make the ignition. This requires extraordinary safety precautions and continuous leakage monitoring protocol.

To address the safety requirements associated with many of the high consumption hydrogen-based applications, the advancement of efficient H<sub>2</sub> sensors that can rapidly and precisely detect H<sub>2</sub> gas leaks are highly in-demand. In the fuel cells application [3], the core of hydrogen-powered vehicles, usually require two types of H<sub>2</sub> sensors: 1) a sensor to detect leaks and 2) a sensor to monitor the quality of the H<sub>2</sub> feed gas. These H<sub>2</sub> sensors should be sensitive to differentiate between trace amount (ppm level) of H<sub>2</sub> in ambient and those produced by leaking. In this and many other cases, the slow response time is identified as the major limitation of the existing commercial H<sub>2</sub> sensors [4]. For example, the sensors that evaluate H<sub>2</sub> content in a mixed gas along with monitor the reaction mechanism need very short response time to follow the fuel cell's power generation as well as to shut down the engine promptly during tank rupture.

Palladium (Pd), among many other sensing materials explored, has shown most promising characteristics suitable for designing fast-response H<sub>2</sub> sensors [5–12]. The key property of Pd-based H<sub>2</sub> sensors is attributed to its specific atomic structure that enables to catalytically break the H–H bond in diatomic hydrogen, allowing monoatomic hydrogen to diffuse into the material. Importantly, this hydrogenation phenomenon catalyzed by palladium is reversible even at room temperature, which makes the device simple architecture, resulting in less power consumption. Many different forms of Pd sensors for H<sub>2</sub> using planar (films) or nano-structured surface with different topographies (particles, pores, wires, rods and etc.) used for sensor designs (electrodeposition, photolithography, sputtering and etc.) have been explored in recent years [7,8,10]. The nanogaps in Pd films have been also investigated for H<sub>2</sub> gas sensors, which concept was demonstrated a decade ago using Pd meso-wire arrays [6]. Since their introduction, several advancements in their sensing performances based on improving nanogap fabrication using sophisticated lithographic techniques [13–16], exploring different geometries, sizes and resolution [17–20] were reported. Despite these improvements, many challenges still remain in terms of further advancing these nanogap sensors at level to be considered for a commercially-viable option for H<sub>2</sub> detection. For example, to provide a broad range of detection, the nanogap sensors should contain a continuum of nanogap spacings which sequentially close when H<sub>2</sub> concentration increases, and it is difficult to achieve. To improve the lower detection limits, the formation of Pd with sub-20 nm gaps is required, which is hard to achieve using conventional lithographic techniques [21]. In addition, lowering the detection limit by reducing the nanogaps leads to the limitation in terms of providing a Pd-substrate interface. Simultaneously, the interface resists delamination without excessively hindering the large volume expansions. To overcome

these requirements and limitations, a potential solution is to have a nanogap sensor with a large size of nanogap with controllable spacing that can provide an overall signal to continuously vary between the low and high detection limits.

To address these challenges in the design and development of nanogap sensors, in this paper, we present a simple design of mechanical bending deformation on Pd/Cr film to fabricate high performing H<sub>2</sub> nanogap sensors with high sensitivity and ultra-fast response. The fabrication is made by depositing a layer of chromium (Cr) with a thickness of 1–3 nm onto the mechanically compliant substrate (kapton/steel), followed by deposition of Pd film (2 nm) to create Pd/Cr films on the substrate. The nanogap is created by a single-step bending deformation of Pd/Cr film by using a solid cylinder (1–6 mm) to induce a single crack. The concept as presented in Fig. 1, showing four-layer structure of the Pd/Cr film, wherein kapton and steel substrate are selected to provide ideal condition for creating nanogap on the top Pd layer. By using this method, nanogaps with dimensions ranging from 8 to 80 nm can be created to significantly improve the response time and the detection limit of the developed H<sub>2</sub> sensor. The nanogap sensors can be transacted as an on-off switch when the nanogap spacing is exposed toward H<sub>2</sub> at low concentration (ppm). The transduction of volume expansion (H<sub>2</sub> uptake) into an electrical signal by closure of nanogaps for electrons flowing or tunneling can happen within seconds. Moreover, in this study, computational modelling is also performed to optimize fabrication conditions to create nanogap in Pd film with controllable distances (8–80 nm) which is the most critical step in this fabrication method. Influence of several key parameters including curvature of bending tool, film thickness, and controlled nanogap size in enhancing H<sub>2</sub> sensing performance such as fast response-recovery time, wide detectable range, durability and stability of fabricated Pd/Cr nanogap sensor. Results demonstrate that this mechanically-induced nanogap can be used as a promising, low-cost and scalable fabrication technology to produce Pd-based H<sub>2</sub> sensors with excellent sensing performance for a broad range of applications.

## 2. Experimental section

### 2.1. Fabrication of Pd/Cr nanogap sensor by a single-step bending deformation technique

A Kapton tape (60- $\mu$ m-thick polyimide layer) was attached on the top of a steel foil substrate (dimensions: 45 × 10 × 0.127 mm<sup>3</sup>) (Fig. 1a). By applying a shadow mask (40 × 8 mm<sup>2</sup>) sequentially, chromium (Cr, iTASCO, 99.95% purity) and palladium (Pd, iTASCO, 99.98% purity) were deposited on the top of Kapton tape (Fig. 1b and c) using the RF magnetron sputtering machine. Detailed deposition parameters are listed in Table S1. After that, this four-layer structure was bent by using a metal rod with various radius of curvature (1–6 mm) to form a crack throughout Pd/Cr film, which worked as a nanogap sensor for detecting H<sub>2</sub> gas (Fig. 1d). However, after releasing the mechanical force, this four-layer structure keeps its bent structure with an overall height of ~20 mm. To facilitate the electrical resistance measurements (two-probe), electrical contacts are connected with each end of this four-layered structure using silver (Ag) paste (Fig. 1e). Additionally, the titular thickness of the as-deposited Pd/Cr film on Kapton are summarized in Table 1.

### 2.2. Structural and compositional characterization of Pd/Cr based nanogap sensor

The surface morphology of the four-layered samples was investigated by field emission scanning electron microscopy

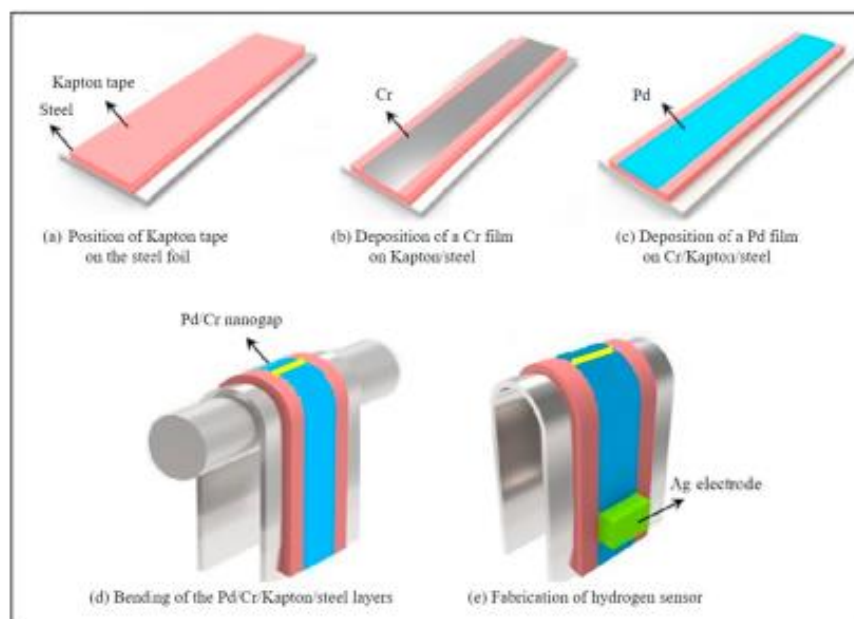


Fig. 1. Schematic diagram of the fabrication process of Pd/Cr nanogap sensor.

(FESEM; JEOL JSM-7600F). Water contact angle was measured by contact angle goniometry (Kruss DSA 100 drop shape analyzer) using sessile drop method at room temperature. By using a microsyringe, deionized (DI) water (about 3  $\mu$ L droplets) was dropped on the surface of the thin film. The material composition of the sensing material was studied with an energy-dispersive spectrometer (EDS- JEOL JEM-2010F). The structural characteristics of the bimetallic film structures were examined by using an X-ray diffractometer (XRD, Rigaku Ultima IV, Cu K $\alpha$  ( $\lambda = 0.15418$  nm),  $2\theta = 10$ – $90^\circ$ ). X-ray photoelectron spectroscopy (XPS, Thermo Fisher K-Alpha) was carried out on the as-prepared samples by Al K $\alpha$  radiation that used as the X-ray source. The peaks fitting was performed using Casa XPS software with the primary peak (adventitious carbon) calibrated at 284.8 eV.

### 2.3. Hydrogen gas sensing characterization of Pd/Cr based nanogap sensor

For transport measurement of H<sub>2</sub> gas, Pd/Cr based nanogap sensors were cautiously installed in the center of a U-shaped support-stand in an air environment condition. For all the sensor characterizations, a Keithley 274 probe station (SCS-4200) with a bias voltage at 1 V was used. To confirm the flow of a H<sub>2</sub> gas, a narrow metal tube was installed on the top of the as-fabricated sensor. To control the numerous concentrations of H<sub>2</sub> gas, a computerized mass flow controller (ATO-VAC, GMC 1200) instrument was used. The gas mixture (H<sub>2</sub> and N<sub>2</sub>) under numerous H<sub>2</sub> concentrations was transported to the sensors at a constant flow

rate of 50 sccm (standard cubic centimeters per minute). The sensor response (*S*) was calculated by using this formula:  $R_g - R_a/R_a$ , where  $R_a$  is the resistance of the as-fabricated sensor in air environment and  $R_g$  is the resistance of the sensor in H<sub>2</sub> medium at certain concentration. The response-recovery time of the sensor was calculated as the time to reach 90% of the total resistance change. The relative humidity (RH) in our experimental environment was varied from 40 to 80% by a water bubbler controller, and monitored by a Testo 625 hygrometer. All the performance characterizations related to as-fabricated sensors were carried-out at room temperature (25 °C).

## 3. Results and discussion

### 3.1. Computational analysis of bimetallic Pd/Cr based nanogap

In order to fabricate Pd nanogap sensors with controllable and different nanogaps based on the Pd/Cr film thickness and radius of curvature, we initially performed computational modelling using Comsol Multiphysics Simulation software (structural mechanics and electrostatics (es) physics study) to identify the optimized fabrication condition. After deforming-/bending the four-layered structure, crack formation occurred throughout the bimetallic Pd/Cr film due to tensile stress. This tensile stress was distributed across the cross-section of layered structure by varying the compressive stress from the concave surface (maximum stress) to neutral axis (zero stress) followed by tensile stress (maximum) at the convex surface (Fig. 2c). After finishing this process, the concave surface experienced a compression which decreased its length while the convex surface was placed under tension which increased its length since the increased length,  $L'$ , is given by  $L' = L (\epsilon + 1)$  where  $\epsilon = r/(R + r)$ . Basically, the stress patterns scenario of this four-layered structure was quite different from the ideal one-layer structure because of bottom layer (steel). This bottom layer is not only thicker than other layers, but also has the maximum yield

Table 1  
Fabrication details of different Pd and Cr thickness on Kapton/steel substrates.

Samples	S <sub>1</sub>	S <sub>2</sub>	S <sub>3</sub>	S <sub>4</sub>	S <sub>5</sub>	S <sub>6</sub>	S <sub>7</sub>	S <sub>8</sub>	S <sub>9</sub>
$d_{Pd}$ (nm)	2	2	3	4	2	3	5	6	7
$d_{Cr}$ (nm)	2	3	3	2	1	2	2	2	2

K. Hassan, T.T. Tung, P.L. Yap et al.

Analytica Chimica Acta 1138 (2020) 49–58

strength. This steel layer was first started to bend when the bending moment ( $M$ ) was applied on the four-layered structure and this deformation was continued until the force was removed. As a result, after removing the force, partial spring back pressure was established on the layered structure because of the elastic strain recovery.

During the bending deformation, the layer of Cr and kapton performed a substantial act which significantly decreases the tensile stress planted on the Pd film. As a result, there was no loss of bonding in between the adhesive (Cr and kapton) along with steel resulting from this interfacial movement. The slippage created could protect the bimetallic-film against erratic as well as excessive crack formation. The tensile strength along with break elongation between Pd/Cr film as well as the steel attached by kapton can be well-described using Comsol Multiphysics Structural Mechanics modelling. In this work, the Solid Mechanics interface was intended for Pd/Cr/kapton/steel architecture. The stress/plane strain assumption was used in the 2D design. This Solid Mechanics interface is primarily based on resolving Navier's equations with its outcomes resulting in adhesive strength, break elongation, and young modulus are computed. By using the Non-linear Structural Materials Module -/Geomechanics Module, the interface was extended to Pd, Cr, Kapton and steel. From the computational analysis, it clearly showed that with the reduced thickness of Pd and Cr, the adhesive strength also decreased along with the increase of break elongation (Fig. 2d). However, the difference between the adhesive strength and break elongation for the 2/1 nm

thickness of Pd/Cr is higher than other thickness studied, which created several non-parallel cracks on the sample surface. Fig. 2e shows the relation between nanogap size and curvature radius for sample S<sub>6</sub>. It can be observed that with the increase of curvature, the radius of the nanogap reduced. Therefore, sample S<sub>6</sub> with the 3/2 nm thickness of Pd/Cr was chosen as the optimized condition for further performance studies.

### 3.2. Characterization of Pd/Cr nanogap structure and composition

Water contact angle analysis based on Young's method [22] was performed to understand the wettability behavior of the Kapton, and as-sputtered metal surface. From the analysis, it was found that contact angle of Pd/Kapton (107.7°) was higher than Pd/Cr/Kapton (91.3°) as well as bare kapton substrate (78.2°) (Fig. S-1). These indicatory results reveal the increased hydrophobic nature of Pd/Kapton compared to other samples. It was evident from the literature that surface energy of a material depends on the wettability behavior that leads Pd/Kapton towards lower surface energy due to its high hydrophobic nature [23,24]. As a result, the inter-grain distances between Pd was higher for Pd/Kapton samples with smaller Pd grain size. Meanwhile, upon the deposition of the Pd/Cr on the Kapton, Pd capped the Cr NPs to form continuous film with high uniformity along with roughly equal distances between all grains. This analysis clearly demonstrated that a continuous Pd layer was formed as a film manner on the top of continuous Cr layer because of their wettability behavior between two metals.

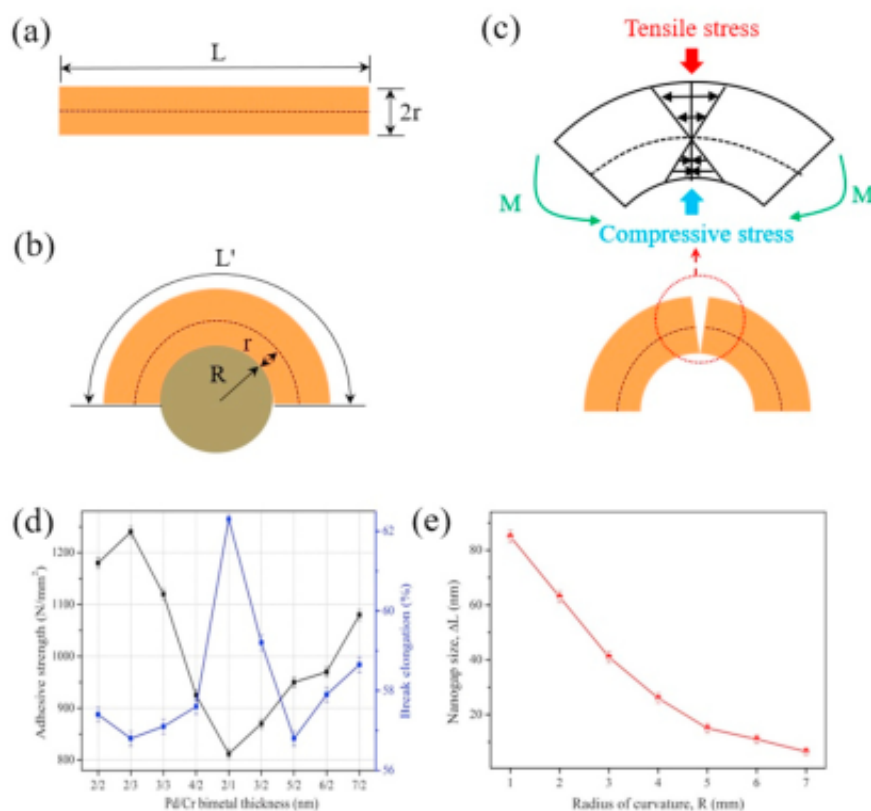


Fig. 2. Parameters of the Pd/Cr film for simulation when mechanical bending was applied on (a) laminate film with a length ( $L$ ) and width ( $2r$ ), (b) a radius of curvature ( $R$ ), (c) Schematic diagram of the stress distributions occurring when a bending moment ( $M$ ) is applied to the ends of a sample. (d) Simulation result of mechanical property of the materials as a function of film thickness and (e) nanogap size as a function of radius of curvature ( $R$ ).

Fig. 3a shows an SEM image of the crack formed on the surface of Pd films of a sample (S<sub>6</sub>) after mechanical bending. Single linear crack was found to be perpendicular to the tensile/compressive stress direction. In addition, due to the adhesive behavior of Cr, crack was only formed at the center of the sample where the stress was maximum to create single crack. With the increase of curvature radius, the stress on the surface of the samples also increased and created single crack with different size (Table 2). For sample S<sub>6,5</sub> the measured width of the crack was 15 nm, which can be regarded as a nanogap. The presence of Cr and Pd elements along with their purity was confirmed by the EDS spectra (Fig. 3b). The size and the appearance of the cracks were studied using energy dispersive mapping technique (Fig. 3c and d), revealing that the Pd/Cr films exist only outside of the crack, supporting the breakdown of the bimetal around the cracks.

Depth profiling of the as-fabricated material was achieved by argon-ion sputtering XPS system to examine the chemical state of the chromium (Cr) as well as palladium (Pd). Fig. S-2 illustrates the outcomes of the XPS analysis for Pd 3d peaks (Pd 3d<sub>3/2</sub>, Pd 3d<sub>5/2</sub>) (Fig. S-2a) and the Cr 2p peaks (Cr 2p<sub>1/2</sub>, Cr 2p<sub>3/2</sub>) (Figs. S2–b). From the results, it was evident that after each sputtering, the binding energy for the Pd 3d peaks stay similar such as Pd 3d<sub>3/2</sub> at 340.6 eV and Pd 3d<sub>5/2</sub> at 335 eV as like initial except the integrated peak area, which was decreased because of the surface absorbed carbon and oxygen removal (Fig. S-2a). Moreover, the atomic ration between Pd/Cr was obtained from the XPS wide scan (11.11) and tabulated in the supplementary information (Table S3). This circumstance directs that the chemical state of palladium (Pd) remains the same at

Table 2

Various nanogap size of sample S<sub>6</sub> (average of three samples) based on the curvature radius.

Samples	S <sub>6-1</sub>	S <sub>6-2</sub>	S <sub>6-3</sub>	S <sub>6-4</sub>	S <sub>6-5</sub>	S <sub>6-6</sub>
Curvature radius, R (mm)	1	2	3	4	5	6
Nanogap size (±1 nm)	80	70	55	35	15	8

different depth. On the other hand, the chromium peaks in Figs. S2–b clearly demonstrated the shift of the Cr 2p<sub>1/2</sub> and Cr 2p<sub>3/2</sub> peaks from lower binding energy to higher binding energy, which happened because of the oxidized (Cr<sub>2</sub>O<sub>3</sub>) surface of Cr. As evidenced from Ellingham diagram, with more than 10<sup>-40</sup> atm partial pressure (oxygen), Cr can easily oxidize at room temperature [25].

### 3.3. Pd/Cr nanogap sensor performance studies

Fig. 4 illustrates the comparison of real-time electrical resistance variation between 5 nm thick Pd film (bare) and 3 nm Pd/2 nm Cr based nanogap sensors to 1% H<sub>2</sub> at room temperature along with the schematic representation of the H<sub>2</sub> sensing mechanism in nanogap sensor. Significant outcome of buffer layer (Cr) in layered structure on the characteristics of nanogap sensor was evident in Fig. 4a and b. Based on Fig. 4a and b, the value of the baseline resistance in air medium was varied by a factor of more than three between 5 nm Pd (MΩ) and 3 nm Pd/2 nm Cr (kΩ) based sensors. From the literature, it was evident that Cr has superior electrical resistivity compared to Pd [26,27], which causes the abundant

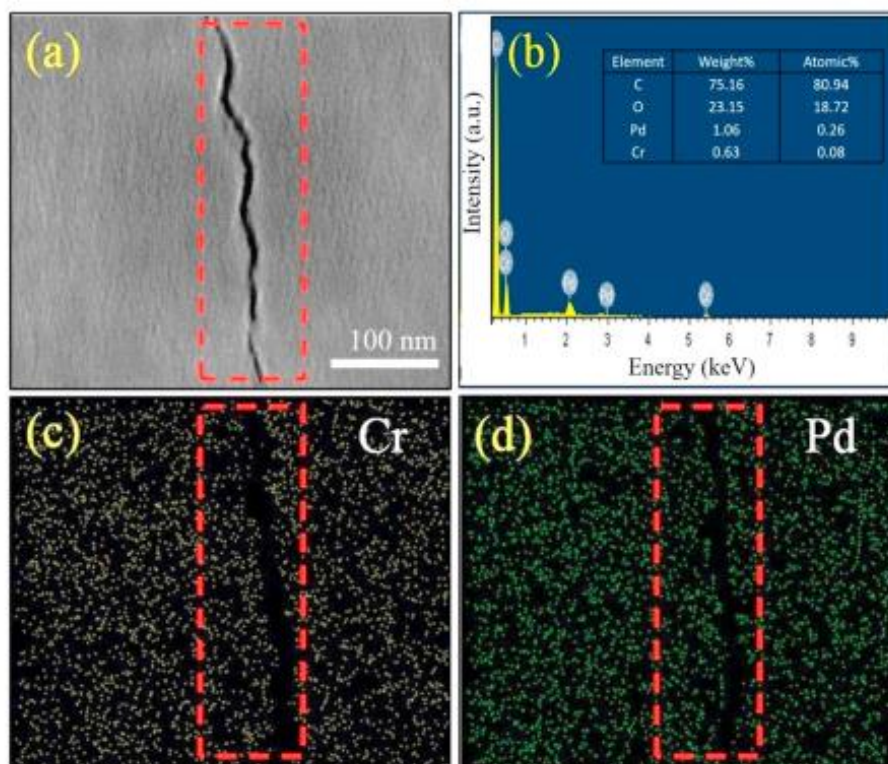


Fig. 3. (a) SEM image shows the single nanogap in the Pd/Cr continuous film. (b–d) Typical EDS spectrum and elemental mapping of the Pd/Cr nanogap on the kapton substrate.



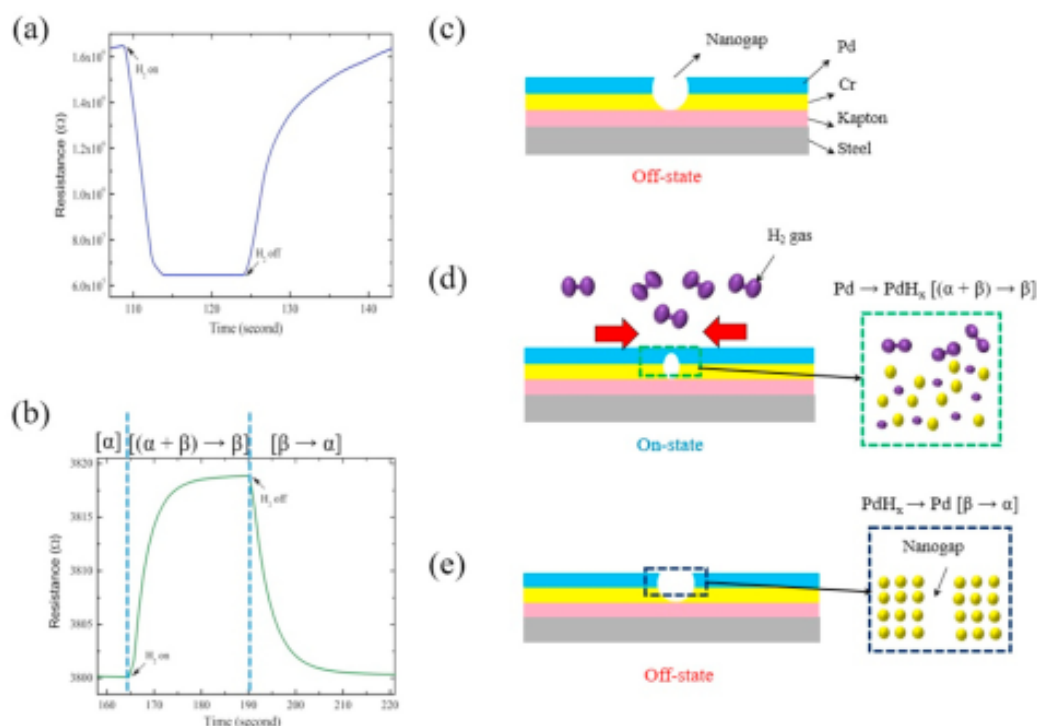


Fig. 4. Comparison of the H<sub>2</sub> responses of (a) bare 4 nm Pd film, and (b) 2 nm Pd/2 nm Cr film to 1% H<sub>2</sub> gas at room temperature (25 °C). (c)–(e) Illustration of the on-off operation of the Pd/Cr nanogap sensor corresponding to the electrical response shown in (b).

reduction of Pd/Cr based sensor resistance than pure Pd. In addition, the response characteristics was also affected by the morphological changes of discrete 5 nm Pd film and continuous 3 nm Pd/2 nm Cr based film in terms of electrical resistance variation. For 5 nm Pd film-based sensor, resistance was decreased in contrast for 3 nm Pd/2 nm Cr based electrical resistance, which was increased upon exposing H<sub>2</sub> gas at room temperature (Fig. 4a and b). These results indicate that Pd layer (3 nm thickness) was electrically connected in the Pd/Cr film, which gives the justification for formatting Pd/Cr film as continuous manner on kapton surface. This morphological circumstance created between two metals due to their wettability behavior was investigated by water contact angle measurement. It can be observed that the deposition of Cr on the surface of Kapton as layer-by-layer manner due to reduced surface wettability, which promotes three-dimensional (3D) growing process [28]. The low resistance of our control samples with the Cr and Pd thickness of 2 nm and 3 nm, respectively, on kapton (sample S<sub>6</sub> in Table 1) indicates the continuity of Pd film that dominates their electrical properties.

The chemo-resistive sensing response of nanogap sensor towards H<sub>2</sub> gas is based on the surface chemistry change of the Pd/Cr film that induced volume expansion (Fig. 4c–e). This sensing mechanism showed the response time for different gaps needed for conversion into PdH<sub>x</sub> (from  $\alpha$  stage to  $(\alpha + \beta) \rightarrow \beta$  stage), followed by the dissociation of H<sub>2</sub> gas, the PdH<sub>x</sub> was converted back to Pd ( $\beta \rightarrow \alpha$  stage), and film contraction. When the Pd film was exposed to hydrogen gas, the dissolved H<sub>2</sub> atoms was penetrated from the Pd surface to Pd film, which causes the increment of interatomic distances. As a result, Pd film was swelling on each side of the nanogap and contacted between the ends of the cracked Pd piece that represented “on” state (Fig. 4d). Therefore, lower saturated current was achieved from this swelled Pd film after exposing H<sub>2</sub> gas

(absorption process). At the time of desorption process, absorbed H<sub>2</sub> atoms quickly desorbed that causes reduction of interatomic distances/recovery to equilibrium dimensions between Pd atoms (Fig. 4e). The drop of resistance to initial baseline resistance happened in this desorption process can be denoted as “off” state.

Fig. 5a–f show the response-recovery time behavior of the four-layered sensors to 1% H<sub>2</sub> gas at room temperature. It can be seen that sample S<sub>6-5</sub> exhibited faster response-recovery time (3/4.5 s) than that of the S<sub>6-1</sub> (13/22 s), S<sub>6-2</sub> (10/16 s), S<sub>6-3</sub> (8/11 s), S<sub>6-4</sub> (5/8 s), and S<sub>6-6</sub> (9/5 s) samples due to narrower nanogap size, which reduced the current path at the time of hydrogenation. During the hydrogenation process, physisorption as well as chemisorption are important within H<sub>2</sub> and Pd surface before H<sub>2</sub> atoms penetrate or diffuse into the Pd lattice. During chemisorption, palladium hydride (PdH<sub>x</sub>) was formed by the incorporation of Pd crystal structure with H<sub>2</sub> molecules. Meanwhile, the interstitial sites of Pd NPs interacted with the physisorbed molecules [29]. As a result, the carrier mobility was reduced for these sites, which acted as electron scattering centers. Both mechanisms create a hydrogen-induced change in electrical resistance of Pd film, which is generally named as electronic effect during sensing. Moreover, formation of a  $\beta$ -PdH<sub>x</sub> phase in the tetragonal sites causes an increased lattice constant as well as decrease in the work function, which eventually changed the electronic characteristics of the metallic nanoparticles [30]. On the contrary, sample S<sub>6-6</sub> has lower nanogap size compared with the sample S<sub>6-5</sub> and showed higher response-recovery time. This contradictory behavior of nanogap size in terms of sensing was happened because, firstly, Fermi level shift occurred due to the adsorption of H<sub>2</sub> molecules on the Pd surface, which changed the resistance on the surface, immediately followed by the catalytically-activated Pd layer dissociates H<sub>2</sub> molecules into H<sub>2</sub> atoms [31–33]. Secondly, by expanding the initial volume, the

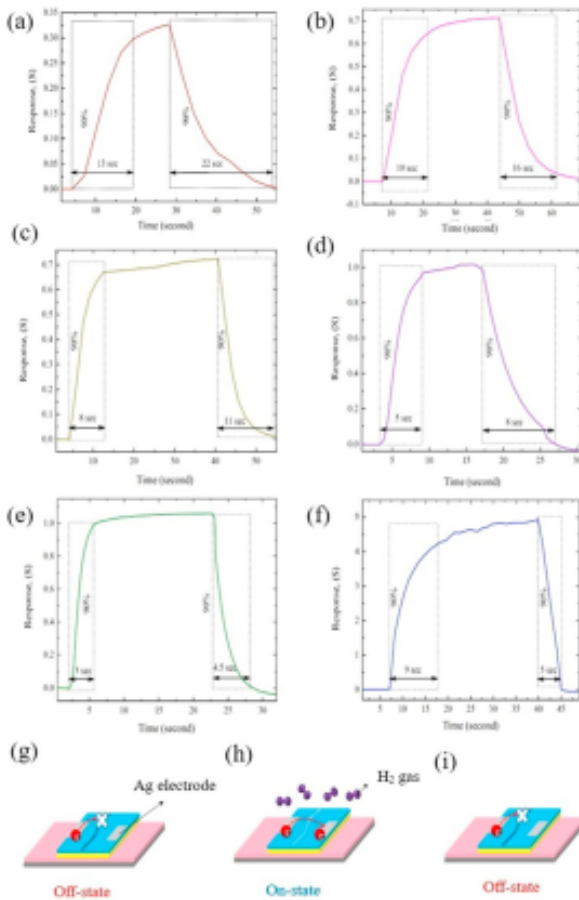


Fig. 5. Response-recovery time characteristics for samples (a) S<sub>6-1</sub> (b) S<sub>6-2</sub> (c) S<sub>6-3</sub> (d) S<sub>6-4</sub> (e) S<sub>6-5</sub> and (f) S<sub>6-6</sub> to 10,000 ppm H<sub>2</sub> at room temperature (25 °C). (g–i) Schematic illustrations of the electron scattering as a mechanism of on-off switch for nanogap based H<sub>2</sub> sensor.

dissociated H<sub>2</sub> atoms increased the rate of electron scattering during the palladium-to-palladium hydride transformation. Owing to the volume expansion, hydride formation was interrupted for sample S<sub>6-6</sub> due to narrower nanogap. Therefore, the shortest current path plays a trade-off factor between the sensor characteristics of response as well as recovery rate. Fig. 5(g–i) shows the schematic illustration of electron scattering for the nanogap sensor that acts as an on-off switch during the hydrogenation process.

The dynamic response variations of the controlled sensor were examined by testing numerous H<sub>2</sub> concentrations at room temperature (Fig. 6a). The sensor showed good linear response behavior over a broad range of H<sub>2</sub> gas concentrations tested (10–40,000 ppm). Hydrogen adsorption in palladium-materials, such as thin films [34], nanodisks [35], and nanowires [9] exhibits breaking of the palladium nanostructures after a few cycles of H<sub>2</sub> adsorption within the confined range of detection concentrations. Remarkably, in this study, the developed nanogap sensor demonstrates a translucent advancement in the response magnitude as a function of H<sub>2</sub> concentration. In addition, the sensor exhibits the capability to sense H<sub>2</sub> levels over a broad range of concentrations using the similar principle of detection, which has not been reported previously for Pd-based sensors. By using the Langmuir isotherm formula of the dissociative adsorption of gases, the linear

relationship between response and the square root of H<sub>2</sub> has been accredited. Because of the adsorption of H<sub>2</sub> molecules on the palladium surface, the work function of palladium was changed, in a way that might be proportional to the fractional coverage of hydrogen ( $\theta$ ) on the Pd surface. Moreover, the workable charge concentrations in palladium film also change linearly with  $\theta$  [36]. Thus, the change in resistance,  $R/R_{\text{air}}$  is proportional to  $\theta$ . The proposed reaction mechanism for hydrogen dissociation on the Pd surface is



where  $S_{\text{Pd}}$  represents available Pd surface sites, and is suggested to be proportional to  $(1 - \theta)$ . According to Langmuir isotherm formula, at equilibrium position,

$$K_a \times P \times (1 - \theta)^2 = K_d \times \theta^2 \quad (2)$$

or

$$\frac{\theta}{(1 - \theta)} = \sqrt{\left(\frac{K_a}{K_d}\right)} \times \sqrt{P} = \sqrt{K} \times \sqrt{P}. \quad (3)$$

where  $K_a$  and  $K_d$  are the adsorption and desorption constants, respectively, and  $P$  is the hydrogen partial pressure. Using Eq. (3), at low coverage of H<sub>2</sub> ( $\theta \ll 1$ ), the change in resistance is given by

$$\frac{\Delta R}{(R_{\text{air}})} \approx \theta \approx \frac{\theta}{(1 - \theta)} = \sqrt{K} \times \sqrt{P}, \quad (4)$$

where  $\Delta R$  is the change in resistance upon H<sub>2</sub> adsorption,  $R_{\text{air}}$  is the baseline resistance, and  $K$  is the equilibrium constant. Hence, response characteristics of the sensor is linearly correlated with the square root of H<sub>2</sub> concentration (Fig. 6b).

Sensor characteristics of the developed Pd nanogap based sensor towards H<sub>2</sub> gases with its fabrication techniques, nanogap size, and maximum concentration of detection, response time, and operating temperature was compared with some relevant sensors from the literature as summarized in Table 3.

Fig. 7a illustrates the selectivity behaviors of the S<sub>6-5</sub> sensor under exposure to 1000 ppm of various tested gasses at room temperature. These include H<sub>2</sub>, nitrogen (N<sub>2</sub>), carbon monoxide (CO), oxygen (O<sub>2</sub>), carbon dioxide (CO<sub>2</sub>), methane (CH<sub>4</sub>), ethane (C<sub>2</sub>H<sub>6</sub>), and nitrogen dioxide (NO<sub>2</sub>) at a concentration of 100 ppm for each individual gas. This nanogap sensor (S<sub>6-5</sub>) demonstrated superior selectivity behavior towards H<sub>2</sub> gas owing to its immense selective absorption capacity of the Pd for H<sub>2</sub> molecules. Remarkably, the hydrogen Pd can dissolve more than 600 times compared to its own volume in relative to other gases that permits Pd to be the most selective material for H<sub>2</sub> gas sensing [2]. Moreover, catalytic activity of the Pd based sensor (e.g. H<sub>2</sub> decomposition) was strongly facilitated because of the exothermic process at room temperature. Importantly, as-fabricated sensor (S<sub>6-5</sub>) resistance was decreased at room temperature and demonstrated p-type behavior with oxidizing gas (NO<sub>2</sub> and O<sub>2</sub>). This phenomenon happened because of the adsorbed oxygen molecules on the sensor surface at open air environment along with the trapped electrons from the conduction band of the sensing layer, leaving oxygen absorbents (O<sub>2</sub><sup>-</sup>) at room temperature, Eq. (5) [42].



When NO<sub>2</sub> gas is introduced, it interacts with the Pd surface, acting as an oxidizing gas that traps electrons and is dissociated in the form of NO, thus leaving oxygen absorbents (O<sub>2</sub><sup>-</sup>). This O<sub>2</sub><sup>-</sup> anion

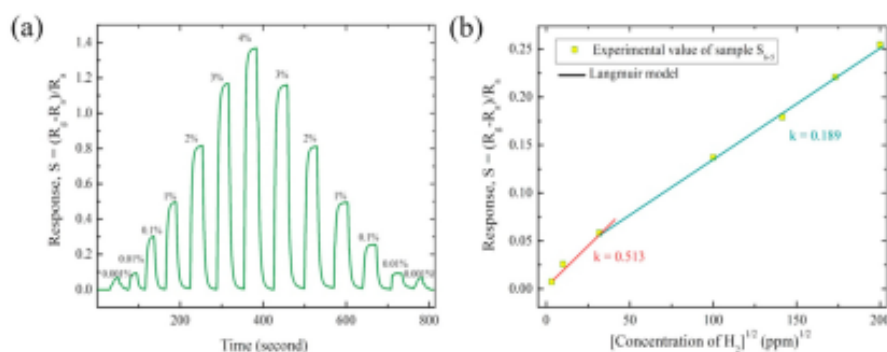


Fig. 6. (a) Real-time resistance sensing response of optimized Pd/Cr gap sensor ( $S_{e-s}$ ) for various H<sub>2</sub> concentrations (10–40,000 ppm) and (b) resultant linear correlation according to the Langmuir model with standard deviation:  $\pm 5\%$  for total number of 10 repetition.

Table 3  
Comparison of different Pd nanogap-based hydrogen sensors.

Fabricated sensor	Fabrication technique	Nanogap size	Response time	Detection limit	Operating temperature	Ref.
Pd (93%)-Ni (7%)/PDMS	Co-sputter/mechanical stretching	1–2 $\mu\text{m}$	0.67 Sec (2% H <sub>2</sub> )	0.1–4%	RT	[37]
Pd (11 nm)/PDMS	Sputter/mechanical stretching	2 $\mu\text{m}$	<1 Sec (1% H <sub>2</sub> )	0.4–4%	RT	[17]
Pd (87.5%)-Ni (12.5%)/PDMS	Co-Sputter/mechanical stretching	100 nm	<1 Sec (1% H <sub>2</sub> )	0.01–10%	RT	[38]
Pd/PDMS	Sputter/mechanical elongation	10 nm	–	0.1–10%	RT	[39]
PMMA/Pd/PMMA/PDMS	O <sub>2</sub> Plasma/sputter/mechanical stretching	420 nm	0.7 Sec (1% H <sub>2</sub> )	0.1–10%	RT	[40]
Pd/PMMA/PET	SAM/STAMP technology	110–130 nm	3.6 Sec (1% H <sub>2</sub> )	0.1–10%	RT	[41]
Pd/Cr/Kapton/Steel	Sputter/mechanical bending	8–80 nm	3 Sec (1% H <sub>2</sub> )	0.001–4%	RT	This study

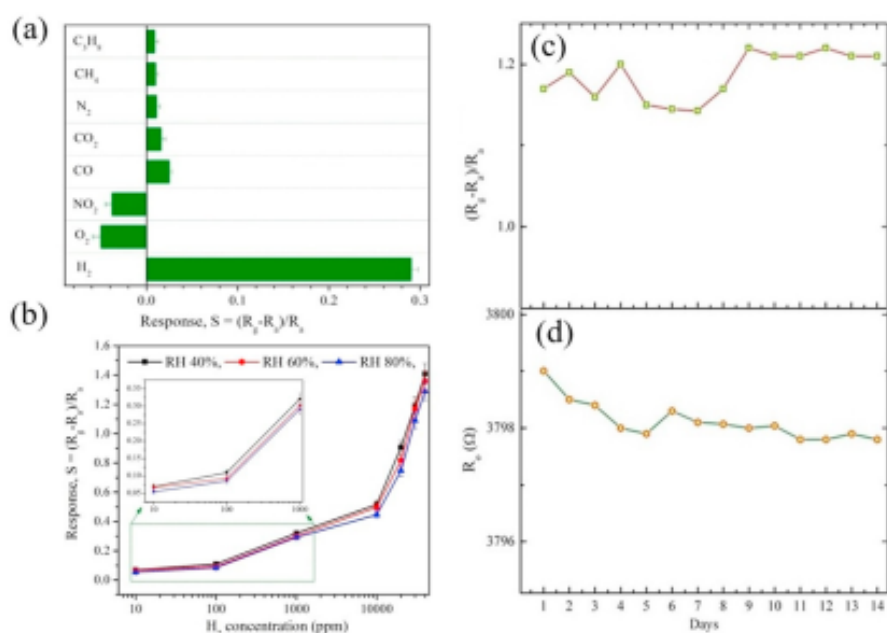
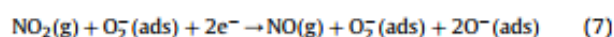
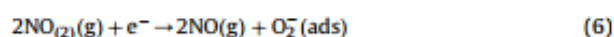


Fig. 7. (a) Selectivity histogram of the controlled ( $S_{e-s}$ ) sensor with numerous test gases. (b) Transient response of the controlled sample ( $S_{e-s}$ ) to three different humidity concentrations at room temperature (25 °C). Time reliance of the controlled sensor (c) response value and (d) baseline resistance value, monitored over a fourteen-day period, where on each day the optimized sensor ( $S_{e-s}$ ) was exposed to 1% of H<sub>2</sub> at room temperature (25 °C).

then becomes an active site to absorb NO<sub>2</sub> molecules. Subsequently, NO can again be converted into NO<sub>2</sub> after reacting with half of an O<sub>2</sub> molecule [43].



In contrast, in an open air environment, H<sub>2</sub> first physisorbs on the Pd surface, dissociates, chemisorbs, and subsequently forms the Pd-hydride (Pd–H) as follows,



The electrical resistivity of PdH<sub>0.7</sub> is almost a factor of 2 higher than that of Pd, which allows the detection of H<sub>2</sub> due to the increase in the resistance of the Pd resistor [1]. Similar process happened for other reducing gases (e.g. CO, CH<sub>4</sub>, C<sub>3</sub>H<sub>8</sub> etc.). As a result, in comparison to other test gases, surface of nanogap sensors is more capable to respond with the bond energy of H<sub>2</sub>. Meanwhile, the H<sub>2</sub> gas sensing characteristics are greatly affected by the presence of water vapor (in humid environment) which reduces the sensor response that can be attributed to the interfering dissociation of H<sub>2</sub> molecules on the Pd surface [44,45]. Due to this phenomenon, for hands-on H<sub>2</sub> sensor, humidity interference is a great concern. Fig. 7b depicts the H<sub>2</sub> gas sensing characteristics of the nanogap sensor (sample S<sub>6-5</sub>) towards different relative humidity (RH) levels at room temperature. The outcomes showed that the humidity interference on the sensing material (Pd) is insignificant because of its aversion toward oxygen molecules, which was a result of the high reduction potential. In addition, Pd/Cr sensing film as well as Kapton show hydrophobic behavior in nature which prevents the presence of water vapor in humid condition during the hydrogenation/dehydrogenation process.

Reliability and durability for nanogap based sensor are major concerns that could lead to material failure feature during sensing. Among several types of materials failure features, it appears that open circuit failure is quite common for nanogap based sensors as a single gap was traversing the full length of the as-fabricated sensor. However, this is not the actual scenario practically. To prove this assumption wrong, in this study approximately various types configured of 20 sensors were used, none of them demonstrated an open circuit failure even upon exposure to H<sub>2</sub> gas severally along with bending. In fact, these as-fabricated nanogap sensors have shown robust behavior. For further assessment, a single as-fabricated nanogap sensor was exposed to 1% concentration of H<sub>2</sub> gas over a 14-day period in an open-air environment. Fig. 7c and d illustrate the tested sensor response as well the effect on its baseline resistance, which demonstrated exceptional durability and stability. In addition, to represent the expression between the laboratory research and the end-user of these research data, the uncertainty of measurement as a function of H<sub>2</sub> concentration and compare that function with a criterion of fitness for purpose was analyzed for as-fabricated (sample S<sub>6-5</sub>) sensor. By using the "law of propagation of uncertainty" principal with standard deviation of ±5% and total 10 number of repetition for each experiments, it was found that effect of the other factors is too small to detect within the uncertainty associated with the particular test for significance [46].

#### 4. Conclusions

In summary, a simple chemo-resistive nanogap H<sub>2</sub> sensing device based on Pd/Cr film cracked was successfully developed by mechanical bending. Optimized thickness (3/2 nm) of Pd/Cr along with different nanogap size (80 nm–5 nm) by varying the curvature radius (1 mm–7mm) was initially confirmed using Comsol Multiphysics Simulation software. Excellent sensor performance was achieved using the as-fabricated controlled sensor (Sample S<sub>6-5</sub>; 3/2 nm Pd/Cr thickness and 15 nm nanogap size) at room

temperature (25 °C) to detect H<sub>2</sub> gas from 10 ppm to 40,000 ppm with a very fast response-recovery time (3/4.5 s). The on-off switching phenomenon of sensor can be imposed to the confinement-induced suppression of a phase transition in the Pd/H system. Furthermore, outcome of this study demonstrates that the characteristics of H<sub>2</sub> sensors based on palladium nanostructures is far beyond the advantages expected from the shorter diffusion distances. The developed method and sensing devices not only demonstrated advanced sensing podium towards broad-range H<sub>2</sub> detection for safety application such as H<sub>2</sub> fueled cars, H<sub>2</sub> filling station, but also acknowledge the impetus to accept this concept to other analytes those are amenable to nanogap sensing technologies.

#### CRediT authorship contribution statement

**Kamrul Hassan:** Writing - original draft. **Tran Thanh Tung:** Supervision, Writing - original draft. **Pei Lay Yap:** contributing with materials characterization and results processing. **Md J. Nine:** Writing - original draft. **Hyeon C. Kim:** contributing with experimental design and reading final paper. **Dusan Losic:** Supervision, Writing - review & editing.

#### Declaration of competing interest

The authors declare that they have no known competing financial interests or personal relationships that could have appeared to influence the work reported in this paper.

#### Acknowledgements

The authors acknowledge the support from the Australian Research Council, (ARC Research Hub for Graphene Enabled Industry Transformation IH 15000003).

#### Appendix A. Supplementary data

Supplementary data to this article can be found online at <https://doi.org/10.1016/j.aca.2020.09.012>.

#### References

- [1] K. Hassan, A.I. Uddin, G.-S. Chung, Fast-response hydrogen sensors based on discrete Pt/Pd bimetallic ultra-thin films, *Sensor. Actuator. B Chem.* 234 (2016) 435–445.
- [2] K. Hassan, G.-S. Chung, Catalytically activated quantum-size Pt/Pd bimetallic core-shell nanoparticles decorated on ZnO nanorod clusters for accelerated hydrogen gas detection, *Sensor. Actuator. B Chem.* 239 (2017) 824–833.
- [3] G.W. Crabtree, M.S. Dresselhaus, M.V. Buchanan, The hydrogen economy, *Phys. Today* 57 (2004) 39–44.
- [4] W.J. Buttner, M.B. Post, R. Burgess, C. Rivkin, An overview of hydrogen safety sensors and requirements, *Int. J. Hydrogen Energy* 36 (2011) 2462–2470.
- [5] J. Kong, M.G. Chapline, H. Dai, Functionalized carbon nanotubes for molecular hydrogen sensors, *Adv. Mater.* 13 (2001) 1384–1386.
- [6] F. Favier, E.C. Walter, M.P. Zach, T. Benter, R.M. Penner, Hydrogen sensors and switches from electrodeposited palladium mesowire arrays, *Science* 293 (2001) 2227–2231.
- [7] T. Xu, M. Zach, Z. Xiao, D. Rosenmann, U. Welp, W. Kwok, G. Crabtree, Self-assembled monolayer-enhanced hydrogen sensing with ultrathin palladium films, *Appl. Phys. Lett.* 86 (2005) 203104.
- [8] J. Van Lith, A. Lassesson, S. Brown, M. Schulze, J. Partridge, A. Ayeshe, A hydrogen sensor based on tunneling between palladium clusters, *Appl. Phys. Lett.* 91 (2007) 181910.
- [9] F. Yang, D.K. Taggart, R.M. Penner, Fast, sensitive hydrogen gas detection using single palladium nanowires that resist fracture, *Nano Lett.* 9 (2009) 2177–2182.
- [10] P. Offermans, H. Tong, C. Van Rijn, P. Merken, S. Brongersma, M. Crego-Calama, Ultralow-power hydrogen sensing with single palladium nanowires, *Appl. Phys. Lett.* 94 (2009) 223110.
- [11] F. Yang, D.K. Taggart, R.M. Penner, Joule heating a palladium nanowire sensor for accelerated response and recovery to hydrogen gas, *Small* 6 (2010) 1422–1429.

- [12] F. Yang, S.-C. Kung, M. Cheng, J.C. Hemminger, R.M. Penner, Smaller is faster and more sensitive: the effect of wire size on the detection of hydrogen by single palladium nanowires, *ACS Nano* 4 (2010) 5233–5244.
- [13] T. Kiefer, F. Favier, O. Vazquez-Mena, G. Villanueva, J. Brugger, A single nanotrench in a palladium microwire for hydrogen detection, *Nanotechnology* 19 (2008) 125502.
- [14] M. Zhao, M. Wong, C. Ong, Achievement of controlled resistive response of nanogapped palladium film to hydrogen, *Appl. Phys. Lett.* 107 (2015), 033108.
- [15] S. Jebri, M. Elbahri, G. Titazu, K. Subannajui, S. Essa, F. Niebelschütz, C.C. Röhlig, V. Cimalla, O. Ambacher, B. Schmidt, Integration of thin-film-fracture-based nanowires into microchip fabrication, *Small* 4 (2008) 2214–2221.
- [16] S. Mubeen, B. Yoo, N.V. Myung, Fabrication of nanoelectrodes and nanojunction hydrogen sensor, *Appl. Phys. Lett.* 93 (2008) 133111.
- [17] J. Lee, J.-S. Noh, S.H. Lee, B. Song, H. Jung, W. Kim, W. Lee, Cracked palladium films on an elastomeric substrate for use as hydrogen sensors, *Int. J. Hydrogen Energy* 37 (2012) 7934–7939.
- [18] T. Kiefer, L. Villanueva, F. Fargier, F. Favier, J. Brugger, Fast and robust hydrogen sensors based on discontinuous palladium films on polyimide, fabricated on a wafer scale, *Nanotechnology* 21 (2010) 505501.
- [19] C.H. Moon, N.V. Myung, E.D. Haberer, Chemiresistive hydrogen gas sensors from gold-palladium nanopropods, *Appl. Phys. Lett.* 105 (2014) 223102.
- [20] S. Cherevko, N. Kulyk, J. Fu, C.-H. Chung, Hydrogen sensing performance of electrodeposited conical palladium nanowire and nanotube arrays, *Sensor. Actuator. B Chem.* 136 (2009) 388–391.
- [21] J. Lee, W. Shim, J.S. Noh, W. Lee, Design rules for nanogap-based hydrogen gas sensors, *ChemPhysChem* 13 (2012) 1395–1403.
- [22] T. Young III, An essay on the cohesion of fluids, *Phil. Trans. Roy. Soc. Lond.* (1805) 65–87.
- [23] D.K. Owens, R. Wendt, Estimation of the surface free energy of polymers, *J. Appl. Polym. Sci.* 13 (1969) 1741–1747.
- [24] K. Hassan, A.I. Uddin, G.-S. Chung, Hydrogen sensing properties of Pt/Pd bimetal decorated on highly hydrophobic Si nanowires, *Int. J. Hydrogen Energy* 41 (2016) 10991–11001.
- [25] L. Zhang, E.F. McCullen, M.H. Rahman, J.S. Thakur, L. Rimai, R.J. Baird, R. Naik, G. Newaz, G.W. Auner, K.S. Ng, Response to hydrogen of a metal/AlN/Si thin film structure: effects of composition and structure of a combination Pd–Cr gate, *Sensor. Actuator. B Chem.* 113 (2006) 843–851.
- [26] A. Kulkarni, L. Chang, Electrical and structural characteristics of chromium thin films deposited on glass and alumina substrates, *Thin Solid Films* 301 (1997) 17–22.
- [27] R.A. Matula, Electrical resistivity of copper, gold, palladium, and silver, *J. Phys. Chem. Ref. Data* 8 (1979), 1147–1298.
- [28] B. Ealet, B. Robrieux, E. Gillet, A surface analytical study of the formation and adhesion of chromium films on alumina, *J. Adhes. Sci. Technol.* 6 (1992) 1221–1231.
- [29] F. Lewis, *The Hydrogen Palladium System*, Academic Press, London, 1967.
- [30] P.F. Ruths, S. Ashok, S.J. Fonash, J.M. Ruths, A study of Pd/Si MIS Schottky barrier diode hydrogen detector, *IEEE Trans. Electron. Dev.* 28 (1981) 1003–1009.
- [31] K. Yoshimura, Y. Yamada, M. Okada, Hydrogenation of Pd capped Mg thin films at room temperature, *Surf. Sci.* 566 (2004) 751–754.
- [32] H. Conrad, G. Ertl, E. Latta, Adsorption of hydrogen on palladium single crystal surfaces, *Surf. Sci.* 41 (1974) 435–446.
- [33] T. Mitsui, M. Rose, E. Fomin, D. Ogletree, M. Salmeron, Dissociative hydrogen adsorption on palladium requires aggregates of three or more vacancies, *Nature* 422 (2003) 705.
- [34] E. Lee, J.M. Lee, E. Lee, J.-S. Noh, J.H. Joe, B. Jung, W. Lee, Hydrogen gas sensing performance of Pd–Ni alloy thin films, *Thin Solid Films* 519 (2010) 880–884.
- [35] C. Langhammer, I. Zorić, B. Kasemo, B.M. Clemens, Hydrogen storage in Pd nanodisks characterized with a novel nanoplasmonic sensing scheme, *Nano Lett.* 7 (2007) 3122–3127.
- [36] Y. Sun, H.H. Wang, High-performance, flexible hydrogen sensors that use carbon nanotubes decorated with palladium nanoparticles, *Adv. Mater.* 19 (2007) 2818–2823.
- [37] J. Lee, W. Shim, E. Lee, J.S. Noh, W. Lee, Highly mobile palladium thin films on an elastomeric substrate: nanogap-based hydrogen gas sensors, *Angew. Chem. Int. Ed.* 50 (2011) 5301–5305.
- [38] E. Lee, J. Lee, J.-S. Noh, W. Kim, T. Lee, S. Maeng, W. Lee, Pd–Ni hydrogen sponge for highly sensitive nanogap-based hydrogen sensors, *Int. J. Hydrogen Energy* 37 (2012) 14702–14706.
- [39] H. Jung, B. Jang, W. Kim, J.-S. Noh, W. Lee, Ultra-sensitive, one-time use hydrogen sensors based on sub-10 nm nanogaps on an elastomeric substrate, *Sensor. Actuator. B Chem.* 178 (2013) 689–693.
- [40] B. Jang, K.Y. Lee, J.-S. Noh, W. Lee, Nanogap-based electrical hydrogen sensors fabricated from Pd-PMMA hybrid thin films, *Sensor. Actuator. B Chem.* 193 (2014) 530–535.
- [41] Y. Pak, N. Lim, Y. Kumaresan, R. Lee, K. Kim, T.H. Kim, S.M. Kim, J.T. Kim, H. Lee, M.H. Ham, Palladium nanoribbon array for fast hydrogen gas sensing with ultrahigh sensitivity, *Adv. Mater.* 27 (2015) 6945–6952.
- [42] S.-W. Choi, S.-H. Jung, S.S. Kim, Significant enhancement of the NO<sub>2</sub> sensing capability in networked SnO<sub>2</sub> nanowires by Au nanoparticles synthesized via  $\gamma$ -ray radiolysis, *J. Hazard Mater.* 193 (2011) 243–248.
- [43] U. Yaqoob, D.-T. Phan, A.I. Uddin, G.-S. Chung, Highly flexible room temperature NO<sub>2</sub> sensor based on MWCNTs/WO<sub>3</sub> nanoparticles hybrid on a PET substrate, *Sensor. Actuator. B Chem.* 221 (2015) 760–768.
- [44] Y.K. Gautam, R. Jain, S.K. Tanwar, R. Agrawal, R. Chandra, Studies on hydrogen sensing properties of nanostructured Pd and Pd/Mg thin films prepared by pulsed laser deposition, *Sensor. Actuator. B Chem.* 176 (2013) 453–459.
- [45] K. Hassan, A.I. Uddin, G.-S. Chung, Mesh of ultrasmall Pd/Mg bimetallic nanowires as fast response wearable hydrogen sensors formed on filtration membrane, *Sensor. Actuator. B Chem.* 252 (2017) 1035–1044.
- [46] M. Thomson, S. Ellison, R. Wood, Harmonized guidelines for single-laboratory validation of methods of analysis, *Pure Appl. Chem.* 74 (2002) 835.

## Supporting information for

**Fast response hydrogen gas sensor based on Pd/Cr nanogaps fabricated by a single-step bending deformation**

Kamrul Hassan<sup>1,2</sup>, Tran Thanh Tung<sup>1,2</sup>, Pei Lay Yap<sup>1,2</sup>, Md J. Nine<sup>1,2</sup>, Hyeon C. Kim<sup>3</sup>, Dusan Losic<sup>1,2\*</sup>

<sup>1</sup>*School of Chemical Engineering and Advanced Materials, The University of Adelaide, SA 5005, Australia*

<sup>2</sup>*ARC Research Hub for Graphene Enabled Industry Transformation, The University of Adelaide, SA 5005, Australia*

<sup>3</sup>*School of Electrical Engineering, University of Ulsan, 93 Daehak-ro, Nam-gu, Ulsan 680-749, Republic of Korea*

\*Corresponding authors: email [dusan.losic@adelaide.edu.au](mailto:dusan.losic@adelaide.edu.au)

Table S1: Deposition parameters of the RF magnetron sputtering.

Parameters	Conditions	
	Pd	Cr
Target	Pd	Cr
Gas	100% Ar	100% Ar
Sputtering pressure (mTorr)	9	9
Target-substrate distance (cm)	8	5
RF power (W)	110	150
Substrate temperature (°C)	RT	RT
Deposition rate	1 nm/3.5 s	0.017 nm/1 s

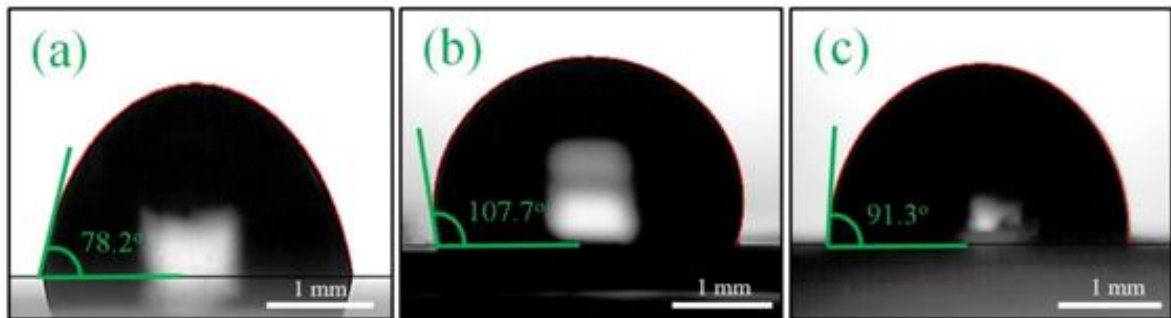
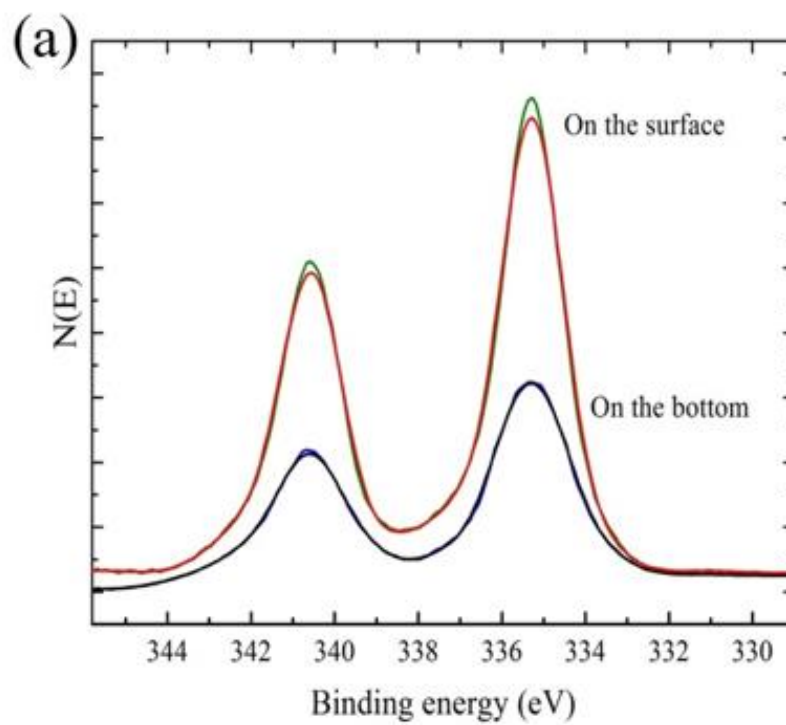


Fig. S-1. The water droplet contact angle images of (a) kapton tape, (b) Pd film on the kapton tape, and (c) Pd/Cr film on /Kapton tape.



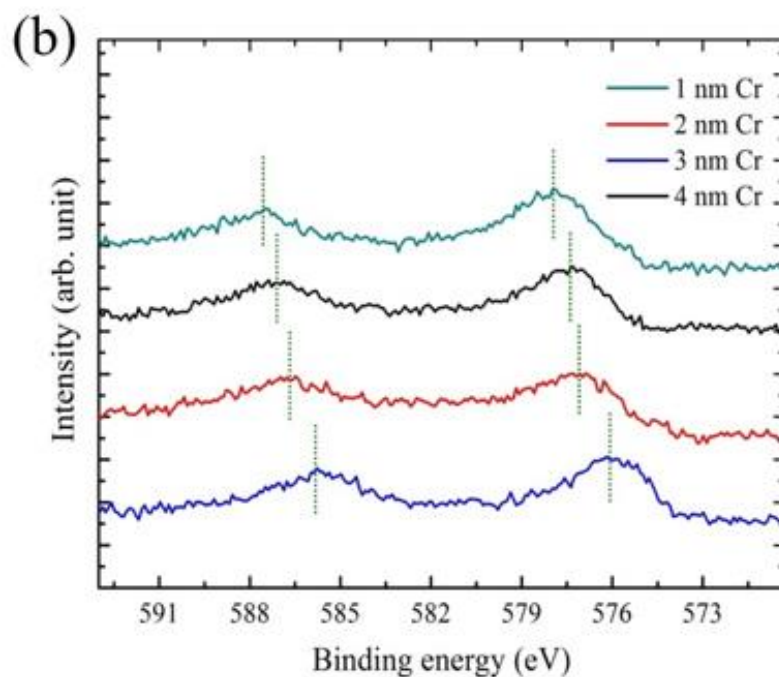


Fig. S-2. XPS high resolution scans of the (a) Pd 3d and (b) Cr 2p for binding energy regions of the Pd/Cr.

Table S3: Atomic ratio between Pd/Cr (obtained from the XPS wide scan).

Element	At%	Ratio
Pd 3d	31.89	11.11
Cr 2P	2.87	



# Chapter 7

## Conclusion and future directions

---

**I**n this chapter, the main findings and future direction of this Ph.D. thesis are summarized. This includes the summary of the conducted experiments, contributions of each chapter, and conclusions of the researches carried out in this project. In addition, the recommendation for future work and directions are provided.

---

## 7.1 Conclusions

This Ph.D. thesis attempted to address the challenges in the sensor application for detecting VOC/gas through developing some advanced sensor devices. In essence, this thesis is devoted to the development of advanced VOC/gas sensor devices by introducing a new approach of sensor fabrication method by optimizing sensor design geometries. The main findings of this research are outlined below:

➤ **Chapter 3** describes an underutilized 3D extrusion-printing technique for the fabrication of chemo-resistive patterned electrodes, which is fabricated by using specially designed graphene ink to achieve larger SA/V aspect ratio for enhanced volatile organic compound (VOC) detection. Following are the main findings and contributions of this chapter:

- The new graphene ink combining ethyl cellulose and Cyrene provides a facile route to obtain environmentally friendly, sustainable, low cost sensing devices fabricated by high quality 3D extrusion printing.
- The graphene ink has been printed as patterned structures with high-resolution. After annealing at 250 °C for 30 min, these patterned structures shows low resistivity (70  $\Omega$ .cm).
- Patterns printed in the form of lines that are used as a chemoresistive sensing electrodes for VOC detection at room temperature. Results show high sensitivity for different VOCs (acetone, ethanol, and methanol) compared with a sensor prepared by a conventional drop casting method with the same ink. In terms of selectivity, this printed sensor shows higher sensitivity towards ethanol due to the polarity and permittivity of the printed ink. The printed sensors also showed a broad detection range of 5-30 ppm with good linearity for ethanol at room temperature.

➤ **Chapter 4** described the development of bio-inspired fractal designed VOC sensors, fabricated by the extrusion printing process. Following are the main findings and contributions of this chapter:

- The fabrication of three fractal designed sensors such as Sierpinski, Peano, and Hilbert was fabricated using specially formulated graphene ink by extrusion printing technique to achieve stable structures of fabricated patterns with high SA/V aspect ratio.
- The graphene ink formulated by combining ethyl-cellulose and Cyrene provides a facile route to achieve sustainable, environmentally friendly, low cost sensing modules. This graphene ink was successfully used for printing at high-resolution

biomimetic fractal patterned architectures with resistivity as low as  $70 \Omega\cdot\text{cm}$  after annealing at  $250^\circ\text{C}$  for 30 min, as a chemo-resistive sensing device for VOCs detection at room temperature.

- Performance characteristics evaluated for Hilbert designed sensor to ethanol vapour showed fast response time ( $\sim 6$  sec @ 30 ppm), high response value (14% @ 30 ppm), broad detection limit (5-100 ppm), and high selectivity to ethanol vapour at room temperature ( $20^\circ\text{C}$ ) among a set of VOCs (ethanol, methanol, and acetone), which was prominent than Sierpinski, Peano, and conventional interdigitate designed VOC sensors characteristics. Furthermore, as-fabricated sensor exhibited sensitivity to mechanical deformation, and illustrated enhanced response-time ( $\sim 4.5$  sec @ 30 ppm) to ethanol vapour at room temperature for positive bending.
  - The main significance of this chapter is to explore the potential of this Hilbert designed sensor for real-field application. For practical application experiment, real-time monitoring of ethanol evolved from rotten strawberry confirmed the concept and the feasibility of our developed sensing device for real-life application.
- **Chapter 5** describes the advancement of a CNT-graphene-based sensor array with embedded MXene heater, fabricated by an extrusion printing technique for detecting trace amounts of  $\text{NO}_2$  gas. Besides the sensor array, the development of new embedded MXene heater prepared by spray coating on the back of the printed sensor array also demonstrated, which nicely overcomes the challenge of integrating a heater within the sensor system to achieve the optimal operating temperature with low power consumption for selective detection of  $\text{NO}_2$  gas. Following are the main findings and contributions of this chapter:
- The specially designed hybrid ink was formulated by combining 1D CNT and 2D graphene with Cyrene as a solvent to provide a facile route to achieve sustainable, environmentally friendly, low cost sensors fabrication.
  - The new CNT-graphene ink was successfully used for printing at high-resolution compact, array patterned architectures with resistivity as low as  $\sim 70 \Omega\cdot\text{cm}^{-1}$  after annealing at  $70^\circ\text{C}$  for 30 min, as a chemo-resistive sensing device for  $\text{NO}_2$  detection.
  - By controlling the loading of MXene nanosheets and PEDOT:PSS, the embedded heater into the sensor systems achieved temperature up to  $73^\circ\text{C}$  within less than 45 sec from a 12 V voltage supply at a power of 2W.

- Excellent performance characteristics were demonstrated for the sensor array towards NO<sub>2</sub> gas as highlighted by fast recovery time (~2.9 min at 5 ppm), good response time (7.6 min at 5 ppm), high response value (8 at 5 ppm), a detection limit of 1 ppm, excellent stability, and reproducibility with high selectivity towards NO<sub>2</sub> gas at temperature (65 °C) in the presence of various gases (H<sub>2</sub>, CO<sub>2</sub>), and a set of VOCs (ethanol, methanol, and acetone).
- **Chapter 6** describes the synthesis and characterization Pd/Cr nanogap based H<sub>2</sub> sensing device, which was successfully developed by mechanical bending by overcoming the challenges of complex nanogap fabrication techniques. Following are the main findings and contributions of this chapter:
- Optimized thickness (3/2 nm) of Pd/Cr along with different nanogap size (80 nm-5 nm) by varying the curvature radius (1 mm-7mm) was initially confirmed using Comsol Multiphysics Simulation software. Excellent
  - Excellent sensor performance was achieved using the as-fabricated controlled sensor (Sample S6- 5; 3/2 nm Pd/Cr thickness and 15 nm nanogap size) at room temperature (25 C) to detect H<sub>2</sub> gas from 10 ppm to 40,000 ppm with a very fast response-recovery time (3/4.5 s).
  - The on-off switching phenomenon of sensor can be imposed to the confinement-induced suppression of a phase transition in the Pd/H system. Furthermore, outcome of this study demonstrates that the characteristics of H<sub>2</sub> sensors based on palladium nanostructures is far beyond the advantages expected from the shorter diffusion distances.
  - The developed method and sensing devices not only demonstrated advanced sensing podium towards broad-range H<sub>2</sub> detection for safety application such as H<sub>2</sub> fueled cars, H<sub>2</sub> filling station, but also acknowledge the impetus to accept this concept to other analytes those are amenable to nanogap sensing technologies.

## 7.2 Some challenges of performed PhD study

The key challenges during this PhD work is outlined below.

**Chapter 3** aims to develop a chemo-resistive sensor device for detecting VOC biomarkers employing graphene inks composed of pristine graphene and ethyl-cellulose by using 3D

extrusion printer. The key challenges to achieve proposed objectives goals reported in this chapter includes:

- ✓ Medium annealing temperature is required to reduce the conductivity of the printed patterns which limits the applicability of various temperature sensitive substrate.
- ✓ Limited VOC analytes detections have conducted in this study due to the limitation of advanced calibration system and VOC/gas standards. Therefore, for further studies, it is required to have an advanced calibration system.
- ✓ Achieved detection limit up to ppm level for selective VOCs, which need to improve up to ppb level by improving the sensor architecture.
- ✓ Limitation of selection the polymer that is used in ink formulations (as not every polymer can use for inks, some polymer design for VOC capture but cannot use for ink formulations).

**Chapter 4** aims to impart exploit the extraordinary properties of fractal design for advancing the performance of chemo-resistive sensors. The key challenges of this study includes:

- ✓ Lack of comprehensive fractal design studies such as theoretical calculations, and simulation modelling.
- ✓ Limited VOC analytes detections have conducted in this study due to the limitation of advanced calibration system and VOC standards.

**Chapter 5** aims to develop extrusion printed CNT-graphene sensor array with embedded MXene/PEDOT:PSS heater for enhanced NO<sub>2</sub> sensing at low temperature. The key challenges of this study includes:

- ✓ Lack of implementation of electrical connections within the sensor array to monitor the gas sensing signals simultaneously.
- ✓ This work include embedded heater within the sensor array, which also limits the uses of various temperature sensitive substrate for sensor devices.
- ✓ Lack of study on the effect of MXene nanosheets on the composite materials of heater thoroughly.

**Chapter 6** concentrated on developing a fast response hydrogen gas sensor based on Pd/Cr nanogaps fabricated by a single-step bending deformation technique. The key challenges of this study includes:

- ✓ The temperature effect on the fabricated sensors have not addressed in this work.

- ✓ Single bending deformation technique limits the range of application for this nanogap based H<sub>2</sub> sensor..

### 7.3 Recommendations for Future work

This Ph.D. thesis made a significant contribution to the development of new-generation chemoresistive sensors that highlight the advanced sensor fabrication methods including printing technology for VOC/gas sensing application through employing different polymers and nanomaterials. This work opened new frontiers that deserved further research in the future. Thus, several recommendations and pathways are highlighted here for future work to fully realize the potential of new-generation VOC/gas sensors:

- 1. Design of different nanocomposite sensing materials through employing other types of 2D nanomaterials and their hybrids:** Since 2D nanomaterials are at the infancy stage, only a few types of 2D nanomaterials have been exploited in the area of VOC/gas sensing application. Thus, as the family of 2D nanomaterials is expanding, it is expected new types of 2D nanomaterials will be exploited in the design of VOC/gas sensing materials. In addition, obtaining synergistic properties resulting from the combining of different nanomaterials is another emerging trend, which is expected to grow in the future. Such synergistic properties hold great promise for enhancing the efficacy of printed functional constructs, necessitating more efforts to combine different nanomaterials. Taking advantage of the extraordinary features of 2D nanomaterials to add new functionality to the conventional sensing material is the current trend in the developments of 2D nanocomposite based sensing devices.
- 2. Utilization of conducting polymer for hybridizing with 2D materials as a future pathway for VOC/gas sensing:** Conducting polymers as a sensing materials provides a versatile pathway for VOC/gas sensor development by including gas adsorption induced through the orientation change of molecular chains of polymers and doping of proton/charge. Besides, these conductive polymers also suitable for numerous solution processing methods and ink formulation techniques. Importantly, polymers could be easily functionalized with anticipated surface groups for realizing particular gas recognition compared to inorganic nanomaterials. The negative side of polymers is their relatively low conductivity, which can be overcome by forming composites with 2D materials such as graphene, MXene.

- 3. Improving sensor designs and performances for advanced VOC/gas sensing applications:** During the time of designing sensing materials for electronic gas sensor application, among several parameters considerable key parameter is the trade-off between the surface energy and sensor recovery, high conductivity and sensitivity, and the reactivity and stability of the sensing material. Besides, for real-life applications, efforts in advancing these functional sensing materials should be predominantly devoted for improving their durability and stability, especially under conditions of changing temperature, humidity, and mechanical strain. New materials or advanced material architectures that combine sensitive electronic characteristics, structural stability, and surface activities are need to be explored (e.g. versatile MOF materials, materials related to MXene family).
- 4. Introducing multivariable sensor for advanced VOC/gas sensing:** Majority of the printed gas sensors developed in past years mainly based on the single output sensors that reflects vary poor selectivity due to the sensor drift and unstable output in presence of unknown interferences, which is a key issue for their commercialisation from research to industrial scale. To counter the above challenges of the conventional sensors faces, multivariable sensors are required that promises as a new generation gas sensor system. A multivariable sensor contains a single sensing material with multi-response mechanisms to various gases, coupled with a multivariable transducer for producing independent, for instance, electrical, electrochemical, and optical outputs corresponding to the numerous sensing responses. Multivariable gas sensors can distinguishes particular VOC/gas among several gases in a mixture by showing the high response value. Nevertheless, it is challenging to fabricate multivariable VOC/gas sensors by employing printing technology that required coordinated advancements in VOC/gas sensing materials, printable ink formulation, sensor designs, and importantly, printing resolution. High quality semiconductor crystals, which are able for responding to various VOCs/gases both electrically and optically can overcome the above challenges of multivariable sensor. Multivariable VOC/gas sensors are therefore ideally poised to replace conventional gas sensors in the future.
- 5. Introducing machine learning for advanced neural VOC/gas sensor system:** Although multivariable sensors and sensor arrays united with computational methods for processing data has been facilitated enhanced sensor characteristics, VOC/gas detection scenarios with unknown and complex gas environment may need additional data collection, modelling and machine learning. Traditional learning algorithms such as the neural network with the

nonlinear approximation capability is able to conduct both quantitative and qualitative. Advancement in machine learning for enabling the generalization of information based on current accumulated data can permit forecasting unseen situations, offering new chances for compensating the boundaries of materials networks via powerful computational methods. Consequently, an amalgamation of machine learning for enhanced characteristics and printing for the large scale sensor fabrication is anticipated in future for a broad range of internet of things (IoT) and automated sensor networks.